

---

---

---

**NEW NANOMATERIALS  
TO BOOST  
NONLINEAR AND ULTRAFAST  
NANOPHOTONICS**

---

---

---

Benjamin Tilmann  
München 2023





---

# **New Nanomaterials to Boost Nonlinear and Ultrafast Nanophotonics**

**Benjamin Tilmann**

---

Dissertation  
to obtain the doctoral degree of  
natural sciences (Dr. rer. nat.)  
at the Faculty of Physics  
of the  
Ludwig-Maximilians-Universität München

submitted by  
Benjamin Tilmann  
from München

München, 25/05/2023

Erstgutachter: Professor Dr. Stefan A. Maier  
Zweitgutachter: Professor Dr. Jonathan Finley  
Tag der Prüfung : 11.07.2023

---

# Neue Nanomaterialien für nichtlineare und ultraschnelle Nanophotonik

Benjamin Tilmann

---

Dissertation  
zur Erlangung des Doktorgrads der  
Naturwissenschaften (Dr. rer. nat.)  
an der Fakultät für Physik  
an der  
Ludwig-Maximilians-Universität München

eingereicht von  
Benjamin Tilmann  
aus München

München, 25/05/2023

First referee: Professor Dr. Stefan A. Maier  
Second referee: Professor Dr. Jonathan Finley  
Date of the oral examination : 11.07.2023

*This work is dedicated to the memory of Christel and Hans.*



---

**Publications part of this thesis**

- Benjamin Tilmann, Tahiyat Huq, Thomas Possmayer, Jakub Dranczewski, Bert Nickel, Haizhong Zhang, Leonid Krivitsky, Arseniy I. Kuznetsov, Leonardo de S. Menezes, Stefano Vezzoli, Riccardo Sapienza, and Stefan A. Maier  
*Comparison of harmonic generation from crystalline and amorphous gallium phosphide nanofilms*  
Advanced Optical Materials (accepted, 2023)
- Ibrahim Abdelwahab, Benjamin Tilmann, Yaze Wu, David Giovanni, Ivan Verzhbitskiy, Menglong Zhu, Rodrigo Berté, Fengyuan Xuan, Leonardo de S. Menezes, Goki Eda, Tze Chien Sum, Su Ying Quek, Stefan A. Maier, Kian Ping Loh  
*Giant second-harmonic generation in ferroelectric NbCl<sub>2</sub>*  
Nature Photonics 16(9), 644-650 (2022)
- Benjamin Tilmann, Avanindra Kumar Pandeya, Gustavo Grinblat, Leonardo de S. Menezes, Yi Li, Chandra Shekhar, Claudia Felser, Stuart S.P. Parkin, Amilcar Bedoya-Pinto, Stefan A. Maier  
*Ultrafast Sub-100 fs All-Optical Modulation and Efficient Third-Harmonic Generation in Weyl Semimetal Niobium Phosphide Thin Films*  
Advanced Materials 34(15), 2106733 (2022)
- Benjamin Tilmann, Gustavo Grinblat, Rodrigo Berté, Mehmet Özcan, Viktoria F. Kunzelmann, Bert Nickel, Ian D. Sharp, Emiliano Cortés, Stefan A. Maier, Yi Li  
*Nanosstructured amorphous gallium phosphide on silica for nonlinear and ultrafast nanophotonics.*  
Nanoscale Horizons 6(11), 1500-1508 (2020)
- Gustavo Grinblat, Haizhong Zhang, Michael P. Nielson, Leonid Krivitsky, Rodrigo Berté, Yi Li, Benjamin Tilmann, Emiliano Cortés, Rupert F. Oulton, Arseniy I. Kuznetsov, Stefan A. Maier  
*Efficient ultrafast all-optical modulation in a nonlinear crystalline gallium phosphide nanodisk at the anapole excitation.*  
Science Advances 6(34), eabb3123 (2020)

**Publications not included in this thesis**

- Romain Tirole, Stefano Vezzoli, Emanuele Galiffi, Iain Robertson, Dries Maurice, Benjamin Tilmann, Stefan A. Maier, John B. Pendry, Riccardo Sapienza  
*Double-slit time diffraction at optical frequencies*  
Nature Physics (2023)
- Ibrahim Abdelwahab, Benjamin Tilmann, Xiaoxu Zhao, Ivan Verzhbitskiy, Rodrigo Berté, Goki Eda, William L. Wilson, Gustavo Grinblat, Leonardo de S. Menezes, Kian Ping Loh, Stefan A. Maier  
*Highly Efficient Sum-Frequency Generation in Niobium Oxydichloride NbCl<sub>2</sub> Nanosheets*  
Advanced Optical Materials 11(7), 2202833 (2023)

- Lucca Kühner, Luca Sortino, Benjamin Tilmann, Thomas Weber, Kenji Watanabe, Takashi Taniguchi, Stefan A. Maier, Andreas Tittl  
*High-Q Nanophotonics over the Full Visible Spectrum Enabled by Hexagonal Boron Nitride Metasurface*  
Advanced Materials 35(13), 2209688 (2023)
- Romain Tirole, Emanuele Galiffi, Jakub Dranczewski, Taran Attavar, Benjamin Tilmann, Yao-Ting Wang, Paloma A. Huidobro, Andrea Alú, John B. Pendry, Stefan A. Maier, Stefano Vezzoli, Riccardi Sapienza  
*Saturable Time-Varying Mirror Based on a  $n$  Epsilon-Near-Zero Material*  
Physical Review Applied 18(5), 054067 (2022)
- Thomas Possmayer, Benjamin Tilmann, Lauro J.Q. Maia, Stefan A. Maier, Leonardo de S. Menezes  
*Second to fifth harmonic generation in individual  $\beta$ -barium borate nanocrystals*  
Optics Letters 47(7), 1826 (2022)

# Contents

|  |           |
|--|-----------|
| Zusammenfassung                                      | xxi       |
| Abstract   | xxiii     |
| <b>1 Introduction</b>                                | <b>1</b>  |
| <b>2 Fundamentals</b>                                | <b>9</b>  |
| 2.1 Theory of electrodynamics                        | 9         |
| 2.1.1 Maxwell's equations in nonmagnetic media       | 9         |
| 2.1.2 The linear refractive index                    | 11        |
| 2.2 Optical properties of materials                  | 13        |
| 2.2.1 Metals   | 13        |
| 2.2.2 Dielectric materials                           | 14        |
| 2.2.3 Two-dimensional materials                      | 15        |
| 2.2.4 Weyl semimetals                                | 16        |
| 2.3 Light interaction at the nanoscale               | 16        |
| 2.3.1 Mie theory                                     | 16        |
| 2.3.2 Optical resonances and the anapole excitation  | 19        |
| 2.4 Concepts of nonlinear optics                     | 22        |
| 2.4.1 High-harmonic generation                       | 22        |
| 2.4.2 The nonlinear refractive index                 | 25        |
| 2.5 Basics of ultrafast optics                       | 27        |
| 2.5.1 Transform-limited pulses and chirp             | 27        |
| 2.5.2 Dispersion effects                             | 29        |
| 2.5.3 Multiphoton intrapulse interference phase scan | 30        |
| 2.6 Optical Simulations                              | 33        |
| 2.6.1 Finite-difference time-domain simulations      | 33        |
| 2.6.2 The finite-element method                      | 35        |
| <b>3 Methodology</b>                                 | <b>39</b> |
| 3.1 Nanofabrication                                  | 39        |
| 3.1.1 Thin film deposition                           | 39        |
| 3.1.2 Electron beam lithography                      | 41        |

|          |   |            |
|----------|---|------------|
| 3.1.3    | Reactive ion etching . . . . .  | 42         |
| 3.2      | Material characterization . . . . .                                       | 43         |
| 3.3      | Optical characterization . . . . .  | 46         |
| 3.3.1    | Spectral ellipsometry . . . . .   | 46         |
| 3.3.2    | Nonlinear optical measurements and HHG . . . . .                          | 48         |
| 3.4      | Pump-probe spectroscopy . . . . .   | 50         |
| 3.4.1    | White-light generation and pulse compression . . . . .                    | 50         |
| 3.4.2    | Optical delay line and signal detection . . . . .                         | 53         |
| <b>4</b> | <b>Amorphous and crystalline gallium phosphide nanostructures</b>         | <b>55</b>  |
| 4.1      | Nonlinear characterization of GaP thin films . . . . .                    | 57         |
| 4.1.1    | Structural characterization of GaP thin films . . . . .                   | 58         |
| 4.1.2    | SHG from crystalline GaP . . . . .  | 58         |
| 4.1.3    | Extraction of $\chi^{(2)}$ . . . . .                                      | 61         |
| 4.1.4    | THG from GaP films and extraction of $\chi^{(3)}$ . . . . .               | 64         |
| 4.1.5    | Tuning of the nonlinear signal . . . . .                                  | 66         |
| 4.1.6    | High-harmonic generation from GaP thin films . . . . .                    | 67         |
| 4.1.7    | Conclusion . . . . .  | 67         |
| 4.1.8    | Experimental details and supplementary material . . . . .                 | 68         |
| 4.2      | Amorphous gallium phosphide nanopatches . . . . .                         | 71         |
| 4.2.1    | Nanofabrication and structural analysis . . . . .                         | 71         |
| 4.2.2    | Enhanced SHG from a-GaP nanopatches . . . . .                             | 74         |
| 4.2.3    | Nondegenerate pump-probe spectroscopy . . . . .                           | 77         |
| 4.2.4    | Conclusion . . . . .  | 79         |
| 4.2.5    | Experimental details and supplementary material . . . . .                 | 80         |
| 4.3      | Crystalline gallium phosphide nanostructures . . . . .                    | 83         |
| 4.3.1    | Nanodiscs at the anapole excitation . . . . .                             | 83         |
| 4.3.2    | All-optical switching with c-GaP nanodiscs . . . . .                      | 85         |
| 4.3.3    | Conclusion . . . . .  | 89         |
| 4.3.4    | Experimental details and supplementary material . . . . .                 | 89         |
| <b>5</b> | <b>Nanofilms of the Weyl semimetal niobium phosphide</b>                  | <b>93</b>  |
| 5.1      | Fabrication of niobium phosphide thin films . . . . .                     | 94         |
| 5.2      | Third-harmonic generation boosted by topological surface states . . . . . | 95         |
| 5.3      | Ultrafast optical response influenced by the Weyl cone . . . . .          | 99         |
| 5.4      | Conclusion . . . . .  | 104        |
| 5.5      | Experimental details and supplementary material . . . . .                 | 104        |
| <b>6</b> | <b>Ferroelectric semiconductor nanoflakes</b>                             | <b>107</b> |
| 6.1      | Fabrication and structural characterization . . . . .                     | 108        |
| 6.2      | Second-harmonic generation of NbOI <sub>2</sub> nanoflakes . . . . .      | 112        |
| 6.3      | Manipulation of the nonlinear optical response . . . . .                  | 119        |
| 6.4      | Conclusion . . . . .  | 123        |

---

|          |   |            |
|----------|---|------------|
| 6.5      | Experimental details and supplementary material . . . . .             | 123        |
| <b>7</b> | <b>Summary and Outlook</b>  | <b>127</b> |
| 7.1      | Outlook: frequency conversion at the nanoscale . . . . .              | 129        |
| 7.2      | Outlook: all-optical switching . . . . .                              | 130        |
| <b>A</b> | <b>Supplementary Information</b>                                      | <b>133</b> |
| A.1      | Fabrication - parameters . . . . .                                    | 133        |
| A.2      | Fabrication of c-GaP nanostructures . . . . .                         | 133        |
| <b>B</b> | <b>Supplementary works</b>  | <b>135</b> |
| B.1      | Hybrid nanostructures made of GaP and ITO . . . . .                   | 135        |
| B.1.1    | From classic to photonic gap antenna . . . . .                        | 136        |
| B.1.2    | Comparison and discussion of the photonic gap antenna . . . . .       | 139        |
| B.1.3    | Conclusion . . . . .  | 143        |
| B.2      | Time-varying experiments with indium tix oxide metasurfaces . . . . . | 145        |
| B.2.1    | Saturable time-varying mirror based on an ENZ material . . . . .      | 145        |
| B.2.2    | Double-slit time diffraction at optical frequencies . . . . .         | 153        |
| <b>C</b> | <b>Publisher Permissions</b>  | <b>163</b> |
|          | <b>Bibliography</b>   | <b>167</b> |
|          | <b>Acknowledgements</b>   | <b>196</b> |



# List of Figures

|      |  |    |
|------|--|----|
| 1.1  | A nonlinear mirror . . . . .                               | 1  |
| 1.2  | Applications of nonlinear optics . . . . .                 | 2  |
| 1.3  | Range of optical radiation . . . . .                       | 3  |
| 1.4  | Ultrafast time scales . . . . .                            | 6  |
| 2.1  | Reflection at an interface between two materials . . . . . | 11 |
| 2.2  | Differentiation of different material classes . . . . .    | 13 |
| 2.3  | Dielectric function of silicon and gold . . . . .          | 14 |
| 2.4  | Sketch of Mie theory . . . . .                             | 17 |
| 2.5  | Simulation of scattering according to Mie theory . . . . . | 20 |
| 2.6  | Simulation of the anapole in a silicon nanodisc . . . . .  | 21 |
| 2.7  | Sketch of HHG . . . . .                                    | 23 |
| 2.8  | Sketch of TPA and subsequent 2PPL . . . . .                | 26 |
| 2.9  | Illustration of linear chirp . . . . .                     | 27 |
| 2.10 | Overview over an ultrafast pulse train . . . . .           | 28 |
| 2.11 | Spatial and temporal dispersion . . . . .                  | 29 |
| 2.12 | Autocorrelation and FROG . . . . .                         | 31 |
| 2.13 | Working principle of MIIPS . . . . .                       | 32 |
| 2.14 | Yee cell in one dimension . . . . .                        | 33 |
| 2.15 | Visualization of the TFSF source . . . . .                 | 35 |
| 2.16 | Mesh of FDTD and FEM . . . . .                             | 36 |
| 3.1  | Thin film fabrication techniques . . . . .                 | 41 |
| 3.2  | Fabrication work flow . . . . .                            | 42 |
| 3.3  | Sketch of the ICP-RIE process . . . . .                    | 43 |
| 3.4  | X-ray characterization methods . . . . .                   | 44 |
| 3.5  | Sketch of ellipsometry . . . . .                           | 46 |
| 3.6  | The ultrafast laser setup . . . . .                        | 48 |
| 3.7  | Sketch of pump-probe spectroscopy . . . . .                | 50 |
| 3.8  | The nondegenerate pump-probe setup . . . . .               | 51 |
| 3.9  | Supercontinuum light spectrum . . . . .                    | 51 |
| 3.10 | Realization of MIIPS . . . . .                             | 53 |

|      |  |     |
|------|--|-----|
| 4.1  | Transmission measurement of a GaP and silicon wafer . . . . .                      | 55  |
| 4.2  | The GaP thin film system . . . . .   | 59  |
| 4.3  | SHG and transmission from GaP . . . . .  | 60  |
| 4.4  | Measured polarization dependence of SHG . . . . .                                  | 62  |
| 4.5  | Extracted second-order susceptibility values for GaP . . . . .                     | 63  |
| 4.6  | Transmission of a 400 nm thick a-GaP thin film . . . . .                           | 64  |
| 4.7  | Extraction of the third-order nonlinear susceptibility . . . . .                   | 65  |
| 4.8  | Simulation of SHG/ THG thickness dependence . . . . .                              | 66  |
| 4.9  | Power dependence of SHG and THG from GaP . . . . .                                 | 67  |
| 4.10 | HHG from GaP . . . . .   | 68  |
| 4.11 | XPS measurement of a-GaP thin films . . . . .                                      | 72  |
| 4.12 | XRD measurements of GaP . . . . .  | 73  |
| 4.13 | Refractive index and extinction coefficient for different semiconductors . . . . . | 73  |
| 4.14 | SHG from a-GaP . . . . .   | 74  |
| 4.15 | Multipole analysis of resonant nanopatches . . . . .                               | 75  |
| 4.16 | Comparison of SHG measurements and simulation . . . . .                            | 76  |
| 4.17 | SHG of the a-GaP nanorods under vertical polarization . . . . .                    | 77  |
| 4.18 | Ultrafast response of a-GaP nanorods . . . . .                                     | 78  |
| 4.19 | Ultrafast response with exchanged pump and probe pulses . . . . .                  | 79  |
| 4.20 | Single time traces for exchanged pump and probe pulses . . . . .                   | 80  |
| 4.21 | c-GaP nanodiscs at the anapole . . . . .   | 84  |
| 4.22 | Ultrafast response under excitation at the anapole . . . . .                       | 85  |
| 4.23 | Simulated electric energy of the nanodiscs . . . . .                               | 86  |
| 4.24 | Pump-probe temporal traces . . . . .   | 86  |
| 4.25 | Experimental and simulated nonlinear responses . . . . .                           | 87  |
| 4.26 | Modulation performance at different pump powers . . . . .                          | 88  |
|      |  |     |
| 5.1  | Fabrication of NbP thin films . . . . .  | 94  |
| 5.2  | Optical characterization . . . . .   | 95  |
| 5.3  | THG from NbP thin films . . . . .  | 96  |
| 5.4  | Theoretically calculated thickness dependence of the THG signal . . . . .          | 97  |
| 5.5  | Polarization dependence of the THG signal . . . . .                                | 98  |
| 5.6  | Extracted THG efficiency . . . . .   | 98  |
| 5.7  | Ultrafast pump-probe reflective spectroscopy of NbP . . . . .                      | 99  |
| 5.8  | Ultrafast dynamics in NbP crystal and thin film . . . . .                          | 100 |
| 5.9  | Single pump-probe traces at short and long timescales . . . . .                    | 101 |
| 5.10 | Power dependence of the change in reflectivity . . . . .                           | 101 |
| 5.11 | Simulation of the refractive index change . . . . .                                | 102 |
| 5.12 | Ultrafast dynamics in NbP crystal and thin film . . . . .                          | 103 |
|      |  |     |
| 6.1  | Atomic structure of ferroelectric layered NbOI <sub>2</sub> . . . . .              | 108 |
| 6.2  | DFT calculations for bulk and monolayer NbOI <sub>2</sub> . . . . .                | 109 |
| 6.3  | ARPES measurements and GW calculated band structure . . . . .                      | 110 |

|      |  |     |
|------|--|-----|
| 6.4  | Linear optical characterization of NbOI <sub>2</sub> . . . . .                       | 111 |
| 6.5  | NbOI <sub>2</sub> under varying polarization angle . . . . .                         | 112 |
| 6.6  | Characterization of ShG in NbOI <sub>2</sub> . . . . .                               | 113 |
| 6.7  | Nonlinear optical processes in NbOI <sub>2</sub> . . . . .                           | 114 |
| 6.8  | Intensity dependence of SHG on the fundamental wavelength . . . . .                  | 115 |
| 6.9  | Calculated single particle SHG susceptibility for NbOI <sub>2</sub> . . . . .        | 115 |
| 6.10 | Nonlinear optical response of NbOI <sub>2</sub> as a function of thickness . . . . . | 116 |
| 6.11 | Ferroelectric domain walls in NbOI <sub>2</sub> . . . . .                            | 117 |
| 6.12 | Polarization dependence of SHG from NbOI <sub>2</sub> . . . . .                      | 118 |
| 6.13 | Characterization of ShG in NbOI <sub>2</sub> . . . . .                               | 118 |
| 6.14 | Polarization-resolved SHG in NbOI <sub>2</sub> . . . . .                             | 119 |
| 6.15 | Effects of strain on SHG in NbOI <sub>2</sub> . . . . .                              | 120 |
| 6.16 | Characterization of wrinkled NbOI <sub>2</sub> flake . . . . .                       | 120 |
| 6.17 | Effects of temperature and electric field on SHG in NbOI <sub>2</sub> . . . . .      | 121 |
| 6.18 | Electric field dependent SHG of NbOI <sub>2</sub> nanosheet . . . . .                | 122 |
| A.1  | Scheme of the fabrication for c-GaP nanostructures . . . . .                         | 134 |
| B.1  | Nanogap antennas . . . . .   | 138 |
| B.2  | Characterisation of the nanodisk's nonlinear signals . . . . .                       | 140 |
| B.3  | Mechanisms reducing harmonic generation from the ITO layer . . . . .                 | 142 |
| B.4  | Ellipsometry of the nanogap film . . . . .   | 143 |
| B.5  | Concept of a purely time-varying mirror . . . . .                                    | 147 |
| B.6  | Sketch of a pump-probe experiment . . . . .  | 148 |
| B.7  | Experimental evolution of the probe reflection . . . . .                             | 149 |
| B.8  | Measured evolution with pump/probe delay of the FWM signal . . . . .                 | 151 |
| B.9  | Concept and realization of the double-slit diffraction experiment in time . .        | 154 |
| B.10 | Observation of a spectral diffraction pattern from temporal double-slits . .         | 156 |
| B.11 | Characterization of the temporal double slit with a short probe pulse . . .          | 158 |
| B.12 | Modelled reflection coefficient . . . . .  | 159 |
| B.13 | Comparison of the models against experimental data . . . . .                         | 161 |



# List of Tables

|     |  |     |
|-----|--|-----|
| 3.1 | Parameters of the laser system . . . . .   | 49  |
| 4.1 | Second-order nonlinear susceptibilities . . . . .  | 64  |
| 4.2 | Third-order nonlinear optical susceptibilities . . . . .                                 | 66  |
| 4.3 | All-optical switching of various nanomaterials . . . . .                                 | 90  |
| 6.1 | Transitions of the SHG susceptibility . . . . .  | 116 |
| 6.2 | SHG efficiencies for different materials . . . . .                                       | 124 |
| 6.3 | Crystal data and structure refinement for NbOI <sub>2</sub> at 298 K and 100 K . . . . . | 125 |
| A.1 | Parameters for sputter deposition . . . . .  | 133 |
| A.2 | Parameters for PECVD . . . . .   | 133 |
| A.3 | Parameters for ICP-RIE . . . . .   | 133 |



# Zusammenfassung

Die nichtlineare Optik im Nanometerbereich ist ein wichtiger Teil der Nanophotonik mit potenziellen Anwendungen in der Quantenoptik und zur Kommunikation und dem Schalten in optischen Schaltkreisen. Allerdings sind die Anforderungen hier anders als in etablierten nichtlinearen optischen Systemen. Anstelle des Kriteriums der Phasenanpassung, müssen geeignete nichtlineare Nanomaterialien einen großen Brechungsindex zusammen mit hohen nichtlinearen Koeffizienten und idealerweise geringen optischen Verlusten aufweisen. Diese Arbeit bietet eine umfassende Studie über drei verschiedene Materialien in Bezug auf ihre linearen und nichtlinearen optischen Eigenschaften und insbesondere ihre Eignung für nichtlineare nanophotonische Anwendungen.

Beginnend mit Galliumphosphid (GaP), einem indirekten Halbleiter mit Bandlücke, werden amorphe und kristalline Dünnschichten untersucht, wobei gezeigt wird, dass sie die ausgezeichneten optischen Eigenschaften des Kristalls besitzen, mit einem großen Transparenzbereich und hohen nichtlinearen Koeffizienten. Darüber hinaus ermöglicht die Nanostrukturierung und Anregung spezifischer optischer Resonanzen eine Verstärkung der nichtlinearen Prozesse um mehrere Größenordnungen, insbesondere für die nichtlineare Frequenzumwandlung und das ultraschnelle optische Schalten.

Das zweite Material ist Niobphosphid (NbP), ein Mitglied der Familie der Weyl-Halbmatalle einer Gruppe von Kristallen, die topologische Oberflächenzustände und eine elektronische Struktur aufweisen, die mit der von Graphen vergleichbar ist. Hier wird gezeigt, dass ein Nanofilm des Materials eine hohe Effizienz bei der nichtlinearen Frequenzumwandlung und eine ultraschnelle optische Antwort aufweist, in beiden Fällen stärker als beim Kristall. Darüber hinaus ermöglicht die Analyse des nichtlinearen Signals die Identifikation der Ursache für die verbesserten Eigenschaften in der einzigartigen elektronischen und topologischen Struktur des Materials.

Schließlich werden exfoliierte Nanoflocken des Halbleiters Nioboxid-Diiodid ( $\text{NbOI}_2$ ) hinsichtlich ihrer anisotropen Struktur und Ferroelektrizität analysiert. Es wird gezeigt, dass die intrinsische Polarisierung zu effizienten nichtlinearen Prozessen führt, wobei die Effizienz der Effekte durch das Absenken der Temperatur, das Anlegen eines elektrischen Feldes oder mechanischer Spannung weiter gesteigert werden kann. Mit letzterem wird ein Rekordwert in der Umwandlungs-Effizienz von mehr  $10^{-2}$  % bei nur zwanzig Nanometern des Materials erreicht.

Die in dieser Arbeit präsentierten Ergebnisse zeigen, dass etablierte Materialien wie GaP sowie kürzlich realisierte Materialien wie NbP und  $\text{NbOI}_2$  ausgezeichnete lineare und nicht-

lineare optische Eigenschaften im Nanobereich aufweisen. Sie vereinen die Notwendigkeit hoher nichtlinearer Koeffizienten mit den Anforderungen der Nanotechnologie und sind daher vielversprechende Kandidaten für zukünftige nichtlineare nanophotonische Anwendungen.

# Abstract

Nonlinear optics at the nanoscale are an important part of nanophotonic research with potential applications in on-chip quantum optics and optical switching, computing and communication. However, the material requirements at the nanoscale are different than that for established bulk optics. Instead of the crucial phase-matching condition, suitable nonlinear nanomaterials need to have a large refractive index together with high nonlinear coefficients and ideally low losses. This thesis provides the comprehensive study of three different materials regarding their linear and nonlinear optical properties and particularly their suitability for nonlinear nanophotonic applications.

Starting with amorphous and crystalline thin films of the indirect bandgap semiconductor gallium phosphide (GaP), it is shown that the nanofilms inherit the excellent optical properties of the bulk crystals, with a large transparency window and high nonlinear coefficients. Furthermore, the nanostructuring and excitation of specific optical resonances allows to enhance the nonlinear performance by orders of magnitude with is particularly shown for nonlinear frequency conversion and all-optical switching.

The second material is niobium phosphide (NbP), member of the Weyl semimetal family, which is a group of bulk crystals that has topological surface states and an electronic structure that is comparable to the one of graphene. Here, it is shown that a nanofilm of the material exhibits a high nonlinear frequency conversion efficiency and ultrafast optical response, both more pronounced than for the bulk crystal. Moreover, the analysis of the nonlinear signal allows to attribute the enhanced response to the unique electronic and topological structure of the material.

Finally, exfoliated nanoflakes of the semiconductor niobium oxide di-iodine (NbOI<sub>2</sub>) are thoroughly analyzed with respect to their anisotropic structure and ferroelectricity. It is presented that this intrinsic polarization leads to efficient second-order nonlinear processes with the possibility to further enhance the nonlinear conversion efficiency by lowering the temperature, applying an electric field or by introducing strain. With the last, a record-value conversion efficiency of more 10<sup>-2</sup> % is achieved with only twenty nanometers of the material.

The results presented in this thesis show that the established materials as GaP as well as recently realized systems like NbP and NbOI<sub>2</sub> exhibit excellent linear and nonlinear optical properties at the nanoscale. They collectively merge the need for high nonlinear coefficients with the requirements for nanophotonic engineering which proposes them as promising candidates for future nonlinear nanophotonic applications.



# Chapter 1

## Introduction

The basic principles of optics are well-known for centuries, with first discoveries being dated back to the ancient Egyptians and Greeks [1]. Our daily life is fundamentally defined by the ability to see the world around us and therefore the propagation of light and its interaction with matter. This gives us generally a good intuition for many optical phenomena, for example the refraction of light at the surface of water or the reflection from a mirror. These effects are well understood and described in terms of linear optics which include the fundamental properties of the light and which are the basis for the design of lenses, mirrors or objectives. These everyday optical systems are casually changing the direction of light, but never the color (or frequency) of light. In fact, it would appear very disturbing if the reflected image of an object would suddenly appear in different colors (see Fig. 1.1). The reason for this is that light follows the superposition principle which implies that light waves are not interacting with each other. Although they can locally overlap and can for example add up constructively or destructively, there is no energy transfer from one to another light wave. In the realm of nonlinear optics, this is no longer guaranteed. Inside a nonlinear optical material, light waves can interact with each other and energy transfer can take place. For example, the light of two different frequencies can combine to generate light which has a frequency which is equally to the sum of their individual frequencies, a process called sum-frequency generation. Typically, these processes are scaling with higher powers of the incident intensity.

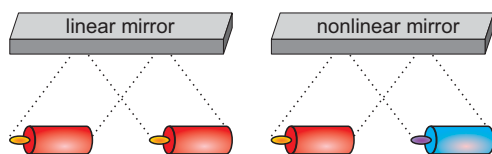


**Figure 1.1:** Sketch of a linear and a nonlinear Mirror

Although this might sound like an exotic field of physics, nonlinear optical processes are a fundamental building block of today technologies and are part of extensive research (see Fig. 1.2). Examples include multi-photon microscopy, which allows to measure biological samples (e.g. tumor cells in Fig. 1.2a) in a label-free and non-destructive way [2] or current laser sources that make use of nonlinear parametric amplification to extend the usable wavelength

range [3]. Furthermore, nonlinear effects enable the control and modulation of light with

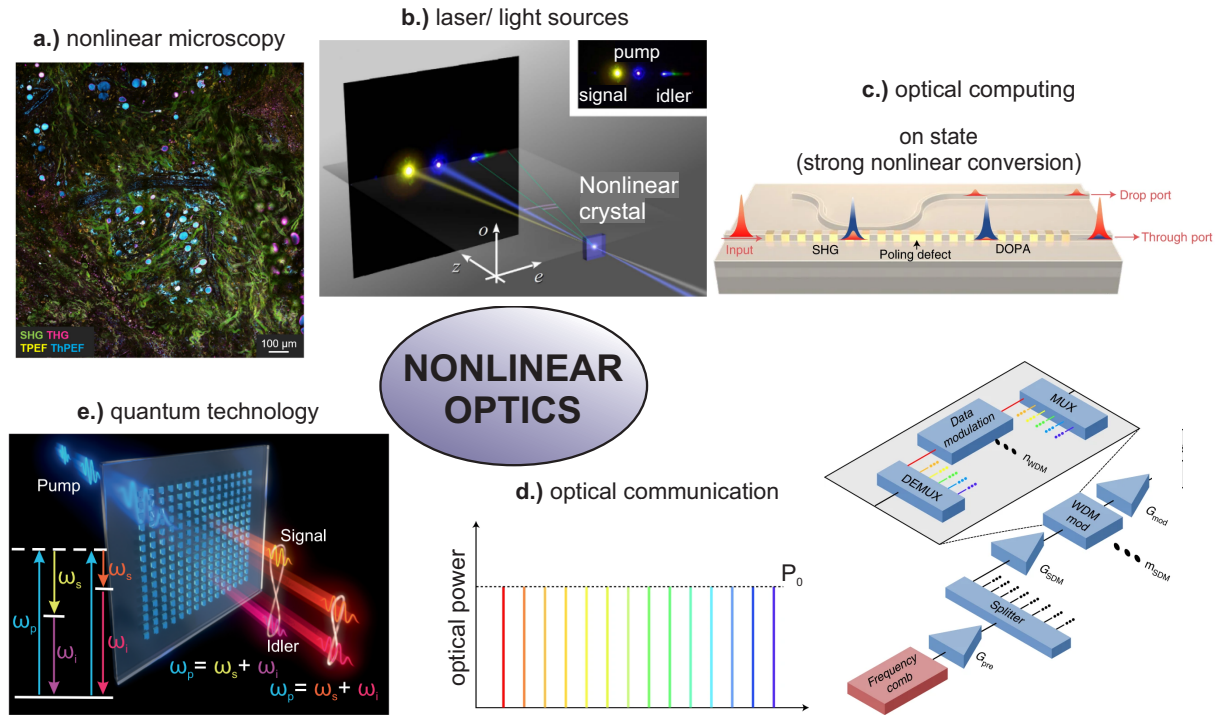


**Figure 1.2:** Applications of nonlinear optics. **a.)** Nonlinear microscopy image of a tumor cell. Adapted from ref. [2]. **b.)** Demonstration of the generation of light at new frequencies. Adapted from ref. [3]. **c.)** Example for a waveguide system that realizes nonlinear optical switching. Adapted from ref. [4]. **d.)** Sketch of an optical network that makes use of nonlinear multiplexing. Adapted from ref. [7]. **e.)** Demonstration of the generation of entangled photons with a nonlinear metasurface. Adapted from ref. [9].

light which is a requirement for logical operations and optical computing [4]. A major part of the modern high-speed communication technology is based on optical systems, where elements such as wavelength-division-multiplexing [5] or optical signal processing devices [6,7] are based on and make use of nonlinear optics effects. Recently, more attention is growing towards quantum computing and quantum optics, where nonlinear optical interaction can be a convenient source of entangled photon pairs [8,9].

### Nonlinear optics below the diffraction limit

Nevertheless, nonlinear optical interactions have one fundamental drawback, which is that they are intrinsically weak due to small nonlinear coefficients of materials. In current systems, this is compensated by bulk elements, where the light can travel over a long distance to achieve the needed interaction strength. However, this works against the trend of current miniaturization and the possibilities that are proposed by photonic integrated circuits and nanoscale systems. One way to approach this problem is to utilize the methodology of nanophotonics and the principles of optical antennas.

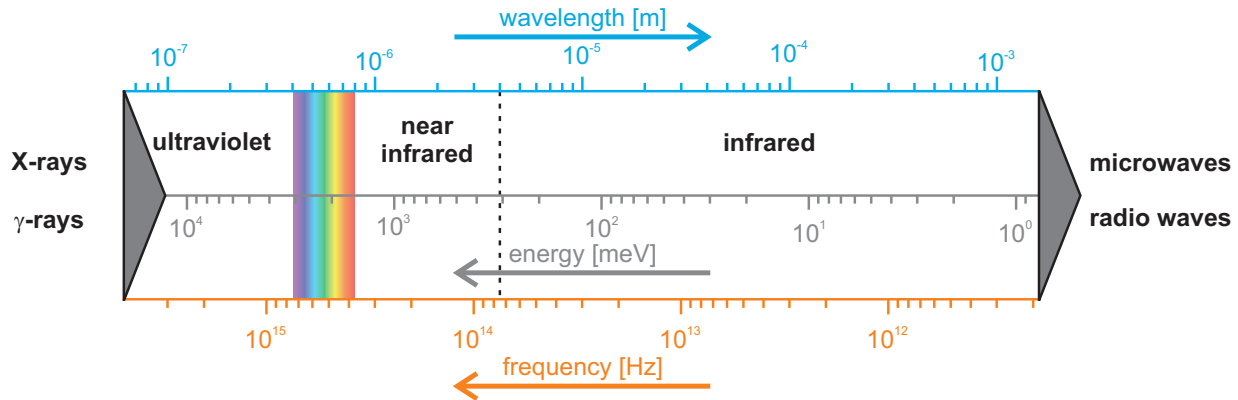


**Figure 1.3:** Frequency range of the optical radiation, having longer wavelength than X-ray and  $\gamma$ -radiation but shorter than micro- and radio waves. The visible spectrum is illustrated at the respective wavelengths.

Analogous to classical antennas for radio frequency (RF) or microwave technologies, optical antennas are built on the possibility to transfer energy from far field radiation to the near field, and vice versa. Hereby, the size of the structures is related to the wavelength which, in case of optical radiation, is ranging from  $10^{-7}$  m to  $10^{-3}$  m (Fig. 1.3). In particular for the technically relevant visible and near infrared part of the spectrum, this requires nanometer size structures as antennas [10]. Enabled by the advance of nanofabrication techniques, first results towards the realization were done with metallic (mostly gold and other noble metals) structures. Here, for optical frequencies, the electric field of incident light can induce an oscillation the negatively charged electrons of the material [11]. For small nanoparticles, this can lead to distinct resonances that can efficiently couple to the far field and that can be tailored to exhibit electric field hotspots with extreme intensities, confined into sub-wavelength volumes [12]. Alongside a wide range of applications, for example in the field of photocatalysis [13], optical sensing [12] or as active optical material [14], these hotspots present a promising way to boost nonlinear interactions. Since they scale in powers of the incident intensity, there were great advances, both with single metallic structures [15, 16] or large-scale periodic arranged metasurfaces [17].

Albeit the strong optical resonances of metallic nanostructure, the oscillating electrons are accompanied by a few drawbacks. First, this corresponds to the movement of electrons through a material with finite resistance which therefore experience Ohmic losses and heating. This reduced the efficiency of processes and gives metallic nanostructures a typically low damage threshold [18]. Furthermore, the direct response of the free electrons to the incident electric field means that all fields inside the metal will immediately be compensated. As a consequence, the light will not translate through the material and (nonlinear) light-matter interactions are limited to the surface region of metallic nanostructures.

An alternative approach that circumvents this problem is to use high-refractive index dielectric materials for the fabrication of nanostructures. Here, electromagnetic fields are allowed to propagate and losses are reduced to optical absorption of the respective ma-

terial. Instead of oscillating electrons, the light induces currents to the bound electrons which lead to a wealth of Mie resonances with electric and magnetic character [19]. Particularly semiconductors with high refractive indices show excellent optical properties for light wavelengths longer than their respective bandgap, leading to a wide range of results for example on energy conversion [20], surface enhanced fluorescence [21] or biosensing [22]. Particularly for nonlinear optical applications, dielectric nanostructures outperform their metallic counterparts because tailored resonances can generate electric field hotspots inside the volume of the structure [23].

Unfortunately, materials that are used in current bulk nonlinear optical systems are not necessarily promising choices at the nanoscale. Particularly for frequency conversion, classical nonlinear crystals are chosen by mainly two parameters:

- The phase matching condition needs to be fulfilled:  $\vec{k}_0 - \vec{k}_{new} = \vec{0}$ . This is usually achieved by having birefringence which strongly limits the pool of possible materials.
- the material should be transparent to avoid any absorption process.

If these conditions are fulfilled, the magnitude of the actual nonlinear coefficient is less critical, and the nonlinear signal can efficiently be built up [24].

At the nanoscale, the appearing structures are typically small enough such that the phase matching requirement can be lifted [25,26]. Although the losses of a material should still be small, it is less critical than in the bulk case, where the light travels through the material over a long distance. However, for efficient nanophotonics, the following requirements move into the foreground [27]:

- **Accessibility:** Obviously, a suitable material should be accessible for common (or new) nanofabrication techniques. Moreover, an ideal material would be compatible with current silicon technologies which is the industry standard for electronic integrated circuits.
- **High nonlinear coefficients:** On the macroscopic scale, high nonlinear coefficients are beneficial, but can in principle be compensated by more material. For a nanophotonic system however, the increase of the particle size would change the resonant behavior. As a consequence, higher nonlinear coefficients are a good strategy to account for the small interaction volumes.
- **High refractive index:** The refractive index can generally be seen as a measure for the optical interaction strength of a material. Consequently, a higher refractive index allows stronger Mie resonances with more control over the electric near field and hotspots. Typically, the intensity of the electric field that can be associated with specific resonances scales with the refractive index of the material.

Consequently, the search for new nanomaterials to boost nonlinear interactions must divide into two aspects. First, suitable materials have to be identified and it has to be ensured that they fulfill the aforementioned requirements. Moreover, additional restrictions might apply

for different nonlinear effects. As an example, any second-order nonlinear process requires a material with no inversion symmetry, which immediately excludes popular materials as silicon or germanium. The second aspect is the development and exploitation of optical resonance that allow control over the nonlinear processes, ideally with the possibility to boost efficiencies. This opens the field to extensive possibilities, ranging from different geometries as single structures, large-scale periodic metasurfaces or photonic crystals.

This is the main topic of this thesis, which is built as follows. It starts with a brief introduction to the theoretical background in **Chapter 2**, including fundamentals of linear, nonlinear and ultrafast optics and basic concepts of nanophotonics. It is followed by **Chapter 3** and the discussion of the main methodology that is used to fabricate, analyze and characterize the different nanomaterials. Furthermore, the chapter includes the description of the ultrafast laser setup which builds the basis for a large part of the used experiments. In **Chapter 4** of this thesis, both of these aspects will be thoroughly discussed for the semiconductor gallium phosphide (GaP) and particularly thin films of the material. First, it is shown that its structure enables efficient second and third-order nonlinear processes, whereas the thin films perform comparable or even better than the bulk crystal. This is followed by the realization of GaP nanostructures and their application for nanoscale frequency conversion. It is shown that this allows a broad control over the nonlinear process, e.g. by tuning the nanostructures size or orientation and that it enhances the nonlinear signal by more than two orders of magnitude.

The following two chapters are focused the identification of new suitable materials for nonlinear optics at the nanoscale. It starts with **Chapter 5**, where a thin film of the Weyl semimetal niobium phosphide (NbP) is discussed. This newly discovered class of materials is characterized by a linear electron dispersion and topological surface states which lead to a plethora of new and exciting properties [28]. In this thesis, it is shown that this furthermore enables efficient third-order nonlinear effects and that the thin film allows an enhanced interaction with the topological surfaces states.

The second material in **Chapter 6** is the two-dimensional semiconductor niobium oxide di-iodine (NbOI<sub>2</sub>). It is shown that its ferroelectric character enables efficient frequency conversion with single, nanometer thin flakes of the material.

Finally, **Chapter 7** concludes the thesis and provides an outlook for possible applications of the investigated materials, particularly for nonlinear frequency conversion and all-optical switching.

## Beyond the Speed of Electronics

A second aspect of this thesis is to apply nonlinear nanophotonics to boost the speed of all-optical switching. The motivation for this lies in the continuous miniaturization of current electronic components, which already allows millions of transistors to fit onto a micrometer scaled chip [29]. However, the industry is approaching a size limit where smaller electronic elements are physically no longer possible, which would fundamentally be reached at the scale of single atoms [30]. As a consequence, new technologies are required to satisfy the demand for high-speed data processing and computing.

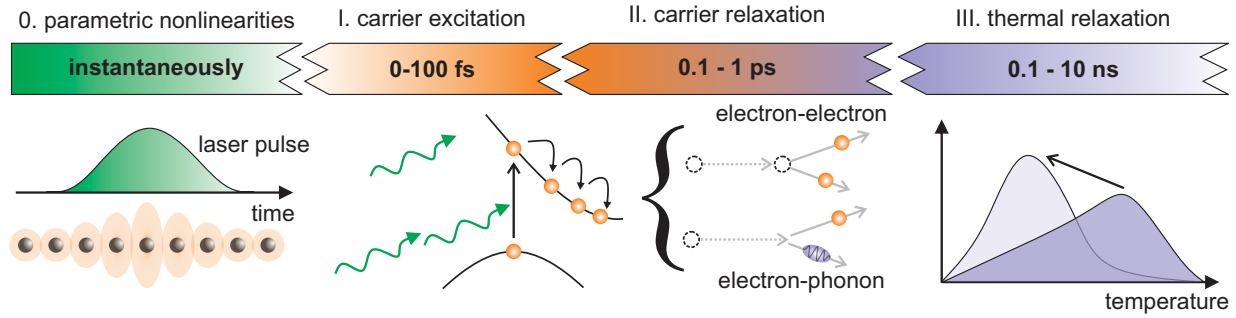


**Figure 1.4:** Overview over the processes at ultrafast timescales.

One popular approach is the development of optical systems, where photons instead of electrons would carry and process the information [31, 32]. Hereby, one of the basic requirements is the modulation (or switching) of light with light, which could efficiently be realized by making use of nonlinear optics and the light-induced changes to the optical properties of a material. For this, optical nonlinearities can be divided into two main categories, the parametric or non-parametric interactions, see Fig. 1.4. The first happen only via virtual electron transitions which means that the energy of the photons is conserved and the quantum mechanical states in the system are not changed [24]. Here, the optical modulation occurs as the displacement of bound electrons in anharmonic regions of the electronic potential and therefore a deformation of the material's potential [33], see Fig. 1.4 most left sketch. As a consequence, these processes happen virtually instantaneous and are temporally limited only by the duration of the incident pulse. The most popular example are self-phase modulation and the optical Kerr effect [34], which modulate the linear refractive index by adding an intensity dependent term.

The non-parametric nonlinearities include processes where the interaction of light and matter involve an actual change of the states in the material. They typically happen at slower timescales and parts of the light's energy are transferred to the material. An example is where incident photons get absorbed by electrons of the system, which can happen via direct or nonlinear processes (e.g. two-photon absorption) [35]. Hereby, the absorbing electron is promoted in the electronic bandstructure, either inter- or intraband transitions, and is followed by a sequence of relaxation processes, sketched in Fig. 1.4, points I-III. Typically, the excitation of electrons and first ultrafast relaxation processes (e.g. Landau damping [36]) happen within the first 100 fs after the arrival of the light pulse. This is followed by the slower relaxation via electron-electron or electron-phonon scattering (II in Fig. 1.4), which typically have the shape of exponential decay functions with separate decay constants. The relevant time scales depend on the respective system and can vary over a wide range but are typically in the range of below one picosecond [37]. Finally, the consecutive build-up of phonons leads to the heating of the crystal lattice, which will the slowly cool down again, what can take up to a few nanoseconds. In contrast to the 'fast' modulation, these thermal modulations are a modification to the bonding energy itself (by introducing energy to the system) and have generally a larger impact on the optical

response [38].

Evidently, the fastest optical switching requires a material with high nonlinear coefficients to boost the 'fast' processes while carrier and thermal effects should be as small as possible. As a consequence, the most promising results that were achieved at the nanoscale are based on large bandgap semiconductors with illumination below their bandgap energy. As an example, a silicon metasurface achieved a 65 fs full-width half maximum switching timewith a change of transmittance in the range of 50 % [35] or GaP crystals where below 30 fs response times with up to 60 % change in transmittance were reported [39]. Another possibility to improve all-optical switching is to work with the thermal response of materials but to minimize the relaxation time of the 'slow' processes. Examples here are indium tin oxide (ITO) at its epsilon near-zero (ENZ) wavelength which was shown to exhibit below 1 ps and about 20 % change of transmittance [40,41]. Although this has the advantage of the inherently larger modulation of the refractive index, the time scales are still magnitudes larger than the pure nonlinearity driven reports.

In this thesis, all-optical switching is investigated in parts of **Chapter 4**, where the ultrafast response of amorphous and crystalline nanostructures investigated. It is shown that the response can be tune to be dominated by a nonlinear refractive index modulation and that it can be enhanced by more than one order of magnitude by excited a specific resonant condition. With this, a modulation depth of more than 40 % and below-100 fs relaxation can be achieved.

In **Chapter 5** the ultrafast optical response of the previously discussed NbP thin film is investigated using below 10 fs resolution. Again it is shown that the ultrafast response of the film is highly enhanced compared to the bulk crystal and that the thermal response can be tuned by changing of the probe wavelength. The latter is explained to be a direct consequence of the unique band structure of the material.



# Chapter 2

## Fundamentals

This chapter introduces the theoretical fundamentals of nanophotonics which are the basis for the experimental results of this thesis. It starts with an introduction to the theory of electromagnetism, optical properties of materials and nanostructures before it continues with the basics of nonlinear photonics and ultrafast laser physics.

### 2.1 Theory of electrodynamics

The principles of optics and optical systems are defined by the theory of electromagnetism, which describes the wave nature of light and associated phenomena. Unless differently stated, the following sections are based on common textbooks on these topics, mainly [26, 42, 43].

#### 2.1.1 Maxwell's equations in nonmagnetic media

Maxwell's equations are a set of four differential equations that are the foundation for the theory of electromagnetic waves and their propagation through arbitrary media. They connect the electric ( $\vec{E}$ ) and magnetic ( $\vec{H}$ ) fields with material properties such as the charge density  $\rho$  and sources of electromagnetic fields as the current density  $\vec{j}$ .

$$\nabla \cdot \vec{D} = \rho \quad (2.1)$$

$$\nabla \cdot \vec{B} = 0 \quad (2.2)$$

$$\nabla \times \vec{E} = -\partial_t \vec{B} \quad (2.3)$$

$$\nabla \times \vec{H} = \partial_t \vec{D} + \vec{j} \quad (2.4)$$

Here,  $\vec{D}$  corresponds to the electric displacement field and  $\vec{B}$  is referred to as magnetic induction, which describe the electric and magnetic fields inside a medium, respectively. Assuming nonmagnetic materials (which is true throughout this thesis), the magnetization  $\vec{M}$  vanishes such that the magnetic induction is simply defined by

$$\vec{B} = \mu_0 \vec{H} + \mu_0 \vec{M} = \mu_0 \vec{H} \quad (2.5)$$

Analogue, the displacement field  $\vec{D}$  is the combination of the electric field  $\vec{E}$  and the induced polarization  $\vec{P}$  inside a material.

$$\vec{D} = \epsilon_0 \vec{E} + \vec{P} \quad (2.6)$$

Hereby,  $\vec{P}$  is the net alignment of microscopic charges to the electric field, i.e. the density of induced electric dipole moments. As such it is connected to the charge and current densities of the respective material.

$$\nabla \cdot \vec{P} = -\rho \quad (2.7)$$

$$\vec{j} = \partial_t \vec{P} \quad (2.8)$$

In the linear optical regime (the nonlinear case will be part of section 2.4),  $\vec{P}$  presents a linear response to the electric field, connected by the susceptibility  $\chi$ .

$$\vec{P} = \epsilon_0 \chi \vec{E} \quad (2.9)$$

Here,  $\chi$  is generally a rank-2 tensor that can depend on space and frequency and can be complex valued. As such, it comprises the properties that determine how a material is responding to electromagnetic radiation. It is convenient to define the dielectric function or permittivity  $\epsilon = 1 + \chi$  such that the displacement field can be expressed as

$$\vec{D} = \epsilon_0 \epsilon \vec{E} \quad (2.10)$$

One important application of Maxwell's equations is the derivation of the so-called wave equations, which fully describe the propagation of electromagnetic fields in arbitrary media. Assuming a material without free charges ( $\rho = 0; \vec{j} = \vec{0}$ ), the homogeneous wave equations can be calculated to be

$$(c^2 \Delta - \partial_t^2) \vec{E} = 0 \quad (2.11)$$

$$(c^2 \Delta - \partial_t^2) \vec{B} = 0 \quad (2.12)$$

with the Laplace operator  $\Delta = \nabla \cdot \nabla$ . Additionally, the speed of light  $c = (\mu\epsilon)^{-1/2}$  was introduced, dependent on the permeability  $\mu$  and dielectric function  $\epsilon$  of a material. This implies that the vacuum speed of light  $c_0 = (\mu_0\epsilon_0)^{-1/2}$  is modified (in case of a nonmagnetic material):

$$c = c_0 / \sqrt{\epsilon} \quad (2.13)$$

The solutions to equations 2.11 and 2.11 are fully transversal waves, where electric and magnetic field are perpendicular while both are normal to the direction of propagation  $\hat{k}$ . In its most general form, a solution reads as  $\vec{E}(\vec{r}, t) = \vec{g}(\omega t \pm \vec{k} \cdot \vec{r})$ , where  $\vec{g}$  is an arbitrary function and the wave's angular frequency  $\omega$  and wave vector  $\vec{k} = \hat{k}k$  were introduced. The quantity  $k$  is referred to as wavenumber and is proportional to the inverse of the

wavelength  $\lambda = \frac{2\pi}{k}$ , which defines the wave's oscillation period in space. From this, the well-know dispersion relation follows, which relates the velocity of a wave to its wavelength and frequency.

$$c = \frac{\omega}{|\vec{k}|} = \lambda f \quad (2.14)$$

where,  $f$  is the frequency, i.e. the inverse of the wave's oscillation period  $T$  in time:  $f = \frac{\omega}{2\pi} = \frac{1}{T}$ . When light travels through a material with the dielectric function  $\epsilon$ , the modification of the velocity leads to a change of the wavelength and wavenumber, accordingly.

$$\lambda = \lambda_0 / \sqrt{\epsilon} \quad (2.15)$$

$$k = k_0 \cdot \sqrt{\epsilon} \quad (2.16)$$

Here, the quantities indexed with 0 correspond to the respective values in vacuum, where the dielectric function is unity  $\epsilon = 1$ . The frequency on the other hand can be associated to the energy of the wave and is therefore conserved for light traveling through a material:  $E \propto f = \text{const}$ . It should be noted that this is only true for time-translation invariant systems, examples where this is not the case are discussed in the Appendix B.2.

### 2.1.2 The linear refractive index

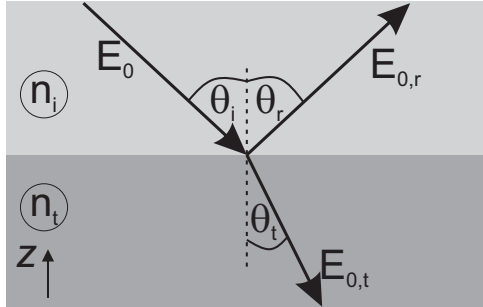


**Figure 2.1:** Reflection at an interface between two materials.

A common way to express the optical properties of a material is by using the complex refractive index

$$\tilde{n} = n - ik \quad (2.17)$$

Here,  $n$  is called the linear refractive index while  $k$  corresponds to the extinction coefficient and describes the optical losses of a system. The complex refractive index is defined as the square root of the dielectric function that was introduced in the previous section, or consequently

$$\epsilon = \tilde{n}^2 = n^2 + k^2 - i(2nk) \quad (2.18)$$

Evidently,  $\epsilon$  and  $\tilde{n}$  can be used interchangeably to describe the same physics, however it is historically grown to use  $\tilde{n}$  for classical optics and the phenomena discussed in the following.

Examples for all-day optical processes are the reflection, refraction and transmission at the interface between two materials. Assuming a situation as sketched in Fig. 2.1, where an arbitrary polarized plane wave is incident on an interface between two media with the complex refractive indices  $\tilde{n}_1$  and  $\tilde{n}_2$ , respectively. Without loss of generality, in the following two lossless materials are considered such that  $\tilde{n}_i = n_i$  for  $i = 1, 2$ . For convenience, this

wave can be split into two plane waves with the electric field being aligned perpendicular and parallel to the plane of incidence, called (*s*) and (*p*) polarized, respectively.

$$\vec{E}(\vec{r}, t) = \vec{E}_0 e^{i\vec{k}\cdot\vec{r} - i\omega t} = (\vec{E}^{(s)} + \vec{E}^{(p)}) e^{i\vec{k}\cdot\vec{r} - i\omega t} \quad (2.19)$$

The different materials act on the plane wave by modifying the wavevector  $\vec{k}_i = \vec{k}_0 \cdot n_i$ , where  $i = 1, 2$  refers to the two materials and the index 0 to vacuum. By positioning the interface in the  $z = 0$  plane, three different waves can be identified. The incident wave (*i*) and transmitted wave (*t*), both traveling in negative  $z$ -direction, and the reflected wave (*r*) that moves in positive  $z$ -direction. By solving for applicable boundary conditions (the full calculation can e.g. be found in [1]), the following relations can be derived.

$$\theta_i = \theta_r \quad (2.20)$$

$$n_i \sin \theta_i = n_t \sin \theta_t \quad (2.21)$$

The first equation is known as the law of reflection and the second is commonly called Snell's law and the collectively allow to determine the angles that are present in Fig 2.1. Furthermore, the so-called Fresnel equations express the ratio of the reflected ( $r = E_{0,r}/E_{0,i}$ ) and transmitted ( $t = E_{0,t}/E_{0,i}$ ) wave. For the (*s*) polarized part of a wave, they read

$$r_{(s)} = \frac{n_i \cos \theta_i - n_t \cos \theta_t}{n_i \cos \theta_i + n_t \cos \theta_t} \quad (2.22)$$

$$t_{(s)} = \frac{2n_i \cos \theta_i}{n_i \cos \theta_i + n_t \cos \theta_t} \quad (2.23)$$

and for the (*p*) polarized light

$$r_{(p)} = \frac{n_t \cos \theta_i - n_i \cos \theta_t}{n_i \cos \theta_t + n_t \cos \theta_i} \quad (2.24)$$

$$t_{(p)} = \frac{2n_i \cos \theta_i}{n_i \cos \theta_t + n_t \cos \theta_i} \quad (2.25)$$

If now a material has a nonzero imaginary part of  $\tilde{n}$ , from equation 2.19 it follows that the amplitude of the plane wave will decrease exponentially. Evidently, the imaginary part  $k$  describes the optical losses of a material what is commonly expressed in terms of Beer's law which describes the exponential decrease of the wave's intensity  $I$ .

$$I(l) = I_0 e^{-\alpha l} \quad (2.26)$$

with the traveled distance  $l$ . Here, the absorption coefficient  $\alpha$  was introduced, which is related to  $k$  as follows:

$$\alpha = \frac{4\pi k}{\lambda} \quad (2.27)$$

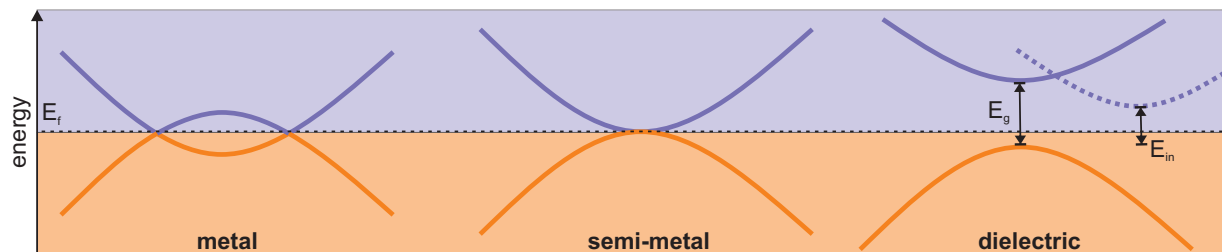


**Figure 2.2:** A sketch of the electronic band structure for three classes of materials. The states below the Fermi energy are occupied by electrons (indicated in orange) while the remaining bands are empty (purple color). For the dielectric material, the direct bandgap  $E_g$  and indirect bandgap  $E_{in}$  are indicated.

Without discussing the mathematical details here, it can be shown that the real and imaginary part of the refractive index have a fixed relationship which is called the Kramers-Kronig relation [43]. It can be expressed as

$$n(\omega) = 1 + \frac{c}{\pi} \mathcal{P} \int_0^{\infty} d\Omega \frac{\alpha(\Omega)}{\Omega^2 - \omega^2} \quad (2.28)$$

Here,  $\mathcal{P}$  corresponds to the Cauchy principal value. It should be noted that this integral is not trivial to evaluate, but the Kramers-Kronig relation imply that the imaginary part of the refractive index can always be calculated from the real part and vice versa. This is a general relation that holds for any complex function, in particular as well for the dielectric function  $\epsilon$ .

## 2.2 Optical properties of materials

This section discusses the optical properties of materials, which can differ significantly and which are a direct consequence of the respective electronic structure. Therefore it is convenient to divide materials into categories according to their electronic band structure as sketched in Fig. 2.2. It should be noted that this section focuses on the optical frequency range that is in the focus of the remaining thesis. For significantly smaller or larger frequencies, the optical response of materials can differ.

### 2.2.1 Metals

Starting with metals, their optical response is fundamentally determined by the presence of free electrons and their high conductivity. When a light wave impacts on a metal's surface, the oscillating electric field will affect the free electrons, which will follow the oscillation at the same frequency, but with a phase shift. As a consequence, the electromagnetic wave inside the conductor interferes destructively and it will not propagate throughout the bulk of the metal. At the same time, the free electrons efficiently backscatter the incident radiation which leads to the high reflectivity of metals at optical frequencies. This behavior

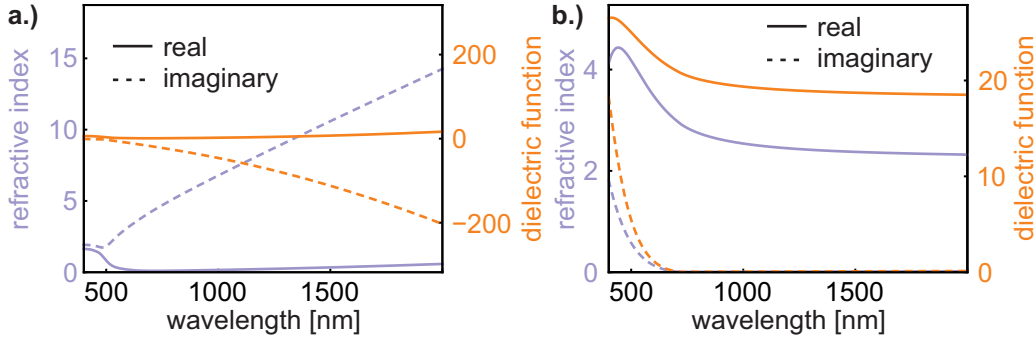


**Figure 2.3:** Optical constants for a.) amorphous silicon and b.) gold. Shown are the refractive index in purple and the dielectric function in orange with the respective real part as solid and the imaginary part as dashed line.

is described by a large negative real part of the dielectric function that together with the positive imaginary part leads to comparably low refractive indices as exemplary shown for gold in Fig. 2.3a.

This is true for radiation frequencies that are below the material specific plasma frequency  $\omega_p$ . If the oscillation becomes faster, the electrons can no longer respond to the oscillating electric field and the metal becomes transparent. Typically,  $\omega_p$  lies in the ultraviolet to extreme ultraviolet regime for metals. However, it should be noted that this is not necessarily true for other conductive materials, for example highly doped semiconductors. The group of transparent conductive oxides (TCOs) can have plasma frequencies in the visible to near-infrared regime [40], what makes them transparent in the visible but reflective in the infrared.

The characteristic colors exhibited by certain metals, such as copper appearing orange or gold's characteristic yellow, can be attributed to interband transitions within their electronic band structures. These transitions enable an increased absorption of the incident radiation, resulting in reduced reflection and the manifestation of the specific colors. Furthermore, it is important to mention that although light cannot propagate through a metal, there are evanescent fields that exponentially decay at the surface. Under certain conditions, this can give rise to a set of phenomena, including the emergence of surface plasmon polaritons. These guided surface waves exhibit subwavelength confinement and play a fundamental role for an entire branch of optics, called plasmonics. For more details on this topic, the reader is referred to [11].

### 2.2.2 Dielectric materials

Most materials that are discussed throughout this thesis are dielectrics, which refers to matter without free carriers such as intrinsic semiconductors and insulators. Their optical properties are fundamentally determined by a finite bandgap in the electronic band structure as sketched in Fig. 2.2. For light with photon energies  $E_\gamma = \hbar\omega$  smaller than the gap energy  $E_g$ , electrons cannot absorb the incident photons which leads to a small

imaginary part of the refractive index. If the band energy is large enough to cover all of the visible spectrum, the materials appear transparent and colorless. Popular examples are all kinds of different glasses, quartz or diamond. Materials with smaller bandgap energies are transparent for light with  $E_\gamma$  below the respective  $E_g$ , while the absorption significantly increases after this point. Consequently, they appear only semi-transparent and have a generally higher refractive index.

Hereby, two kinds of bandgap have to be differentiated (see solid and dashed line in Fig. 2.2). If the minimum of the conduction band and the maximum of the valence band are at similar positions in momentum space, the bandgap is called direct. Then the optical absorption is particularly high because one photon can be absorbed by one electron to promote the latter into the conduction band. Then the total energy of momentum is conserved with the electron/ photon system. This is usually accompanied by a strong photoluminescence emission that is a consequence of the inverse process and where a photon is emitted with a wavelength that corresponds to the bandgap energy. Prominent examples of direct bandgap semiconductors are indium arsenide or gallium arsenide. Contrarily, if the minimum of the conduction band is shifted with respect to the maximum of the valence band (dashed lines in Fig. 2.2), optical absorption is possible but must be accompanied by the transfer of momentum to the crystal lattice (the emission of a phonon) in order to conserve the total momentum in the system. As a consequence the absorption of a so-called indirect bandgap material is typically lower without significant photoluminescence. As an example, Fig. 2.3a shows the refractive index and the dielectric function of silicon, an indirect bandgap semiconductor. It has the typical shape with real and imaginary part that show a peak around the bandgap wavelength.

### 2.2.3 Two-dimensional materials

Since the realization of monolayer graphene in 2004 [44] and the associated Nobel prize (2010), the group of low-dimensional materials is constantly growing. Hereby, the electronic structure can vary from metallic, over semimetallic (e.g. graphene) to semiconductors (e.g. transition metal-dichalcogenides - TMDs) or even organic compounds [45]. As such, they generally have the optical properties that were previously introduced for the respective material group. However, due to their low-dimensional nature, these materials also exhibit unique behaviors resulting from electron confinement and quantum effects. For example the semimetal graphene has a reported ultrafast optical response [46] and resonantly enhanced nonlinear effects [47]. TMDs on the other hand, are semiconductors and behave accordingly. However, the position of their electronic bandgap and even the character (direct or indirect gap) can be influenced by changing the number of layers. A consequence are exceptionally strong optical transition and strongly bound excitons [48]. Additionally, it was shown that TMDs can exhibit extremely strong nonlinear optical responses with large nonlinear coefficients [49]. Altogether, the discovery of low-dimensional materials opened up a vast playground with new and unique electronic and optical properties. Two dimensional materials will be addressed in chapter 6 of this thesis in more detail. Furthermore, the publications [50] and [51] which are not part of this thesis discuss this topics in

more detail.

### 2.2.4 Weyl semimetals

A group of materials that were recently experimentally realized are Weyl semimetals (WSM) [52], which are often described as the three dimensional analogue of graphene. Similar to the monolayer of carbon atoms, WSMs have a single touching point of conduction and valence bands in the electronic band structure and a linear dispersion relation in the vicinity of these points [53]. This is the so-called Weyl cone, in which the electrons behave quasi-relativistic and are described by the name-giving Weyl equation, a solution to the three dimensional Dirac equation [54]. These touching points in the band structure always appear in pairs which are separated in momentum space and which can be associated with opposite chiralities. If these pairs of nodes are projected to the surface of the material, they are connected by so-called Fermi-arcs which are topologically protected surface states [55]. This peculiar electronic structures gives WSM some outstanding properties which makes them part of extensive research. While their optical properties will be discussed in chapter 5 of this thesis, other popular examples will be given here. The Adler-Bell-Jackiw anomaly is a characteristic effect of WSM, where the chirality of the Weyl nodes are not preserved [56] and it was shown that materials of the family exhibit huge magnetoresistance [57] together with a strong anomalous Hall effect [28].

## 2.3 Light interaction at the nanoscale

A first approach to solve the interaction of light with small structures was already described by Lord Rayleigh in the 19th century, where he could explain the scattering off particles that are much smaller than the wavelength. With his derived relation of an inverse proportionality, [11]

$$\sigma_{scat} \propto \lambda^{-4} \quad (2.29)$$

this could explain phenomena as the blue color of the sky or the red light at the sun set or sun rise. This concept was expanded in the early 20th century by the physicist Gustav Mie, who evolved the theory to include structures that are in the same order of magnitude as the wavelength of light [58]. This so-called Mie theory is discussed in the following as it builds the foundation to solve scattering problems at the nanoscale. The section is followed by the introduction of optical resonances which are the fundamental toolbox of nanophotonics.

### 2.3.1 Mie theory

The following derivation is based on the clear and comprehensive book from Bohren and Huffmann [59], to which the reader is referred for more details. The goal is to solve the situation sketched in Fig. 2.4, where a plane wave  $E_{in}$  illuminates a sphere of material

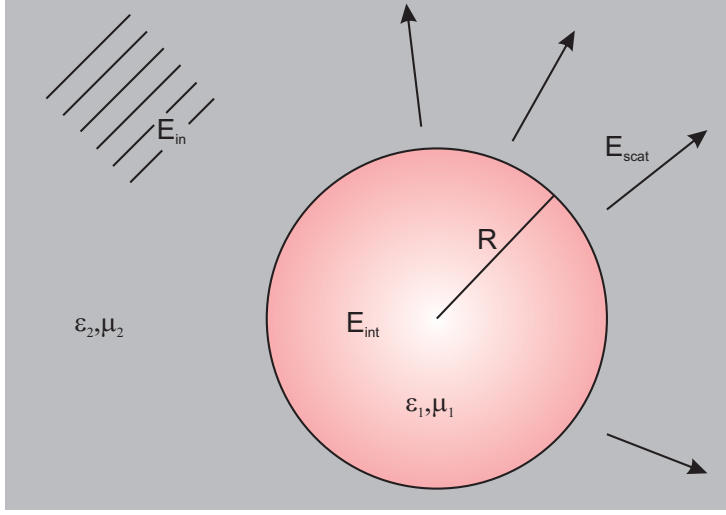


**Figure 2.4:** Sketch of a spherical homogeneous sphere ( $\epsilon_1, \mu_1$ ) with radius  $R$  in an arbitrary medium ( $\epsilon_2, \mu_2$ ). Three domains of electric field can be identified as indicated, the incident field  $E_{in}$ , the internal field  $E_{int}$  and the scattered field  $E_{scat}$ .

( $\epsilon_1, \mu_1$ ) with radius  $R$ , embedded in the surrounding ( $\epsilon_2, \mu_2$ ). The electric (and magnetic) fields will separate into the internal field  $E_{int}$  inside the sphere and the scattered field  $E_{scat}$  outside. For this, two general vector fields  $\vec{M}$  and  $\vec{N}$  are constructed.

$$\vec{M} = \nabla \times (\vec{c}\psi) \quad (2.30)$$

$$\vec{N} = \frac{\nabla \times \vec{M}}{k} \quad (2.31)$$

Here,  $\vec{c}$  is a constant vector,  $\psi$  is a scalar function and  $k$  is a constant number. It can be shown that both functions are divergence free ( $\nabla \cdot \vec{M} = \nabla \cdot \vec{N} = \vec{0}$ ) and they respectively satisfy the homogeneous wave equation 2.11, under the condition that  $\psi$  fulfills the scalar wave equation.

$$\Delta\psi + k^2\psi = 0 \quad (2.32)$$

This trick reduces the problem to a one dimensional, homogeneous differential equation, which can be further simplified by symmetries that are present in a particular geometry. For a spherical particle, as sketched in Fig. 2.4, it is advantageous to switch into polar coordinates ( $r, \vartheta, \varphi$ ) with the constant vector  $\vec{c}$  equal to the space vector  $\vec{r}$ . Thus, the rewritten (scalar) wave equation reads

$$\frac{1}{r^2} \partial_r r \partial_r \psi + \frac{1}{r^2 \sin \vartheta} \partial_\varphi \sin \varphi \partial_\varphi \psi + \frac{1}{r^2 \sin^2 \vartheta} \partial_\vartheta^2 \psi + k^2 \psi = 0 \quad (2.33)$$

That can be solved by separation of variables, which finally leads to a series of independent solutions

$$\psi_{even}^{mn} = \cos(m\varphi) P_n^m(\cos \vartheta) z_n(kr) \quad (2.34)$$

$$\psi_{odd}^{mn} = \sin(m\varphi) P_n^m(\cos \vartheta) z_n(kr) \quad (2.35)$$

where  $P_n^m$  are the associated Legendre polynomials,  $z_n$  are Bessel functions and  $n, m$  are positive integer values. From this, the so-called vector spherical harmonics can be constructed:

$$\vec{M}_{even}^{mn} = \nabla \times (\vec{r}\psi_{even}^{mn}) \quad \vec{N}_{even}^{mn} = \frac{\nabla \times \vec{M}_{even}^{mn}}{k} \quad (2.36)$$

$$\vec{M}_{odd}^{mn} = \nabla \times (\vec{r}\psi_{odd}^{mn}) \quad \vec{N}_{odd}^{mn} = \frac{\nabla \times \vec{M}_{odd}^{mn}}{k} \quad (2.37)$$

As mentioned previously, the vector functions  $\vec{M}$  and  $\vec{N}$  are solenoidal and solutions to the wave equation. Since they form an orthogonal basis of functions, they can be used as expansion for an arbitrary incident plane wave.

$$\vec{E}_{in} = \sum_{m=0}^{\infty} \sum_{n=m}^{\infty} \left( B_{even}^{mn} \vec{M}_{even}^{mn} + B_{odd}^{mn} \vec{M}_{odd}^{mn} + A_{even}^{mn} \vec{N}_{even}^{mn} + A_{odd}^{mn} \vec{N}_{odd}^{mn} \right) \quad (2.38)$$

with the expansion coefficients  $A_{odd}^{mn}$ ,  $A_{even}^{mn}$ ,  $B_{odd}^{mn}$  and  $B_{even}^{mn}$ . If we now return to the original problem the goal was to solve for the incident  $E_{in}$ , internal  $E_{int}$  and scattered fields  $E_{scat}$  (see Fig. 2.4). For each, different boundary conditions and physical restrictions can be applied, such that the expansions in terms of spherical harmonics simplify to:

$$\vec{E}_{in} = E_0 \sum_{n=1}^{\infty} i^n \frac{2n+1}{n(n+1)} (\vec{M}_{odd}^{mn} - i\vec{N}_{even}^{mn}) \quad (2.39)$$

$$\vec{E}_{int} = E_0 \sum_{n=1}^{\infty} i^n \frac{2n+1}{n(n+1)} (c_n \vec{M}_{odd}^{mn} - id_n \vec{N}_{even}^{mn}) \quad (2.40)$$

$$\vec{E}_{scat} = E_0 \sum_{n=1}^{\infty} i^n \frac{2n+1}{n(n+1)} (ia_n \vec{N}_{even}^{mn} - b_n \vec{M}_{odd}^{mn}) \quad (2.41)$$

With this, the scattered and internal field can be seen as the superposition of normal modes (= spherical harmonics) that are respectively weighted by the coefficients  $a_n$  and  $b_n$  or  $c_n$  and  $d_n$ . For the evaluation of the scattering,  $a_n$  and  $b_n$  are the relevant parameters that can be further simplified by introducing the so-called Riccati-Bessel functions:

$$\psi_n(x) = xj_n(x) \quad \zeta_n(x) = xh_n^{(1)}(x) \quad (2.42)$$

where  $j_n(x)$  are spherical Bessel functions,  $h_n^{(1)}$  are spherical Henkel functions and the parameters  $x = k_2 a = \frac{2\pi\tilde{n}_2 R}{\lambda}$  and  $m = \tilde{n}_1/\tilde{n}_2$  were introduced. The coefficients then read

$$a_n = \frac{m\psi_n(mx)\psi'(x) - \psi_n(x)\psi'(mx)}{m\psi_n(mx)\zeta'_n(x) - \zeta_n(x)\psi'(mx)} \quad (2.43)$$

$$b_n = \frac{\psi_n(mx)\psi'(x) - m\psi_n(x)\psi'(mx)}{\psi_n(mx)\zeta'_n(x) - m\zeta_n(x)\psi'(mx)} \quad (2.44)$$

It can be shown that the  $\vec{N}$  normal modes describe fields without a radial  $\vec{H}$  component, while  $\vec{M}$  fields appear without  $\vec{E}$  in radial direction. Therefore,  $a_n$  is commonly referred to as electric and  $b_n$  consequently as magnetic mode coefficient, where  $n$  describes the order of the so-called multipole expansion. As macroscopic quantity, the scattering is commonly as cross section  $\sigma_{scat}$ , where the scattered energy flow is considered. This is done by integrating the Poynting vector  $\vec{S}_{scat}$  of the scattered field  $\vec{E}_{scat}$  over a closed surface that encloses the particle of interest, which is then weighted by the incident intensity  $I_0$ .

$$w_{scat} = \oint_A d\vec{A} \cdot \vec{S}_{scat} \quad (2.45)$$

$$\sigma_{scat} = \frac{w_{scat}}{I_0} \quad (2.46)$$

With the knowledge of the multipole expansion, this can be rewritten as

$$\sigma_{scat} = \frac{w_{scat}}{I_0} = \frac{2\pi}{k^2} \sum_{n=1}^{\infty} (2n+1) (|a_n|^2 + |b_n|^2) \quad (2.47)$$

A common way to express the scattering of a nanoparticle is by normalizing it to its geometrical cross section, which is referred to as scattering efficiency.

$$Q_{scat} = \frac{\sigma_{scat}}{\sigma_{geom}} \quad (2.48)$$

Although the finding of an analytic solution for more complex structures becomes challenging, the advance of simulation techniques allows the numerical solving scattering problems for arbitrary geometries (more Details on the simulations can be found in section 2.6.1). Then, the knowledge of the electric and magnetic near fields enable a multipole expansion that can be calculated by evaluating the associated scattering current densities [43, 60, 61].

### 2.3.2 Optical resonances and the anapole excitation

Starting with analytical solution of the spherical particle, the difference between metallic and dielectric particles can be explored, using the simplification if a lossless and nonmagnetic material. For a metal ( $\epsilon < 0$ ), magnetic multipole contributions ( $\propto b_n$ ) are negligible such that the response is dominated by the electric coefficients ( $\propto a_n$ ), see Fig. 2.5a. This is a consequence of the fact that electromagnetic fields are not penetrating the volume of the nanoparticle [19], which as discussed in section 2.2 is caused by the free electrons that only allow evanescent fields in the vicinity of the surface. Dielectric particles on the other hand ( $\epsilon > 0$ ) exhibit both electric ( $\propto a_n$ ) and magnetic ( $\propto b_n$ ) contributions. Fig. 2.5b shows the multipole composition for a sphere of a lossless dielectric material ( $\tilde{n} = 4$ ), which exhibits clear distinct resonances that can be associated to the respective Mie coefficients. For a real material, as shown in Fig. 2.5c for silicon, similar peaks can be identified, however, the wavelength dependence of the refractive index and particularly the absorption at smaller wavelengths lead to damping and shifting of the resonances. All apparent peak

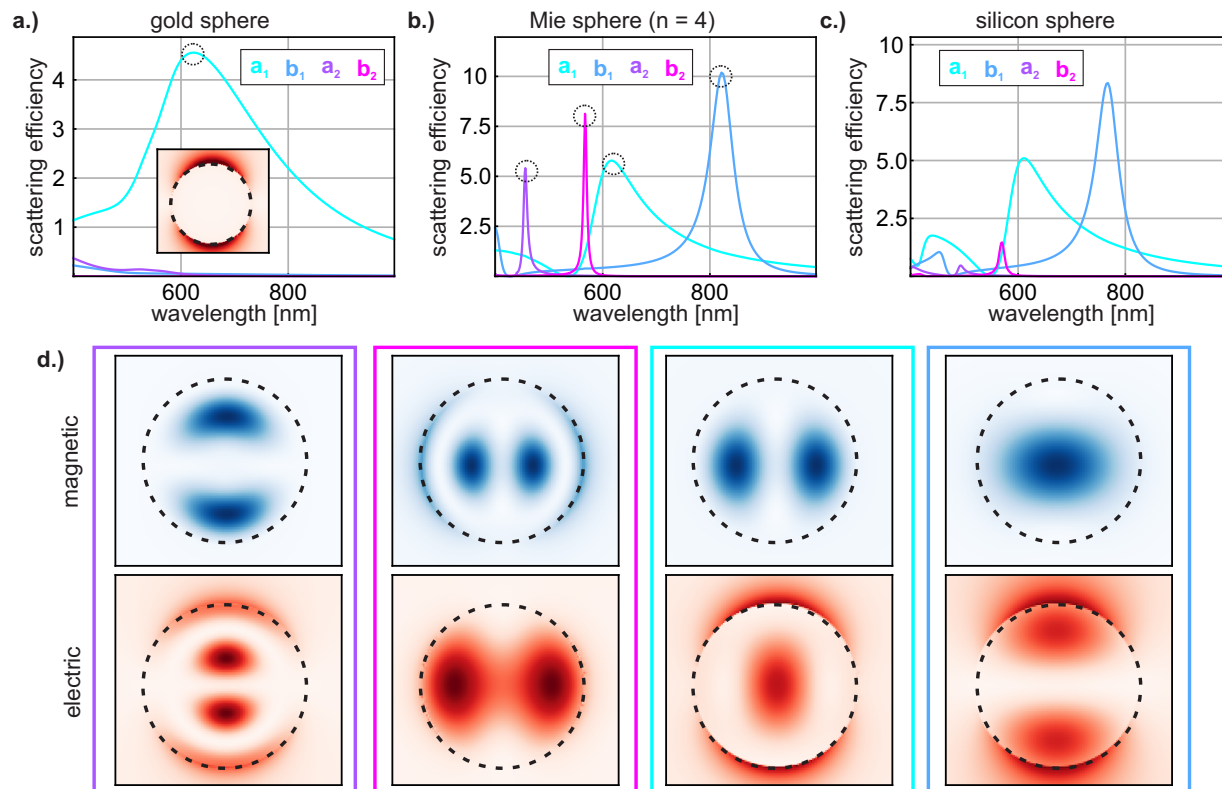


**Figure 2.5:** FDTD simulations of the scattering efficiency according to Mie theory for a sphere with radius  $r = 100$  nm. **a.)** For a sphere made of gold. **b.)** For a lossless sphere with refractive index  $\tilde{n} = 4$ . **c.)** For a silicon sphere. The surrounding medium for all simulations was set to vacuum. The multipole coefficients were extracted using the code provided in reference [60]. **d.)** Simulated near field distributions for the respective peaks of the Mie sphere in b, taken at the center of the sphere.

show scattering efficiencies that are larger than one, what indicates the concentration of electromagnetic energy. Fig. 2.5d shows the magnetic (blue) and electric (red) near field distribution at the respective peak wavelengths of the first four multipole coefficients. Evidently, the field distribution differ significantly with hotspots inside and outside of the sphere. This is an important difference to the gold sphere (inset in Fig. 2.5a), where the electric field is only concentrated at the surface of the structure, as expected.

The ability of dielectric nanoparticles to have strong electric and magnetic resonances enables a wide range of possibilities and a versatile playground to explore [23]. Different shaped structures made of various materials can have a multitude of resonances that can overlap spectrally with complex radiation patterns and interference phenomena. Consequences are Fano-like line shapes [62] and the possibilities to control the farfield emission patterns [63] as well as the electric and magnetic near field distribution [19]. One popular example is the so-called anapole resonance that is a combination of electric and toroidal dipole moments. While the first corresponds to the lowest order of the electric multipole

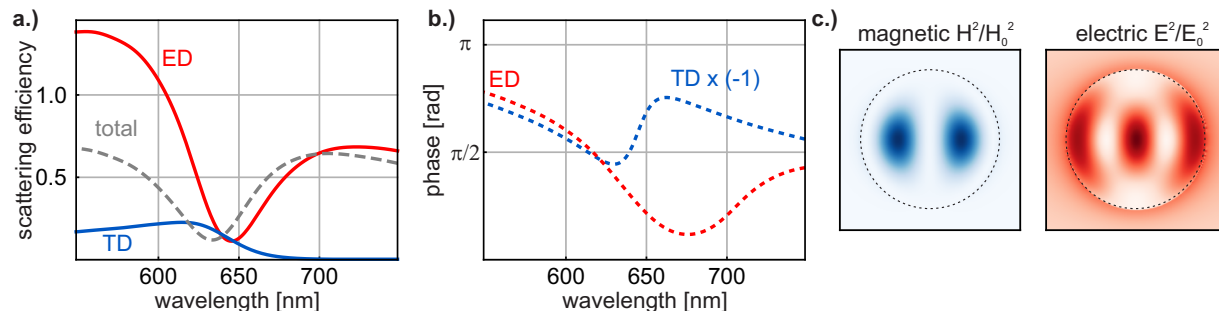


**Figure 2.6:** FDTD simulations of the anapole state for a silicon disc with height 50 nm and radius 310 nm. **a.)** Multipole decomposition of the scattering efficiency. For better visibility, only the electric (ED) and toroidal (TD) modes are shown, together with the total scattering in gray. **b.)** Simulation of the corresponding phase, where the anapole can be identified by the wavelength where both phases are similar. **c.)** Magnetic (blue) and electric (red) near field simulation under the anapole condition.

coefficients, the second is generated by a bound current flow along the cross-section of a torus structure, leading to a radiation pattern that is very similar to the electric dipole [64]. As a consequence, if a nanostructure is designed carefully such that electric and toroidal dipole are out-of phase with a phase difference of exactly  $\pi$ , the two far field emission patterns interfere destructively and no energy is radiated into the far field. This is a so called dark-mode condition and therefore a non-radiating photonic state. These are particularly interesting as their low far-field scattering losses are typically accompanied by a strong energy confinement in the near field of the system [65].

An exemplary simulation of a the anapole is shown for silicon nanodisc with a height of 50 nm and radius 310 nm in Fig.2.6. The condition is met where electric (ED - red line) and toroidal (TD - blue line) have a similar contribution to the scattering efficiency ( $\sim 640$  nm in Fig.2.6a) which is evidently accompanied by a minimum in the total scattering, shown by the dashed gray line in Fig.2.6. The additional requirement for the anapole resonance is that ED and TD are out-of phase such that they interfere destructively. This is confirmed by the simulation of their respective phase factors, shown in Fig. 2.6b. As a result, the electric and magnetic fields are strongly concentrated inside the volume of the nanodisc as shown by the simulated near field distribution in Fig. 2.6c.

It was shown that the anapole condition can be realized with a wide range of different materials and structures, including silicon [64], titanium di-oxide [20] or gallium phosphide [66] nanodiscs. Hereby, the concentrated electric field was, among others, used to the enhance the photocatalytic activity [67] or to significantly boost the efficiency of nonlinear optical frequency conversion [68,69].

## 2.4 Concepts of nonlinear optics

This section will introduce the principles of nonlinear optics and is generally based on the standard textbooks on this topic, for example [24] and [70]. As described in section 2.1, the polarization of a material can be expressed in terms of the electric field  $\vec{E}$  and the material's response function  $\chi$ . For conventional optics, this relation is linear as described in equation 2.9. However, if the field strength is strong enough, this is no longer true and higher orders have to be considered. Then it is convenient to express the polarization in terms of a power series of the incoming electric field:

$$\vec{P}/\epsilon_0 = \chi^{(1)} \cdot \vec{E} + \chi^{(2)} : \vec{E}\vec{E} + \chi^{(3)} : \vec{E}\vec{E}\vec{E} + \dots \quad (2.49)$$

Here, the (non)linear susceptibilities  $\chi^{(i)}$  were introduced, where  $i = 1, 2, 3, \dots$  refers to the order of the nonlinear process. Generally,  $\chi^{(i)}$  is a tensor of rank- $(i+1)$  that can depend on space and frequency. Altogether, equation 2.49 covers a multitude of nonlinear phenomena with a plethora of technical and fundamental applications of which a few will be discussed in the following.

### 2.4.1 High-harmonic generation

High-harmonic generation (HHG) is among the most recognized phenomena in the realm of nonlinear optical interactions. It can be shown that for a nonlinear material that is illuminated with a plane wave of frequency  $\omega_0$ , there is a term for each order  $i = 2, 3, \dots$  in equation 2.49 that oscillates at the frequency  $i \cdot \omega_0$ . This corresponds to a self-interaction of the electromagnetic wave, where  $i$  incident photons with energy  $\hbar\omega_0$  get converted into a single new photon with the energy  $i \cdot \hbar\omega_0$ , a process that is therefore energy conserving (see Fig. 2.7). As a consequence, the interaction with the electrons in the nonlinear material can only happen via "virtual" energy states. This means that no classical absorption process takes place and the electron is not promoted to a higher energy state in the band structure, which makes the HHG process to happen virtually instantaneous. In contrast, multi-photon absorption processes are nonlinear effects where the multiple incident photons are actually absorbed to finally promote an electron in the bandstructure, which will be discussed in section 2.4.2.

#### Second-harmonic generation

Second-harmonic generation (SHG) describes the case of  $i = 2$ , where two incident photons of frequency  $\omega_0$  convert to a new photon with  $2\omega_0$  and is described by the elements of the second-order nonlinear polarization

$$P_i^{(2)} = \epsilon_0 \chi_{ijk}^{(2)} E_j E_k \quad (2.50)$$

where the indices  $ijk$  are the directions of space ( $xyz$ ) and Einstein notation is used. In general, this leads to a total of 27 elements for  $\chi_{ijk}^{(2)}$  that can depend on space and frequency.

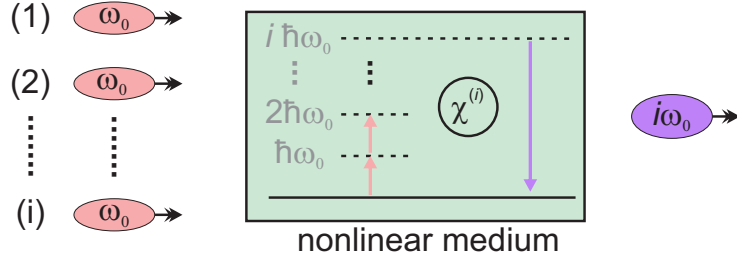


**Figure 2.7:** Sketch of the general process of high-harmonic generation. Inside the nonlinear medium  $\chi^{(i)}$ ,  $i$  photons with the original frequency  $\omega_0$  get converted into a single new photon of frequency  $i \cdot \omega_0$ . A quasi energy diagram of the process is sketched inside the nonlinear medium. The virtual electron states are sketched by the dashed lines.

However, numerous symmetries can be used to simplify the general tensor, particularly for specific crystal structures. Most importantly,  $\chi^{(2)}$  vanishes completely for any material with a center of inversion, which is the case for 11 out of the 32 crystal classes or for any isotropic material. Any other spatial symmetry that is present in a crystal leads to further constraints to the  $\chi^{(2)}$  tensor, for example the zinc blende (*zb*) crystal (43*m* symmetry class). Here, all elements of the tensor vanish, except of

$$\chi_{xyz}^{(2)} = \chi_{xzy}^{(2)} = \chi_{yzx}^{(2)} = \chi_{yxz}^{(2)} = \chi_{zxy}^{(2)} = \chi_{zyx}^{(2)} \quad (2.51)$$

that are all identical. Similar relations are true for all other crystal classes, a full list can be found in [24].

For SHG, equation 2.50 can be further simplified by applying the so-called Kleinmann symmetry. It is based on the assumption of a dispersion-free  $\chi^{(2)}$  and vanishing losses of the nonlinear material. This is approximately true for illumination away from electronic resonances. Then, full permutation symmetry applies such that the rank-3 tensor can be rewritten in terms of a new defined  $3 \times 6$  matrix.

$$\begin{pmatrix} P_x \\ P_y \\ P_z \end{pmatrix} = 2\epsilon_0 \begin{pmatrix} d_{11} & d_{12} & d_{13} & d_{14} & d_{15} & d_{16} \\ d_{11} & d_{12} & d_{13} & d_{14} & d_{15} & d_{16} \\ d_{11} & d_{12} & d_{13} & d_{14} & d_{15} & d_{16} \end{pmatrix} \begin{pmatrix} E_x^2 \\ E_y^2 \\ E_z^2 \\ 2E_y E_z \\ 2E_x E_z \\ 2E_x E_y \end{pmatrix} \quad (2.52)$$

The elements  $d_{il}$  translate to  $\chi_{ijk}^{(2)}$  as follows:

$$\begin{array}{l} jk : \\ l : \end{array} \begin{array}{cccccc} 11 & 22 & 33 & 23, 32 & 31, 13 & 12, 21 \\ 1 & 2 & 3 & 4 & 5 & 6 \end{array} \quad (2.53)$$

Returning to the zinc blende crystal structure with the elements from equation 2.51, the contracted notion simplifies to only three nonzero elements of the  $d$  matrix,  $d_{14} = d_{25} =$

$d_{36} \equiv d_{zb}$  and consequently

$$\begin{pmatrix} P_x^{zb} \\ P_y^{zb} \\ P_z^{zb} \end{pmatrix} = 2\epsilon_0 d_{zb} \begin{pmatrix} 2E_y E_z \\ 2E_x E_z \\ 2E_x E_y \end{pmatrix} \quad (2.54)$$

It should be noted that at the surface of a material, the local symmetry differs from the bulk and is naturally broken. Consequently, the  $\chi^{(2)}$  tensor differs, again exemplary for the zinc blende structure the surface nonlinear polarization reads [70]:

$$\vec{P}_{(S)}^{(2)} = \epsilon_0 \begin{pmatrix} 2d_{15}E_x E_z + 2d_{14}E_y E_z \\ 2d_{15}E_y E_z - 2d_{14}E_x E_z \\ 2d_{13}(E_x^2 + E_y^2) + d_{33}E_z^2 \end{pmatrix} \quad (2.55)$$

Not only the structural symmetry of a material is broken at the surface. Additionally, the electric field exhibits a discontinuity of the component normal to the surface that gives rise to a non-local response inside the bulk of the material. This can be the source of a nonlinear response (even for materials with inversion symmetry) that is beyond the dipole approximation on which the previous analysis was based. Mathematically, this can be expressed as [71]:

$$\vec{P}_{hot}^{(2)} = \alpha(\vec{E} \cdot \nabla)\vec{E} + \beta\vec{E}(\nabla \cdot \vec{E}) + i\gamma\left(\frac{2\omega}{c}\right)(\vec{E} \times \vec{B}) \quad (2.56)$$

with three material dependent constants  $\alpha$ ,  $\beta$ ,  $\gamma$ . The first two terms ( $\alpha$ ,  $\beta$ ) can be attributed to an electric quadrupole excitation while the  $\gamma$  part refers to the magnetic dipole. For most parts of this thesis, the bulk SHG is the dominating effect while higher-order and surface contributions will be neglected.

### Phase matching

For SHG (or in general processes where new frequencies are generated) the efficiency is limited by the so-called phase matching condition. To understand this, the total SHG intensity  $I_{2\omega}$  after traveling through a material of length  $L$  can be calculated. It reads

$$I_{2\omega} \propto L^2 \left( \frac{\sin(x)}{x} \right)^2 \quad (2.57)$$

with the newly defined variable  $x = \frac{\Delta k L}{2}$  and the phase-mismatch  $\Delta k = k_{2\omega} - 2k_\omega$ , which is the difference of the wavenumber at the fundamental  $k_\omega$  and new  $k_{2\omega}$  frequency. It follows that for any nonlinear material, the conversion efficiency drops significantly for a nonzero phase mismatch. Then, if  $\Delta k \neq 0$ , the generated SHG waves have a varying phase factor which eventually leads to destructive interference and dropping nonlinear signal. On the other hand, if the phase matching condition  $\Delta k = 0$  is met, the generated ways can

interfere constructively to build a growing SHG signal. With the know relations, this can be reformulated in terms of the refractive index

$$\tilde{n}(2\omega) = \tilde{n}(\omega) \quad (2.58)$$

Since this is typically not possible for materials with dispersion, the most common way to realize this is by using birefringent crystals. For example. in beta barium borate (BBO), the refractive index differs along the different crystal axes and therefore equation 2.58 can be fulfilled. It should be mentioned that there are other techniques to achieve phase-matching, e.g. by using periodically poled crystals, for more details on this topic, the reader is referred to [24]. As mentioned in the introduction to this thesis, the phase matching condition is less relevant at the nanoscale, or in general for materials that are thinner than the so-called coherence length  $l_{coh}$ , which is the first root for the  $(\sin(x)/x)$  term.

### Third- and higher-harmonic generation

Third-harmonic generation (THG) is the logical continuation of SHG where three instead of two photons with frequency  $\omega_0$  convert into a new photon of frequency  $3\omega_0$ . With the third-order nonlinear susceptibility  $\chi^{(3)}$ , the components of the polarization can be written as

$$P_i^{(3)} = \epsilon_0 \chi_{ijkl}^{(3)} E_j E_k E_l \quad (2.59)$$

Besides this, all properties that were discussed for SHG are valid for THG as well. The process is energy conserving, happens via virtual electron states and (at the macroscale) needs to fulfill the phase matching condition to happen efficiently. The  $\chi^{(3)}$  tensor depends generally on space, frequency and has 81 independent elements and can be simplified by spatial symmetries of a crystal. However, THG does not necessarily vanish in centrosymmetric materials.

In a similar fashion,  $n$ th-harmonic generation can be defined for any integer  $n$ . As previously mentioned, the process is determined by the nonlinear susceptibility  $\chi^{(n)}$ , which is a rank- $(n + 1)$  tensor. A general restriction to  $\chi^{(n)}$  is, that for even  $n$ , the (bulk) contribution to the nonlinear process will always vanish in centrosymmetric materials, whereas odd-orders are generally allowed under any symmetry condition. It should furthermore be noted that phase matching has to be guaranteed for any nonlinear frequency conversion process to occur efficiently.

#### 2.4.2 The nonlinear refractive index

When multiplying out the term of third-order nonlinear effects (cubic term in equation 2.49), it contains a part that oscillates with the frequency  $\omega$  of the fundamental beam. It can be shown that this corresponds to a nonlinear modification  $\tilde{n}_2$  of the (complex) linear refractive index  $\tilde{n}_0$  which scales with the intensity of the fundamental beam.

$$\tilde{n} = \tilde{n}_0 + \tilde{n}_2 I(\omega) \quad (2.60)$$

In case of a modification to the real part of the refractive index and therefore a real valued  $\tilde{n}_2 = n_2$ , this is commonly referred to as the optical Kerr effect (OKE), which generally describes the change of the refractive index in dependence of an electric field. As such it is the nonlinear equivalent of the Pockels effect, where the change of the refractive index is linearly dependent on the electric field strength. The Kerr coefficient  $n_2$  can be related to the nonlinear susceptibility by [23]

$$n_2 = \frac{3}{4c^2 n_0^2 \epsilon_0} \Re \chi^{(3)} \quad (2.61)$$

If  $n_2$  is positive, high intensity laser beams can induce a refractive index profile into a nonlinear material which acts like a focusing lens for the beam itself, leading to a process called self-focusing. Since focusing leads to an increase of the intensity, this process will theoretically cascade until the beam collapses [72] or the medium is optically damaged. Nevertheless, the Kerr effect has important technical applications such as Kerr-lens mode-locking or parametric amplification [73]. Self-focusing occurs after the incident intensity exceeds a threshold power  $P_{th}$ , defined as [74]

$$P_{th} = \alpha \frac{\lambda^2}{4\pi n_0 n_2} \quad (2.62)$$

where  $\alpha$  is a constant that depends on the beam profile.

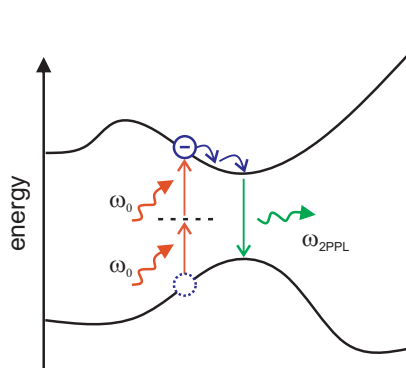


**Figure 2.8:** Sketch of TPA and subsequent 2PPL.

An additional contribution to the nonlinear refractive index is induced by two-photon absorption (TPA), where two photons get absorbed via a virtual energy state (see Fig. 2.8). In contrast to the Kerr effect, this corresponds to a modification of the absorption coefficient  $\alpha_0$ , is proportional to the imaginary part of  $\chi^{(3)}$  and similarly scales with the beams intensity.

$$\alpha = \alpha_0 + \beta I(\omega) \quad (2.63)$$

with the TPA coefficient  $\beta$ . In case of a suitable band structure of the material, TPA can be accompanied by a photoluminescence (2PPL) as sketched in Fig. 2.8. Hereby, the excited TPA electron relaxes towards the bandgap and can then recombine with a hole in the valence band by emitting a photon of frequency  $\omega_{2PPL}$ . Since there are relaxation processes (via electron-electron or electron phonon-scattering), the emission of the 2PPL photon happens with a time delay and there is energy transferred to the material. Consequently, the following inequality must be true:

$$\omega_{2PPL} < 2 \cdot \omega_0 \quad (2.64)$$

This is an important difference to the previously discussed SHG process where the energy of the photons is conserved.

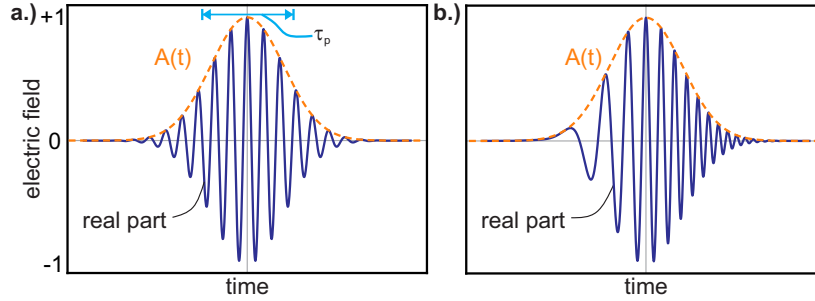


**Figure 2.9:** Visualization of two ultrafast laser pulses, **a.)** without and **b.)** with linear chirp. The envelope function is respectively shown.

## 2.5 Basics of ultrafast optics

In contrast to continuous wave (CW) radiation, many modern laser systems employ a series of consecutive light pulses, each with a finite duration (see Fig. 2.9a). This approach offers distinct advantages, particularly in nonlinear optical experiments, as it allows for higher peak intensities by confining the laser energy to much smaller time scales. The generation of laser pulses involves the superposition of monochromatic plane waves with varying frequencies and a fixed phase relationship. Unless differently stated, the following section is based on ref. [75], to which the reader is referred for more details. For simplicity, in the following Gaussian shaped pulses in one spatial dimension are considered, however, the principles discussed can be extended to encompass pulse shapes of any profile.

### 2.5.1 Transform-limited pulses and chirp

The time-dependent electric field of a Gaussian pulse at a fixed position in space can be described as the product of the function  $e^{-\gamma t^2}$  and the oscillating electric field. For a real valued  $\gamma = \gamma_1$ , this corresponds to a Gaussian envelope  $A(t)$  that modulates the electric field as shown in Fig. 2.9a. This leads to an intensity  $I(t) \propto |E(t)|^2$  that can be expressed as

$$I(t) \propto e^{-2\gamma_1 t^2} \quad (2.65)$$

It has a pulse length defined as the full-width half-maximum (FWHM) of  $\tau_p^2 = 2 \ln 2 / \gamma_1$ . If instead  $\gamma = \gamma_1 - i\gamma_2$  becomes a complex parameter,  $\gamma_2$  introduces an additional phase term. By defining the instantaneous frequency  $\omega$  as the derivative of the total phase  $\phi(t) = \omega_0 t + \gamma_2 t^2$ , this leads to an additional time dependence.

$$\omega(t) = \frac{d\phi(t)}{dt} = \omega_0 + 2\gamma_2 t \quad (2.66)$$

If this so-called 'chirp' is positive, the instantaneous frequency will grow with time, if it is negative it will decrease. Fig. 2.9 shows the comparison of a pulse without and with a positive chirp, where the growing frequency is clearly visible.

As a pulse is achieved by the superposition of monochromatic waves with different frequencies, the associated frequency spectrum can be calculated by applying a Fourier transform

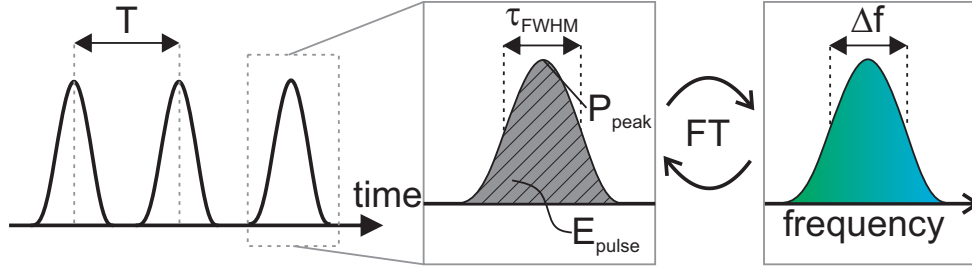


**Figure 2.10:** Overview over an ultrafast pulse train. The pulses are separated in time by the period  $T$ . A single pulse is characterized by its temporal width  $\tau_{FWHM}$ , the peak power  $P_{peak}$  and the pulse energy  $E_{pulse}$ , which corresponds to the integral over the dashed area. Additionally, the connection between the temporal shape and frequency spectrum of a pulse via Fourier transform (FT) is shown.

to the temporal function of the pulse. For the Gaussian example from equation 2.65, this reads

$$\tilde{I}(\omega) \propto e^{-4\ln(2)\left(\frac{\omega-\omega_0}{\Delta\omega}\right)^2} \quad (2.67)$$

In contrast to the temporal width of the pulse, it can be shown that the spectral width  $\Delta\omega$  depends on real and imaginary part of  $\gamma$  and is given by

$$(\Delta\omega)^2 = 8\ln(2)\gamma_1 \left( 1 + \left( \frac{\gamma_2}{\gamma_1} \right)^2 \right) \quad (2.68)$$

A common quantity to describe the quality of ultrashort pulses is the time-bandwidth product (TBP), which is simply defined as

$$TBP = \tau_p \Delta f = \tau_p \Delta\omega / 2\pi \quad (2.69)$$

From this follow a few points that are generally true for an arbitrary pulse shape and spectrum. First, the bandwidth  $\Delta\omega$  and pulse length  $\tau$  are inversely proportional, a consequence of the Heisenberg uncertainty principle. This means that when reducing the pulse length in time, a broadening of the spectrum is needed, and vice versa. Furthermore, from equation 2.68 it follows for a nonzero chirp  $\gamma_2 \neq 0$ , the spectral bandwidth of the pulse is larger than for  $\gamma_2 = 0$ . Therefore, the TBP is minimized for vanishing chirp, which is called a transform-limited (TL) or bandwidth-limited pulse. This minimum TBP depends on a given pulse shape/ envelope function, for of a Gaussian pulse it can be calculated to be  $TBP_{min} = 0.4413$ .

In the work with pulsed laser systems, it is convenient to introduce the following quantities that are sketched in Fig. 2.10.

- The pulse train refers to the laser beam, consisting of the series of laser pulses.

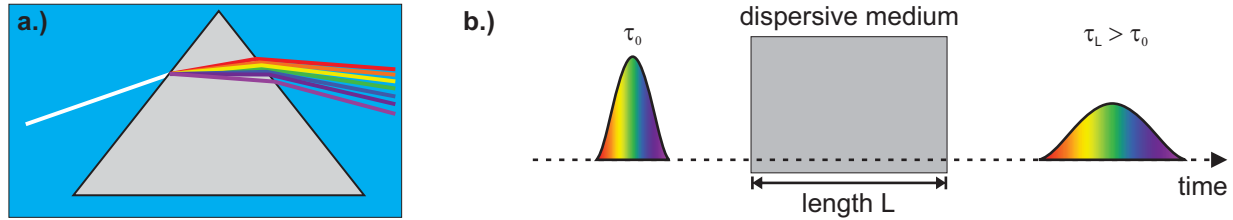


**Figure 2.11:** a.) Spatial dispersion experienced by a white-light beam that is caused by traveling through a prism with normal dispersion ( $\partial_\lambda n < 0$ ). b.) Sketch of temporal dispersion that an ultrashort pulse experiences when traveling through a dispersive medium with length  $L$ .

- The temporal distance  $T$  between two pulses. The inverse is the so-called repetition rate  $f_{rep} = 1/T$ , which describes the number of pulses per second, i.e. the frequency of the pulse train.
- The average power  $P_{av}$  is defined as the power that is delivered by a pulse train, integrated over 1 s.
- The pulse energy  $E_{pulse}$  is the energy contained in a single pulse, defined as  $E_{pulse} = P_{av}/f_{rep}$ .
- The peak power  $P_{peak}$  is defined as the peak of the energy that is reached by a pulse. Therefore it depends on the time duration and is typically approximated as  $P_{peak} = E_{pulse}/\tau$ .

## 2.5.2 Dispersion effects

In section 2.2 it was introduced that the refractive index of materials depends on the frequency and therefore the light's wavelength and velocity can be seen as functions of the frequency. This leads to well-known effects when working with multi-wavelength light, prominent examples are the formation of rainbows or the color separation in a prism, sketched in Fig. 2.11a. When dealing with short laser pulses, which consequently have a large spectral bandwidth, this phenomenon becomes a fundamental challenge. In a dispersive medium, each frequency component will travel with a slightly different velocity ( $c = c_0/n$ ) and the pulse will slowly lose its confinement in time (Fig. 2.11b). Mathematically, this can be derived by expanding the wavenumber  $k = \omega/c$  for small deviations  $\Delta\omega$  around the center frequency  $\omega_0$

$$k(\omega) = k(\omega_0) + \frac{dk}{d\omega}\Delta\omega + \frac{1}{2}\frac{d^2k}{d\omega^2}(\Delta\omega)^2 + \dots \quad (2.70)$$

The term linear in  $\Delta\omega$  corresponds to the dispersion of a material and is defined as the inverse of the group velocity  $v_g$ .

$$v_g = \frac{1}{\partial_\omega k(\omega)} \quad (2.71)$$

While the earlier introduced, so-called phase velocity  $c(\omega) = c_0/n(\omega)$  describes the speed of each individual, single frequency wave in a pulse,  $v_g$  is the resulting velocity of the envelope function. Consequently, the term in 2.70 describes a temporal shift that the pulse experiences when traveling through a material and is commonly referred to as group delay .

The quadratic term in 2.70 on the other hand, which is called group delay dispersion (GDD), leads to a temporal broadening of the pulse, i.e. it introduces a chirp into the phase. Assuming a Gaussian, TL-pulse with a temporal width of  $\tau_0$ , traveling through a dispersive material of length  $L$  leads to a broadening by

$$\frac{\tau_p(L)}{\tau_p(0)} = \sqrt{1 + \frac{(4 \ln(2)Ld)^2}{\tau_p^4(0)} (\partial_\omega^2 k)^2} \quad (2.72)$$

This affects the pulse only in the time domain while the frequency spectrum doesn't change. Furthermore, 2.72 shows that it depends on the original pulse length  $\tau_p(0)$ , why (for common glasses) the effect is negligible and becomes only relevant for laser pulses that are shorter than 100 fs. Typically, the GDD  $\partial_\omega^2 k$  is expressed in terms of the accumulated phase shift  $\partial_\omega^2 \phi(\omega) = \partial_\omega^2 (kn(\omega)L)$ , which then has the unit  $\text{fs}^2$ . It should be noted that there can be higher order dispersion processes that can affect the pulse shape when traveling through a material which will not be discussed in more detail here.

### 2.5.3 Multiphoton intrapulse interference phase scan

The work with ultrafast pulsed lasers naturally raises the question of how to resolve and measure their temporal extent and shape. Ultrashort pulses are the fastest events generated by humanity and after their duration became shorter than picoseconds, a measurement of the pulses based on traditional detectors is no longer possible. Therefore, other techniques had to be invented which were not based on (slow) electronic components.

#### Autocorrelation and frequency-resolved optical gating

It turns out that an easy way to investigate ultrafast pulses is to measure their self-interaction. This can be done by implementing a setup that measures the autocorrelation (AC) as sketched in Fig. 2.12a. The laser is divided into two beams which are then send through two different pathways with a controllable path difference  $\Delta s$ . With modern high-precision stages, it is possible to tune the temporal delay  $\tau = \Delta s/c_0$  with below 1 fs precision. The two beams are then recombined and overlapped inside a nonlinear crystal, where new frequency light is generated and sent to a (slow) photodiode. Before,

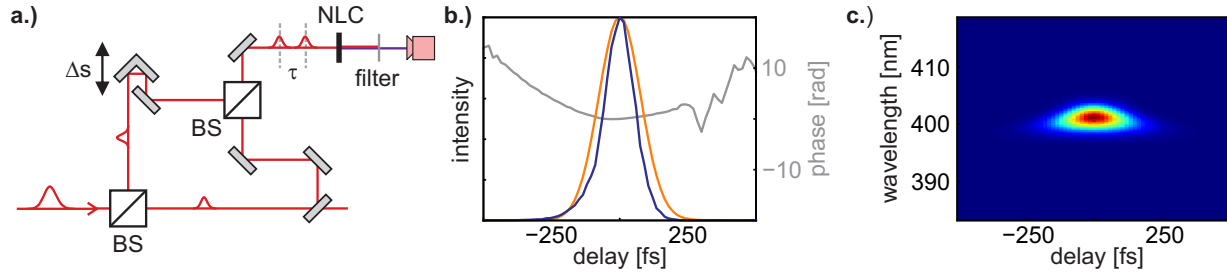


**Figure 2.12:** a.) Sketch of an optical autocorrelation setup, BS refers to beamsplitter and NLC to a nonlinear crystal. b.) Exemplary result of an autocorrelation trace for a  $\tau_p = 130$  fs pulse (orange curve). The results of the same pulse retrieved by a FROG measurement is shown blue, the phase in gray. c.) measured FROG trace of the pulse from (b.)

an appropriate filter ensures that no light of the original laser frequency arrives at the detector. Now, the path difference can be tuned by moving the delay stage and the (time averaged) intensity of generated light can be recorded accordingly. The result has the mathematical structure of an autocorrelation function and can be expressed as (in case of SHG as nonlinear process):

$$I_{2\omega}(\tau) \propto \int_{-\infty}^{+\infty} dt I(t) I(t - \tau) \quad (2.73)$$

However, since only intensities  $I \propto |E|^2$  are measured in the end, all phase information of the pulse are lost, for example the spectral shape and the chirp. Nevertheless, an autocorrelation measurement allows to extract the temporal FWHM for a known beam shape with a flat phase. An exemplary measured AC trace is shown by the orange curve 2.12b.

In case that more information are needed, more advanced techniques were invented that can record phase and envelope function, prominent examples are frequency-resolved optical gating (FROG) and spectral phase interferometry for direct electric-field reconstruction (SPIDER). In the following, FROG will be discussed more in detail. The general setup is identical to the Fig. 2.12a with the difference that the photodiode is replaced by a detector with spectral sensitivity. Typically, this is realized by a spectrometer and a charge-coupled device (CCD) camera. This allows to measure the intensity as a function of the pulse frequency  $\omega$  and the time delay  $\tau$  between the two beams (see Fig. 2.12c. If the nonlinear interaction is again SHG, the measured intensity reads:

$$I_{FROG}(\omega, \tau) = \left| \int_{-\infty}^{\infty} dt E(t) E(t - \tau) e^{-i\omega t} \right|^2 \quad (2.74)$$

The retrieval of the pulse shape in time and frequency from a measured FROG trace is not trivial and a variety of algorithms exist to perform that task. This thesis uses a popular variant that is done with the codes provided by Trebino's group that pioneered

in that field [76, 77]. The blue line in Fig. 2.12b corresponds to the retrieved pulse from the FROG trace in subfigure c, together with the extracted phase in gray. Evidently, the details in the shape are different to the result that was extracted from the autocorrelation measurement.

### Pulse compression and phase retrieval

An alternative technique for the characterization of ultrashort pulses is multiphoton intrapulse interference phase scan (MIIPS), which not only measures a pulse, but simultaneously compensates for phase distortions [78]. Instead of FROG and AC, where a temporal delay is used to characterize a pulse, MIIPS is based on spectral phase functions that can be controlled by an adaptive pulse shaper. The general working principle is sketched in Fig. 2.13, whereas the experimental realization is discussed in section 3.4. After leaving the pulse shaper, the setup is similar to FROG, with a nonlinear crystal (NLC) where nonlinear light (typically SHG) is generated and a filter that removes light of the original frequency after which the generated light is analyzed with a spectrometer. The pulse shaper allows to manipulate the phase for each of the frequency components in the ultrashort pulse. During the MIIPS algorithm, different well-known phase functions  $f(\omega)$  are applied to the pulse, such that the measured SHG intensity at frequency  $2(\omega + \Delta)$  can be expressed as [78]

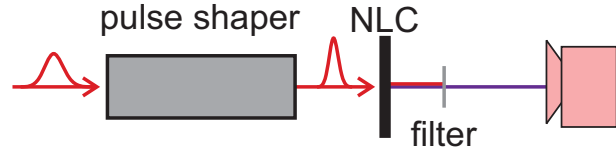


**Figure 2.13:** Working principle of MIIPS.

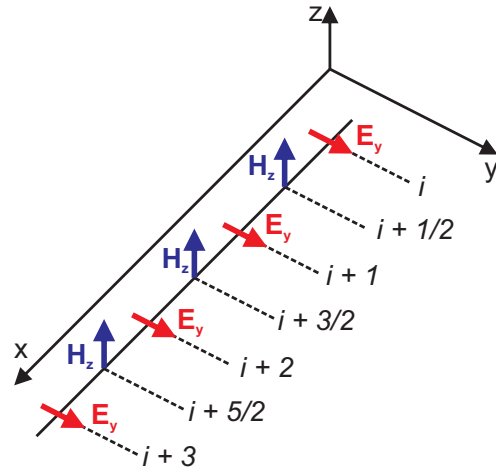
$$I(\Delta) = \left| \int d\Omega |E(\Delta + \Omega)| |E(\Delta - \Omega)| e^{i(\varphi(\Delta + \Omega) + \varphi(\Delta - \Omega))} \right|^2 \quad (2.75)$$

The total phase is now  $\varphi_{tot}(\omega) = \phi(\omega) + f(\omega)$ , with the original (unknown) phase  $\phi_{pulse}(\omega)$  of the pulse. By measuring the SHG intensity, which is proportional to  $\phi_{tot}$ , this allows to extract the phase  $\phi_{pulse}$ . It can be shown that when considering the leading order terms, the SHG signal is maximized if the the second order derivative of the total phase vanishes.

$$\varphi''_{tot}(\Delta) = \partial_{\Omega}^2 \varphi_{tot}(\Delta) = \phi''(\Delta) + f''(\Delta) = 0 \quad (2.76)$$

A common example is to use functions of the form  $f(\Delta) = \alpha \cos(\gamma\Delta - \delta)$ . Then, the sweeping of the  $\delta$  parameter and the collection of the SHG spectra generates a MIIPS data set and the ideal phase correction  $\delta_{max}$  can be determined. From this, the original phase  $\phi$  can be retrieved and corrected by applying  $-\phi$ , such that the resulting pulse is transform limited. In the MIIPS spectrum, this can be seen by parallel lines that are respectively separated by  $\pi$ . An exemplary measurement and the experimental realization of MIIPS is part of section 2.5.3. For more details including for example higher order corrections, the reader is referred to refs. [78–80].

**Figure 2.14:** Yee cell in one dimension with the electric and magnetic fields indicated at the positions where they are defined and saved.



## 2.6 Optical Simulations

Although Maxwell's equations and the wave equation are solvable for arbitrary geometries, the process can become very complex and computationally intensive. Particularly at the nanoscale, interactions are increasingly complex and difficult to predict and solve. Here optical simulations are a powerful tool that allow to numerically model a nanophotonic system and to gain insights before fabricating and measuring them in the laboratory. For this thesis, two different simulation methods were used that are discussed in the following.

### 2.6.1 Finite-difference time-domain simulations

The finite-difference time-domain (FDTD) method is a commonly used numerical technique for simulating the behavior of electromagnetic fields in nanophotonic structures. As the name indicates, it is a time-domain method, where Maxwell's equations 2.1 - 2.4 are solved for every time step  $\Delta t$ . This allows to solve for many frequencies within one simulation and it is therefore a convenient choice for cases where a broadband analysis is needed. In FDTD, the desired structures are divided into small rectangular cells ('mesh') which all are associated with values of the electric and magnetic field according to Maxwell's equations. These are then updated with each time step iteratively by solving a set of differential equations that are discussed in the following. For simplicity, the mathematics are limited to the one dimensional case, the two and three dimensional derivations can for example be found in [81].

#### Yee's algorithm in one dimension

The numerical solution provided by the FDTD method is based on the discretization of Maxwell's equations in space and time. This is done by approximating the appearing

derivatives by the so-called centered difference form which for example reads

$$\partial_t f|_i^n = \frac{f_{i+1}^n - f_{i-1}^n}{2\Delta t} + O(\Delta t)^2 \quad (2.77)$$

for the time derivative of an arbitrary function  $f$ . The index  $n$  corresponds to the iteration number in time and  $\Delta t$  to the step size. Analogous, the derivative in space can be defined with the index  $i$  which refers to the spatial grid point and  $\Delta x$  as the distance of mesh cells. To solve Maxwell's equations based on this, the FDTD algorithm was invented by Kane S. Yee and makes use of the so-called interleaved leapfrog method. For this, intermediate points are introduced into the space-time grid, located at  $i \pm 1/2$  and  $n \pm 1/2$  (see Fig. 2.14 for a z-polarized wave). Then, the one dimensional wave equations (for  $y$ -polarized electric field) read

$$E_y|_i^{n+1} = E_y|_i^n - \frac{\Delta t}{\epsilon_i \Delta x} \left( H_z|_{i+1/2}^{n+1/2} - H_z|_{i-1/2}^{n+1/2} \right) \quad (2.78)$$

$$H_z|_{i+1/2}^{n+1/2} = H_z|_{i+1/2}^{n-1/2} - \frac{\Delta t}{\mu_{i+1/2} \Delta x} \left( E_y|_{i+1}^n - E_y|_i^n \right) \quad (2.79)$$

with the material parameters  $\epsilon$  and  $\mu$ . As illustrated in Fig. 2.14, the electric field component in grid point  $i$  and at time step  $n + 1$  is calculated from the previous time step  $n$  and the difference of the magnetic field values at the neighboring, half-integer grid points  $i \pm 1/2$  at the time step  $n + 1/2$ . Once starting values are defined, the iterative procedure allows to solve for the fields over the entire (time and space) grid.

### Implementation in Lumerical FDTD

The simulation software that is used for the simulations of this thesis is Lumerical FDTD from the Ansys software suit. It allows to generate arbitrary structures in two or three dimensions with a set of different boundary and symmetry conditions. The electric and magnetic field values can be recorded with monitors that can be freely positioned. The software allows to choose the simulated wavelength range, spectral resolution of the saved fields and to implement any material of choice. For this thesis, the materials were defined by using measured optical properties from ellipsometry measurements, which will be discussed in section 3.3.1.

In the case of single structure simulations, the total-field scattered-field (TFSF) source is used, which is particularly convenient to investigate scattering problems. The source is defined as two or three dimensional cuboid that should be placed inside the simulation regime. A plane wave  $\vec{E}_{in}$  is then launched from one of the edge faces. Inside the TFSF borders, the solver will save the total electric field present (see Fig. 2.15), which is  $\vec{E}_{tot} = \vec{E}_{scat} + \vec{E}_{in}$ . For the field outside the TFSF source on the other hand, the launched plane wave is subtracted such that only the scattered field is present. Exemplary, in Fig. 2.15, the field outside the border is zero when there is no scatterer. In case of a scattering object on the other hand, only the scattered field can be seen in that area. This allows

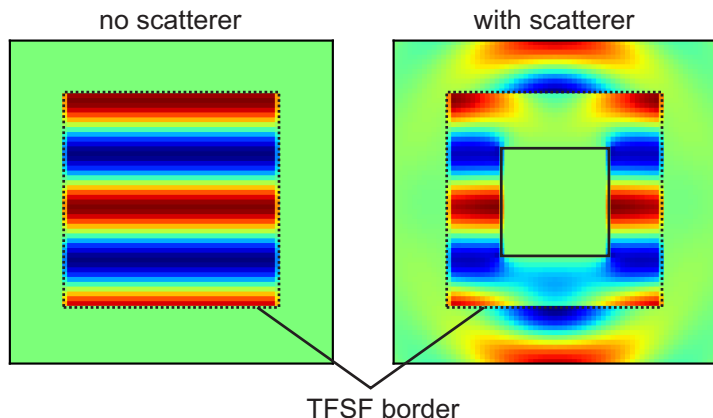


**Figure 2.15:** Visualization of the total-field scattered-field (TFSF) source in Lumerical FDTD. Inside the borders of the source, the total field is present, outside, only the scattered field. Shown is the case without (left) and with (right) a scattering object

to simply extract the scattering cross section by placing a monitor surrounding the TFSF source which records the outgoing power flux  $P_s$ . A similar monitor placed inside the source boundaries consequently records the power flux of the total field  $P_{tot}$  in the system. In combination this allows to extract the scattering  $\sigma_s$  and absorption  $\sigma_a$  cross section by simply normalizing with the source intensity  $I_{in}$ .

$$\sigma_s = P_s/I_{in} \quad (2.80)$$

$$\sigma_a = P_{tot}/I_{in} - P_s/I_{in} \quad (2.81)$$

For most simulations, the goal is to simulate the respective particle in an infinite space. To mimic this, Lumerical FDTD allows the usage of so-called perfectly matched layer (PML) boundary conditions. These are design to absorb any incident electromagnetic radiation without causing any reflection at the interface. It should be noted that this far from trivial and the definition of PMLs is theoretically extensive, for more details the reader is referred to [81].

### 2.6.2 The finite-element method

An alternative numerical method is the finite-element method (FEM), which is a widely used tool for any physical simulation where differential equations are involved, e.g. mechanical or fluid flow problems. In contrast to FDTD, where the geometry is always divided into rectangular elements (see Fig. 2.16a), FEM allows generally arbitrary shapes and orientation what makes it very flexible and practicable for complex structures. A common example is a tetrahedral mesh which becomes denser in areas where more complex fields are expected, for example the boundary of the sphere in Fig. 2.16b. In FEM, the solution to Maxwell's equations is approximated by minimizing a functional that includes the electromagnetic wave equations 2.11 and 2.12 and appropriate boundary conditions. Hereby, the interfaces ('nodes') between neighboring cells are of particular importance and it is to be ensured that Maxwell's equations are fulfilled here. This is done by expanding the

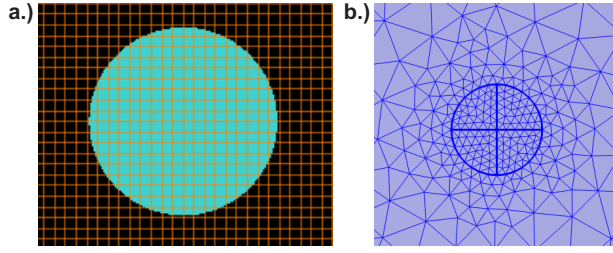


**Figure 2.16:** Comparison of the meshing procedure between **a.)** Lumerical FDTD and **b.)** COMSOL Multiphysics. The first contains always a rectangular elements while FEM allows arbitrary shaped mesh, in this case tetrahedons.

electric field with a set of suitable functions  $\vec{N}$  [82].

$$\vec{E} = \sum_{j=1}^N E_j \vec{N}_j(\vec{r}) \quad (2.82)$$

where  $N$  is the number of nodes. With this, the FEM algorithm rewrites to a linear algebra problem with the sparse matrix  $M$ , the (unknown) electric field  $\vec{E}$  and a vector related to the sources terms of the system  $\vec{b}$ .

$$M\vec{E} = \vec{b} \quad (2.83)$$

To solve this set of equations, different algorithms are available which will not be discussed in detail here, prominent examples are Galerkin's or Ritz's methods [81]. All this makes FEM practicable for complex and particularly curved structures, where the rectangular mesh of FDTD can lead to staircase effects.

### The implementation in COMSOL Multiphysics

The FEM simulations in this thesis are performed in COMSOL Multiphysics which is a powerful software to simulate a wide range of physical problems. More precisely, the radio frequency (RF) module is used for simulations in the frequency domain, which is convenient for single-wavelength simulations. The software allows to design arbitrary geometries with custom material parameters that can be defined by the user. For the simulation of single scattering objects, COMSOL allows a similar setup to the TFSF source of Lumerical. Here, a background field is manually defined which should be the solution to Maxwell's equations in the case of no scattering object. This can for example be a simple plane wave in case of a structure in vacuum or the incident, reflected and transmitted waves according to the Fresnel equations 2.22-2.25 for an object on a substrate. The COMSOL solver is then set to only solve for the scattered field, such that the scattering cross section can be calculated by

$$\sigma_{scat} = \int_A d\vec{A} \cdot \vec{P}/P_0 \quad (2.84)$$

Here,  $\vec{A} = A\hat{n}$  is an arbitrary surface  $A$  that completely encloses the scattering object,  $\hat{n}$  is the outwards pointing surface normal. Since the simulation solves for the scattered field,

the Poynting vector  $\vec{P}$  contains only the scattered field and  $P_0$  is the power of the source wave, i.e. by defined in the background field. Similar to the implementation in Lumerical FDTD, COMSOL allows so limit the simulation volume by PML boundary conditions to mimic the infinite space.

One advantage of COMSOL is the possibility to straightforward simulate nonlinear optical processes such as SHG. For this, the simulation is separated into two steps. First, it solves for the exciting field at frequency  $\omega$  and the solution is used to calculate the induced nonlinear polarization as defined by equation 4.1 and hte susceptibility tensor  $\chi^{(2)}$  of the respective material. From this, the current density  $\vec{J}^{(n)}$  can be extracted by

$$\vec{J}^{(n)} = \partial_t \vec{P}^{(2)} = i(n\omega)\epsilon_0 \vec{P}^{(2)} \quad (2.85)$$

This is then used to as the source for the second simulation step, which is done at the SHG wavelength  $2\omega$ . It should be noted that this requires special care when defining the mesh and constants in the software.



# Chapter 3

## Methodology

This chapter describes the methodology used for experiments in this thesis. First, the nanofabrication workflow and structural analysis are discussed, followed by the different optical experiments, both in the linear and nonlinear regime.

### 3.1 Nanofabrication

This section describes the different techniques that are used for the fabrication and structuring of the (nano)materials presented in this thesis. While the details may differ for the different systems, the general procedure is similar. In general, it can be separated in three different steps, starting with the substrate cleaning and thin film deposition where the desired material is prepared, followed by the electron-beam lithography (EBL) that converts the previously designed geometry as hard mask on the thin film. Finally, in the etching steps, the design is transferred into the material and remaining masks and unwanted materials are removed. This section describes the general methodology of the used procedures whereas the specific parameters are given after each experimental section and the appendix A.1.

#### 3.1.1 Thin film deposition

In advance, the substrates of choice are carefully cleaned by an ultrasonic bath first in acetone, in isopropyl alcohol (IPA) and then in deionized water (DI). Finally, a treatment in an oxygen plasma (diener electronic GmbH) at 20 sccm and 100% power for several minutes remove small contamination from the surface. Throughout this thesis, different deposition techniques are used to fabricate thin films of various materials and structure. Their different working principles are sketched in Fig. 3.1.

##### Sputter deposition

Sputter deposition is a physical vapor deposition (PVD) method that is based on the ejection of a material by ion bombardment as sketched in Fig. 3.1a. For this a target of

the desired materials is placed in a vacuum chamber, where a plasma is ignited in a gas mixture of oxygen and argon. The sample is placed on a substrate holder and a voltage is applied with respect to the target. As a consequence, the ions of the plasma are accelerated towards the latter, where they impact with high velocity such that atoms of the material are kicked out. The ejected atoms then deposit on the substrate where eventually the thin film grows. The sputter deposition for this thesis is carried out with an Angstrom deposition tool and materials as gallium phosphide and indium tin-oxide, with the typical deposition parameters noted in Table A.1 in the appendix.

### Molecular-beam epitaxy

Molecular-beam epitaxy (MBE) is a thin-film deposition technique used to produce high-quality, thin films of semiconductor materials with a very precise control over the thickness and composition of the film. It is a process in which atoms or molecules are evaporated from a heated source, and then allowed to deposit on a substrate under ultra-high vacuum conditions, typically in the range of  $10^{-9}$  to  $10^{-11}$  Torr. The sources are typically so-called Knudsen or effusion cells providing a stream of single element atoms that is directed towards the substrate where they condense and form the thin film, which is grown layer-by-layer. According to the composition of the resulting material, multiple cells are combined and the process can be controlled by e.g. the temperature of the sources, the substrate and inside the chamber, which usually are a few hundreds of degree Celsius. Most MBE machines include a reflection high-energy electron diffraction (RHEED) system inside the chamber (see Fig. 3.1b). Without going into too much detail here, RHEED makes use of the diffraction of an electron beam under high angle of incidence. Similar to the techniques that will be discussed in the following section, this allows to observe the growth and crystal quality *in situ* during the process. In this thesis, MBE is used for the fabrication of niobium phosphide thin films which will be part of chapter 5, with the deposition details noted in the end of the chapter.

### Chemical vapor deposition

Chemical vapor deposition (CVD) summarizes two deposition techniques that were used in this thesis and that are based on the chemical reaction of elements contrarily to the physical deposition of layers in the previous methods. Although the details differ, the general arrangement of a CVD machine is shown in Fig. 3.1c.

**Plasma-enhanced chemical vapor deposition (PECVD):** In PECVD, the chemical reaction of the precursor gases occur in the state of a plasma which is usually ignited by high-frequency electric fields. This enables strong chemical reactions of the gas atoms and eventually the formation of a thin film on the substrate. In this thesis, PECVD is used for the deposition of  $\text{SiO}_2$  and amorphous silicon thin films.

**Metalorganic chemical vapor deposition (MOCVD):** While the previous discussed technique generally results in an amorphous structure of the deposited film, MOCVD allows the growth of crystalline thin films. As such, it is comparable to the previously dis-

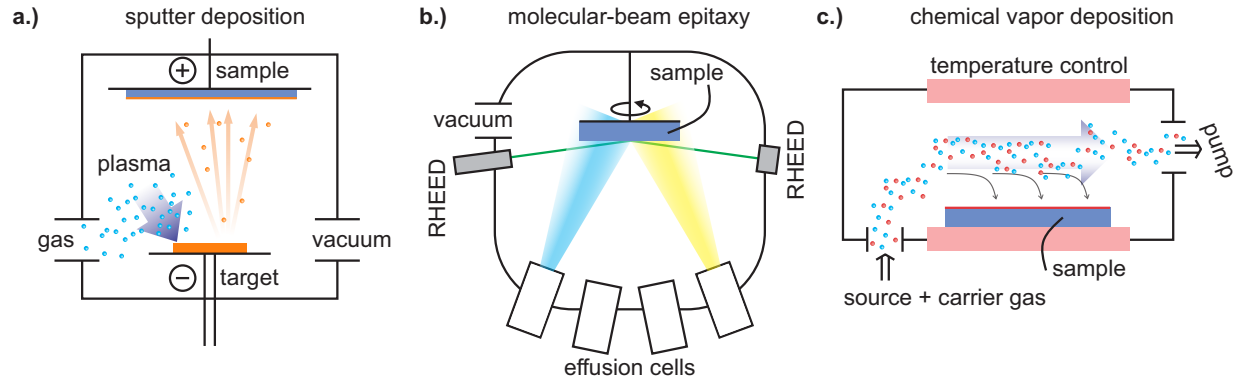


**Figure 3.1:** Overview over the thin film fabrication techniques that were used in this thesis. **a.)** Sputter deposition, **b.)** Molecular-beam epitaxy (MBE) and **c.)** chemical vapor deposition (CVD).

cussed MBE, but is instead based on the chemical reaction of different precursor gases. These are typically combinations of suited metalorganics that are sent into the heated reaction chamber. In the vicinity of the substrate, the gases undergo pyrolysis and divide into the respective subspecies that then react with each other to form the thin film of the desired material. The temperature in the chamber is usually ranging between 600 – 1100°C, depending on the used compounds. For this thesis, MOCVD is used as fabrication technique for crystalline gallium phosphide thin films, which are part of chapter 4.

### 3.1.2 Electron beam lithography

The single steps of the EBL process are sketched in Fig. 3.2. As mentioned previously, EBL is used to define the designed structures in a photoresist, which is done by exposing selected areas with the electron beam of a scanning electron microscope (SEM). This thesis uses the polymer polymethylmethacrylate (PMMA) as resist, that is spin coated on the desired sample and then baked for five minutes at 180°C. Depending on atomic weight and spin speed, the PMMA thicknesses range between 50 – 300 nm. Subsequently, the sample is coated with an electrically conductive polymer (Espacer 300Z) that ensures sufficient conductivity and visibility in the SEM.

The actual EBL process is carried out by an ElinePlus (Raith GmbH) system that is built with a ultra-high vacuum SEM and a laser-controlled sample stage. Based on a structure design that is prepared beforehand, the electron beam is automatically scanned over the sample and precisely exposes the areas, where the desired structures are supposed to be. Where the electrons impact on the PMMA, they break bonds of the polymer and as a consequence the chemical solubility is locally increased.

After the sample is taken out of the SEM chamber, it is rinsed in DI to remove the Espacer layer. Following, it is put into a mixture of methylisobutylketone (MIBK) and IPA (ratio 1:3) which is called the development process. Here the exposed areas with higher solubility get dissolved while the remaining resist stays on the sample. The development is stopped

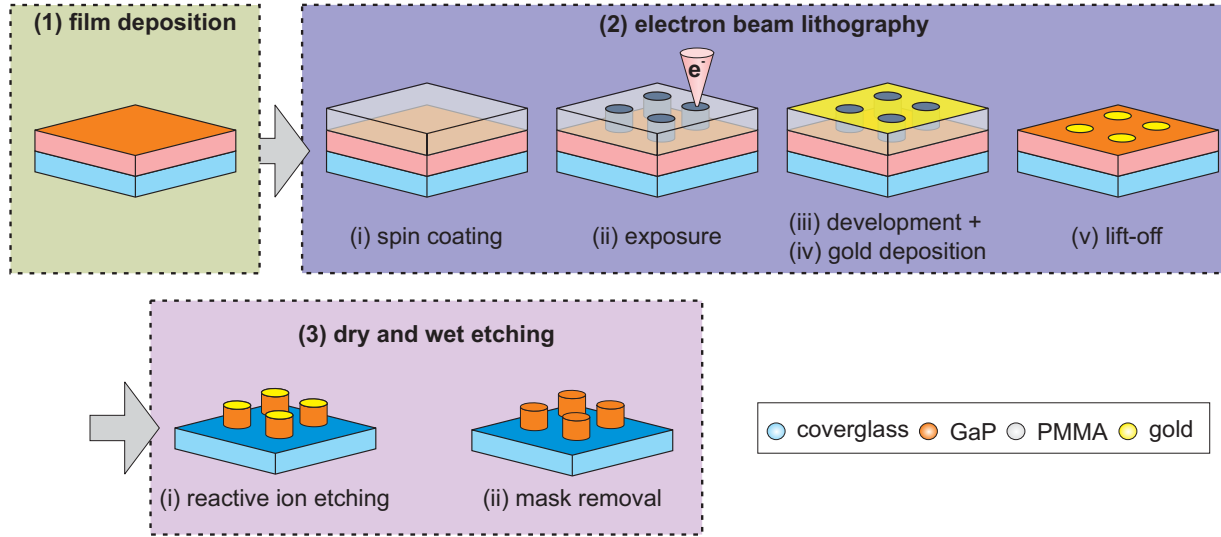


**Figure 3.2:** Scheme of the general fabrication work flow, with (1) the thin film deposition, (2) the different steps of electron beam lithography and (3) the final etching procedures.

by rinsing in pure IPA such that finally the designed patterns appear as holes in the continuous PMMA film, as sketched in Fig. 3.2. The timing of this process depends on the used EBL parameters and are therefore noted in the Experimental details of the respective chapter.

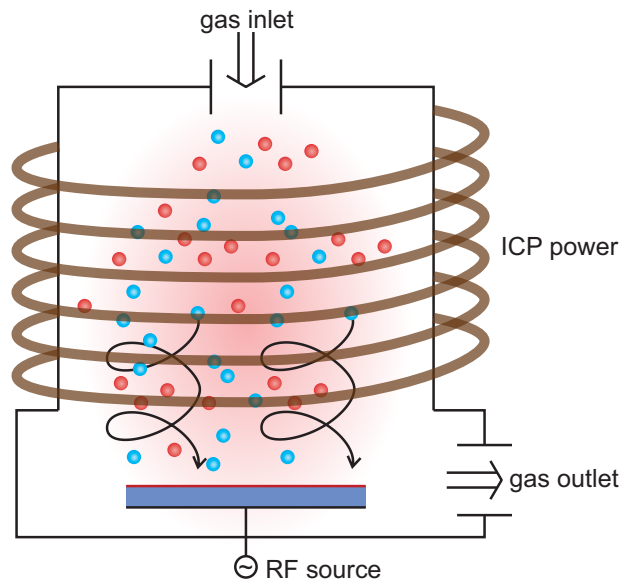
Next, a gold hard mask is deposited on top by ultra-high vacuum electron-beam evaporation (Bestec), using an acceleration voltage of 8.5 kV with deposition rates between  $0.5 - 1 \text{ \AA/s}$ . The mask thickness ranges from 40 – 60 nm. It should be noted, that depending on the sample’s material, an adequate adhesion layer is needed to ensure that the gold sticks on it. For this purpose, a thin layer ( $\sim 2 \text{ nm}$ ) of chromium is deposited before the deposition of the gold using the same machine. Only for  $\text{SiO}_2$  substrates, a self-assembling monolayer (SAM) [83] is used instead, consisting of (3-Mercaptopropyl)trimethoxysilan (MPTMS) in ethanol (80 %). For the preparation of the SAM, the a drop of the MPTMS mixture is dropped on the thin film and left there for 30 s, before it is rinsed in pure ethanol for 40 s. Next, the sample is carefully dried in nitrogen flow and then baked at  $100^\circ\text{C}$  for fifteen minutes. Then, the sample is ready for the gold deposition.

Finally, the lift-off process is performed, where the remaining PMMA film is dissolved such that the designed patterns appear as gold structures on top of the sample. This is done by emerging the sample into a special solvent (Remover 1165 from Microdeposit) or equivalently acetone for several hours and heated to  $80^\circ\text{C}$ .

### 3.1.3 Reactive ion etching

In the final fabrication step, the gold structures that result from the EBL process are transferred into the desired material. This is done by inductively-coupled plasma reactive-ion etching (ICP-RIE, PlasmaPro 100 from Oxford Instruments), a chemical dry etching

**Figure 3.3:** Sketch of the ICP-RIE process. The charged particles in the gas plasma are accelerated towards the sample by an applied RF bias. Additionally, a coil generates a magnetic field inside the chamber to force the particles on a circular trajectory.



technique. The process is based on a combination of different etching gases that are ignited to a plasma and then accelerated towards the sample. This is done by applying a radio frequency (RF) bias and an ICP voltage which drives a magnetic field through a coil (see Fig. 3.3). This field has the purpose to force the charged particles on circular trajectories to increase their path and therefore the etching efficiency. Once the particles arrive at the sample, the plasma enables chemical reactions between the gases and the atoms of the material such that volatile compounds form that are subsequently pumped out of the chamber. By changing the reacting gases, ICP-RIE allows to etch with high material selectivity and a high (vertical) directionality, preserving the shape of the mask and generating steep sidewalls. Finally, the etch mask is removed by wet etching (Au etchant from Aldrich), such that only the structures in the desired patterns remain. The parameters and gases for the dry etching steps are listed in table A.3 in the appendix.

## 3.2 Material characterization

An important part of the material fabrication is the subsequent characterization and specification. The following section discusses a set of techniques for the study of structure, composition and electronic properties of the fabricated materials. They are based on X-ray radiation, which is beneficial due to the high energy of X-ray photons ( $> 100$  eV) and correspondingly small wavelengths ( $< 10$  nm) which allows them to measure with resolutions at the atomic scale. Therefore, the source of the systems is typically based on an X-ray tube, where electric energy gets converted into a continuous beam of X-ray photons. For this, a cathode is placed in a vacuum where electrons are emitted and then accelerated towards the anode. Here, the impact of the incident (accelerated) electrons lead to the emission of high energy photons, with an X-ray spectrum that is specific to the acceleration voltage (typical in the range of  $10^4$  V) and the anode material (typical examples are tung-

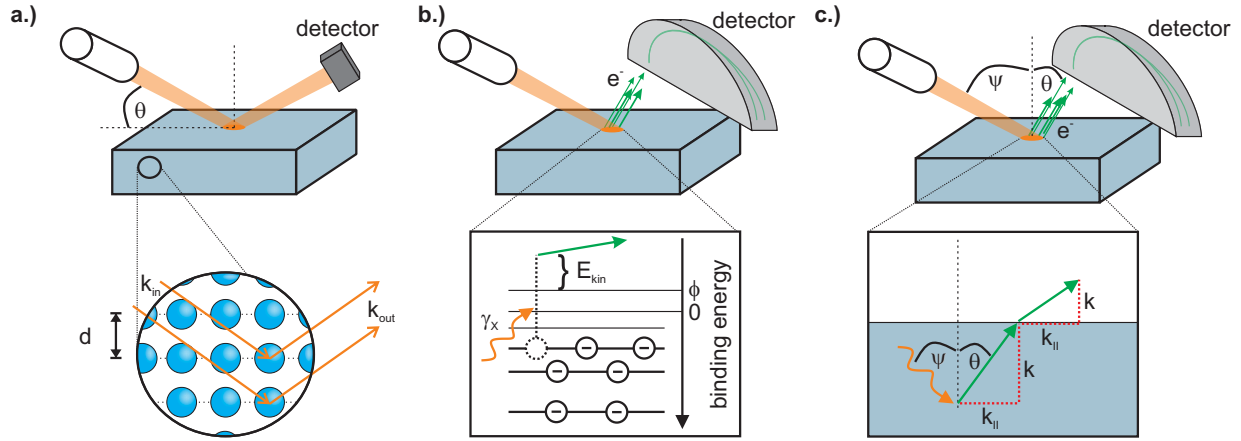


**Figure 3.4:** Sketch of the X-ray characterization methods. **a.)** XRD technique, with a sketch of the X-ray diffraction below. Here, the detector is a standard X-ray detector. **b.)** XPS measurement with a sketch of the photoelectric effect below. In this case the detector requires spectral selectivity. **c.)** ARPES measurement scheme, which is similar to that of XPS, but has additional sensitivity towards the emission angle  $\theta$  of the electrons. Below, a sketch of the electron's momentum distribution is shown.

sten or copper). Special X-ray monochromators furthermore allow to specify the energy and wavelength of the source photons that are then sent to the sample. It should be noted that this section describes the general working principles, the respective instrument details are summarized after each experimental section.

**X-ray diffraction (XRD):** XRD is a technique for the non-destructive investigation of the atomic arrangement in a material, sketched in 3.4a. It is based on the diffraction of X-ray photons by the periodically aligned atoms of a crystalline lattice, which happens due to the similar size of atomic distances and the radiation wavelength. Consequently, the crystal planes of a material act as a diffraction grating on the X-ray photons such that they interfere destructively in most directions and therefore low measured intensity. For certain angles however, constructive interference happens which leads to distinct peaks in the measured intensity. This condition is known as the Laue equation.

$$\Delta \vec{k} = \vec{k}_{out} - \vec{k}_{in} = \vec{G} \quad (3.1)$$

where  $\vec{k}_{out}$  and  $\vec{k}_{in}$  are the wavevector of the outgoing and incoming X-ray beam (see sketch in Fig. 3.4a), respectively, and  $\vec{G}$  is the reciprocal lattice vector. There exist different techniques on how to extract lattice structure from this condition, which involve monochromatic or polychromatic source and different relations between incident and collection angle. Nevertheless, they all measure a characteristic diffraction pattern which is unique for each crystal structure. This makes XRD a powerful technique which allows to identify the crystalline order of a material.

**X-ray photoelectron spectroscopy (XPS):** XPS is an analysis technique that al-

lows to study the elemental composition and chemical state of a material. It is based on the photoelectric effect, where a high-energy X-ray beam is directed to the sample and the incident photons "kick out" electrons at the surface, see 3.4b. By measuring the energy distribution of the ejected electrons, a spectrum can be recorded which is characteristic for each element and contains information on the chemical bonding (or state) of the atoms. For this, usually ultra-high vacuum is needed, together with a monochromatic X-ray source<sup>1</sup> that is focused on the sample. The ejected electrons are then analyzed with respect to their energy, typically with a hemispherical electron energy detector (Fig. 3.4b). From the photoelectric effect, one can deduce the measured binding energy  $E_b$  of the electrons.

$$E_b = E_\gamma - (E_{kin} + \phi) \quad (3.2)$$

Here,  $E_\gamma$  is the (known) energy of the X-ray photons,  $E_{kin}$  is the (measured) kinetic energy of the electron and  $\phi$  corresponds to the work function that is specific for the surface of a material and contains corrections for the individual instrument. As a consequence, the measured spectrum will contain a variety of peaks that can be associated to material-specific electron states. Due to the limited skin depth of electrons, XPS is mostly reduced to the surface region of a material. Furthermore, it should be noted that the analysis of XPS data is a complex process where many aspects have to be considered, e.g. the position and shape/ widths of certain peaks as well as unwanted signal from secondary (so-called Auger-) electrons.

**Angle-resolved photoemission spectroscopy:** Finally, angle-resolved photoemission spectroscopy (ARPES) represents a powerful analysis technique that is related to XPS. Analogously, it is based on the photoelectric effect and aims to extract the energy and additionally the momentum of core electrons in the material. For this, the detection unit is designed to not only measure the energy distribution of the emitted electrons but additionally their angular spread (Fig. 3.4c). From the angle  $\theta$ , the (surface parallel) component of the emitted electron's moment can be extracted by

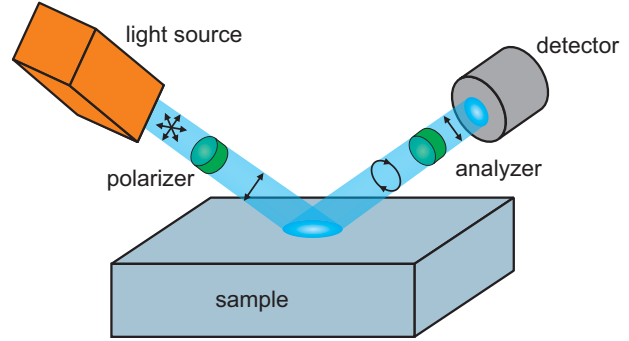
$$\hbar|\vec{k}_\parallel| = \sqrt{2m_e E_{kin}} \sin \vartheta \quad (3.3)$$

Together with the relation from equation 3.2, this allows to fully map the electron's dispersion at the surface of a material and therefore a direct measurement of the electronic band structure. However, it should be noted that ARPES allows only the precise measurement of the parallel momentum  $\vec{k}_\parallel$ , while the normal component  $\vec{k}_\perp$  can only be approximated (see Fig. 3.4c) [84]. Furthermore, it should be added that ARPES is commonly operated at lower photon energies (ultraviolet to extreme ultraviolet instead of X-ray) than the previous techniques, depending on the investigated material.

---

<sup>1</sup>This is true for the techniques used in this thesis. It should be noted that in general, there are XPS techniques that are using broadband X-ray sources.

**Figure 3.5:** The working principle of ellipsometry. An unpolarized light source is sent through a polarizer before it is reflected off the sample. A second polarizer (analyzer) filters the light before it enters the detector.



### 3.3 Optical characterization

The focus of this thesis lies in the optical characterization of different nanomaterials. The following sections discuss the used methodology, starting with the linear characterization which is based on the theory of reflection and transmission that was introduced in section 2.2. The following two sections discuss the nonlinear optical measurement techniques that are built with ultrafast pulsed laser sources. The majority of the experimental results in this thesis are based on the setups introduced there.

#### 3.3.1 Spectral ellipsometry

The content of this section is mainly based on the comprehensive and detailed user guide of the company J.A. Woolam that refers to ref. [85]. Spectral ellipsometry is an experimental method that allows to determine the complex refractive  $\tilde{n} = n - ik$ . For this, an ellipsometer consists of a monochromatic and unpolarized light source that is followed by a linear polarizer to generate linearly polarized light. After reflection from the sample, the light is sent to a rotating polarizer (analyzer) and finally measure at a detector. This allows to investigate the change of the polarization state induced by the reflection off the sample. With a known rotation frequency  $\Omega$  of the analyzer, elliptically polarized light generates an oscillating voltage with a constant offset  $DC$  at the detector:

$$V(t) = DC + a \cos(2\Omega t) + b \sin(2\Omega t) \quad (3.4)$$

This allows to define the two quantities measured by ellipsometry which are  $\alpha = a/DC$  and  $\beta = b/DC$ . To relate these to the optical properties of the material, it is convenient to introduce the Jones-formalism which is based on the two orthogonal  $s$  and  $p$  polarization states, which were introduced in section 2.1.2. Arbitrary polarized light can now be expressed as a (complex valued) Jones vector

$$\vec{E} = \begin{pmatrix} \tilde{E}_p \\ \tilde{E}_s \end{pmatrix} \quad (3.5)$$

With this, any optical component can be expressed as a  $2 \times 2$  matrix that changes the polarization state of the original wave. Thus, the electric field  $\vec{E}_D$  arriving at the detector

can be expressed as

$$\vec{E}_D = \begin{pmatrix} 1 & 0 \\ 0 & 0 \end{pmatrix} \begin{pmatrix} \cos A & \sin A \\ -\sin A & \cos A \end{pmatrix} \begin{pmatrix} r_{(p)} & 0 \\ 0 & r_{(s)} \end{pmatrix} \begin{pmatrix} \cos P & -\sin P \\ \sin P & \cos P \end{pmatrix} \begin{pmatrix} 1 \\ 0 \end{pmatrix} \quad (3.6)$$

Here, the first two matrices correspond to the analyzer with  $A$  being the angle between the polarizer's axis and the plane of incidence. The third matrix is the reflection off the sample, defined by the (complex) Fresnel coefficients  $r_{(s)}$  and  $r_{(p)}$  (see section 2.1.2) for  $s$  and  $p$  polarization, respectively<sup>2</sup>. Finally, the last matrix and vector correspond to the rotation of the source light, given by the angle  $P$  between the polarizer axis and the plane of incidence. This can be evaluated to

$$\vec{E}_D = \begin{pmatrix} r_{(p)} \cos P \cos A + r_{(s)} \sin P \sin A \\ 0 \end{pmatrix} \quad (3.7)$$

It is now convenient to introduce the ellipsometric parameters  $\tan \Psi e^{i\Delta} = \frac{r_{(p)}}{r_{(s)}}$ , such that  $\tan \psi$  is the magnitude of the ratio of the Fresnel coefficients while  $\Delta$  corresponds to their phase difference. With this, the intensity at the detector  $I_D \propto |E_D|^2$ , after normalization with the term independent of  $A$ , reads

$$I_D \propto 1 + \frac{\tan^2 \psi - \tan^2 P}{\tan^2 \psi + \tan^2 P} \cos 2A + \frac{2 \tan \psi \cos \Delta \tan P}{\tan^2 \psi + \tan^2 P} \sin 2A \quad (3.8)$$

Comparing this to the time dependent voltage at the detector that was defined in equation 3.4 and the known time dependence of the angle  $A$ , a Fourier analysis of the measured voltage allows to measure  $\psi$  and  $\Delta$ :

$$\tan \psi = \sqrt{\frac{1 + \alpha}{1 - \alpha}} |\tan P| \quad (3.9)$$

$$\cos \Delta = \frac{\beta \tan P}{\sqrt{1 - \alpha^2} |\tan P|} \quad (3.10)$$

In summary, the time dependent signal at the detector is measured and then Fourier transformed, from which the ellipsometric quantities  $\psi$  and  $\Delta$  can be calculated. To extract the complex refractive index however, a model must be constructed and fitted to the measured data. This model is typically built on known parameters of the material (for example the electronic structure, bandgap, ...) and allows, if chosen wisely, the extraction of the complex refractive index and the thickness of the measured thin film(s). Furthermore, the technique contains information on the surface roughness and imperfections of the measured material.

Throughout this thesis, varying-angle spectral ellipsometry (VASE) is used to determine the optical constants of the investigated materials, done with a VASE system by J.A. Woolam Company. This allows to perform the measurement over a wavelength range from 300 – 2500 nm and with varying angle of incidence. Accordingly, the generation and fitting of the model is done with the WVASE software by the same company. It allows a wide range of models and peak shapes to represent a wide range of materials and structures.

<sup>2</sup>It should be noted that this definition without off-diagonal elements is only valid for isotropic samples with low surface roughness.

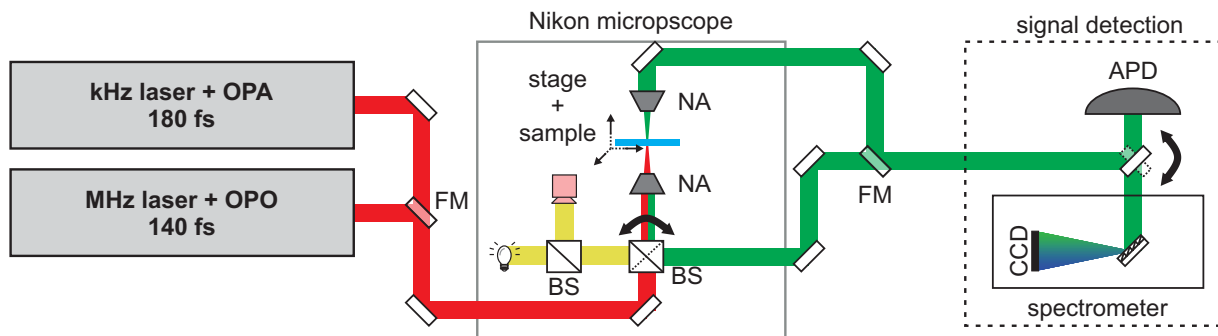


**Figure 3.6:** The experimental setup with both femtosecond laser systems, the Nikon microscope and the available detectors. FM denotes flip-mirrors that can be flipped in and out, depending on the demand, NA are the positions of objectives and BS is short for beamsplitter.

### 3.3.2 Nonlinear optical measurements and HHG

To observe nonlinear optical effects as discussed in section 2.4 high peak intensities are needed. Therefore, two different pulsed laser systems are used, implemented in the experimental setup sketched in Fig. 3.6. Both laser sources provide femtosecond laser pulses that are used to pump two different wavelength extension devices. These are based on parametric amplification which uses different nonlinear processes to selectively generate and enhance a wavelength that can be selected by the user.

- **kHz system:** An ytterbium doped potassium gadolinium tungstate ( $\text{Yb}^{3+} : \text{KGd}(\text{WO}_4)_2$  - short Yb:KGW) laser that is provided by Light Conversion Ltd (Pharos). The laser has an output wavelength of 1030 nm at an average power of about 20 W, a tunable repetition rate  $f_{rep} < 200$  kHz and pulses with 180 fs. It pumps an optical parametric amplifier (OPA, Orpheus HP from Light Conversion Ltd) that allows to freely tune the wavelength between 0.3–3  $\mu\text{m}$ . In the following this is referred to as kHz system.
- **MHz system:** A titanium doped sapphire (Ti:sapphire) laser from Coherent Inc. (Chameleon Ultra II) with a tunable wavelength output  $\lambda = 680 - 1080$  nm, a repetition rate of  $f_{rep} = 80$  MHz and 140 fs short pulses. The laser pumps an optical parametric oscillator (OPO, from Coherent) that extends the wavelength range from the visible to mid-infrared. In the following, this is referred to as MHz system.

Table 3.1 summarizes the properties of the two laser systems, according to the formulas that were introduced in section 2.5. The kHz system is preferable for experiments where high peak powers are needed and is used throughout most of the experiments in this thesis. Additionally, the lower repetition rate allows to minimize unwanted thermal effects that could perturb experiments, particularly when working at higher powers. The MHz laser on the other hand has the advantage of more pulses per second which can be seen as "number of experiments" per second. This generally means a higher signal to noise ratio and is advantageous for experiments where lower peak energies are needed.

As depicted in Fig.3.6, both laser systems are aligned to a confocal microscope (Nikon

| Laser       | $\lambda$ extension | rep. rate            | time width | pulse energy | peak pulse power |
|-------------|---------------------|----------------------|------------|--------------|------------------|
| Yb:KGW      | OPA                 | 200 kHz <sup>†</sup> | 180 fs     | 500 nJ       | 2700 kW          |
| Ti:sapphire | OPO                 | 80 MHz               | 140 fs     | 1.25 nJ      | 8.9 kW           |

**Table 3.1:** Parameters of the used femtosecond laser systems. <sup>†</sup>variable, the value corresponds to the maximum value. Pulse energy and peak power were calculated with the laser parameters and an average power of 100 mW.

Eclipse Ti-U) that allows to measure either in transmission or reflection geometry. For focusing, different objectives are available, all from the Nikon Plan Fluor series. The sample stage consists of a manual XY micrometer positioner and a XYZ piezo stage (MadCity Labs Inc, NanoLPS200). A white light source can be flipped in and out which allows to image samples via a connected camera. When measuring in transmission, the collecting objective is mounted on an arm with controllable XYZ micrometer screws.

For the data collection, a rotatable mirror can direct the light to two different detectors. The first contains of an avalanche photo diode (APD, MPD-PDM series by Picoquant) which allows close-to single photon detection but no spectral selectivity. The second detector is a spectrometer (Princeton Instruments Acton SP2300i ) which is coupled to a CCD camera (Princeton Instruments, Pixis100 - F). For measurements in this thesis, the spectrometer is used with a 150 g/mm and a blazing wavelength of 500 nm.

Finally, a selection of optics can be placed in the beam path throughout the experimental setup and which are changed depending on the specific demands on each experiment. To filter wavelength ranges, long- and shortpass filters are used which, if not stated differently, are exclusively from the premium hard coated series from Thorlabs. Both laser systems are linearly polarized, such that the polarization can be controlled by the implementation of  $\lambda/2$  waveplates and polarizers, both from Thorlabs. The power throughout the setup can be controlled with optical density (OD) filter wheels (Thorlabs) and measured by different calibrated power sensors (Thorlabs; S120VC, S470C, S122C). For the measurement below their detection sensitivity, a calibrated silicon detector is used, for example in the case of SHG signal (Newport 918D-series).

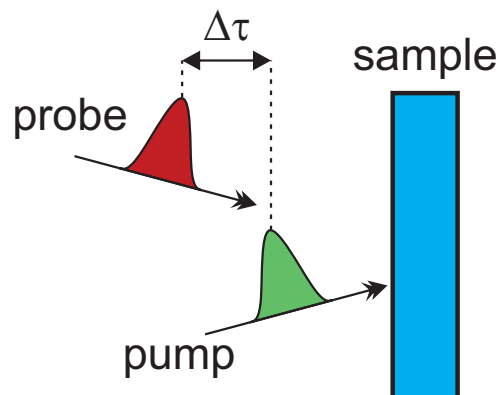


Figure 3.7: General working principle of pump-probe spectroscopy.

### 3.4 Pump-probe spectroscopy

Pump-probe spectroscopy (PPS) is a popular measurements technique and application of pulsed laser systems. The general scheme is sketched in Fig. 3.7. The principle is based on two laser pulses that are sent to the specimen of interest. By interacting with the sample, the higher intensity beam ('pump') creates a non-equilibrium that is then observed by the second, lower intensity beam ('probe'). This is done by comparing the influence of the sample on the probe beam with and without the presence of the pump. By varying the time delay between the arrival of the two pulses, the temporal dynamics of the pump-induced effects can be observed. For this thesis, a nondegenerate pump-probe spectroscopy setup is used, based on super continuum (SC) generation and pulse compression, which is pumped by the kHz laser system introduced earlier. The experimental implementation is sketched in Fig. 3.8 and will be discussed in the following.

#### 3.4.1 White-light generation and pulse compression

Under ideal experimental conditions, the temporal resolution of a pump-probe measurement is fundamentally limited by the length of the used pulses in time. Therefore, in order to measure processes on a faster timescale, the original 180 fs pulses of the kHz laser system are compressed in time. As discussed in section 2.5, ultrashort pulses require a sufficiently broad frequency spectrum.

**Supercontinuum generation** For this, the wavelength of the laser is set to  $\lambda = 1.12 \mu\text{m}$  at an average power between 400 – 600 mW and is focused onto a 3 mm thin sapphire ( $\text{Al}_2\text{O}_3$ ) plate. Here, the high intensity pulses ( $E_{pulse} > 1.5 \mu\text{J}$ ) generate a supercontinuum (SC) spectrum that spans over a wide range from the visible to near-infrared, shown in Fig. 3.9 (grey line). The process of this extreme pulse broadening is quite complex and will therefore not be explained in detail here. It is a combination of multiple and cascading nonlinear effects, including four-wave mixing and coherent Raman scattering, for more details the reader is referred to [86, 87]. The generated light is then collected and collimated with a suitable achromatic lens or a parabolic mirror. Typically, the average power of the generated light lies between 3 – 4 mW. Due to later experimental conditions,

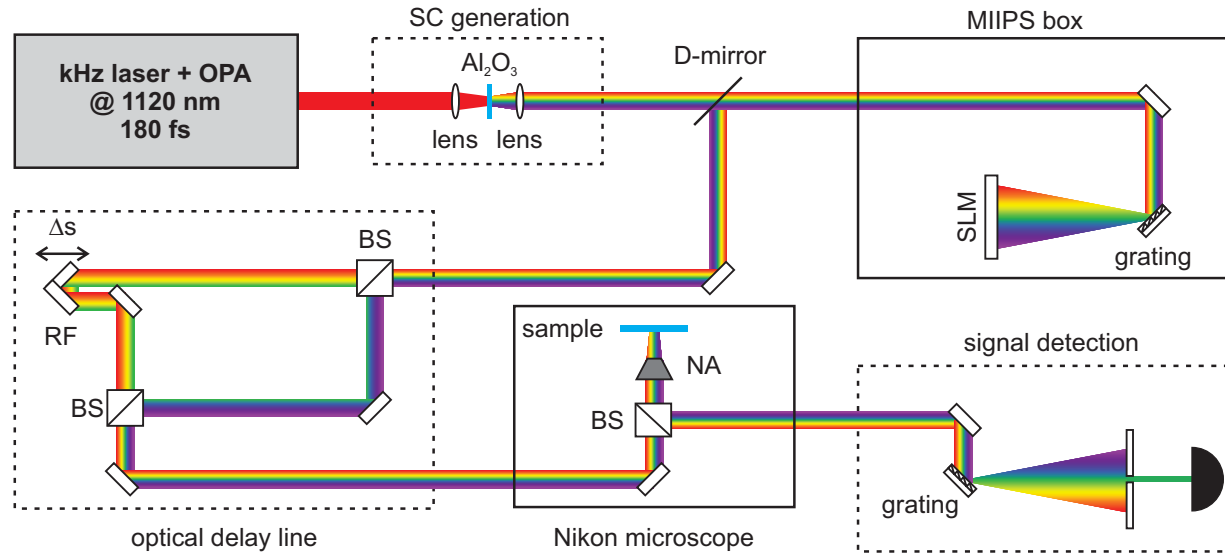


**Figure 3.8:** Experimental Pump-Probe setup using MIIPS. BS is short for beamsplitter, NA for an objective, RF the retro-reflector and D-mirror is a D-shaped mirror. The setup allows as well to measure in transmission geometry, see Fig. 3.6.

the SC spectrum is selectively filtered to a range from 600 nm – 1000 nm with an intended gap at 750 nm, shown in Fig. 3.9. Two spectral regimes can be identified, shown in yellow from 600 – 750 nm, referred to as visible beam (VIS), and red the named near-IR beam, from 750 – 1000 nm.

**Pulse Compression** Next, the SC beam is sent to a MIIPSbox 640-P (Biophotonic Solutions Inc., BSI) which is based on the MIIPS algorithm for pulse compression that was introduced in section 2.5.3. Here, the pulse shaper is realized by an optical grating (Newport Corp. 300g/mm, based on gold) and a spatial light modulator (SLM, Jenoptik SLM-S640 USB). The beam is guided to the grating first, which splits the SC wavelengths into an angular distribution that is then sent to the liquid crystal based SLM. The elements are aligned in a way such that each pixel of the SLM is illuminated by a small

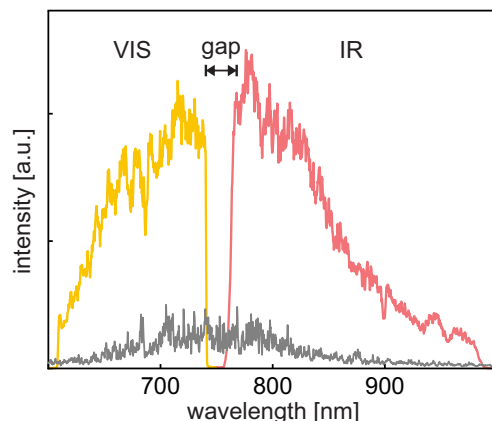


**Figure 3.9:** SC spectrum as generated by pumping with the sapphire crystal. The grey spectrum is recorded right after the collecting lens. After passing all optics, the spectrum is shown in yellow and red, for the visible and near-IR wavelength ranges, respectively. At around 750 nm an intentional gap separates the two regimes. This is realized by placing a hard mask at this position of the SLM.

spectral component of the SC light, respectively, and the optical phase can be modified individually. The light is then send back from the SLM with an offset in height such that the same grating that now collimates the wavelengths back into a single beam that then leaves the MIIPS box. Throughout the following setup, special mirrors (ultrafast enhanced silver mirrors, Thorlabs UM20-AG) are used to direct the beam that minimize temporal dispersion effects. Furthermore, two chirped mirrors (Thorlabs UMC10-15FS) are implemented, which are designed to have a negative chirp (compare section 2.5.2) to compensate for linear dispersion of other optical elements. To perform the actual pulse compression using MIIPS, a microscope detection unit (from BSI) is placed at the position where later real samples will be measured. It contains of a thin nonlinear crystal (BBO), an shortpass filter and a lens that focuses the generated light onto an optical fiber. The SC beam is then focused on the crystal to generate SHG light which is then collected and sent via fiber to a spectrometer (Ocean Optics USB4000). Beforehand, the SC spectrum is recorded with a second spectrometer (Ocean Optics HR4000) that bypasses the microscope. The MIIPS algorithm is then performed by a software that was provided by BSI, based on the iterative MIIPS procedure. For the first iteration a quadratic phase function of the form is used

$$f(\omega - \omega_0) = \frac{1}{2}\varphi''(\omega - \omega_0)^2$$

Here, the parameter is  $\varphi''$  which is scanned over a range from  $-3000$  to  $1000 \text{ fs}^2$ . For the following iterations, a sinusoidal phase function is used that was introduced in section 2.5.3.

$$f(\omega - \omega_0) = \alpha \sin(\gamma(\omega - \omega_0) + \delta)$$

The amplitude of the function is fixed by the parameter  $\alpha$ , usually set between  $\pi$  and  $2\pi$ , while the parameter  $\gamma$  is set as the transform-limited bandwidth of the respective spectrum. Then, the variable  $\delta$  is varied over a range from  $0-2\pi$ , leading to an exemplary MIIPS trace as shown in Fig. 3.10. In the top left, the same figure displays the temporal spread of the SC light right after the generation process. Clearly, the pulse extends over more than 1 ps, instead of the 180 fs of the kHz laser system. This leads to the generation of a SHG signal that is barely visible in the spectrometer (see bottom left of Fig. 3.10). To achieve a reliable TL pulse, throughout this thesis six iterations of the MIIPS algorithm are performed, whereas in principle three to five repetitions are sufficient to achieve convergence. The right hand side of Fig. 3.10 shows the temporal spread of a compressed pulse, having an approximately Gaussian shape with a FWHM of 5.3 fs. Below, the SHG spectrum generated by the compressed pulse is shown, clearly showing a strong and clean SHG. The compression, i.e. the SLM setting for each pixel is then saved such that it can be reloaded for the actual pump-probe experiments. Here it should be noted that the MIIPS algorithm depends crucially on the dispersion that a pulse experiences throughout the experimental beam path. Particularly highly dispersive elements such as objectives or lenses are critical, such that a compression is always performed for a situation that is as close as possible to the later experimental conditions. Finally, for the analysis of the measured data, the instrument response function (IRF) is calculated by determining the convolution of the two (VIS and near-IR) pulses. In this thesis, the IRF typically lies between 5 – 10 fs.

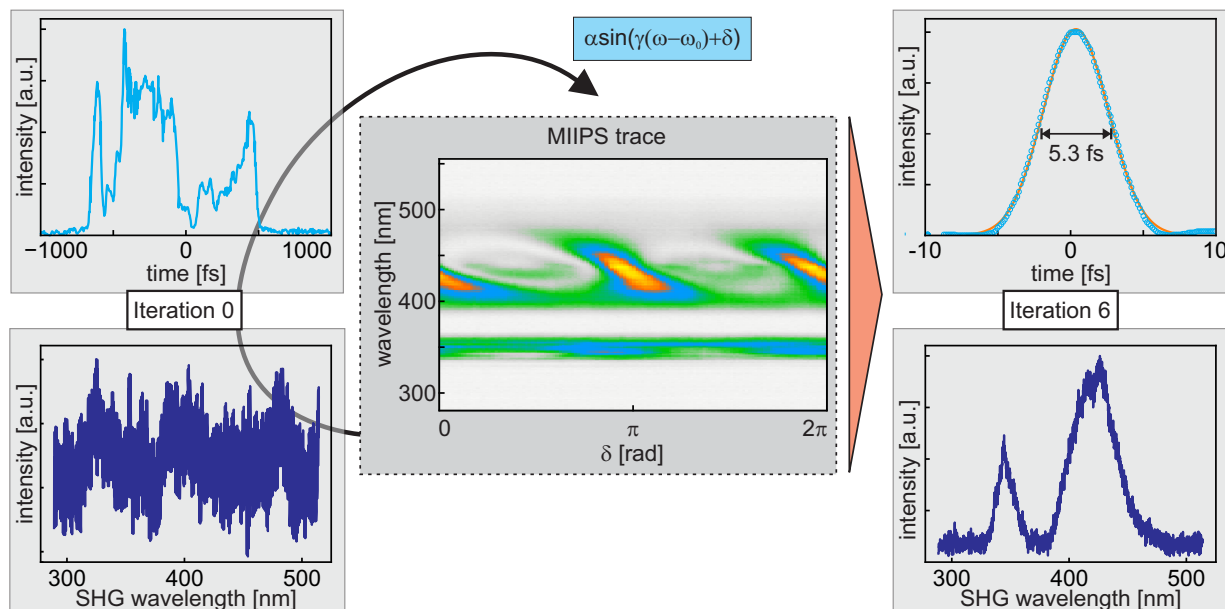


**Figure 3.10:** Application of the MIIPS algorithm. Starting with the non-compressed pulse on the left, finally the compressed pulse shown on the right hand side is reached. In the center, a MIIPS trace of a single iteration is shown.

### 3.4.2 Optical delay line and signal detection

Following the MIIPS box, the beam is sent to the optical delay line where the path difference between pump and probe pulses can be controlled (bottom left in Fig. 3.8). For this, dichroic beamsplitters (Semrock BrightLine series) with a 765 nm cut-on wavelength (longpass) are used. Accordingly, the two spectral regimes are separated into two beams, whereas the near-IR is transmitted and the VIS reflected. Respective long- and shortpass filters are placed after the beamsplitters to remove residuals from the individual beam lines. Next, the near-IR beam is sent to a retroreflector (Newport U-BBR 1-2S100100) that is placed on a movable stage (Thorlabs DDS300/M) that is controllable with 100 nm ( $\equiv$  1 fs delay) resolution. The VIS beampath on the other hand is designed to have a similar length as the near-IR one, before the both beams are recombined in a similar dichroic beamsplitter (Fig. 3.8).

Next, the beam is then sent to the Nikon microscope that was introduced in section 3.3.2, following the beampath that was described for the HHG experiments. Again, different objectives are available to focus and detect the light on the sample. For most experiments in this thesis, a metallic, reverse-Cassegrain objective ( $36\times$ ,  $NA = 0.5$ , Newport 50102-02) was used to minimize dispersion effects. As discussed earlier, the microscope contains a 50:50 beamsplitter and allows to measure in reflection or transmission geometry. In the latter case, a suitable objective is used for the collection after the sample. The collected light is then sent to the spectrometer (section 3.3.2), where instead of going towards the CCD camera, the light is sent to the side port where a silicon based photodiode is mounted

(FEMTO PWPR-2K). A manual slit that can be controlled with a micrometer screw and the optical grating of the spectrometer allow to selectively send specific wavelengths to the detector with  $\sim 5$  nm resolution. The unwanted pump light is filtered by respective long- or shortpass filters in front of the spectrometer's entrance. Finally, the relative signal is measured via lock-in amplification, enabled by an optical chopper (Thorlabs MC2000B) that modulates the pump beam during a pump-probe experiment. A lock-in amplifier (Stanford Research Systems, SR830) is then synchronized to that frequency ( $< 1$  kHz) and takes the signal of the photodetector as input. This technique allows to measure at a higher signal-to-noise ratio, which is particularly beneficial for the small relative changes of the nonlinear refractive index.

The actual pump-probe experiments are performed with a homemade LabView program which controls the relevant devices (delay line, spectrometer) and reads the signal from the lock-in amplifier. A typical pump-probe experiment contains individual time traces, where the relative change of reflectance ( $\Delta R/R$ ) or transmittance ( $\Delta T/T$ ) is recorded for a single probe wavelength and in dependence of the delay between pump and probe pulses. By tuning the position of the grating, the entire range of probe spectrum can be measured individually which additionally maps the signal in dependence of the probe wavelength. Two OD wheels (Thorlabs) in each of the beam paths in the optical delay line allow to precisely tune pump and probe power, respectively, and enable power dependent measurements. Finally, the setup has the possibility to exchange the role of pump and probe pulses, simply by changing the position of the chopper and the moving direction of the delay stage.

# Chapter 4

## Amorphous and crystalline gallium phosphide nanostructures

This chapter is focused on the nonlinear optical properties of gallium phosphide (GaP). The material is a well-known semiconductor from the light-emitting diode (LED) industry, where it is commonly used as optical materials for green emitting light sources [88]. GaP has a large optical and indirect bandgap at  $E_{ind} = 2.22$  eV, together with a direct band transition energy of  $E_{dir} = 2.78$  eV [89], which makes the material ideal for applications in the visible wavelength range. The fact that direct and indirect transition energies are that close together leads to a virtually lossless transparency for any wavelength longer than  $\lambda_{ind} \simeq 560$  nm. As a consequence, GaP crystals appear transparent with a strong orange to red color (see blue line in Fig. 4.1), contrarily to for example silicon which appears almost metallic in the visible and is completely opaque (red line in Fig. 4.1). At the same time, GaP has a linear refractive index that is around three for visible wavelengths: This is among the highest for materials with such a high transparency and is only slightly smaller than silicon.

As a whole, these properties make GaP a promising material for nanophotonic applications, for which however, GaP thin films must be realized to ensure fabrication flexibility.

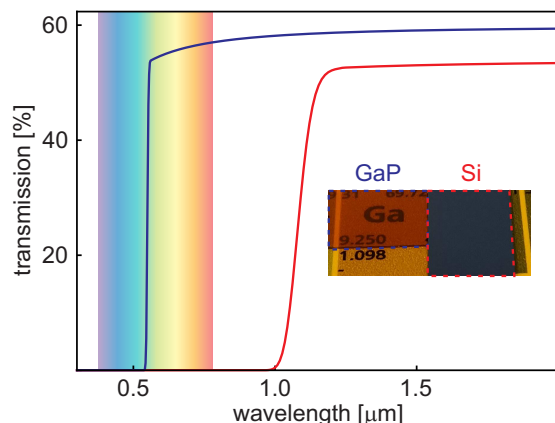


**Figure 4.1:** Transmission measurement of a GaP and silicon wafer. The inset shows an optical image of both samples at ambient illumination and on top of a printed periodic table. The transparency of GaP allows to clearly see the text below.

Therefore, the following sections investigate the suitability and performance of GaP at the nanoscale. It starts with the fabrication and characterization of crystalline and amorphous thin films, with a large focus on their nonlinear optical properties. Next, the amorphous film is discussed in more detail and structured into nanopatches, which are then investigated with respect to their SHG and ultrafast optical response. Finally, nanodiscs made of the crystalline thin films are fabricated and then used to boost ultrafast all-optical switching at the nanoscale.

## 4.1 Nonlinear characterization of GaP thin films

This work is published in [90]:

Benjamin Tilmann, Tahiyat Huq, Thomas Possmayer, Jakub Dranczewski, Bert Nickel,  
Haizhong Zhang, Leonid Krivitsky, Arseniy I. Kuznetsov, Leonardo de S. Menezes,  
Stefano Vezzoli, Riccardo Sapienza, Stefan A. Maier

”*Comparison of harmonic generation from crystalline and amorphous gallium phosphide nanofilms*”

Advanced Optical Materials 2300269 (2023), DOI: 10.1002/adom.202300269  
permission for reprint is granted under the Creative Commons CC BY 4.0 license

As motivated in the introduction of this thesis, efficient nonlinear frequency generation at the macroscale is mainly determined by low intrinsic optical losses, a small phase-mismatch between interacting waves and a high intrinsic nonlinear coefficient [70]. Therefore, common nonlinear crystals are transparent and optically birefringent, with popular examples being barium borate (BBO), lithium niobate ( $\text{LiNbO}_3$ ) or potassium titanyl phosphate (KTP). For nanophotonic applications, where the interaction volumes are comparable to the scale of the operating wavelengths, the material requirements shift due to the relaxation of phase matching conditions found in bulk nonlinear optics [25, 26]. Here, a large linear refractive index is highly beneficial to enable photonic engineering, while large nonlinear susceptibilities are needed to compensate for the small interaction volumes. Finally, experimental realization and technical applications need ease-of-integration with common nanofabrication and ideally silicon photonic techniques. Noble metals are one focus of interest due to their plasmonic resonances and high nonlinear coefficients [15, 16, 91]. However, the high ohmic losses and low damage threshold of metallic particles limit their applications particularly for nonlinear optics [92]. On the other hand, dielectric materials can serve as an alternative and versatile platform with ultralow losses, widely tunable Mie resonances and a good compatibility with silicon fabrication techniques [92, 93]. As mentioned in the the beginning of this chapter, GaP is a prominent example in this family with a large transparency window and high refractive index. First promising results were reported by nanostructuring bulk GaP crystals for efficient second-harmonic generation (SHG) [21, 94–96], the coupling to two-dimensional materials [97, 98], surface-enhanced fluorescence [21] or photonic crystals [99]. However, fabrication from the bulk crystal naturally limits the refractive index contrast in the substrate direction and additionally prevents direct on-chip fabrication. An alternative approach utilizes GaP thin films on top of transparent and low refractive index substrates, which already led to promising results with nonlinear integrated photonics [100] and nanophotonic engineering for dielectric metasurfaces [101–103]. However, so far an in-depth characterization of the nonlinear optical properties of GaP thin films is still missing and will therefore be covered in this section.

### 4.1.1 Structural characterization of GaP thin films

As introduced in section 2.4, optical SHG is the most prominent example of second-order nonlinear phenomena, where two incident photons of frequency  $f_0$  get converted to a new photon with exactly double the frequency  $2 \times f_0$ . This process is only allowed if light travels through a nonlinear medium with non-vanishing second-order susceptibility  $\chi^{(2)}$  and is described by (section 2.4 of this thesis)

$$P_i^{(2)} = \chi_{ijk}^{(2)} E_j E_k \quad (4.1)$$

with  $i, j, k$  running over the spatial coordinates  $x, y, z$ . Generally,  $\chi_{ijk}^{(2)}$  is a rank-3 tensor that is highly sensitive to the symmetries present in the material, e.g. it completely vanishes in all centro-symmetric materials [24]. GaP can be deposited with different techniques, resulting in either in a centrosymmetric amorphous phase (a-GaP) with vanishing  $\chi^{(2)}$  or in a crystalline zinc blende structure (c-GaP), where second-order nonlinear effects are possible. To obtain high-quality c-GaP films, our samples are fabricated via MOCVD growth on top of a gallium arsenide (GaAs) carrier wafer [104]. Subsequently, a direct bonding to a sapphire ( $\text{Al}_2\text{O}_3$ ) substrate using 2  $\mu\text{m}$  layer of  $\text{SiO}_2$  as buffer layer and the removal of the carrier wafer results in the material stack sketched in Fig. 4.2a. A high homogeneity of the layers and the clear distinction of c-GaP to the  $\text{SiO}_2$  layer below is confirmed by a SEM cross section, shown in Fig. 4.2b. Moreover, the XRD measurements that are shown by the green curve in Fig. 4.2c proof the crystalline order of the film. Although there is an amorphous background generated by the underlying  $\text{SiO}_2$  layer and a strong XRD peak from the sapphire substrate, the peak at  $2\theta \simeq 24^\circ$  can be attributed to the c-GaP thin film. This differs markedly to the clear amorphous XRD signal of an a-GaP film, shown by the blue line in Fig. 4.2. It should be noted that in order to minimize the lattice mismatch, the c-GaP layer is grown with the [001] crystal plane tilted with respect to the surface normal. Therefore, the peak appears shifted compared to a reference GaP wafer, cut along the [111] crystal direction and shown in grey in Fig. 4.2c. Here, the peak positions are in excellent agreement with literature values [105].

### 4.1.2 SHG from crystalline GaP

The zinc blende structure of the GaP crystal corresponds to the  $\bar{4}3m$  symmetry class. As it was introduced in section 2.4, the elements of the  $\chi^{(2)}$  tensor from equation 4.1 reduce to only the off-diagonal elements for this crystal, which are all identical.

$$\chi_{eff}^{(2)} = \chi_{xyz}^{(2)} = \chi_{xzy}^{(2)} = \chi_{yxz}^{(2)} = \chi_{yzx}^{(2)} = \chi_{zxy}^{(2)} = \chi_{zyx}^{(2)} \quad (4.2)$$

From this follows that a GaP crystal illuminated normal to the [001] crystal surface, does not generate SHG light and the material behaves as quasi centro-symmetric [63]. This however changes when the illumination is no longer perpendicular to the crystal axes and a rotation matrix has to be applied to the tensor in order to describe the system. In case

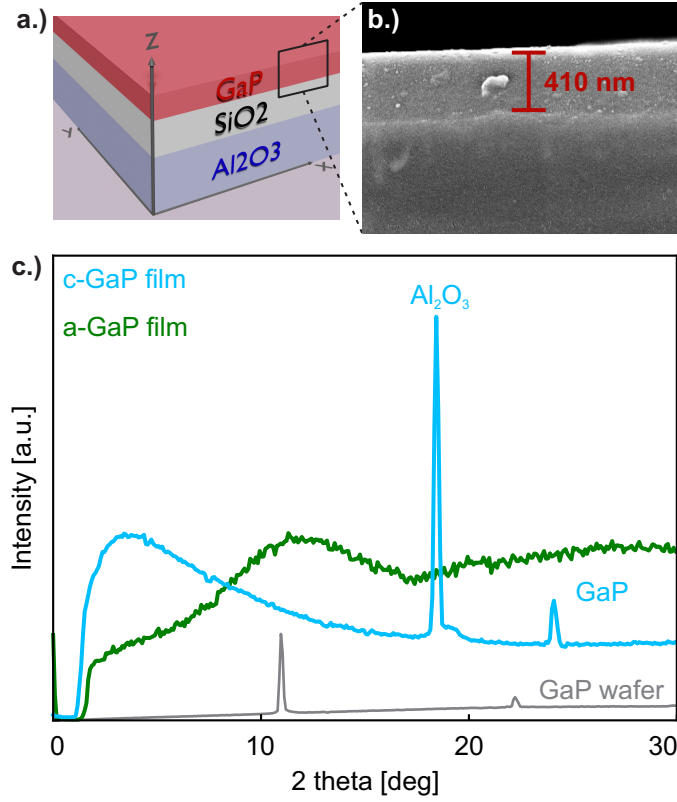


**Figure 4.2:** a.) Scheme of the investigated sample, consisting of an Al<sub>2</sub>O<sub>3</sub> substrate, a layer of SiO<sub>2</sub> and the c-GaP film. The  $x$  and  $y$  axes correspond to the [100] and [010] crystal axes, respectively, while the [100] axis is tilted with respect to the  $z$ -axis. b.) SEM image of the sample edge, clearly showing the GaP layer on top of the SiO<sub>2</sub>. c.) XRD measurements of crystalline GaP film (blue) and an amorphous GaP film (green). In grey, a reference measurement of a bulk [111] oriented GaP wafer is shown.

of the [111] oriented crystal, an appropriate coordinate transformation must be performed. This is done by applying a rotation with the matrix given by

$$R_{111} = \begin{pmatrix} 1/\sqrt{2} & 1/\sqrt{6} & 2/\sqrt{6} \\ -1/\sqrt{2} & 1/\sqrt{6} & 1/\sqrt{6} \\ 0 & -\sqrt{(2/3)} & 1/\sqrt{3} \end{pmatrix} \quad (4.3)$$

which is now applied to the incident electric field

$$\vec{E}' = R_{111}\vec{E} \quad (4.4)$$

Next, this is used to calculate the nonlinear polarization in the crystal reference frame  $\vec{P}(2\omega)'_{111}$  which is then converted back to the laboratory coordinate system by applying the inverse of  $R_{111}$ . This leads to a second order nonlinear polarization of the form

$$\vec{P}(2\omega)_{111} = \begin{pmatrix} P_x(2\omega)_{111} \\ P_y(2\omega)_{111} \\ P_z(2\omega)_{111} \end{pmatrix} = 2\epsilon_0\chi_{eff}^{(2)} \begin{pmatrix} \sqrt{(2/3)}(E_x E_y) \\ 1/\sqrt{6}(E_x^2 - E_y^2) \\ -1/\sqrt{6}(E_x^2 + E_y^2) \end{pmatrix} \quad (4.5)$$

This no longer vanishes under normal incidence and SHG signal can be detected for the c-GaP film and [111] oriented wafer. Fig. 4.3a-b, respectively, show the measured SHG efficiency  $\eta \propto \frac{I_{SHG}}{I_{pump}^2}$  for both materials at fundamental wavelengths ranging from 1.06 –

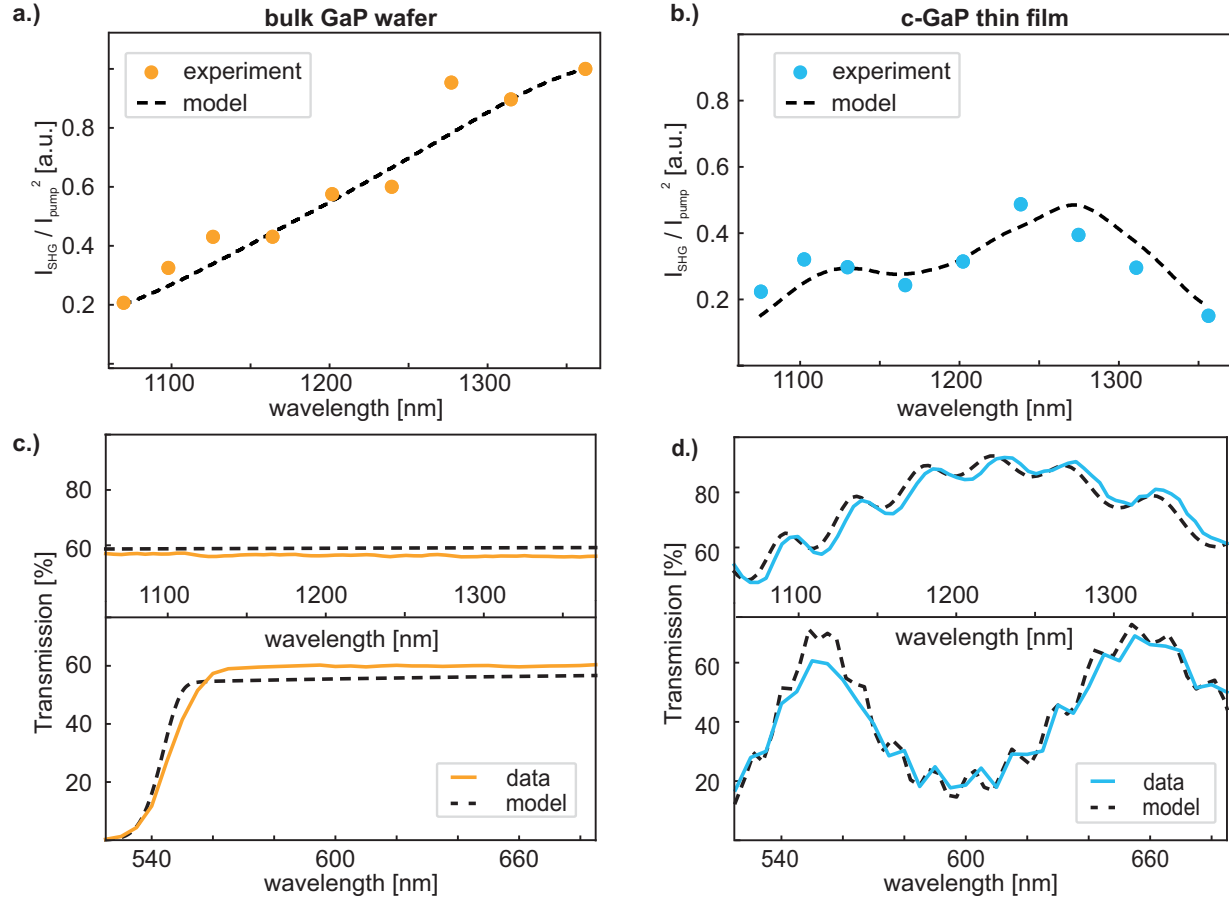


**Figure 4.3:** a.) - b.) Power normalized efficiency  $I_{SHG}/I_{pump}^2$  of the SHG intensity, extracted from experiments (dots) and simulations (dashed line) for (a.) the bulk [111] sample and (b.) the c-GaP film. Both datasets are normalized to the respective maximum value. c.) - d.) Measured (solid line) and simulated (dashed line) transmission spectra for (c.) bulk and (d.) c-GaP film.

1.37  $\mu\text{m}$ . It should be noted that we are using the so-called power normalized efficiency instead of the absolute conversion efficiency  $\eta_{tot} \propto I_{SHG}/I_{pump}$ , which scales linearly with the pump intensity.  $I_{SHG}$  and  $I_{pump}$  refer to the measured peak intensities of SHG and pump light, respectively. The collection of the generated light is performed in transmission geometry while  $I_{SHG}$  and  $I_{pump}$  are determined from the measured average powers, the laser repetition rate and temporal pulse width, normalized by the beam size as measured with a knife-edge technique. A power dependence measurement that is shown in the next section shows the expected quadratic behavior and therefore confirms the second-order nonlinear nature of the measured signal. The SHG efficiency of the c-GaP film (Fig. 4.3b) shows an oscillatory behavior that peaks around 1.25  $\mu\text{m}$  where it compares well to the values measured for the GaP wafer (Fig. 4.3a). For longer wavelengths, however, the bulk efficiency can almost double while the thin film reduces to only 10% of that value. This

is consequence of the fact that GaP is completely transparent over the relevant spectral range and both samples are fully penetrated by the pump light. Therefore, one important property to determine the SHG efficiency is the linear transmission of the samples, shown in Fig. 4.3c-d. The optically thick GaP wafer (Fig. 4.3c), does not show significant spectral features, particularly not in the regime of the pump wavelength (top panel). Only in the SHG regime (bottom panel), the position of the indirect bandgap at 550 nm (lower panel), leads to a fast drop in the transmission, which however, does not have visible impact on the observed SHG efficiency. Therefore, the continuous growth that is measured for  $\eta_{SHG}$  cannot be attributed to the transmission itself, but can be explained by the coherence length of the SHG light that scales with the wavelength of the appearing light [106]. For the thin film on the other hand, coherence length and phase-matching in general are subordinate, and the linear transmission is dominant (Fig. 4.3d). Here, the small thickness leads to strong thin film Fabry-Perot oscillations, with two observable oscillation periods. A shorter one is induced by the thick SiO<sub>2</sub> spacer while the 410 nm GaP layer is responsible for the long-period oscillation. Consequently, the recorded SHG efficiency embodies a product of the transmittance at fundamental and SHG wavelengths leading to the observed oscillatory course.

The dashed black lines in Fig. 4.3c-d represent numerical simulations of the transmission based on the transfer matrix method (TMM) [107] with the complex linear refractive index of GaP as input parameter (as extracted from spectral ellipsometry). It should be noted that the birefringence of the sapphire substrate prevents a direct measurement of the optical constants for the c-GaP film with this method. The nevertheless excellent agreement between measurement and numerical model underlines the high quality and optical similarity of the grown thin film to bulk GaP.

### 4.1.3 Extraction of $\chi^{(2)}$

Based on two linear simulations, a nonlinear model of the SHG process can now be built in order to extract the second-order nonlinear susceptibility. For this, we use nonlinear scattering theory [107] in conjunction with the TMM. There are two current sources involved in the modeling of the nonlinear interactions. The first source represents the nonlinear field at the structure, which is modeled as the collection of nonlinear dipoles on the structure's surface, excited by the pump field. The second current source is positioned at the detector and emits an electromagnetic field towards the structure at the nonlinear wavelength. In order to model the dipole at the detector as described in nonlinear scattering theory, we use a plane wave. The simulated SHG electric field  $I_{SH}(2\omega)$  collected at the detector position can then be calculated as

$$I_{SH}(2\omega) \propto \left| \int_{V_{film}} \chi^{(2)}(\omega) : \vec{P}_{SHG}(\omega) \cdot \vec{E}_{det}(2\omega) dV \right|^2 \quad (4.6)$$

Here  $\vec{P}_{SHG}(\vec{r}, \omega)$  is the second-order nonlinear optical polarisation induced by the incident electric field and  $\vec{E}_{det}(\vec{r}, \omega)$  corresponds to the dummy field that is generated by the polar-

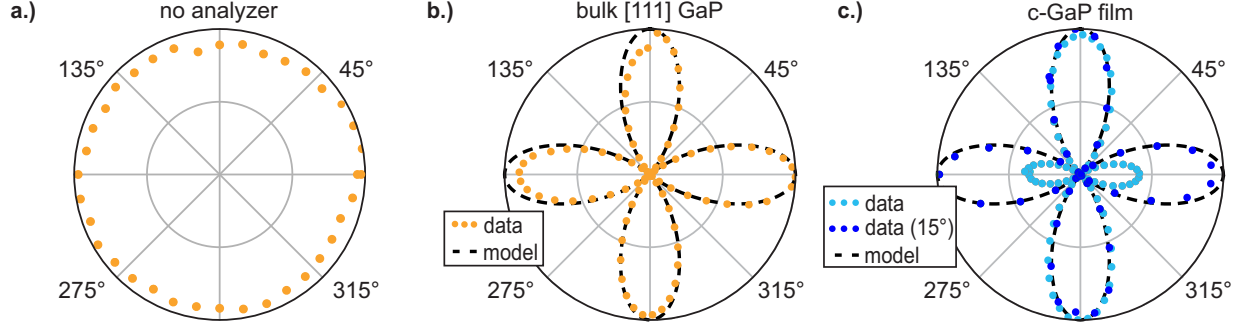


**Figure 4.4:** Polarization dependence of the SHG signal, for a.) no analyzer and with horizontal analyzer and b.) the bulk [111] oriented wafer c.) the c-GaP film

isation current at the detector position. The resulting SHG normalized efficiency for the bulk wafer and c-GaP film are shown by the dashed lines in Fig. 4.3a-b, respectively. The model reproduces the shape and features of the measured data with very good agreement, only for the thin film a small deviation can be observed that is probably caused by the high sensitivity of the model to the exact thickness of the sample. The good agreement confirms the previous arguments and indicates a flat dispersion of the second-order nonlinear susceptibility.

However, as mentioned before, the structure of the nonlinear susceptibility  $\chi^{(2)}$  is strongly dependent on the symmetries of the nonlinear material. After the coordinate transformation to the [111] crystal orientation, the expected SHG intensity ( $I_{SHG} \propto \bar{P}^2$ ) can be extracted from equation 4.5. In dependence of the polarization angle  $\alpha$  (now the angle of the electric field with respect to the [111] axis) it reads [108]

$$I(2\omega)_{111} \propto (\sqrt{2/3} \sin \alpha \cos \alpha)^2 + (\sqrt{1/6}/(\sin^2 \alpha - \cos^2 \alpha))^2 \quad (4.7)$$

For a normal incident beam (traveling along the  $z$ -direction), this SHG intensity is constant relative to rotations of the excitation beam polarization. This is experimentally verified by placing a rotatable  $\lambda/2$  waveplate (*generator*) in the beam path before the sample, see Fig. 4.4a. To further identify the single elements of  $P^{(2)}$ , a linear polarizer (*analyzer*) is added to the beam path after the SHG light collection. For a fixed horizontal analyzer, the GaP wafer generates a four lobe polarization pattern as shown in Fig. 4.4b. This is in excellent agreement with the horizontal component of the second-order polarization or the first term in equation 4.7, shown by the dashed line in Fig. 4.4b. For the c-GaP film, a comparable pattern is shown in Fig. 4.4c (light blue data), however, the lobes in the horizontal direction appear squeezed. This is caused by the oblique growth direction of the c-GaP film, which is confirmed by the fact that a  $15^\circ$  tilting of the sample plane restores the symmetrical shape of the [111] wafer (dark blue data in Fig. 4.4c).

With knowledge of the spectral and polarization dependence of the SHG signal, the value and dispersion of the effective second-order susceptibility  $\chi_{\text{eff}}^{(2)}$  can be extracted over the measured spectral range. This is done by comparing the measured normalized SHG

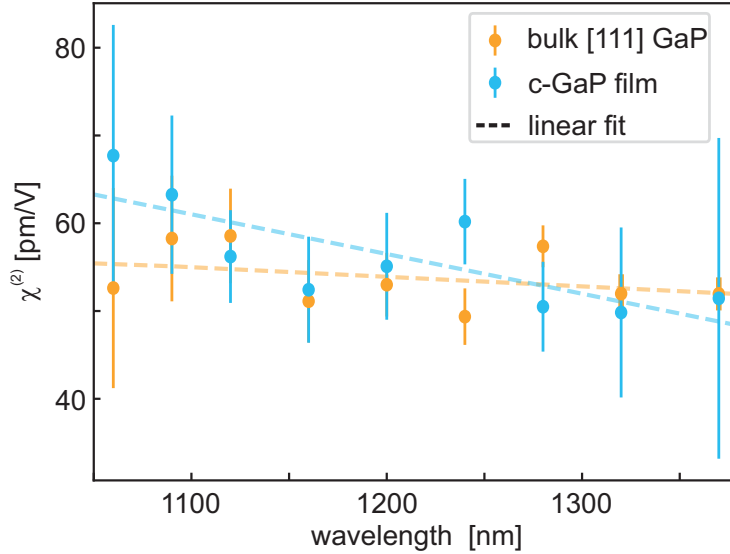


**Figure 4.5:** Extracted second-order susceptibility values of bulk (orange) and c-GaP thin film (blue). The linear trend is indicated by the dashed lines.

intensity with the modelled SHG intensity as defined earlier.

$$\chi_{\text{eff}}^{(2)} \propto \sqrt{\frac{I_{\text{SHG,exp}}/I_{\text{pump,exp}}^2}{I_{\text{SHG,model}}}} \quad (4.8)$$

The results for the GaP crystal (orange) and c-GaP film (blue) are shown in Fig. 4.5, with the associated error bars resulting from experimental uncertainties, with contribution from the beam waist and power measurements. For both samples, the extracted values range between 50 – 80 pm/V and roughly follow a linear trend with negative slope. This is expected from Miller’s rule [109], that predicts that the nonlinear susceptibility is related to the dispersion of the linear refractive index, which slowly decreases for longer wavelengths in the case of GaP. The measured value of the nonlinear susceptibility is in reasonable agreement with literature, where it is reported to be 74 pm/V at 1.313  $\mu\text{m}$  [110]. Table 4.1 summarizes the second-order susceptibility of various nonlinear materials. Remarkably, in comparison to most common nonlinear crystals, e.g. BBO, (D)KDP or LiNbO<sub>3</sub>, the  $\chi_{\text{eff}}^{(2)}$  value of GaP exceeds theirs, for the first two by more than one order of magnitude. Although other III-V semiconductors, like e.g. GaAs can have larger second-order susceptibility, as high as 370 pm/V [24], they always suffer from non-negligible absorption over the visible regime. As discussed previously, the linear properties are critical for the SHG efficiency, particularly for thin film materials. Another promising group of nonlinear materials are atomically thin semiconductors, e.g. MoS<sub>2</sub> [111] or ReS<sub>2</sub> [112], where huge nonlinear coefficients and nonlinear conversion efficiencies were achieved [113]. However, many of these materials typically lose their ability for SHG with increasing layer thicknesses [114] and, due to their unique electronic structure commonly suffer from strong linear absorption by excitonic effects [115] which limits their applicability for nanophotonic systems. It

| Material                            | Thickness | Wavelength ( $\mu\text{m}$ ) | $\chi^{(2)}$ (pm/V) | Ref.     |
|-------------------------------------|-----------|------------------------------|---------------------|----------|
| GaP                                 | bulk      | 1.3                          | 53                  | *        |
| c-GaP                               | 400 nm    | 1.05-1.4                     | 55                  | *        |
| MoS <sub>2</sub>                    | bulk      | 1.56                         | 29                  | [114]    |
| GaAs                                | bulk      | 1.55                         | 120                 | [24]     |
| BBO                                 | bulk      | 1.064                        | 3.7                 | [110]    |
| LiNbO <sub>3</sub>                  | bulk      | 1.5                          | 20-30               | [24, 25] |
| (D)KDP                              | bulk      | 1.064                        | 0.39                | [110]    |
| Al <sub>1-x</sub> Sc <sub>x</sub> N | 500 nm    | 1.54                         | 60                  | [117]    |

**Table 4.1:** Second-order nonlinear susceptibility for several nonlinear materials. Shown are the largest values reported. \*This work.

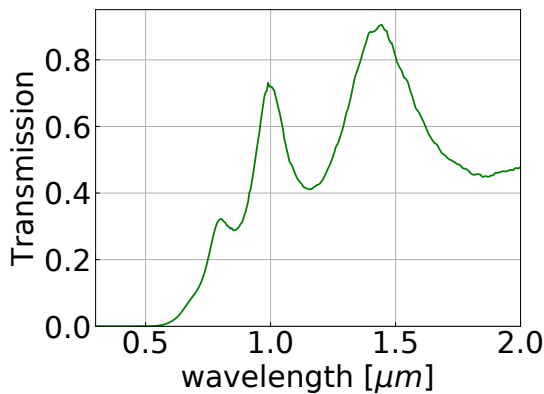


**Figure 4.6:** Transmission of a 400 nm thick a-GaP thin film.

should be noted that there are cases, for example the 3R-phase of MoS<sub>2</sub> where this is not happening and SHG scales with the number of layers [116].

#### 4.1.4 THG from GaP films and extraction of $\chi^{(3)}$

As mentioned previously, GaP thin films can be alternatively deposited via sputter deposition, which results in an amorphous structure of the material (a-GaP) [118]. The higher amount of defects lead to a shifted absorption edge and slightly lower transmission of a-GaP (see Fig. 4.6). Since bulk second-order nonlinear processes are not allowed for the centrosymmetric a-GaP film, the nonlinear response is dominated by third-order nonlinear effects. Here, the analogue to SHG is THG, where three incident photons of frequency  $f_0$  get converted into a new photon of triple the original frequency  $3 \times f_0$ . As introduced in section 2.4, THG is described by the third-order nonlinear optical susceptibility:

$$P_i^{(3)} = \chi_{ijkl}^{(3)} E_j E_k E_l \quad (4.9)$$

As discussed in section 2.4,  $\chi_{ijkl}^{(3)}$  is a rank-4 tensor that contrarily to SHG does not necessarily vanish in centrosymmetric media. In the following, THG measurements are

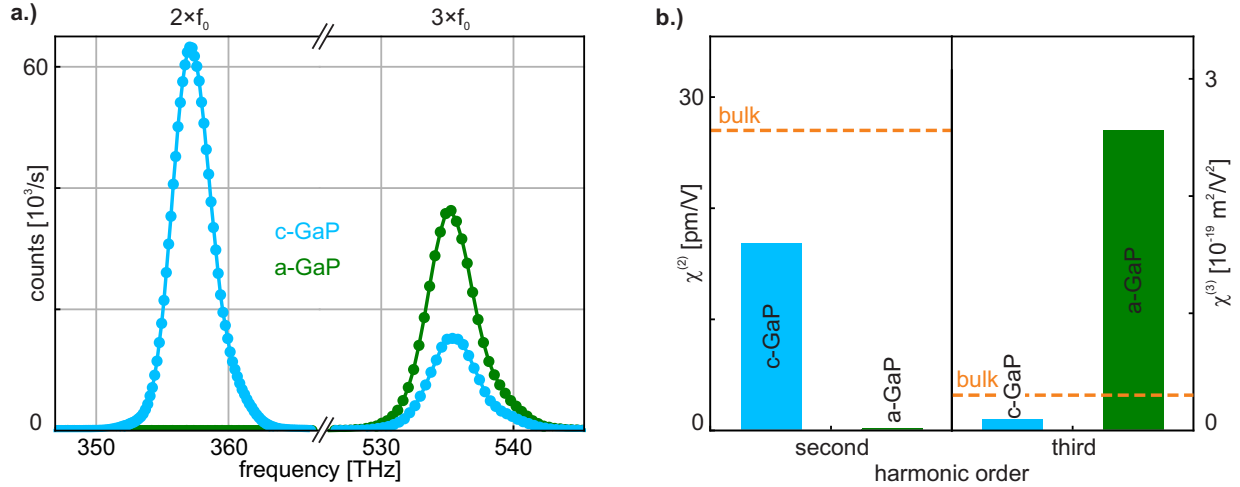


**Figure 4.7:** a.) Spectra of SHG and THG for the c-GaP (blue) and a-GaP (green) film for a pump frequency of  $f_0 = 178.4$  THz. b.) Extracted values of  $\chi^{(2)}$  and  $\chi^{(3)}$  for the c-GaP (blue) and a-GaP (green) film as well as the bulk GaP crystal (orange dashed lines).

performed with a pump wavelength of  $\lambda_0 = 1680$  nm ( $f_0 = 178.4$  THz), which was chosen to be larger than triple the value of the electronic bandgap (550 nm) to avoid significant self-absorption of the generated light. Fig. 4.7a shows the response of the c-GaP (blue) and a-GaP (green) film under normal incident illumination. Clearly, only the first shows a SHG peak at double the original frequency  $2f_0 = 356.8$  THz while both samples exhibit a THG response at  $3f_0 = 535.2$  THz. Interestingly, the THG signal of the a-GaP film exceeds the THG signal of the c-GaP film by more than a factor of two, which is opposite to the trend reported for amorphous and crystalline silicon samples [119]. Analogous to the previous procedure, the nonlinear susceptibilities at  $\lambda_0 = 1680$  nm can be extracted by performing nonlinear scattering and TMM simulations. Here, the THG intensity,  $I_{TH}(3\omega)$  is given by

$$I_{TH}(3\omega) \propto \left| \int_{V_{\text{film}}} \chi^{(3)}(\omega) : \vec{P}_{\text{pump}} \cdot \vec{E}_{\text{det}}(3\omega) dV \right|^2 \quad (4.10)$$

The resulting values are displayed in Fig. 4.7b, for SHG (left panel) and THG (right panel), respectively. For the c-GaP film,  $\chi^{(2)}$  calculates to be 16.9 pm/V, which is slightly lower than the  $\sim 30$  pm/V achieved for the bulk wafer. Continuing with the third-order susceptibility, the c-GaP film and wafer reach values in the range of  $10^{-20}$  m<sup>2</sup>/V<sup>2</sup> while a-GaP sample outperforms them both by more than one order of magnitude, reaching a value of  $25 \times 10^{-20}$  m<sup>2</sup>/V<sup>2</sup>. We believe this is mainly caused by two reasons. First, the generalization of Millers rule [120] would predict a higher nonlinear susceptibility based on the slightly higher refractive index of a-GaP compared to the c-GaP. Second, the nonzero absorption coefficient of a-GaP at the pump and the harmonic frequency leads to THG self-absorption that, on the other hand, increases the effective value of  $\chi_{\text{eff}}^{(3)}$ . In comparison to other nonlinear materials (see Table 4.2), this places a-GaP among the third-order nonlinear materials with the highest nonlinearities, and at the same order of magnitude

|                  | Thickness         | Wavelength ( $\mu\text{m}$ ) | $\chi^{(3)}$ ( $10^{-20}\text{m}^2/\text{V}^2$ ) | Ref.  |
|------------------|-------------------|------------------------------|--|-------|
| GaP              | bulk              | 1.680                        | 3.015  | *     |
| c-GaP            | 400 nm            | 1.680                        | 1.0  | *     |
| a-GaP            | 400 nm            | 1.680                        | 25.6   | *     |
| Cuq <sub>2</sub> | 166 nm            | 1.064                        | 1.85   | [121] |
| Ge               | 1.6 $\mu\text{m}$ | 1.650                        | 56.5   | [69]  |
| Si               | bulk              | 1.650                        | 3.84   | [69]  |
| ITO              | 310 nm            | 1.24                         | 450  | [40]  |
| MoS <sub>2</sub> | bulk              | 1.560                        | 24   | [114] |

**Table 4.2:** Third-order nonlinear optical susceptibility values for selected materials. \*This work.

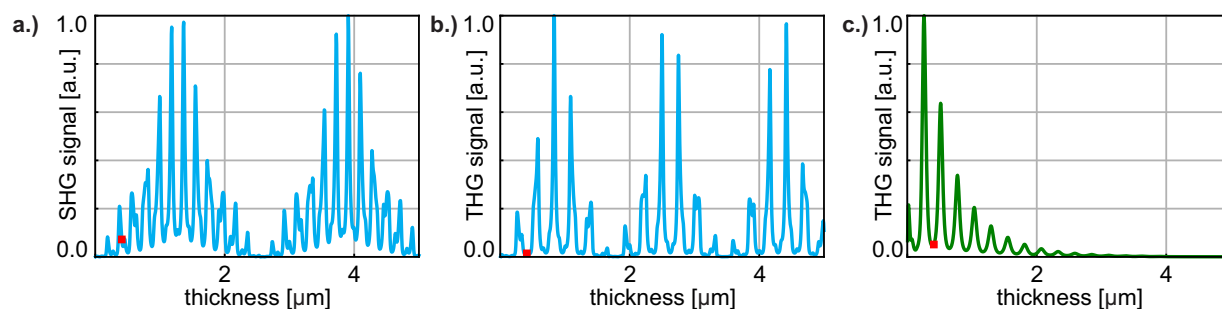


**Figure 4.8:** Calculated thickness dependence of the transmitted nonlinear signal. **a.)** SHG ( $\lambda_0 = 1200$  nm) and **b.)** THG ( $\lambda_0 = 1680$  nm) signal of the c-GaP film. The fast period oscillations correspond to Fabry-Perot resonances of the thin film system, while the slow oscillation is induced by the phase-mismatch and has the period of the coherence length. **c.)** THG ( $\lambda_0 = 1680$  nm) of the a-GaP film. The red square marks the thickness of the thin film that was measured in the main text.

as e.g. amorphous germanium (Ge) films or two-dimensional materials as molybdenum disulfide (MoS<sub>2</sub>). Furthermore, it is only one order of magnitude lower than indium-tin-oxide (ITO) at a very specific condition (epsilon-near zero wavelength at high incidence angle [40]).

#### 4.1.5 Tuning of the nonlinear signal

In order to estimate the thickness dependence of nonlinear signal from GaP thin films, thickness dependent simulations are carried out, following the precious procedure. For simplicity and better comparability of a-GaP and c-GaP, both materials were considered at air without substrate below. The corresponding thickness dependencies are shown in Fig. 4.8 for c-GaP and a-GaP films, at a wavelength of 1200 nm for SHG (Fig. 4.8a) and a wavelength of 1680 nm for THG (Fig. 4.8b-c). For the c-GaP, SHG and THG show very comparable trends with an oscillatory behavior at the period of the coherence length  $l_c$ .

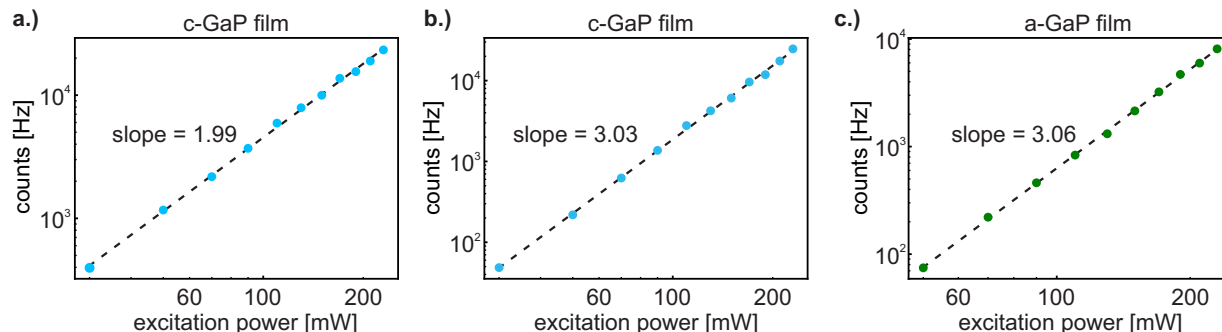


**Figure 4.9:** Nonlinear signal in dependence of the average excitation power, shown on double logarithmic scale. A linear fit to the data is shown by the dashed lines with the respective slope indicated. **a.)** SHG of the c-GaP thin film with a slope close to the expected value of two. **b.)-c.)** THG of the (b.) c-GaP and (c.) a-GaP thin films. Here, the slopes are in excellent agreement with the predicted value of three.

For the a-GaP film (Fig. 4.8c), this differs as the nonzero absorption reduces the signal with increasing thickness until it vanishes completely. It should be noted that coherence length  $l_c = \lambda/(4(n_{nl} - n_0))$  and oscillation period of the fast Fabry-Perot oscillations both are functions of the fundamental wavelength.

Furthermore, it is shown that the nonlinear signal increases in a nonlinear fashion by performing a power dependence measurements, shown in Fig. 4.9. For this, the average excitation power is tuned over a range from 0 – 200 mW and a linear fit (at double logarithmic scale) for all three cases is close to the expected slope of two or three, for SHG or THG, respectively. It should be noted that in the measured range, neither a saturation of the nonlinear signal nor a damaging of the samples can be observed.

#### 4.1.6 High-harmonic generation from GaP thin films

Finally, we show that all GaP samples even allow the generation of HHG light. Under illumination with  $f_0 = 149.9$  THz ( $\lambda_0 = 2 \mu\text{m}$ ) light, again to reduce self-absorption of the generated signal, up to the fifth-harmonic ( $5f_0 = 749.5$  THz) could be observed (see Fig. 4.10). third- and fifth-harmonic of the original frequency. Thus, the crystalline samples generate light at multiple harmonic-orders ( $2^{\text{nd}} - 5^{\text{th}}$ ) while the inversion symmetry of a-GaP prevents the generation of even order harmonics. Therefore, for a-GaP signal could only be observed at the

#### 4.1.7 Conclusion

This chapter investigated the nonlinear optical properties of GaP thin films by means of harmonic generation and compared them to the bulk of the same material. We extracted the value of the second-order susceptibility of the crystalline thin film and showed that it is in the same range as bulk GaP crystals. For bulk and c-GaP film, no significant

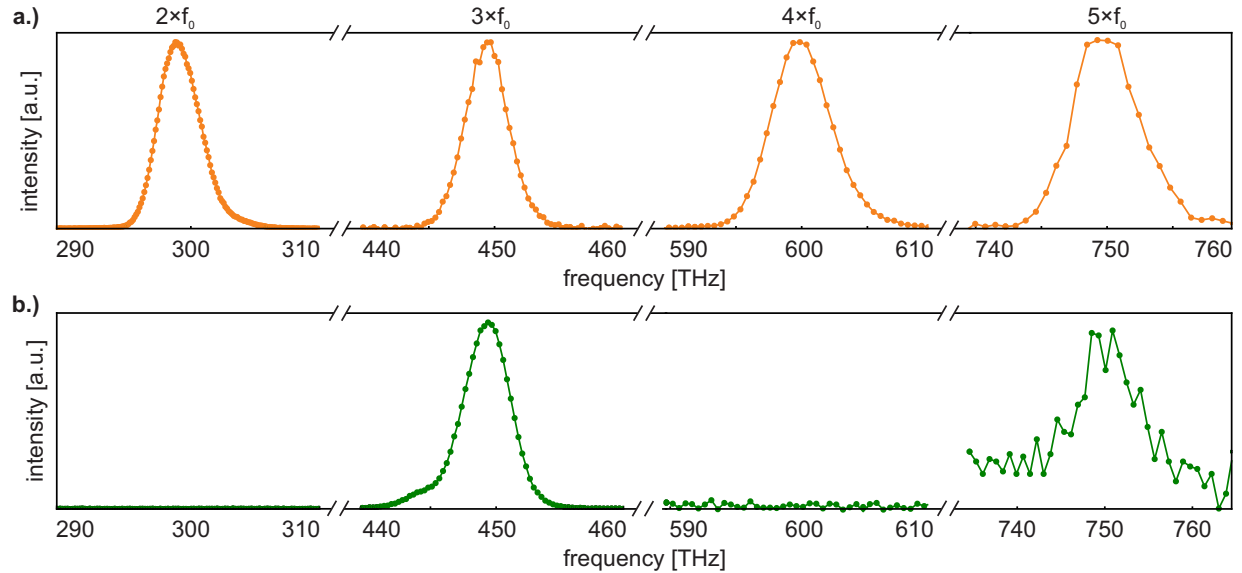


**Figure 4.10:** High-harmonic generation from **a.)** the [111] GaP wafer and **b.)** the a-GaP film. The excitation wavelength is  $2\ \mu\text{m}$ .

spectral dependence could be measured, in particular no resonance effect when approaching the bandgap of the material. Moreover, the presented results show that the crystalline orientation of the c-GaP film allows efficient SHG under normal incidence illumination and, when correcting for the tilted axis, polarization independent SHG. Finally, this chapter showed that for odd-order nonlinear processes, a-GaP thin films are an alternative that exceeds the efficiencies of the crystalline samples, while providing simpler processing and fabrication flexibility. The extraction of  $\chi^{(2)}$  and  $\chi^{(3)}$  were carried out with the nonlinear transfer-matrix method. Altogether, this chapter complement the picture of GaP thin films for nonlinear nanophotonic applications with, as we believe, currently one of the most promising combination of high optical coefficients and virtually no losses over most of the visible regime. This paves the way for future applications of GaP thin films, particularly in low-efficiency nonlinear process such as photon-pair generation.

#### 4.1.8 Experimental details and supplementary material

**Sample fabrication:** The c-GaP films were fabricated by epitaxial growth on GaAs as wafer. A wafer bonding process and subsequent wet etching of the GaAs results in the desired crystalline GaP film on transparent sapphire substrates. More details on the fabrication can be found in refs [102–104, 122]. The a-GaP films were fabricated on coverglass substrates (borosilicate) by sputter deposition in the Angstrom deposition tool. During the process, the substrate temperature was kept constant at  $350^\circ\text{C}$ . The bulk GaP wafer was purchased from the Institute of Electronic Materials Technology (Warsaw, Poland).

**Sample characterization:** XRD measurements were performed using a monochro-

matic Mo-K $\alpha$  X-ray beam with  $\lambda = 0.71073 \text{ \AA}$ . The beam was monochromized by a parabolic multilayer, which yields a line focus, i.e. a highly parallel beam in horizontal direction with considerable vertical divergence. The surface normal of the samples was aligned in the horizontal plane and rotated around a vertical axis. The diffraction intensities in the horizontal plane were recorded using a Pilatus 100k area detector from Dectris. The measurements were not background corrected. The intensities of the amorphous film (a-GaP) are practically identical to the diffraction signal of its bare substrate, i.e. we do not observe notable Bragg signal from the amorphous GaP film. The other samples show Bragg peaks in accordance with the orientation of the crystalline GaP phase, and in case of the sapphire substrate an additional Bragg peak of the crystalline Al<sub>2</sub>O<sub>3</sub> lattice. Linear optical characterization was performed with the VASE system, covering the range of 0.3 – 2.0  $\mu\text{m}$ . Additionally, linear transmission measurements at normal incidence were done with the same tool and over the same spectral range. Both datasets were used to extract the linear refractive index for the respective samples.

**Nonlinear optical measurements:** The nonlinear optical measurements were performed at Imperial College London, with a laser system similar to the one introduced in chapter 2.4, by Light Conversion Ltd. The system provides pulses at 100 kHz repetition rate with a temporal pulse width of around 220 fs, covering a wavelength range between 1 – 1.5  $\mu\text{m}$ . The beam weakly focuses on the sample where the SHG signal is generated (focal length = 300 mm) and the beam size is found using a knife-edge technique. The generated SHG signal is collected by a visible power meter (Thorlabs, S120VC) with visible shortpass filters to exclude the infra-red pump beam.

For the third-harmonic measurements, a similar laser system is used while the sample is illuminated under stronger focusing (NA = 0.9). An objective (NA = 0.4) is then used to collect the generated signal and send it to a spectrometer with CCD camera (Princeton Instruments). Before, strong filtering makes sure to remove any residual pump signal. The high-harmonic and power dependence measurements were carried out with the MHz laser system. By choosing the OPO wavelengths accordingly, an idler wavelength of 2  $\mu\text{m}$  is generated and sent to the microscope. There, a high NA objective by Nikon (60x, NA = 0.95) is used to focus on the sample, while another objective (100x, NA = 0.9) is used to collect the light in transmission geometry. Corresponding filters are used to remove the fundamental wavelength, before the generated light is sent to the same spectrometer as for SHG experiments.



## 4.2 Amorphous gallium phosphide nanopatches

This work is published in [118]:

Benjamin Tilmann, Gustavo Grinblat, Rodrigo Berté, Mehmet Özcan, Viktoria F. Kunzelmann, Bert Nickel, Ian D. Sharp, Emiliano Cortés, Stefan A. Maier, Yi Li  
”*Nanostructured amorphous gallium phosphide on silica for nonlinear and ultrafast nanophotonics*”

Nanoscale Horizons 5(11), 1500-1508 (2020), DOI: 10.1039/D0NH00461H  
permission for reprint is granted under the Creative Commons CC BY 3.0 license

The previous section introduced GaP nanofilms as a promising material system for nonlinear optical applications. The next step is to investigate the actual performance of nanostructures made of the material. As mentioned in section 2.3.1, all-dielectric nanostructures have been shown to outperform plasmonic nanoparticles in a number of nanophotonic applications [19, 123]. In particular in the optical regime, semiconductors exhibit a transparency that is only limited by the spectral position of their electronic bandgap wavelength, while metals show strong Ohmic losses and absorption due to the presence of free carriers at all wavelengths. For nonlinear optics, this effectively restricts the optically active region mainly to the surface while Mie-like resonances in dielectric structures can spread the field over the entire volume [93]. This property has already been employed to successfully explore second- [21, 124–127] and third- [68, 69, 128] harmonic generation as well as frequency mixing [129, 130] with dielectric nanoparticles, exceeding the achieved efficiencies of comparable plasmonic systems. Most of these studies are based on the excitation of electro-magnetic resonant modes that confine the electric and/or magnetic fields in dielectric nano-resonators, thus boosting the intrinsically low efficiency of nonlinear effects [24]. To achieve this, a strong refractive index contrast between the dielectric material and the surrounding medium is needed, leading to a research focus on high refractive index materials such as AlGaAs [126, 131–133], Ge [68, 69, 133] and Si [37, 127, 134].

Consequently, this section is focused on a-GaP thin films by demonstrating the deposition and nanostructuring of the high refractive index films on top of a low refractive index substrate at a CMOS compatible temperature (250 °C). Furthermore, its intrinsic and resonant nonlinear optical response are characterized using SHG and ultrafast pump–probe spectroscopy. Particularly the dependence of the nonlinear signals on the incident polarization is analyzed and numerical simulations that are found to be in good agreement with the experimental findings.

### 4.2.1 Nanofabrication and structural analysis

A GaP film is first sputtered on top of a glass substrate, followed by two dry etching steps to define dielectric nanopatches of different sizes using gold and silicon dioxide as hard masks. The desired design is transferred to the sample using a standard EBL procedure with PMMA as photoresist (more in the Experimental Details). To characterize the composition of the as-deposited, uncapped film, we perform XPS measurements, with the Ga<sub>2p</sub> and P<sub>2p</sub>

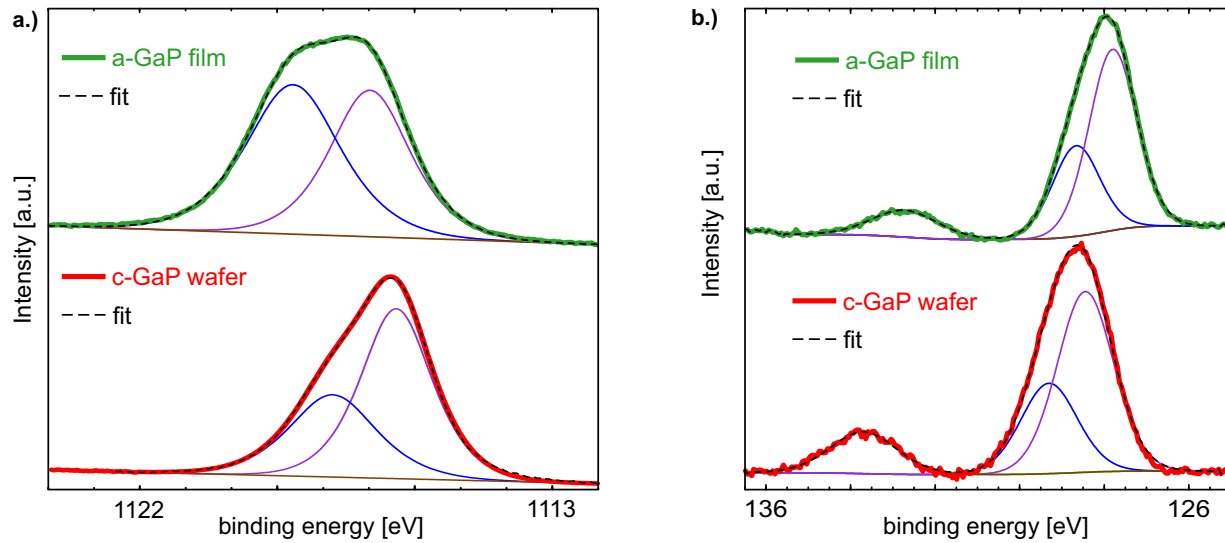


**Figure 4.11:** High resolution XPS measurement of **a.)** the Ga 2p<sub>3/2</sub> region and **b.)** the P 2p peak for the as deposited a-GaP film (green) and the c-GaP wafer (red). The black dashed line represents a peak fitting with the background shown by the brown solid line.

core level peaks shown in Fig. 4.11a and b, respectively (green lines). As a reference, a commercial double side polished wafer of intrinsic c-GaP (Institute of Electronic Materials Technology, Warsaw) is used, shown in red. The measurements exhibit nearly identical features and are in very good agreement with each other and with literature values [135, 136]. Due to the presence of a low energy satellite feature in the P<sub>2p</sub> region (Fig. 4.11b), direct quantitative analysis of the Ga:P elemental ratio was not possible. To overcome this, the intensity ratio of the Ga–P components from the Ga<sub>2p<sub>3/2</sub></sub> region to the P<sub>2p</sub> region was compared between the sputtered film and reference sample, which possesses a known stoichiometric composition. The intensity ratio for the a-GaP is within 5% of that from the c-GaP wafer which is near the error limits of this method, thus confirming that the deposited material is stoichiometric GaP. Furthermore, the XPS survey spectra from the c-GaP reference and the sputtered a-GaP film are nearly identical, with no additional impurity elements observed for the sputtered material. To further prove the amorphous structure of the sputtered film, we perform XRD and compared it again to the [100] oriented wafer, shown in Fig. 4.12. As expected, the latter exhibits clear peaks in the diffraction pattern that correspond to the (200) and (400) orientations, in excellent agreement with literature values [105,137]. In contrast, the a-GaP film shows a weaker and broad response without any clear feature or pronounced peak. Such pattern can be attributed to an amorphous structure without long-range order [138].

Further, to study the optical quality of the amorphous film, we investigate its linear optical properties through spectral ellipsometry. We determine the complex permittivity  $\epsilon$ , with real and imaginary parts shown in Fig. 4.13a and b (green curves), respectively, and compare it to the results of the crystalline wafer (red curves). In good agreement with band structure calculations [89], the c-GaP sample has an imaginary part of  $\epsilon$  that is only

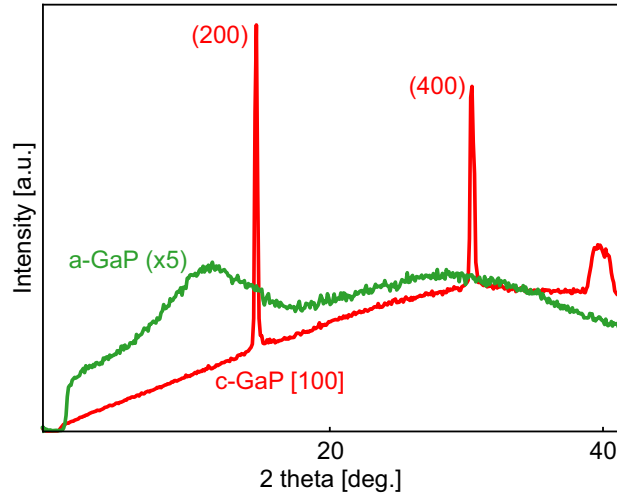


**Figure 4.12:** XRD measurements of the [100] c-GaP wafer (red) and a-GaP film (red). The wafer shows a crystalline pattern with the (200) and (400) orientations indicated.

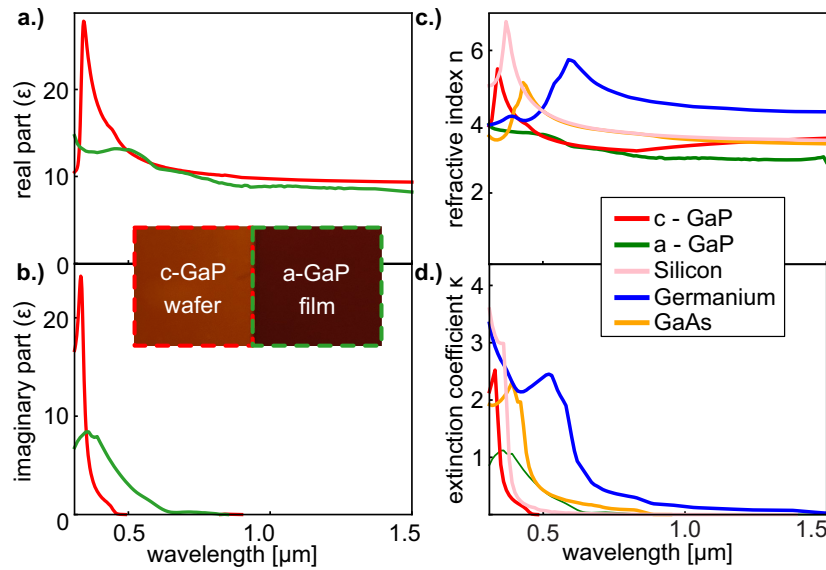


**Figure 4.13:** Dielectric Function of GaP with a.) the real and b.) the imaginary part. Inset: Optical image of the c-GaP wafer and the a-GaP film. c.) Refractive index  $n$  and d.) extinction coefficient  $k$  for different semiconductors. For a-/c- GaP it shows measured data, the others are based on ref. [139].

nonzero for wavelengths shorter than the direct bandgap at 450 nm while being effectively lossless for the remaining extent of the spectrum. In the case of the amorphous film, the absorption edge is red-shifted towards 650 nm, which can be explained by increased impurity-assisted electron transitions in the defect-rich amorphous structure. Nevertheless, the sputtered a-GaP is transparent for part of the visible and all of the near IR spectrum with an extinction coefficient that is lower than that for other common semiconductors such as Ge or GaAs (a comparison is shown in Fig. 4.13c-d). The measured difference in the optical constants between the a-GaP film and the c-GaP wafer results in a darker orange appearance of the former, visible in the optical image in the inset of Fig. 4.13. However, the determined values of the real part of  $\epsilon$  are close to c-GaP for most of the investigated spectral range (500 nm–1.5  $\mu\text{m}$ ), leading to a refractive index larger than 3.

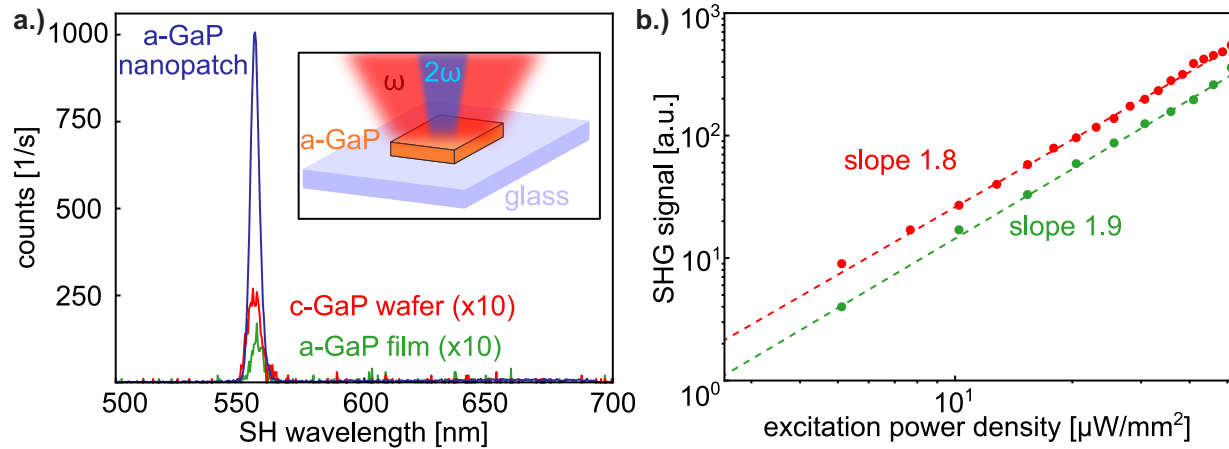


**Figure 4.14:** a.) Spectral SHG response at a fundamental wavelength of 1120 nm and  $10.2 \mu\text{W}/\text{mm}^2$  average pump power for the c-GaP wafer (red), a-GaP film (green) and a single a-GaP nanopatch (blue). Inset: Sketch of the SHG measurement of a GaP nanopatch on glass substrate. b.) Power dependence for the c-GaP wafer and a-GaP film at double logarithmic scale. The dashed lines represent a fitting to a linear model resulting in the indicated slopes.

### 4.2.2 Enhanced SHG from a-GaP nanopatches

Next, we investigate the second-order response of the a-GaP film through SHG measurements at a pump wavelength of 1120 nm (see Experimental Details for specifics). As shown in Fig. 4.14a, a second-harmonic response at the expected wavelength of 560 nm is observed for the a-GaP film (green curve). Comparing the magnitude of the signal to a reference measurement with the c-GaP wafer (red curve) indicates an effective second-order susceptibility  $\chi^{(2)}$  that is smaller for the amorphous film by a factor of 2. As shown in Fig. 4.14b, this trend is confirmed over a wide range of excitation power densities of 0–102  $\mu\text{W}/\text{mm}^2$ . A linear fit in double logarithmic scale leads to the expected slopes close to 2, confirming the second-order nature of the process.

To enhance the nonlinear response of the as-deposited a-GaP film, an array of etched nanopatches with a fixed height of 260 nm is investigated. A scanning electron microscope (SEM) image of the fabricated structures is shown in Fig. 4.15a, where patches with widths and lengths varying from 100 nm to 1000 nm can be observed. In particular, the SHG signals from two patches with dimensions of 675 nm  $\times$  375 nm and 900 nm  $\times$  450 nm, in the following referred as patch 1 and patch 2, respectively, are measured individually. Remarkably, a comparison of patch 1 with the bare film at a pump wavelength of 1120 nm results in an enhancement of the SHG signal by more than two orders of magnitude, as it can be seen in Fig. 4.14a. This is about one order of magnitude lower than for c-GaP, where SHG enhancement by more than three orders of magnitude by nanostructuring was reported [21]. Reasons for this discrepancy could be the difference in the nonlinear susceptibility  $\chi^{(2)}$  or SHG self-absorption, which naturally limits the SHG emission. Furthermore,

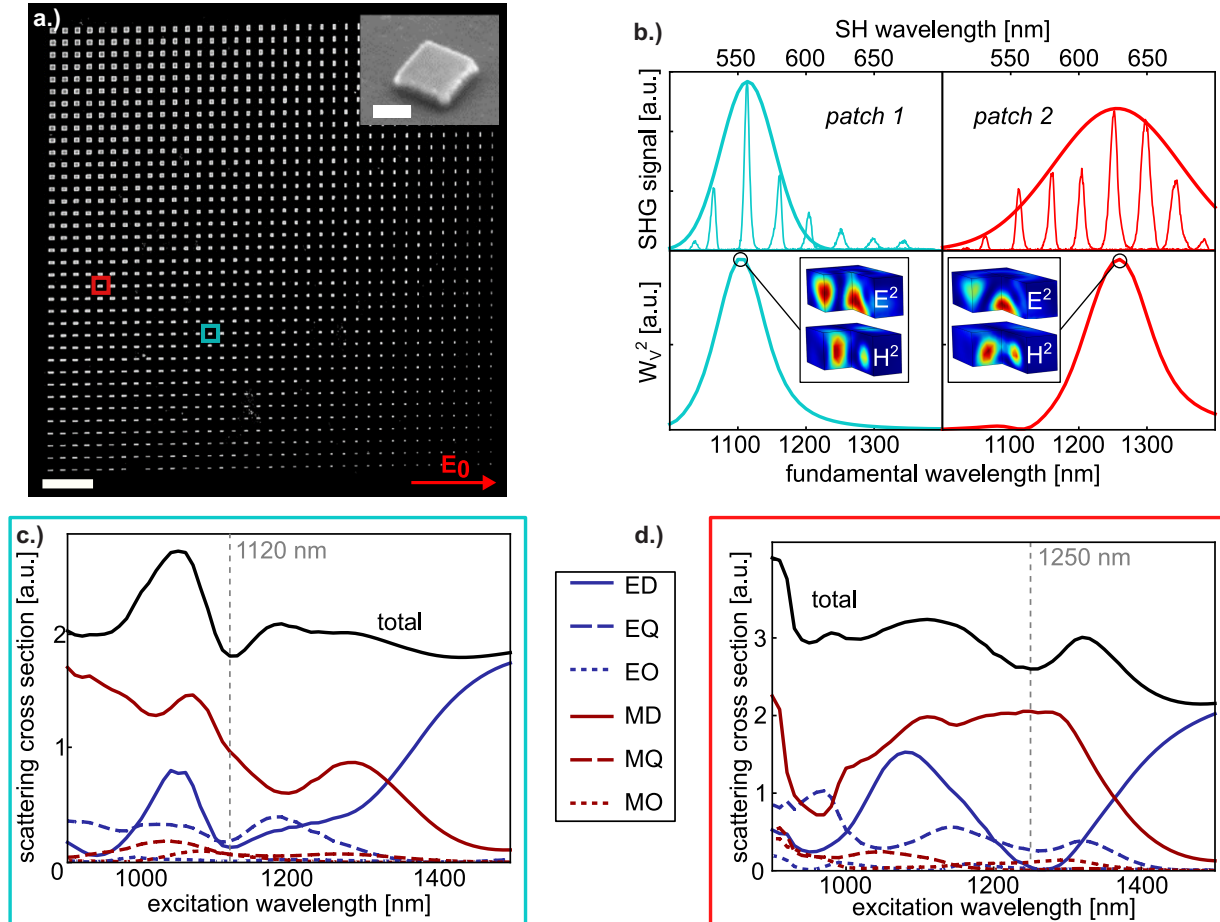


**Figure 4.15:** a.) SEM image of the fabricated a-GaP nanopatch array. The red arrow indicates the pump polarization of the SHG measurements. Scale bar: 10  $\mu\text{m}$ . Inset: Single 1000 nm  $\times$  1000 nm patch, tilted by 45°. Scale bar: 200 nm. b.) Experimental spectral SHG response for patch 1 and patch 2 (top) and corresponding numerical  $W_V^2$  values (bottom). The inset shows the fundamental near field distribution of the electric (E) and magnetic (H) field for the respective maximum wavelengths indicated. Multipole decomposition for c.) patch 1 and d.) patch 2. Included are the first three orders, namely electric/ magnetic dipole (ED/MD), quadrupole (EQ/MQ) and octupole (EO/MO). The black solid line represents the simulated total scattering cross section. The dashed lines mark the wavelengths showing maximum SHG.

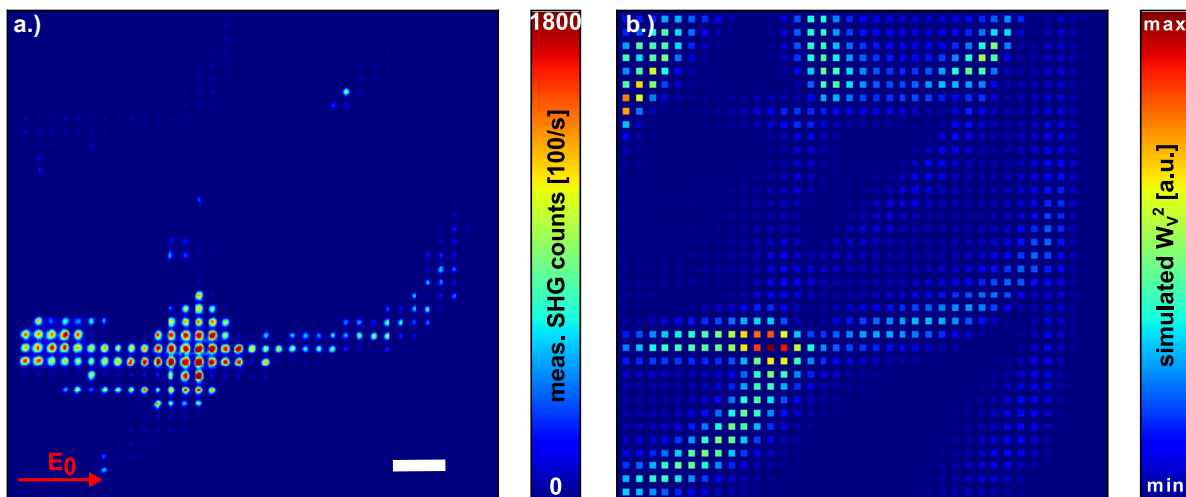


**Figure 4.16:** **a.)** SHG measurement of the entire nanopatch array from Fig. 4.12a. The fundamental wavelength is 1120 nm with an average excitation power of  $25.5 \text{ mW}/\text{mm}^2$ . The red arrow indicates the pump polarization. Scale bar:  $10 \mu\text{m}$ . **b.)** Numerical simulation of the square of the electric energy ( $W_V^2$ ) for the array in (a). Each square represents the respective patch with dimensions corresponding to this position.

we study the second-harmonic response of the two nanopatches over a spectral excitation range of 1000–1400 nm at a constant pump power density of  $10.2 \text{ mW}/\text{mm}^2$ . This leads to clear SHG peaks for 1120 nm and 1250 nm excitation wavelength for patch 1 and patch 2, respectively, as shown in Fig. 4.15b (top panels). To gain a better understanding of this resonant behavior, numerical simulations are carried out, using the FDTD method. We start by calculating the square of the normalized electric energy stored inside the nanoantenna  $W_V^2$ , defined by  $W_V = n^2 \int dV \frac{E^2}{VE_0^2}$  (see bottom panels in Fig. 4.15b), with  $V$  being the volume of the nanopatch. As SHG depends on the square of the incident light intensity,  $W_V^2$  can be regarded as the effective excitation power of the conversion process. In Fig. 4.15b we can see a very good agreement between the calculated curve and the experimentally measured spectral dependence of SHG. The deviation of the peak widths can be attributed to the conversion process itself and emission directionality which were not considered in the numerical analysis. Further simulations including a multipole decomposition, as shown in Fig. 4.15c and d, reveal that the observed peaks in the electric energy are accompanied by a dip in the total scattering (black curves), leading to the respective electric and magnetic field distributions included in Fig. 4.15b. Such a behavior can be attributed to non-radiating, anapole-like excitations in the nanopatches, that are known to strongly enhance the electric energy [64, 140].

To verify our findings on a larger scale, the SHG signal of the entire nanopatch array (accounting for a total of 1369 nanoantennas) is monitored at a pump wavelength of 1120 nm, with the resulting SHG map shown in Fig. 4.16a. As expected, the generated signal de-

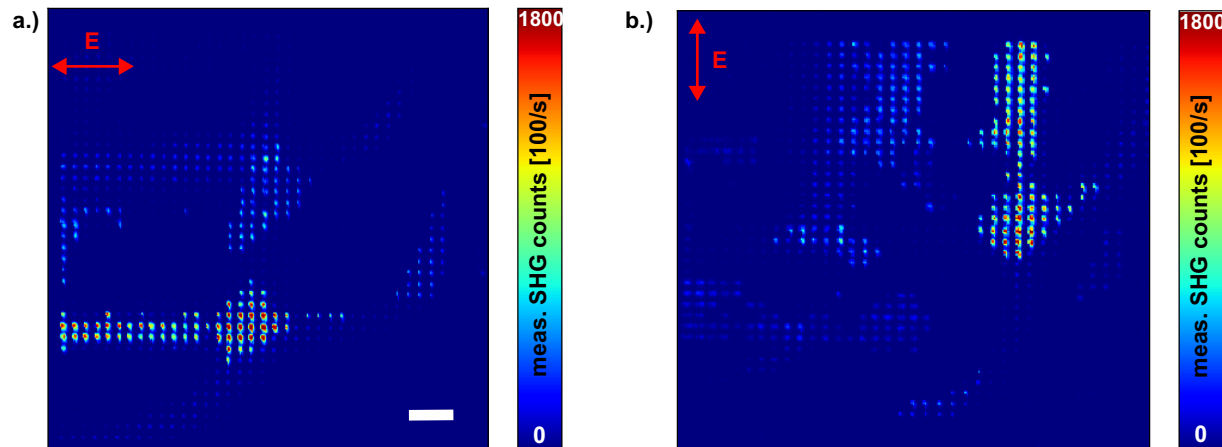


**Figure 4.17:** SHG measurement at a wavelength of 1020 nm. **a.)** At horizontal polarization, comparable to Fig. 4.16. **b.)** The same measurement but at vertical polarization. The average excitation power was  $50 \mu\text{m}$  in both cases.

pends strongly on the nanopatch dimensions, with the strongest signal occurring around the location of patch 1. Even more, we find that the orientation of the patches with respect to the incident polarization plays an important role. While specific antennas that are orientated parallel to the fundamental beam generate the strongest signal, their rotated counterparts appear as almost inert. This behavior is confirmed by a measurement of the same array, but with opposite (vertical) polarization (see Fig. 4.17), where all features appear at the corresponding mirrored positions. As for the single patches in Fig. 4.15, the simulation of  $W_V^2$  in Fig. 4.16b shows a good agreement with the measured SHG signal over a large region of the nanopatch array. Especially close to the position of patch 1, computational results and experiment are in very good agreement, with numerical calculations accurately describing most features visible in the measurement, even for the smallest patches. The observed small deviations between experiment and theory can be attributed to effects such as emission directionality or SHG self-absorption, which are not considered in the calculations. The fact that the latter scales with the volume of the nanopatches, explains the greater deviation for larger structures. To ensure the reproducibility at a different wavelength, an identical measurement for a pump wavelength of 1020 nm can be found in the Fig. 4.17a. As expected for a shorter wavelength, the strongest responses appear shifted towards smaller antennas, also in good agreement with the corresponding simulations.

### 4.2.3 Nondegenerate pump-probe spectroscopy

We now turn our attention to the ultrafast response of the sputtered GaP nanopatches, characterized through nondegenerate pump-probe spectroscopy using sub-10 fs laser pulses in the 600–1000 nm wavelength range. Fig. 4.18a shows the measured differential reflect-

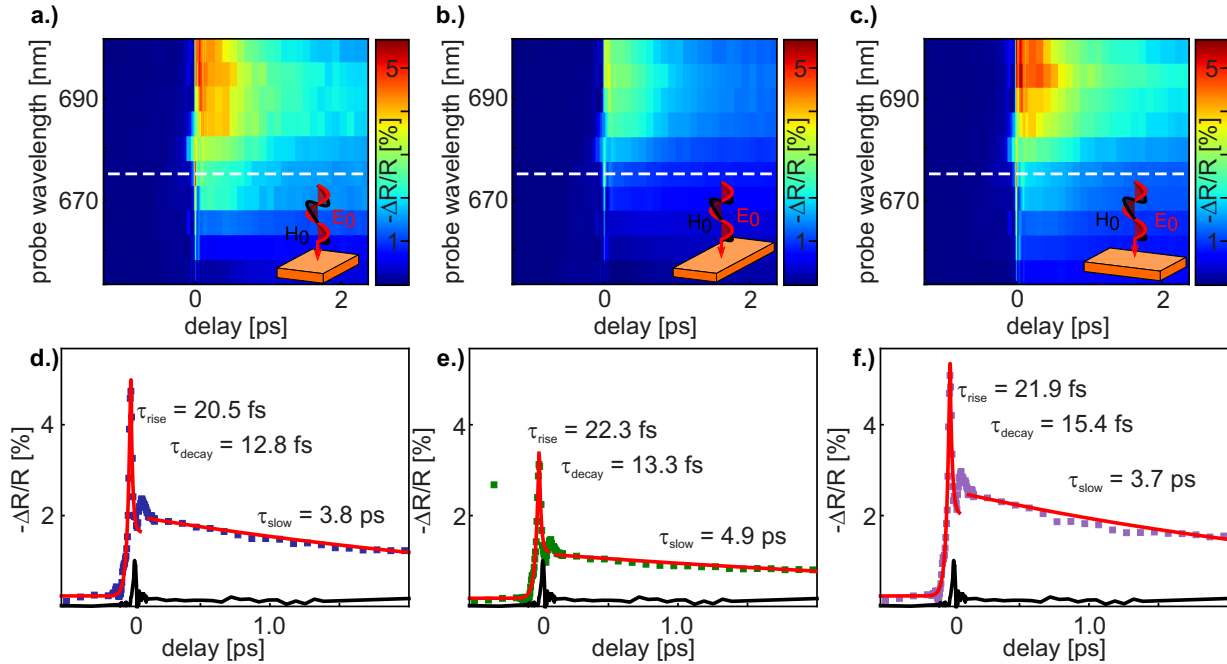


**Figure 4.18:** Differential reflectivity  $\Delta R/R$  contour plots with respect to the probe wavelength and the pump–probe delay time for three patches with dimensions **a.)**  $625 \text{ nm} \times 625 \text{ nm}$ , **b.)**  $625 \text{ nm} \times 850 \text{ nm}$  and **c.)**  $850 \text{ nm} \times 625 \text{ nm}$ . The dashed lines mark the  $675 \text{ nm}$  probe wavelength that is shown in temporal traces **d.)-f.)** for the respective patches. Red solid lines represent fittings to the convolution of exponential rise/decay and the IRF for the ultrafast response and exponential decay for the slow decaying part, respectively. The resulting time constants are indicated. The response of the as-deposited a-GaP film is shown in black.

tivity  $\Delta R/R$  for a square patch pumped (probed) with a  $750\text{--}1000 \text{ nm}$  ( $600\text{--}750 \text{ nm}$ ) wavelength beam. At the temporal pump–probe overlap position ( $t = 0 \text{ fs}$ ), the nanoantenna exhibits a maximum differential reflectivity value of  $5.6 \%$  at a probe wavelength of  $690 \text{ nm}$ , which decreases towards shorter wavelengths. Over the measured spectral range, the response is dominated by a slow decaying modulation that is commonly attributed to free carriers [141], excited by linear and two-photon absorption. However, for a probe wavelength around  $675 \text{ nm}$ , this slow component is overwhelmed by a sharp response at precisely the overlap position  $t = 0 \text{ fs}$ , as it can be seen in the temporal trace presented in Fig. 4.18d. Such an ultrafast response, separated from the slow component, is especially interesting for all-optical signal processing [41] and was previously reported for c-GaP [39,122]. Comparing the performance of the patches with the as-deposited a-GaP film (black curve in Fig. 4.18d), shows that nanostructuring enhances the peak nonlinear signal by more than a factor of 5. Moreover, it should be stressed that an ultrafast response of this magnitude is larger than reported for perovskite single crystals [141] or gold-covered silicon discs [142]. To exploit the observed polarization dependence of the sample, identical measurements are

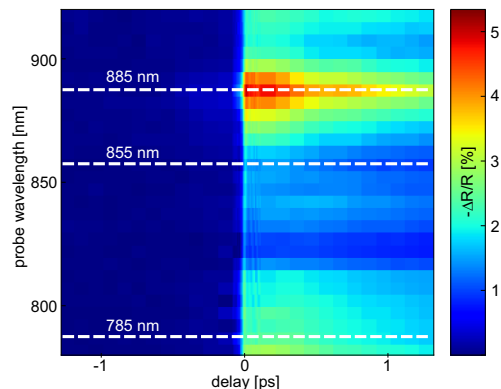


**Figure 4.19:** Pump-Probe measurement of the square patch measured in Fig.4.16) with exchanged pump and probe configuration. Here, the visible beam acts as pump and the infrared beam as probe. Shown is the spectral response of the differential reflectivity versus the pump-probe delay time.

performed on two orthogonally oriented rectangular patches of identical size, as shown in Fig. 4.18b and c. To simplify the analysis, Fig. 4.18d–f shows the temporal traces results taken from Fig. 4.18a–c, respectively, at the specific probe wavelength of 675 nm. A maximum value for the differential reflectivity of 5.6 % is observed for the squared antenna (Fig. 4.18a and d) that is reached after a rising time of 20.5 fs, computed by fitting of a convolution between an exponential and a Gaussian function, with the latter being the approximation of the IRF of our system [39]. To fit the relaxation dynamics of the signal, two exponential decay functions are needed, again a convolution with the IRF for the ultrafast component and a single one for the slow part, respectively. We find that there is a fast decay time of 12.8 fs which can be attributed to a combination of the nonlinear Kerr effect and TPA [39, 141, 142] combined with a slow relaxation component of 3.8 ps, product of the free carrier dynamics, which is comparable to other amorphous semiconductors [143]. When comparing the squared nanoantenna (Fig. 4.18a) with the elongated nanopatches (Fig. 4.18b and c), we find that the responses of all three nanostructures show the same features, differing only in the magnitude of the differential reflectivity. While the patch that is orientated parallel to the incident polarization reaches slightly higher values than the square patch, the rotated antenna reduces the modulation depth by more than 40 %. The same behavior can be observed in the evaluation of the reference temporal traces at  $l = 675$  nm, shown in Fig. 4.18d–f. Nevertheless, it should be noted that even for the perpendicular elongated patch (Fig. 4.18e) the peak response is larger than that of the as-deposited film by a factor of 3. We furthermore note that a measurement with exchanged pump and probe beams (see Fig. 4.19) shows no pronounced ultrafast peak, given that free carrier absorption is dominant when pumping with the short-wavelength beam. The same picture is apparent for the single time traces that are shown in Fig. 4.20.

#### 4.2.4 Conclusion

In summary, thin films of GaP were fabricated using radio frequency sputter deposition, resulting in an amorphous material with optical constants close to the bulk crystalline counterpart. Nanostructuring of the film further improved the SHG signal by more than two orders of magnitude with numerical simulations that are in good agreement over a wide

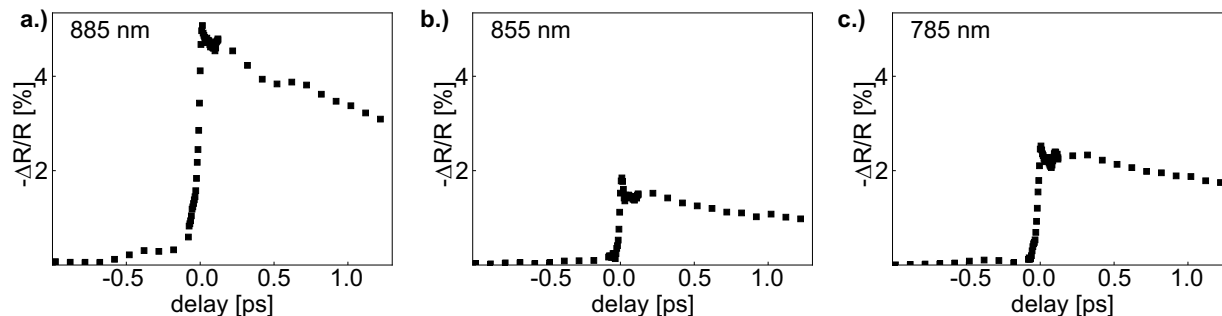


**Figure 4.20:** a.)-c.) Temporal traces at the indicated wavelengths, marked with the dashed lines in Fig. 4.19.

range of the nanopatch dimensions and for different excitation wavelengths. Pump-probe measurements of the nanostructures revealed a strong nonlinear and ultrafast response that decays within 100 fs, accompanied by a smaller slow-decaying feature attributed to free carrier contributions, at a probe wavelength of 675 nm. For both, SHG and ultrafast responses, a strong dependence of the signal and the orientation of the nanopatch with respect to the fundamental beam polarization was observed. Even though the sputtered film has no well-defined crystal structure, the achieved nonlinear responses are close to previously reported values for c-GaP [21, 39], proposing a-GaP as a promising inexpensive and flexible material with excellent optical properties. Moreover, its considerable absorption in the solar spectrum and the observed carrier dynamics make it an exciting candidate for other areas such as photocatalysis at the nanoscale with confined photocarrier transport, as reported for dielectric  $\text{TiO}_x$  nano-resonators [20].

#### 4.2.5 Experimental details and supplementary material

**Sample fabrication:** The films were fabricated using radio frequency sputter deposition with a 3 inch GaP target in an Angstrom deposition tool. The procedure was carried out at a constant rate of  $1 \text{ \AA}/s$  while the glass substrate was constantly heated to  $250 \text{ }^\circ\text{C}$ . After cooling down, the same tool was used to deposit a capping layer of  $\text{SiO}_2$ , again via sputter deposition. Before the procedure, a standard microscopy borosilicate cover glass substrate was cleaned, using acetone and isopropanol (IPA). As a positive photoresist, PMMA was deposited on top using spin coating. The EBL was carried out with an exposure dose of  $400 \text{ mC cm}^{-2}$  with a 10 mm aperture and external high voltage (EHT) of 20 kV. After the development for 30 s in MIBK:IPA and 30 s in IPA, gold as a hard mask was deposited using thermal evaporation. A lift-off procedure was carried out by a bath in acetone for 4 h. In a first inductively coupled plasma reactive ion etching (ICP-RIE) dry etching step, the mask was etched into the silica layer with  $\text{CHF}_6$  (20 sccm) and Ar (30 sccm) as processing gases. Afterwards the gold was removed by rinsing the sample in Au-etchant for a few seconds. Finally, again ICP-RIE with  $\text{Cl}_2$  (10 sccm) and Ar (30 sccm) as processing gases was used to transfer the nanostructures into the GaP film.

**Sample characterization:** The XPS measurements were recorded with a homebuilt setup at TUM, using an Al X-ray source and a pass energy  $E_{\text{pass}} = 25$  eV. The energetic positions of all spectra were calibrated using the adventitious carbon by shifting the C–C bond position in the  $\text{C}_{1s}$  core level spectrum to 284.8 eV. The spectra were fitted to Voigt type line shapes after a Shirley or linear background correction (software CasaXPS). The X-ray source could be switched to Mg, allowing to differentiate Auger and core level XPS peaks for the later analysis.

The XRD measurements were recorded at LMU using the rotating crystal method [144]. A monochromatic Mo K $\alpha$  ( $\lambda = 0.71073$  Å) beam from a sealed tube is selected by a parabolic multilayer monochromator white line focus, i.e., the X-ray beam is highly collimated in horizontal direction and rather divergent in the vertical. At the sample position the beam cross-section is  $10 \times 0.35$  mm<sup>2</sup>. The GaP samples were aligned with their surface normal along the horizontal direction and rotated slowly with constant angular velocity, while the diffracted intensities were recorded by a Dectric Pilatus 100k area detector. The system was calibrated with a standard powder sample measurement under the same conditions (Lanthanum hexaboride).

The ellipsometry measurements were done with the VASE instrument from J. A. Woollam (Chapter 3.3.1) over the visible to near-IR spectral range.

**SHG experiments:** The used laser systems is based on the kHz laser and the Nikon microscope (section 3.3). A 100x/Numerical Aperture (NA) = 0.9 objective was used to focus the beam on the sample, which was mounted on the  $XYZ$ -piezo stage. The generated light was then collected with the same objective. By scanning over the sample and measuring the collected SHG signal in each point, SHG maps as Fig. 4.16a could be recorded.

**Pump–probe experiments:** The pump-probe measurements were based on the setup introduced in section 3.4, the white light generation was carried out with an average power of 600 mW to generate 3 mW of SC light. To reduce dispersion effects, low group velocity dispersion (GVD) mirrors and a dispersion free metal objective with NA = 0.5 were used to direct and focus the beams. Lock-in detection was used by modulating the pump beam using an optical chopper operating at frequencies below 1 kHz. The IRF of the system is described by a Gaussian function with a full-width half-maximum of 11 fs, that approximates the convolution of pump and probe beam.

**Numerical simulation:** The numerical simulations were performed with Lumerical FDTD and the TFSF source. The simulation region was restricted by perfectly matched layer boundaries to imitate antennas in an infinite space. The experimental data of the ellipsometry measurements of the sputtered GaP film as well as for the bare coverglass were used as input for the materials dielectric function in the simulation. The multipole decomposition and calculation of the near field distribution were carried out using COMSOL Multiphysics with the RF module. The multipole analysis follows the procedure published

by COMSOL and is based on the equations of Mie theory. It makes use of the expansion in means multipole coefficients, using the scattering current that is source of the scattering field [60].

## 4.3 Crystalline gallium phosphide nanostructures

This work is published in [122]:

Gustavo Grinblat, Haizhong Zhang, Michale P. Nielson, Leonid Krivitsky, Rodrigo Berté, Yi Li, Benjamin Tilmann, Emiliano Cortés, Rupert F. Oulton, Arseniy I. Kuznetsov, Stefan A. Maier

”*Efficient ultrafast all-optical modulation in a nonlinear crystalline gallium phosphide nanodisk at the anapole excitation*”

Science Advances 6(34), eabb3123 (2020), DOI: 10.1126/sciadv.abb3123

permission for reprint is granted under the Creative Commons CC BY-NC 4.0 license

After exploiting frequency conversion and ultrafast dynamics in a-GaP nanostructures, the following section will focus on the ultrafast refractive index change that can be induced by the OKE or TPA (see section 2.4.2). This has previously been studied in terms of the ultrafast modulation of optical reflectivity and transmission in silicon-based nanoantennas and metasurfaces [35, 142]. As introduced, the OKE and TPA are third-order nonlinear effects that can instantaneously vary the real and imaginary parts of the complex refractive index of a medium [24], respectively, enabling femtosecond control of its optical properties. Modulation depths, defined as [peak differential reflectivity/transmissivity] - [baseline modulation], of up to  $\sim 0.5\%$  at sub-100 fs time scales have been demonstrated for the silicon nanosystems at visible and near-infrared wavelengths [35, 142]. However, substantially larger modulation depths are required before such nonlinear modulators can become suitable for applications. Ultrafast all-optical switches are expected to become a core element in high-speed operating integrated photonic applications using photons as information carriers, such as optical computing and communication, and quantum information processing [31, 32]. The four main performing indices of an all-optical switch are switching time, switching efficiency, control power, and characteristic size. Ideally, an all-optical switch should feature  $< 100$  fs OFF-ON-OFF response times, switching efficiencies close to 100 %,  $< 0.1$  pJ control light energies, and  $< 1$   $\mu\text{m}$  characteristic size. However, no known structure to date behaves as an ideal switch. One possible candidate to improve on the reported modulation performance is GaP. Compared to silicon, GaP presents negligible linear absorption and has larger Kerr nonlinear index ( $n_2$ ) and TPA coefficient ( $\beta$ ) over the whole of the visible and the blue end of the near-infrared spectrum [39, 100, 145]. Furthermore, it has been shown that bulk crystalline GaP can produce modulation depths as high as 70 % [39].

The following section studies the nonlinear and ultrafast dynamics of individual c-GaP nanostructures on  $\text{SiO}_2$  substrate by using nondegenerate pump-probe spectroscopy.

### 4.3.1 Nanodisks at the anapole excitation

Nanodisks made of MOCVD-grown crystalline GaP are patterned on a  $\text{SiO}_2(10\ \mu\text{m})/\text{sapphire}(150\ \mu\text{m})$  substrate through EBL (more information in the Experimental Details). The GaP nanodisks are of 200 nm in height and 500 to 700 nm in diameter (D), with a

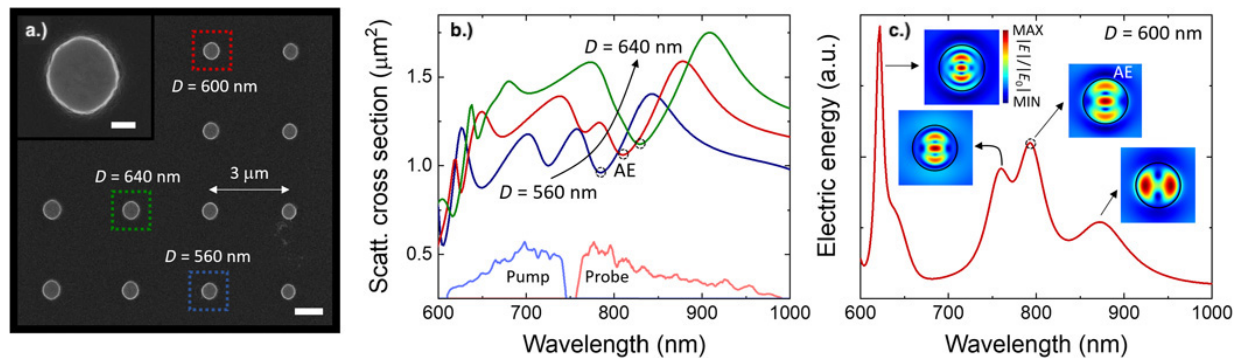


**Figure 4.21:** Design and linear simulations of GaP nanoantennas. **a.)** Scanning electron microscopy image of the fabricated sample. The inset shows a magnified view of a nanodisk of 600 nm diameter. Scale bars, 1 μm (main image) and 200 nm (inset). **b.)** Simulated scattering (Scatt.) cross section for disks of 560, 600, and 640 nm diameter. AE denotes the anapole excitation (encircled minima). In the bottom of the graph, the pump and probe spectra are displayed in arbitrary intensity units. **c.)** Calculated electric energy for the  $D = 600$  nm nanodisk, computed as  $W_E \propto \iiint dV |E|^2$ , with  $V$  denoting the volume of the nanoantenna. The simulated electric field distributions corresponding to the most prominent peaks are included at selected disk heights presenting maximum field accumulation. From lowest to highest wavelength, corresponding height values as measured from the substrate are 25, 70, 20, and 5 nm. a.u., arbitrary units.

center-to-center pitch of 3 μm to prevent optical coupling between adjacent structures (see a representative scanning electron microscopy image of the sample in Fig. 4.21a). To identify the resonances of the fabricated nanoantennas, we simulate their scattering cross section and internal electric energy using the FDTD method for linearly polarized illumination at normal incidence in the 600 to 1000 nm wavelength range. The linear refractive index data of MOCVD GaP used for the calculations are determined through spectral ellipsometry measurements. The obtained refractive index values are found to coincide with those from a commercial crystalline GaP wafer (see section 4.2, Fig. 4.13), within 2% [39]. It is worth mentioning that other common fabrication techniques for growing GaP on a substrate, such as radio frequency magnetron sputtering [146], can only produce the material in an amorphous phase, which does not exhibit negligible linear absorption or as high refractive index values as the case of the MOCVD crystalline GaP used in this section. Fig. 4.21b shows the simulated scattering cross section for the three disk diameters highlighted in Fig. 4.21a ( $D = 560, 600,$  and  $640$  nm), while Fig. 4.21c presents the computed electric energy and corresponding electric field distribution patterns for the case of  $D = 600$  nm (other diameters are shown in Fig. 4.23). It can be seen that there are multiple optical modes confining the field inside the disk, implying that volumetric nonlinear effects can be greatly enhanced over the wave-length region of interest.

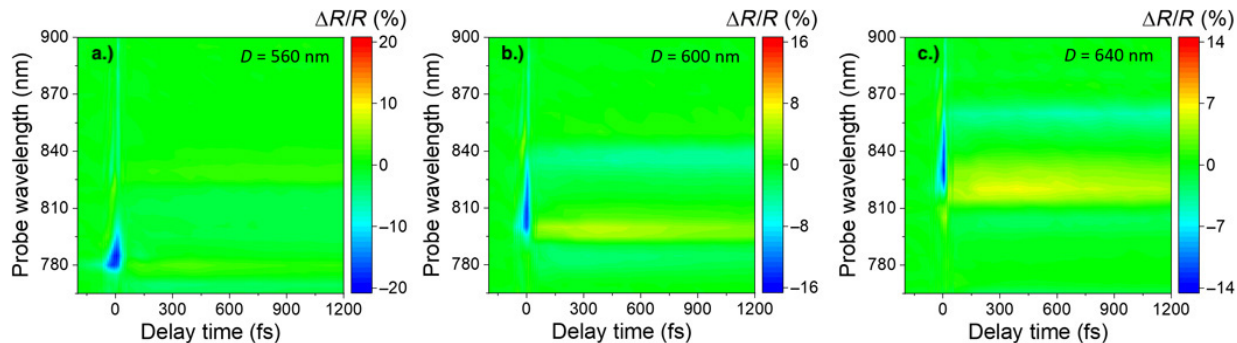


**Figure 4.22:** Pump-probe spectroscopy results of single GaP nanodisks. **a.) - c.)** Differential reflectivity spectra of individual nanoantennas of diameters  $D = 560$ ,  $600$ , and  $640$  nm, registered by pumping the sample at  $P = 10 \text{ pJ}/\mu\text{m}^2$ , with a  $5 : 1$  pump-probe fluence ratio.

### 4.3.2 All-optical switching with c-GaP nanodiscs

To characterize the nonlinear dynamics of the fabricated nanoantennas, we perform nondegenerate pump-probe spectroscopy measurements of individual nanodisks using sub-10 fs pulses. The spectral components of the pump and probe pulses covered the 600 to 750 nm and 750 to 1000 nm wavelength ranges, respectively, as shown in Fig. 4.21b (bottom). Fig. 4.22 shows the measured differential reflectivity ( $\Delta R/R$ ) response from three single nanoantennas as a function of probe wavelength ( $\lambda$ ) and pump-probe delay time ( $t$ ), at a pump peak energy density ( $P$ ) of  $10 \text{ pJ}/\mu\text{m}^2$  and a  $5:1$  pump-probe fluence ratio. A fixed reflectivity background introduced by the glass substrate surrounding the nanodisk scattering cross-sectional area is subtracted from the  $R$  data (see more in the Experimental Details). In the three cases in Fig. 4.22, a strong negative  $\Delta R/R$  signal is observed around  $t = 0$  fs, at wavelengths near minima in the scattering cross section and maxima in the electric energy (see Fig. 4.21, b and c, and Fig. 4.23), which we assign to the anapole excitation. As introduced in section 2.3.1, the anapole excitation is an optical state formed with leading contributions from the electric dipole and toroidal dipole modes and is characterized by a scattering minimum and an electric energy maximum, with a distinctive electric field pattern matching that in Fig. 4.21c [64, 68, 69, 147]. In Fig. 4.22, depending on the disk size, the  $\Delta R/R$  peak response varies between  $-14$  and  $-20\%$  and vanishes within a 100 fs time period. We attribute this nearly instantaneous effect to the nonlinear OKE and TPA, as will be discussed later in this section. At longer delay times, at wavelengths in the vicinity of the ultrafast signals, we find the presence of smaller and much slower  $\Delta R/R$  contributions. The effect is most evident in Fig. 4.21 (b and c) and only slightly noticed in Fig. 4.21a, where its magnitude is just about a tenth of the maximum response. Given the long time scale of these signals, which do not relax within the studied time window of 1.2 ps, we assign their origin to the relaxation of free carriers (FCs) [148], generated through TPA. We highlight, however, that near the center wavelengths of the ultrafast responses, no FC effects are detected, making it possible to

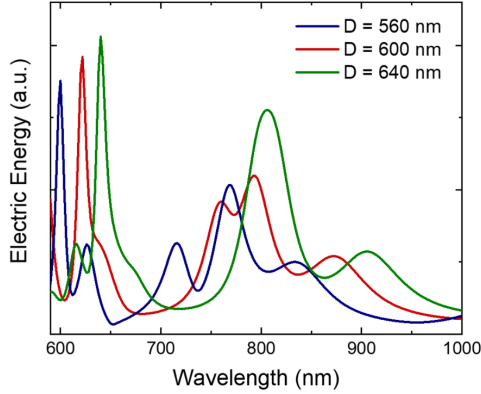
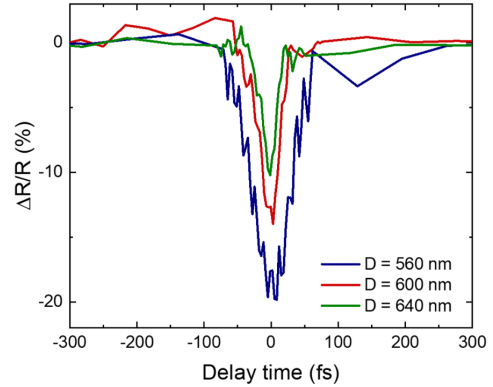


**Figure 4.23:** Simulated internal electric energy for  $D = 560$  nm,  $600$  nm and  $640$  nm. The red curve ( $D = 600$  nm) is the same as that shown in Fig. 4.21c.

**Figure 4.24:** Pump-probe temporal traces at  $P = 10$  pJ/ $\mu\text{m}^2$  for the three studied nanodisks. The data corresponding to the red curve ( $D = 600$  nm) is the same as that of the black triangles shown in Fig. 4.26b.



benefit from clean sub-100 fs modulations at specific wavelengths. To model the ultrafast behavior of the dielectric nanoantennas, we perform nonlinear simulations including the OKE and TPA, considering average degenerate nonlinear values of  $n_2 = 2 \times 10^{-18} \text{m}^2/\text{W}$  and  $\beta = 3 \text{ cm/GW}$  as determined for crystalline GaP in this wavelength range [39]. For the calculations, we approximate GaP complex refractive index as  $\tilde{n} = n_0 + ik_0 + I(n_2 + ik_2)$ , where  $n_0$  and  $k_0$  denote the low-intensity real and imaginary components of the refractive index, respectively (with  $k_0 = 0$  for GaP);  $I$  represents the intensity of the pump beam; and  $k_2$  is the nonlinear absorption, which relates to  $\beta$  through the equation  $k_2 = (\lambda\beta)/(4\pi)$ . In this way, the OKE and TPA enabled modifications of GaP reflectivity through changes in the real and imaginary parts of  $\tilde{n}$ , respectively. Fig.4.25 compares the experimental and simulated differential reflectivity signals at  $t = 0$  fs for the three studied nanodisks. Differences in the precise shape of the curves can be ascribed to simulations using constant average values of degenerate  $n_2$  and  $\beta$  instead of the non-degenerate nonlinear parameters actually involved in the measurement, which may vary depending on the pair of pump and probe wavelengths. A good agreement is nevertheless obtained, with calculations correctly describing peak wavelength, modulation sign, and approximate magnitude of the measured responses.

To determine the individual contributions of the different nonlinear effects to the total response, we perform a decomposition of the OKE and TPA on  $\Delta R/R$ , whose results are shown in the inset of Fig. 4.25b for the case of  $D = 600$  nm. The simulation reveals that

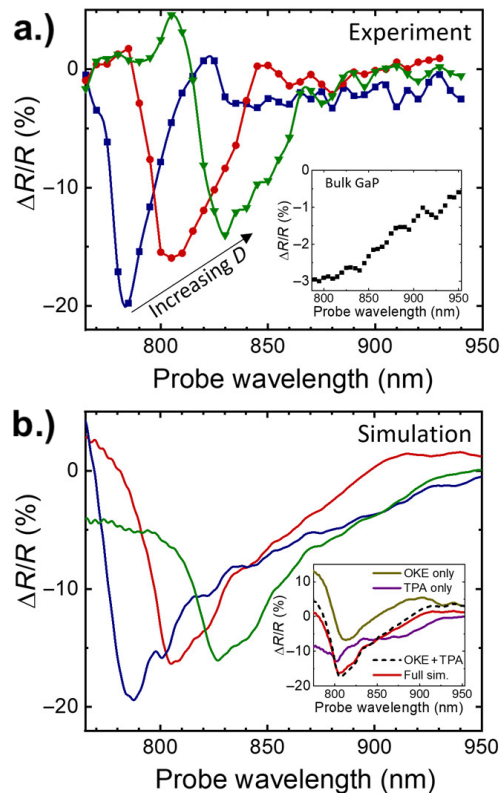


**Figure 4.25:** Experimental and simulated nonlinear responses. **a.)** Experimental and **b.)** simulated differential reflectivity response at  $t = 0$  fs and  $P = 10$  pJ/ $\mu\text{m}^2$  for  $D = 560$  nm (blue), 600 nm (red), and 640 nm (green). The inset of (A) shows the registered response from a commercial double-sided polished 350  $\mu\text{m}$ -thick GaP (100) wafer measured under the same experimental conditions. The inset of (B) exhibits the simulated response of the  $D = 600$  nm antenna when considering the OKE contribution only ( $n_2 = 2 \times 10^{-18}$  m<sup>2</sup>/W and  $\beta = 0$  cm/GW), the TPA contribution only ( $n_2 = 0$  m<sup>2</sup>/W and  $\beta = 3$  cm/GW), their direct sum, and the full simulation (sim.) ( $n_2 = 2 \times 10^{-18}$  m<sup>2</sup>/W and  $\beta = 3$  cm/GW). The latter matches the red curve in the main graph.

the OKE component, which increases the real part of  $\tilde{n}$  ( $n_2 > 0$ ), makes the anapole resonance more pronounced, decreasing  $R$  at anapole excitation wavelengths and increasing it at shorter and longer adjacent wavelengths. The TPA component, on the other hand, leads to a finite positive imaginary part of  $\tilde{n}$  ( $k_2 > 0, k_0 = 0$ ), lowering  $R$  at all wavelengths. Consequently, the combined response peaks at AE wavelengths, where both the OKE and TPA contribute with the same modulation sign. Their relative contribution is estimated to be approximately 40%/60% (OKE/TPA). It is worth mentioning here that the scattering and internal electric energy maxima at  $\sim 875$  nm for  $D = 600$  nm (Fig. 4.21, b and c) are found to produce no substantial effect in their corresponding  $\Delta R/R$  response in Fig. 4.25. The nonlinear decomposition in the inset of Fig. 4.25b reveals that such maxima give rise to positive and negative shoulders in the OKE- and TPA-only responses, respectively, leading to a nearly zero  $\Delta R/R$  net signal. This demonstrates that a scattering maximum is not nearly as efficient as a scattering minimum for producing OKE/TPA nonlinear reflectivity modulations. For reference, the inset of Fig. 4.25a exhibits the measured  $\Delta R/R$  signal at  $t = 0$  fs for bulk GaP, displaying a maximum modulation of 3%, in absolute value, which monotonically decreases with increasing probe wavelength. This effect is thought to be a consequence of GaP linear refractive index decreasing with increasing wavelength, combined with nondegenerate  $n_2$  and  $\beta$  diminishing for longer probe wavelengths. We note that this GaP intrinsic behavior is also present in the response from the nanoantennas, as nanodisks featuring resonances at longer wavelengths are found to present a weaker signal. An additional factor contributing to the smallest nanodisk presenting the strongest modu-

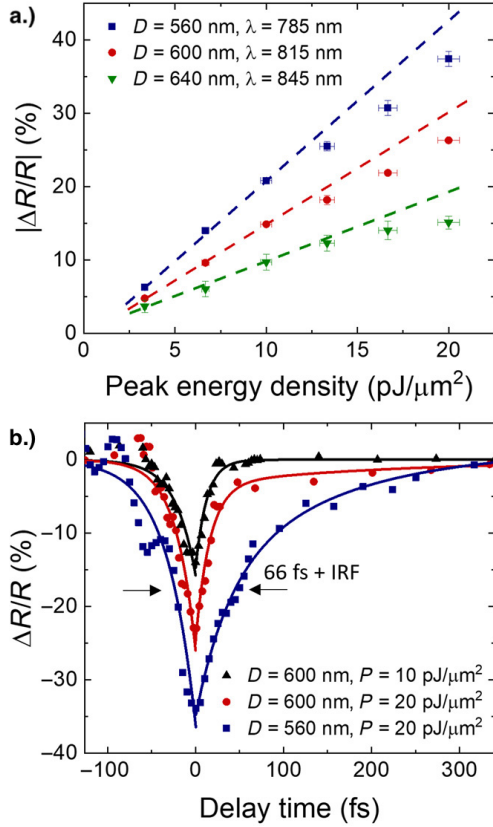


**Figure 4.26:** Modulation performance at different pump powers. **a.)** Pump peak energy density dependence of  $|\Delta R/R|$  at selected probe wavelengths for nanoantennas with  $D = 560$  nm ( $\lambda = 785$  nm),  $D = 600$  nm ( $\lambda = 815$  nm), and  $D = 640$  nm ( $\lambda = 845$  nm). **b.)** Corresponding temporal trace results at specific pump peak energy densities detailed in the graph for the two most efficient disks. Solid lines correspond to exponential fits to the experimental data. IRF, instrument response function.

lation response is its relatively narrow resonance bandwidth, which makes it most sensitive to pump-induced  $\tilde{n}$  changes.

To study the dependence of the magnitude of the ultrafast modulation signal on the pump peak energy density, we perform measurements of the three studied disks in the  $P$  range (0 to 20 pJ/ $\mu\text{m}^2$ ) at specific probe wavelengths exhibiting no FC effects ( $\lambda = 785$  nm for  $D = 560$  nm,  $\lambda = 815$  nm for  $D = 600$  nm, and  $\lambda = 845$  nm for  $D = 640$  nm, as extracted from Fig. 4.22). The results are shown in Fig. 4.26a, where an approximately linear behavior of  $|\Delta R/R|$  with  $P$  is found up to  $P = 10$  pJ/ $\mu\text{m}^2$  for all diameters. For  $P > 10$  pJ/ $\mu\text{m}^2$ , the signals start to saturate, reaching maximum  $|\Delta R/R|$  values of 37, 26, and 15% at 20 pJ/ $\mu\text{m}^2$  for  $D = 560, 600$  and 640 nm, respectively. In Fig. 4.26b, we evaluate the effect of the pump power on the time response of the modulation signals for selected cases. To determine characteristic times and modulation bandwidths, we perform fits to the data by convoluting exponential functions with the IRF, described by a Gaussian profile of 11 fs FWHM [39]. Black and red curves in Fig. 4.26b show results for  $D = 600$  nm at  $P = 10$  and 20 pJ/ $\mu\text{m}^2$ , respectively. At  $P = 10$  pJ/ $\mu\text{m}^2$ , we register a temporal FWHM ( $\tau_{FWHM}$ ) of 19 fs and a  $1/e^2$  modulation bandwidth ( $\nu_{MB}$ ) of 18 THz (see Fig. 4.24 for pump-probe temporal traces of other disk diameters at  $P = 10$  pJ/ $\mu\text{m}^2$ ). Corresponding values in the saturating range ( $P = 20$  pJ/ $\mu\text{m}^2$ ) are  $\tau_{FWHM} = 26$  fs and  $\nu_{MB} = 12$  THz. For  $D = 560$  nm (blue curve in Fig. 4.26b), we find an even longer  $\tau_{FWHM} = 66$  fs ( $\nu_{MB} = 5$  THz), which can be understood from the smaller spectral bandwidth of this resonance compared to

those of the other disks (see Figs. 4.22 and 4.22a). It should be noted that this performance represents a two orders of magnitude improvement with respect to previous reports on dielectric metasurfaces and nanoantennas for sub-100 fs all-optical switching [134, 142]. A direct-gap GaAs semiconductor metasurface demonstrated similar  $\Delta R/R$  values, around 40 %, but with the consequence of much longer characteristic modulation times of several picoseconds due to FC effects [148]. It should also be mentioned that the fastest reported plasmonic-based nanoscale approaches featuring 20 % modulation depth or more [41, 149] showed  $\tau_{FWHM}$  values about one order of magnitude larger compared to the GaP nanodisk.

### 4.3.3 Conclusion

In this section, we have demonstrated that resonant single GaP nanodisks with negligible linear absorption can produce  $1/e^2$  modulation bandwidths of 5, 12, and 18 THz, with approximate maximum modulation depths of 40, 25, and 15 %, respectively, depending on pump power, disk size, and probe wavelength. The observed sub-100 fs effect is modeled through nonlinear-induced variations of GaP complex refractive index due to the OKE and TPA, with a relative contribution of around 40%/60% (OKE/TPA). We find that the ultrafast response occurs in the vicinity of the AE scattering minimum, at wavelengths where TPA-induced FC effects are found to be negligible. We also find that modes featuring scattering maxima do not produce substantial differential reflectivity modulations, as they give rise to OKE and TPA signals with opposite responses. The findings from this investigation open new possibilities for the optimization of nonlinear all-optical modulators and place the GaP nanodisk as the most efficient nanoscale all-optical switch at sub-100 fs time scales demonstrated to date, to the best of our knowledge.

### 4.3.4 Experimental details and supplementary material

**Nanofabrication:** GaP nanodisks were fabricated on a SiO<sub>2</sub>-on-sapphire substrate, starting from a commercially available MOCVD-grown crystalline GaP layer ( $\sim 400$  nm) on a GaAs substrate. The latter structure was directly bonded to the sapphire substrate after depositing  $\sim 5$   $\mu$ m SiO<sub>2</sub> layers on top of both surfaces. The GaAs substrate was later removed by wet etching. The fabrication of the GaP nanodisks started with a standard wafer cleaning procedure (acetone, isopropyl alcohol, and deionized water in that sequence under sonication). The GaP layer was then thinned down to a thickness of 200 nm by ICP-RIE with N<sub>2</sub> and Cl<sub>2</sub> gases. The following step involved O<sub>2</sub> and hexamethyl disilazane (HMDS) priming to increase the adhesion between GaP and the subsequently spin-coated EBL resist of hydrogen silsesquioxane (HSQ). After spin-coating of the HSQ layer with a thickness of  $\sim 150$  nm, EBL and development in 25 % tetramethyl ammonium hydroxide (TMAH) were carried out to define the nanodisks in the HSQ resist. Last, ICP-RIE with N<sub>2</sub> and Cl<sub>2</sub> gases was used again to transfer the HSQ patterns to the GaP layer and generate the GaP nanodisk structures.

| system              | modulation depth | FWHM    | peak energy density     | ref.  |
|---------------------|------------------|---------|-------------------------|-------|
| c-GaP, $D = 640$ nm | 10 %             | 14 fs   | 10 pJ/ $\mu\text{m}^2$  | [122] |
| c-GaP, $D = 600$ nm | 15 %             | 19 fs   | 10 pJ/ $\mu\text{m}^2$  | [122] |
| c-GaP, $D = 600$ nm | 26 %             | 26 fs   | 20 pJ/ $\mu\text{m}^2$  | [122] |
| c-GaP, $D = 560$ nm | 37 %             | 66 fs   | 20 pJ/ $\mu\text{m}^2$  | [122] |
| Au-Si disc          | 0.3 %            | 8 fs    | 28 pJ/ $\mu\text{m}^2$  | [142] |
| Si metasurface      | 0.45 %           | < 65 fs | 0.4 pJ/ $\mu\text{m}^2$ | [134] |
| GaAs metasurface    | 46 %             | 4000 fs | 1.5 pJ/ $\mu\text{m}^2$ | [148] |
| ITO-Au metasurface, | 20 %             | 600 fs  | 6 pJ/ $\mu\text{m}^2$   | [41]  |
| ITO nanorods        | 55 %             | 500 fs  | 58 pJ/ $\mu\text{m}^2$  | [149] |

**Table 4.3:** All-optical ultrafast modulation performance of different nanoscale dielectric and plasmonic-based approaches at visible and near-infrared wavelengths. For the plasmonic cases [41, 149] only reports featuring 20 % modulation depth or more at sub-picosecond time scales are considered.

**Pump-probe experiments:** The measurements were performed with the setup that was introduced in 3.4. The SC light was generated by focusing the beam at 600 mW average power onto the sapphire plate (see spectra of pump and probe pulses in Fig. 4.21b). The pulses are compressed in time to bandwidth-limited  $\sim 7$  fs at the position of the sample. The two pulsed beams were focused onto the sample using a metal objective of 0.5 numerical aperture. The measurements were carried out with lock-in detection by modulating the pump beam at  $< 1$  kHz frequency using an optical chopper. The constant reflectivity background ( $RB$ ) produced by the glass substrate around the nanoantenna’s scattering cross-sectional region was subtracted from the measured  $R$  values.  $RB$  was calculated as the product  $RG*PG$ , where  $RG$  denotes glass reflectivity and  $PG$  represents the proportion of probe power illuminating the substrate surrounding the nanodisk scattering cross-sectional area.

**Numerical simulations:** The nonlinear numerical simulations were performed using Lumerical FDTD, with an instantaneous OKE and TPA implemented following the formalism of Suzuki [150]. The linearly polarized pulses were input via Gaussian focusing using a numerical aperture of 0.5 and with the focal position located at the mid-height of the nanodisks, in agreement with the experimental conditions. Perfectly matched layers were used as the simulation boundary conditions to avoid reflections. The experimental spectra for the pump-probe pulses (as seen in Fig. 4.21b) were imported into the FDTD simulations as custom sources, which resulted in ripples in the simulated differential reflectivity curves, which were removed by smoothing through adjacent averaging. It should be noted that replacing the custom sources by standard Gaussian spectra sources with the same temporal duration resulted in smoother differential reflectivity curves but gave poor agreement with the experimental results. More details on the implementation on the nonlinear simulations can be found in ref. [39]. Ellipsometry measurements were used to determine

the linear optical properties of MOCVD GaP, with the software built-in optical properties used for the SiO<sub>2</sub> substrate. The nonlinear parameters of GaP of  $n_2 = 2 \times 10^{-18} \text{m}^2/\text{W}$  and  $\beta = 3 \text{ cm}/\text{GW}$  were used in agreement with the results from a previous work [39], with the input pump and probe powers matched to the experimental conditions. No nonlinear effects were assumed for the underlying SiO<sub>2</sub> substrate. For the linear simulations depicted in Fig. 4.21, the nanodisks were illuminated by broadband linearly polarized plane waves at normal incidence. The electric energy inside the GaP nanodisk was calculated using monitors placed around the nanodisk to define the volume  $V$ .



# Chapter 5

## Nanofilms of the Weyl semimetal niobium phosphide

This work is published in [151]:

Benjamin Tilmann, Avanindra Kumar Pandeya, Gustavo Grinblat, Leonardo de S. Menezes, Yi Li, Chandra Shekhar, Claudia Felser, Stuart S. P. Parkin, Amilcar Bedoya-Pinto, and Stefan A. Maier

*”Ultrafast Sub-100 fs All-Optical Modulation and Efficient Third-Harmonic Generation in Weyl Semimetal Niobium Phosphide Thin Films”*

Advanced Materials 34(15), 2106733 (2022), DOI: 10.1002/adma.202106733

permission for reprint is granted under the Creative Commons CC BY 4.0 license

After the previous chapter that thoroughly discussed the optical properties of a well-known material, in the following a recently discovered member from the group of Weyl semimetals (WSM) is addressed. As previously introduced in section 2.2, WSMs are materials with a single touching point of valence and conduction band in the electronic band structure together with a linear electron dispersion. In addition to the phenomena that were discussed earlier, WSMs exhibit a row of outstanding optical properties that have been thoroughly investigated. It was shown that the second-order susceptibility of tantalum arsenide (TaAs) is two orders of magnitude larger than for high refractive index non-centrosymmetric dielectrics [152], an efficient nonlinear photocurrent generation was also demonstrated [153], the near infrared glass-coefficient was found to be the strongest so far reported [154] and efficient catalytic activity was observed for the hydrogen evolution reaction [155]. So far, experimental reports were limited to bulk [156,157] or micro structuring of the bulk crystal [154,158,159], representing a natural restriction to the development of on-chip applications.

In the following chapter, the linear and nonlinear optical response of recently reported epitaxially grown thin films [160,161] of the prototypical type-I WSM niobium phosphide (NbP) are investigated and compared to the performance of the bulk single crystal [57].

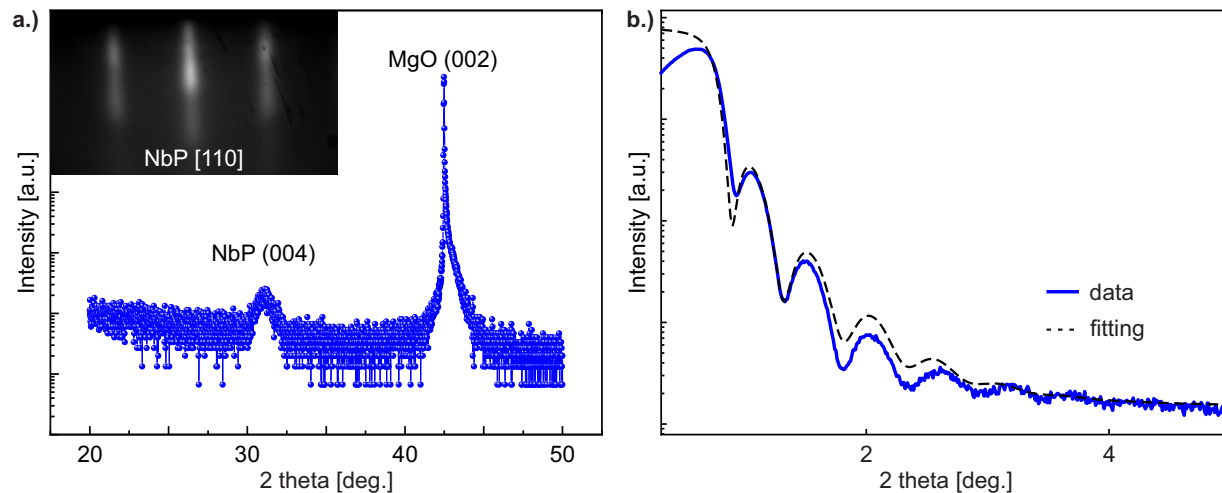


**Figure 5.1:** a.) XRD pattern of the NbP film, with the (004) peak of NbP and the (002) peak of the MgO substrate indicated. Inset: In situ RHEED pattern of NbP, along the [110] direction. b.) XRR measurement of the NbP film with the corresponding fit indicated by the dashed line.

## 5.1 Fabrication of niobium phosphide thin films

NbP (100) thin films are grown by molecular-beam epitaxy along the [100]-direction of atomically flat MgO substrates [162]. To compensate for the MgO-NbP lattice mismatch, a Nb seed layer is grown with an in-plane rotation of  $45^\circ$  to the MgO substrate and phosphorized prior to the epitaxial growth of NbP (001). The layer growth is monitored in-situ via RHEED at all stages. Fig. 5.1a shows the XRD pattern of the NbP thin film used in this chapter, which displays only the MgO substrate (002) and the NbP film (004) peak, demonstrating that the NbP film grows in a single crystalline fashion along the [001] direction, corresponding to the  $c$ -axis of the  $I4_1md$  crystal structure of NbP. Streaky RHEED patterns along the in-plane directions are observed on this sample, indicating layer by layer growth, as exemplified in the inset of Fig. 5.1a. Furthermore, the presence of X-ray reflectivity (XRR) oscillations (Fig. 5.1b) confirm the structural long-range order and low roughness of the film. A numerical fit to the oscillations results in a thickness of 16 nm. In order to obtain the dielectric function and therefore the optical constants  $n(\omega), k(\omega)$  of the NbP thin film, we perform spectral ellipsometry measurements. To maintain Kramers-Kronig consistency and extract the real and imaginary parts of the dielectric function  $\epsilon_1(\omega)$  and  $\epsilon_2(\omega)$ , respectively, (Fig. 5.2a) a numerical model is fitted to the ellipsometry data, considering Drude conductivity in the near infrared [163, 164] and Lorentz curves in the visible regime. In contrast to common noble metals [139], the real part  $\epsilon_1(\omega)$  is positive over the entire measured range and grows towards longer wavelengths. Only at the short wavelength limit around 300 nm, the sign changes, corroborating theoretical calculations [165]. At the same time, the imaginary part  $\epsilon_2(\omega)$  is dominant and one order of magnitude larger than for most noble metals in the same spectral regime [139] and

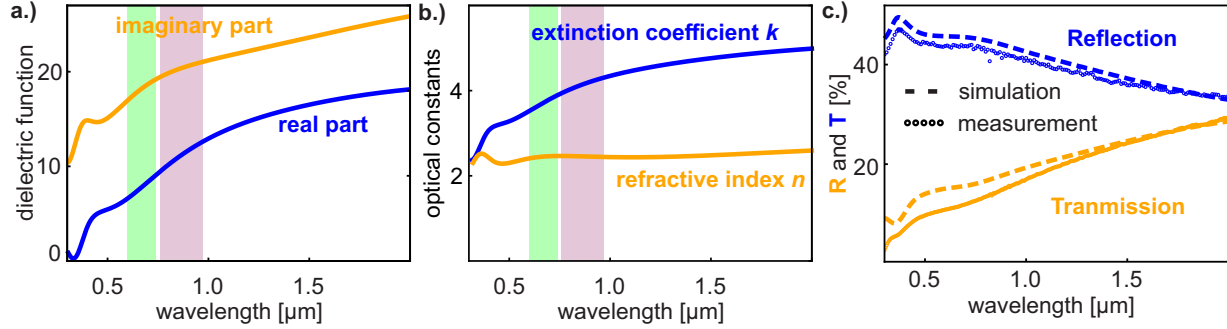


**Figure 5.2:** **a.)** Real (blue) and imaginary (orange) part  $\epsilon_1(\omega)$  and  $\epsilon_2(\omega)$ , respectively, of the dielectric function of NbP as determined by spectral ellipsometry. The shaded backgrounds indicate the spectral regime of the visible (green) and infrared (purple) beam of the pump-probe experiments. **b.)** Refractive index  $n$  and extinction coefficient  $k$  as determined by spectral ellipsometry. The shaded background represents the spectral position of the visible (green) and infrared (salmon) beam of the pump-probe experiments, respectively. **c.)** Transmission (orange) and reflection (blue) measurements of a NbP film at normal incidence with the respective results from FDTD simulations (dashed lines).

underlines the semimetallic character of NbP. It should be noted that an out-of-plane anisotropy found in the theoretical calculations was not observed here [166]. Most likely, the small thickness of the film prevents significant signs of the anisotropy to appear in the ellipsometry data. Using the relations  $\epsilon_1 = n^2 - k^2$  and  $\epsilon_2 = 2nk$ , the dielectric function can be converted to the refractive index  $n(\omega)$  and the extinction coefficient  $k(\omega)$ , as shown in Fig. 5.2b. Remarkably, the refractive index stays nearly constant over the spectrum with slightly anomalous dispersion ( $dn/d\lambda > 0$ ), while the extinction coefficient shows a peak around 350 nm and monotonically grows for increasing wavelengths. The values of the optical constants are further confirmed by transmission (orange) and reflection (blue) measurements that are shown in Fig. 5.2c. The high refractive index combined with the strong linear absorption leads to a maximum transmission of only 30 % and a reflection that stays below 50 %. The measurement is modeled by FDTD simulations that reproduce the achieved data with good agreement (see dashed lines in Fig. 5.2c).

## 5.2 Third-harmonic generation boosted by topological surface states

Next, the third-order nonlinear optical response of the NbP film is further investigated. Following the introduction in section 2.4, THG is described by the nonlinear susceptibility  $\chi^{(3)}(3\omega_0)$  and corresponds to the conversion of three incident photons of frequency  $\omega_0$  into a single higher energy photon with three times the original frequency  $\omega_{THG} = 3\omega_0$ , or equivalently  $\lambda_{THG} = 1/3\lambda_0$  [24, 70, 167]. Consequently, Fig. 5.3a shows respective THG spectra for fundamental wavelengths ranging from 1400 – 1950 nm, located at the respec-

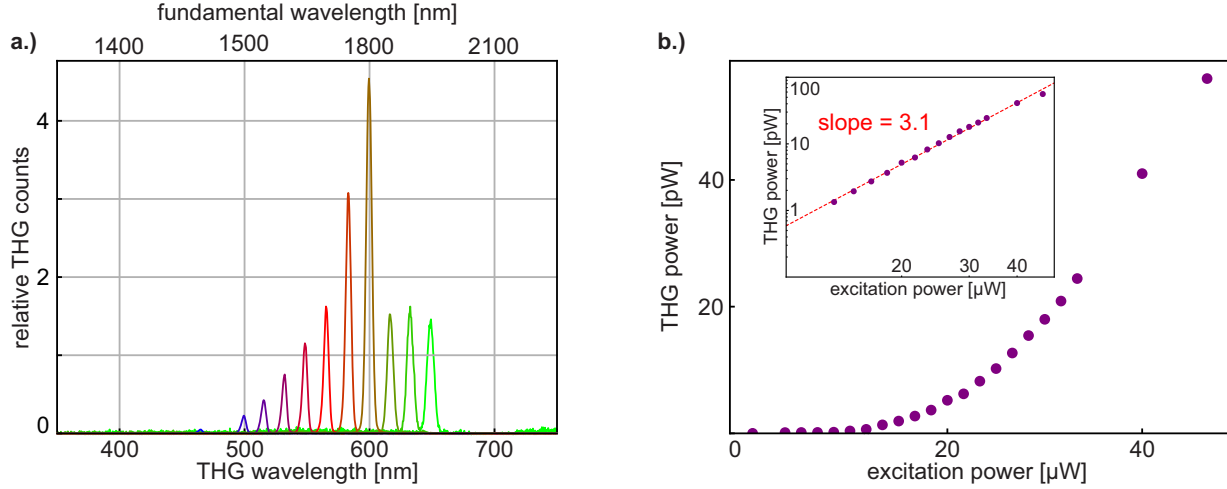


**Figure 5.3:** a.) Relative THG spectra of the NbP thin film for different fundamental wavelengths ranging from 1400 – 1950 nm. b.) Power dependence of the measured THG signal on the excitation power. The inset shows the same data on double logarithmic scale. A linear fit is shown by the dashed line, giving a slope of 3.1.

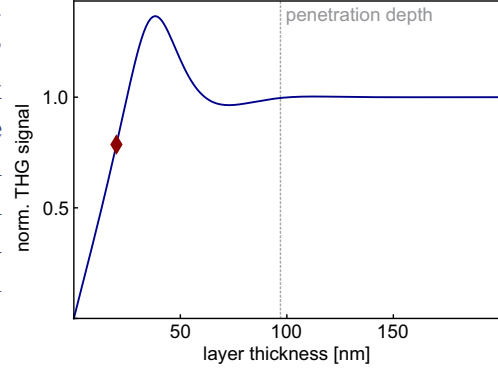
tive third-harmonic wavelengths. Furthermore, in a power dependent measurement in Fig. 5.3b, the THG power clearly scales nonlinear with the excitation power. The inset shows a linear fit on a double-logarithmic scale, resulting in a slope close to three what proves the third-order nature of the observed signal. The efficiency of the THG efficiency can be estimated by directly measuring the reflected THG power with strong filtering of the fundamental beam, which results in  $\eta_{refl} = P_{THG}/P_{FW} \sim 6 \cdot 10^{-5} \%$ . Taking that a comparable amount of THG signal is emitted in the opposite half space, the efficiency can be assumed to be at least a factor of two stronger. Including the fact that THG light is only partially collected by the finite NA of the objective (NA = 0.9), a lower bound for the efficiency of the NbP thin film can be given to be  $\eta_{THG} \simeq 10^{-4} \%$ , notably more than one order of magnitude larger than for the bulk crystal measured under identical conditions, three orders of magnitude larger than that of a germanium thin film, and only one to two orders of magnitude smaller compared to resonant germanium nanostructures [69, 141].

Based on the theory from Bloembergen et al. [168], we calculate the reflected THG signal, assuming only in-plane  $\chi^{(3)}$  components and normal incidence. Following comparable calculations for graphene [169], the reflected THG field can be expressed as

$$E_{3\omega} = \frac{4\pi P_{NL}}{n_{3\omega}^2 - n_{\omega}^2} \frac{a(n_{MgO} - n_{\omega}) - b(n_{\omega}n_{MgO} - n_{3\omega}^2)}{e^{2i\varphi_h}(1 - n_{3\omega})(n_{MgO} - n_{3\omega}) - (1 + n_{3\omega})(n_{MgO} + n_{3\omega})} \quad (5.1)$$

With the angular frequency  $\omega$  the complex refractive index of NbP  $n_{\omega}, n_{3\omega}$  at fundamental and third-harmonic frequency, respectively, the refractive index of MgO ( $n_{MgO}$ ) at the third-harmonic frequency.  $P_{NL} = \chi^{(3)}E_{\omega}^3$  represents the nonlinear polarization and was assumed to be constant for the calculation of the following thickness dependence. The factors  $a = 1 + e^{2i\varphi_h} + 2e^{i(\varphi_h - \varphi_i)}$  and  $b = 1 - e^{2i\varphi_i}$  include the phase corrections for the

**Figure 5.4:** Theoretically calculated thickness dependence of the THG signal, reflected from a NbP film. The signal is normalized to the value of a bulk crystal ( $H > 200$  nm). The red diamond marks the thickness of the film thickness, discussed in the main text. The calculation results in an optimal film thickness for THG of around 40 nm. The dashed line shows the penetration depth calculated from the measured extinction coefficient.



inhomogeneous  $\varphi_i = 2n_\omega\omega H/c$  and homogeneous  $\varphi_h = 3n_{3\omega}\omega H/c$  waves and therefore introduce a dependence of the film thickness  $H$ , shown in Fig. 5.4. It should be noted that once the penetration depth of the NbP film is reached, the measured THG signal saturates as electric fields don't reach further into the material and consequently do not reach the NbP-MgO interface. Therefore, we take the convergence value of the THG signal as estimation for bulk NbP.

To understand the origin of the measured THG, we investigate the signal in dependence on the fundamental beam polarization, shown in Fig. 5.5a,b, for 1400 and 1800 nm excitation wavelengths, respectively. Evidently, at 1400 nm the THG signal clearly peaks when the incident electric field is aligned with the b-axis of the crystal, while at 1800 nm it appears as almost polarization independent with a small dip at the a-axis. The  $I4_1md$  crystal structure of NbP corresponds to the  $4mm$  symmetry group. Therefore, the spatial symmetries reduce the originally 81 elements of the nonlinear susceptibility  $\chi^{(3)}$  to only 21 nonzero elements, namely [24]:

$$\begin{aligned} xxx &= yyy, zzz \\ yyz &= xxz, yzy = xzx, xxy = yyx \\ zzy &= zxx, yxy = xzx, xyy = yxy \\ zyz &= xxz, zzy = zxx, xyx = yxy \end{aligned}$$

Using the fact that the experimental conditions imply that the incident electric field lies in the xy-plane, it is sufficient to consider the components, where the z-component of the electric field does not appear ( $E_z = 0$ ). Further simplification can be achieved by defining  $\chi_{diag} = \chi_{xxx} = \chi_{yyy}$  and  $\chi_{mixed} = \chi_{xxy} + \chi_{xyx} + \chi_{yyz} + \chi_{yyx} = \chi_{yyz} + \chi_{yxy} + \chi_{yxy}$  to represent the diagonal and mixed components of the susceptibility, respectively. Together, this leads to a third-polarization of the form

$$\vec{P}^{(3)} \propto \chi_{diag} \begin{pmatrix} E_x^3 \\ E_y^3 \\ 0 \end{pmatrix} + \chi_{mixed} \begin{pmatrix} E_x E_y^2 \\ E_x^2 E_y \\ 0 \end{pmatrix}$$

Interestingly, this nonlinear polarization can only generate THG with a fourfold polariza-

**Figure 5.5:** Polarization dependence of the THG signal at a.) 1400 nm and b.) 1800 nm. The solid line represents a fit of the non-linear tensor elements to the data.

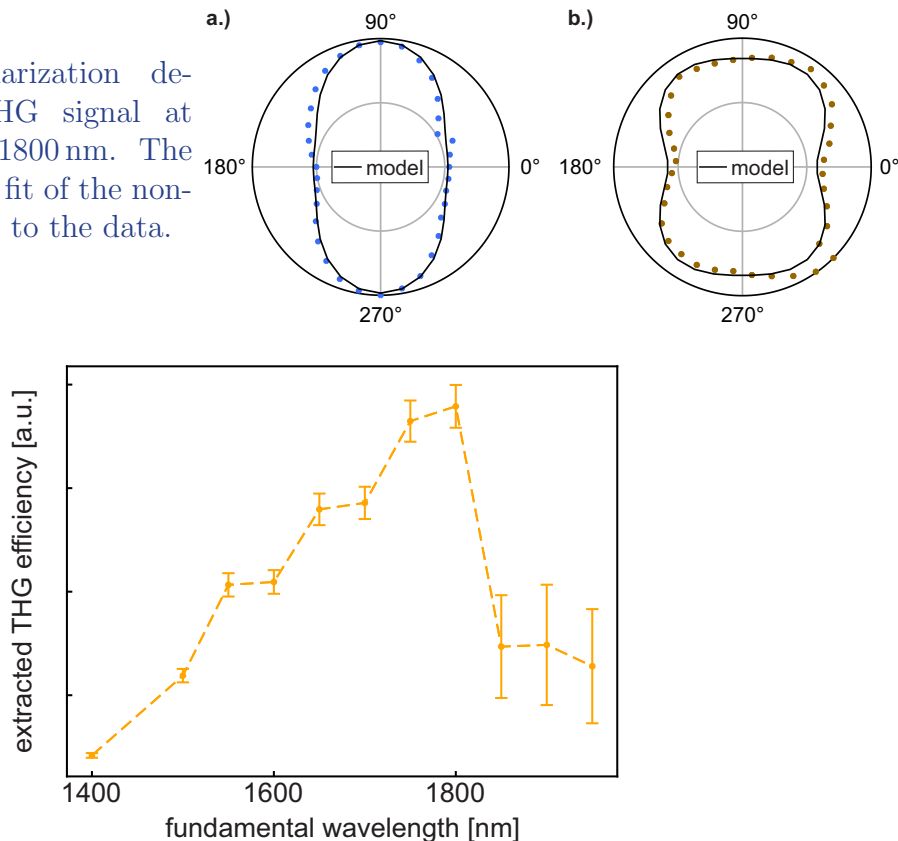


**Figure 5.6:** Extracted relative THG efficiency for the NbP thin film at excitation wavelengths from 1400 – 1950 nm. The error bar is estimated from the uncertainty of the power measurement.

tion pattern [24, 70], contrarily to the measurements shown in Fig.5.5a,b. However, at the surface of the material, the symmetry of the structure reduces to a  $C_{2v}$ -symmetry [170,171] that allows twofold polarization patterns, indicating that the observed THG is mostly generated by the surface states of NbP. A fitting of the surface nonzero tensor elements are shown by solid lines in Fig. 5.5a,b, giving a good agreement with the experimental data. As it was recently shown that the surface states in identically fabricated NbP thin films are almost exclusively topological, due to a suppression of the trivial surface states via atomic engineering [162], we attribute the high observed efficiency to the topological surface states of NbP, in particular as they were shown to generate extremely high signal in other topological materials [172]. Fig. 5.6 shows the relative THG efficiency over the excitation wavelength range from 1400 – 1950 nm with a clear peak  $\simeq 1800$  nm. A comparison with calculations of the band structure of NbP [160,162] indicates that the small plateau in the conduction band, located at the  $\Gamma$ -point of the Brillouin zone is responsible for this resonance. Here the energy difference of valence and conduction bands equals the energy of the third-harmonic photon, enhancing the third-order NL process with two virtual electron states. A comparison with the performance of the bulk NbP crystal shows

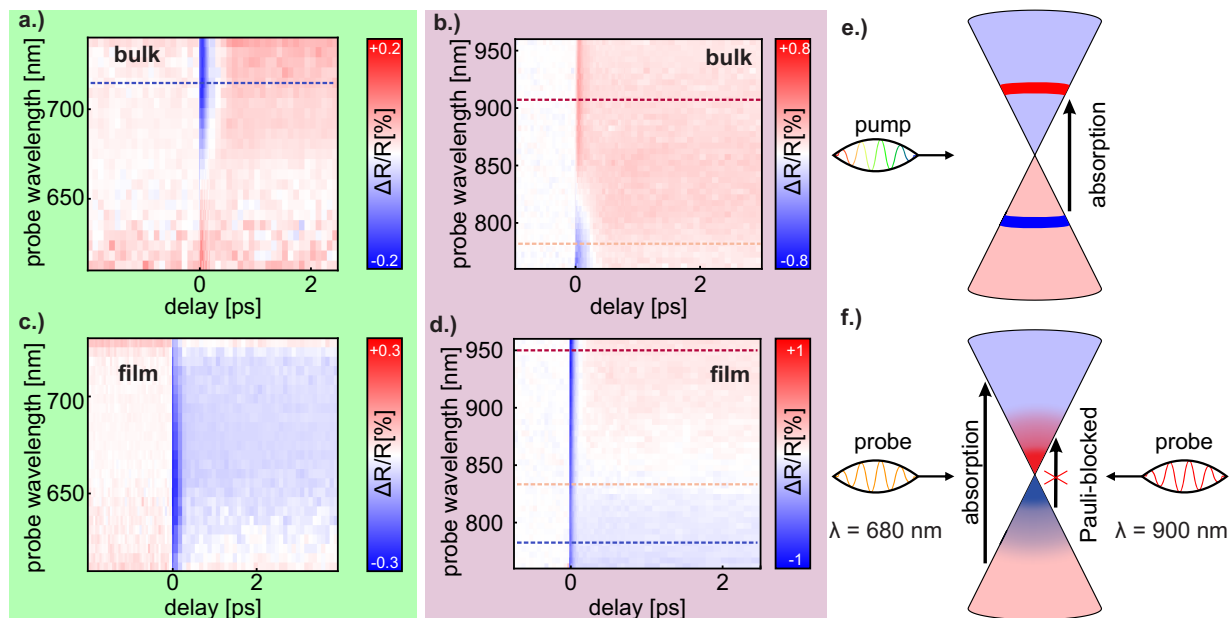


**Figure 5.7:** a.)-d.) Ultrafast pump-probe reflective spectroscopy of the bulk NbP crystal (a.-b.) and the thin film (c.-d.). The shaded background indicates the IR pulse (green) or visible pulse (purple) acting as pump beam, respectively. The dashed lines indicate the probe wavelength shown in Fig. 5.8a,b. e.) - f.) Sketch of the electron dynamics in the Weyl cone at the arrival of the pump pulse ( $t = 0$  fs) (e.) and at the arrival of the probe pulse ( $t > 0$  fs) (f.).

that the THG has a comparable behavior, but the resonant increase is not as large as for the thin film. This is not surprising since the latter is fully penetrated by the incident light, making it therefore possible to interact with the topological surface states at the top and the bottom of the film. Finally, it should be noted that due to the growth direction and the geometry of the experimental setup, the NbP film is illuminated along the polar  $c$ -axis of the crystal where it appears centrosymmetric and consequently the previously reported efficient second-harmonic generation could not be observed [152, 173].

### 5.3 Ultrafast optical response influenced by the Weyl cone

Next, the the ultrafast optical response of the NbP films is investigated using nondegenerate pump-probe spectroscopy with sub-10 fs pulses in the 600 – 1000 nm wavelength range, based on the setup from section 2.5.3. Dichroic beam splitters are used to divide the broadband beam into two beams of separate spectral components, the visible (600–750 nm) and infrared (750 – 1000 nm), which can act as pump and probe pulses interchangeably, while a motorized stage allows to tune the optical delay between them. The resulting

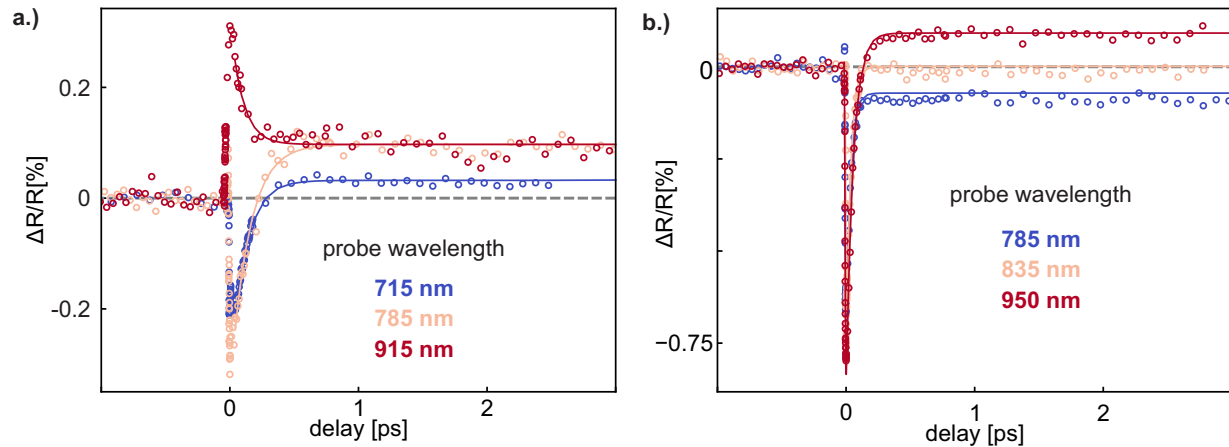


**Figure 5.8:** a.) Single time traces for the bulk NbP crystal at 715 (blue), 785 (beige), and 915 nm (dark red) probe wavelengths, respectively. The solid lines represent a fit of an exponential decay function to the slow decaying part of the signal. b.) Time traces of the NbP thin film at 785 (blue), 835 (beige), and 950 nm (dark red) probe wavelengths, respectively. The solid lines represent fittings of an exponential decay function, convoluted with the instrument response function of the system.

differential reflectivity spectrum of the bulk (top graphs) and thin film (bottom graphs) are shown in Fig. 5.7a-d for both pump/probe configurations. To understand the observed response, the electronic behavior in the Weyl cone is sketched in Fig. 5.7e,f, following previous reports on ultrafast dynamics in WSMs [156, 157, 174] and graphene [46, 175]. Starting from the intrinsic band structure, electrons absorb the incident pump photons and get promoted into the conduction band (Fig. 5.7e). Via electron-electron (fast) and electron-phonon (slow) scattering, the excited electrons relax to lower energy states. As the density of states highly reduces toward the Weyl node, the relaxing electrons accumulate and delay the recombination process, leading to the formation of electron and hole seas above and below the Weyl node, respectively. Then, when the probe photons arrive, the optical response depends on whether their energies are high enough to excite electrons above the occupied states in the valence band (Fig. 5.7f). Due to the lower energy of photons in the infrared beam, this is the case when probing with the visible beam and the arriving probe photons experience an increased absorption and thus a negative change of the reflectivity is observed (Fig. 5.7a). This is not the case, however, when pumping the bulk crystal with the visible and probing with the lower energy infrared beam (Fig. 5.7b). Here, photons in the high energy part of the probe beam (760 – 820 nm) are still absorbed by electrons and the change in reflectivity is negative but grows toward higher wavelengths. On the other hand, for wavelengths longer than 850 nm, the energy of the photons is no longer sufficient to excite valence electrons to available states and optical absorption is therefore Pauli blocked. As a consequence, the relative change of reflectivity becomes positive as the absorption of the materials gets reduced. In the intermediate regime  $\simeq 830$  nm, a mixture of both situations is present that leads to a vanishing change

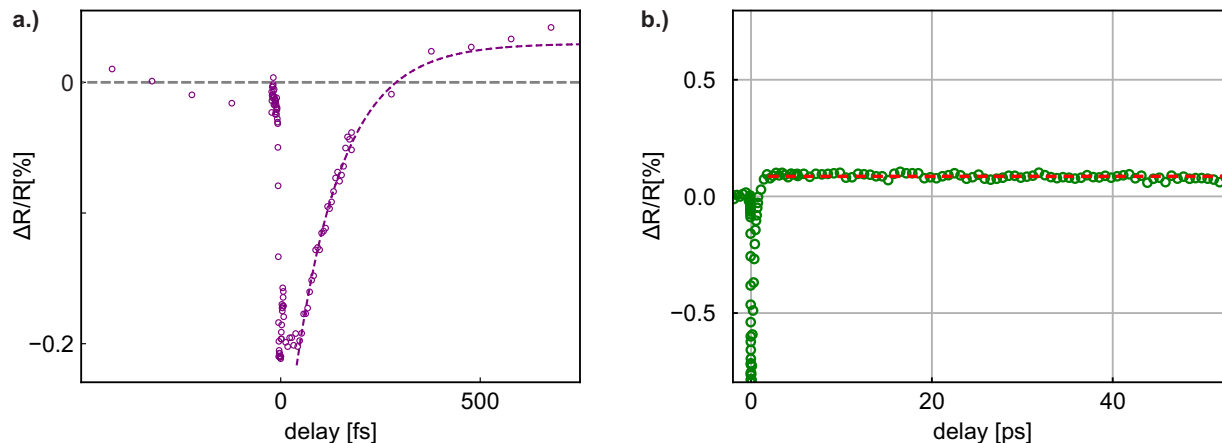


**Figure 5.9:** a.) Zoom into the first hundreds of femtoseconds at the pump-probe trace at 715 nm probe wavelength of the bulk NbP crystal, shown in the main text. The dashed line represents a fitting to an exponential decay function. b.) Long time scale trace for the NbP thin film at 950 nm probe wavelength, covering 50 ps after the overlap at  $t = 0$  fs. The red dashed line represent a horizontal line as guide for the eye.

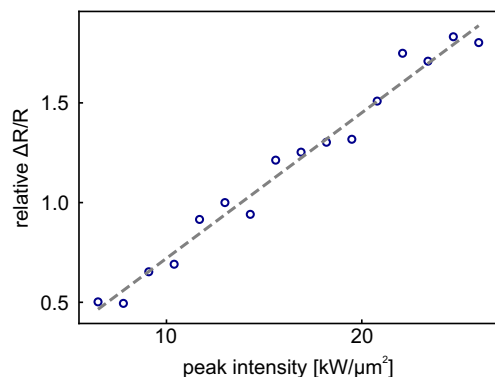
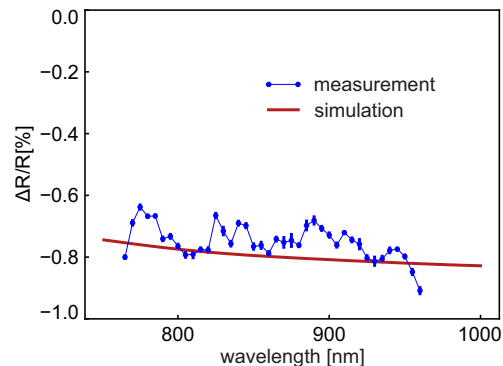


**Figure 5.10:** Power dependence of the measured maximum change in reflectivity, measured with the NbP thin film at 825 nm probe wavelength. A clearly linear trend without saturation effects is clearly visible. The dashed line represents a guide for the eye. Average beam intensities were calculated from the known laser parameters and the assumption of diffraction limited beam spots.

in reflectivity.

Recent theoretical calculations of WSMs in ultrafast laser fields [176] predicted that the fast electron-electron scattering toward the Weyl node happens in the first 10 fs after the pump pulse arrives. Even though this is at the limit of the temporal resolution of the experimental setup, we attribute the sharp peak at the temporal overlap in Fig. 5.7a,b to this ultrafast relaxation, visible in the single traces at selected 715 and 785 nm probe wavelengths in Fig. 5.8a. A zoomed-in image of the first 500 fs is shown in Fig. 5.9a. After the initial  $\sim 19$  fs peak, a slower decay is observed, which can be fitted by an exponential decay function and can be fitted to the measured data resulting in 30, 97, and 97 fs for a probe wavelength of 715, 785, and 915 nm, respectively, as shown in Fig. 5.8a. This is at the same scale as previously reported values for NbP crystals [156] or 2D graphene layers and comparable materials [175, 177–179]. A very slow response with  $> 100$  ps characteristic decay time is found afterwards (see Fig. 5.9b), which is attributed to phonon-phonon scattering and is therefore present for all probe wavelengths. The measured change of

**Figure 5.11:** Linear simulation of the relative reflectivity from the NbP film, assuming a change in the complex refractive index by 0.02. The corresponding measurement from the main text is shown in blue.



reflectivity for the NbP thin film, shown in Fig. 5.7c,d, markedly differs from the response of the bulk crystal. In particular at the temporal overlap, the sign of the modulation is negative for all probe wavelengths. When pumping with the infrared beam while probing with the visible beam (Fig. 5.7c), the behavior of the film is comparable to that of the bulk crystal and therefore gives a response with the same sign and comparable magnitude. This can be attributed to the higher extinction coefficient in the pump wavelength regime and therefore ultrafast dynamics that are dominated by linear absorption, similar to the bulk case. On the other hand, when pumping with the visible beam (Fig. 5.7d), the shape of the modulation differs fundamentally. The maximum change of reflectivity has a constantly negative sign and lacks a significant spectral dependence on the probe wavelength and completely decays within 100 fs.

Moreover, a power dependence of the modulation depth (Fig. 5.10) shows a clear linear scaling with increasing pump intensity. This indicates that the change in reflectivity is caused by a pump-induced change of the refractive index that was defined in section 2.4.2,  $\tilde{n}(I_{pump}) = \tilde{n}_0 + n'I_{pump}$ . Here,  $n_0$  indicates the complex linear refractive index while the nonlinear coefficient  $n'$  encompasses the effective nonlinear refractive index  $n_2$  and the two-photon absorption coefficient  $\beta$ . The first corresponds to a change of the real part of the refractive index, while the latter represents a change of the imaginary part. Even though both processes are third-order nonlinear effects, the high peak electric field strengths and the high third-order susceptibility of NbP as revealed by the pronounced THG efficiency lead to the observed modulation. Simulations shown in Fig. 5.11 show with good agreement that the observed modulation corresponds to a homogeneous change of the complex refractive index by roughly 5%.

For three representative probe wavelengths, single temporal traces are shown in Fig. 5.8b, including exponential decay functions convoluted with the IRF of the system that are fitted to the measured data. The resulting time constants of 32, 33, and 55 fs for 785, 835, and 950 nm probe wavelengths, respectively, evidence the ultrafast nature of the measured modulation. The fact that these values are in the same range as reported for all-optical modulations in dielectric materials [39, 118, 122] further corroborates the nonlinear nature of the observed signal. We explain the difference between the electronically dominated dynamics in the bulk crystal and the nonlinear optical modulation in the thin film with the fact that even though both have the same nonlinear properties, linear absorption in the

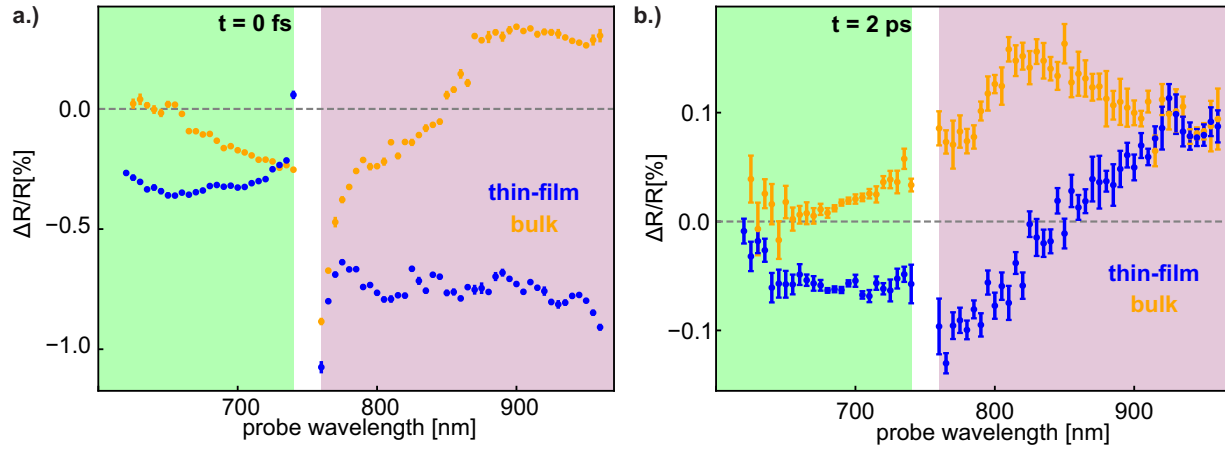


**Figure 5.12:** a.) Maximum relative change of reflectivity at the overlap of pump and probe pulse ( $t = 0$  fs) for the NbP thin film (blue) and bulk crystal (orange). b.) Relative change of reflectivity after the ultrafast relaxation ( $t = 2$  ps) for the NbP thin film (blue) and bulk crystal (orange). The shaded backgrounds indicate the visible (green) or infrared (purple) beam acting as the pump, respectively.

bulk crystal is too dominant and therefore limits direct pump and probe pulse interactions necessary for all-optical modulations. Comparing the maximum change in reflectivity of  $-0.8\%$  for the NbP film shows this is in the same range as reported values for 2D perovskite nanosheets [141] and amorphous gallium phosphide thin films [118].

A better representation of the detected sign change is shown in Fig. 5.12, where the modulation at the temporal overlap ( $t = 0$  fs) for each probe wavelength is displayed. Two sign changes can be observed here, whereas the one of bulk NbP was already discussed (Fig. 5.12a). The second can be observed for the thin film, where at long timescales a negative to positive sign change is found when increasing the probe wavelength, as noticeable in Fig. 5.12b at a fixed 2 ps delay time. The modulation is negative for wavelengths shorter than 850 nm and becomes positive for longer wavelengths, while completely vanishing in between. As the wavelength of the sign change is close to the corresponding value for the bulk crystal at the temporal overlap (Fig. 5.12a), we attribute this slow response again to the carrier dynamics in the Weyl cone. Since the pump beam travels through the entire thin film (which consists of only 15-20 unit cells [160]), the number of available states around the illuminated spot is significantly reduced compared to the bulk crystal. Therefore, the relaxation process of the electrons is further delayed and the electron accumulation above the Weyl node is still visible after 2 ps. This indicates that when probing with a wavelength of 850 nm, the beam exhibits a strong optical modulation from the pump beam and the nature of the Weyl cone prevents linear absorption effects. Therefore, the ultrafast signal completely decays in less than 100 fs, lacking a slow residual component. This suggests that further engineering would allow (nano) devices based on NbP with all-optical switching bandwidths of up to 10 THz, outperforming other systems such as indium tin oxide (ITO) at the epsilon near-zero wavelength by almost one order of magnitude [40, 41, 149]. Even

for the other probe wavelength in the infrared pulse, the ratio between the peak ultrafast modulation and the slow relaxing tail is large enough to obtain clear on- and off-states, emphasizing NbP as a promising material for all optical switching. It should further be noted that the slow response far from the sign change region appear temporally almost constant, even for longer timescale measurements (see Fig. 5.9). This indicates long electronic lifetimes in the nanosecond time range and could be a promising property for light harvesting or detection applications.

## 5.4 Conclusion

In conclusion, we have investigated the linear and third-order NL optical properties of a NbP thin film with a bulk single crystal as reference. Even though the imaginary part of the linear dielectric function was measured to be dominant over the studied spectral range, we detected strong THG from the thin film, exceeding the efficiency of the bulk material by more than a factor of 12. Moreover, a clear contrast in the response of the two samples was found through ultrafast differential reflectivity measurements. We observed the electron dynamics change from an optical absorption dominated response in the bulk crystal to a optical nonlinear regime in the thin film, enabling sub-100 fs reflectivity modulations at wavelengths close to 850 nm. The work in this chapter strengthens the potential of WSM thin films as promising material platforms with possible applications in the fields of nanophotonics, including all-optical switching, efficient frequency conversion and light harvesting.

## 5.5 Experimental details and supplementary material

**Sample Fabrication:** The NbP thin films were grown by molecular-beam epitaxy in a custom made ultra-high vacuum chamber ( $p_{\text{base}} = 1 \times 10^{-10}$  mbar), using electron-beam heating of a niobium rod and parallel thermalization of a gallium phosphide compound effusion cell to get the phosphide species. A cross-beam mass spectrometer was used to calibrate the atomic fluxes, while the substrate temperature was controlled by radiation heating. More details on the fabrication of the NbP films can be found in ref. [160]. The bulk NbP crystals were grown via chemical transport reaction with iodine as transport agent and a temperature gradient from 850 °C at the source to 950 °C at the sink. Beforehand, a polycrystalline powder of NbP was synthesized from niobium and red phosphorus via direct chemical reaction at 800 °C. The fabrication was carried out in the Max-Planck Insitute of Microstructure Physics in Halle (Saale), Germany [160, 162].

**Sample Characterization:** XRD and XRR measurements were performed with a commercial diffractometer from Bruker, using Cu  $K_\alpha$  radiation. In situ RHEED monitoring was performed with a 15 kV electron beam. Ellipsometry measurements were done with the variable- angle spectroscopic ellipsometry (VASE) instrument introduced in section 3.3

and were performed over the visible to near-infrared spectral range (300 – 2000 nm). The numerical fitting was done with the WVASE using a model of multiple Lorentz-like peak functions and a Drude dispersion model in the low energy regime. The same tool was used to perform the linear transmission and reflection measurements.

**THG Experiments:** The measurements were performed with the kHz-laser system introduced in section 3.3 and the sample was mounted to the microscope with a 100x/ NA = 0.9 objective that was used for focusing. The generated THG light was then collected by the same objective (reflection) or by a NA = 0.6 objective (transmission) and subsequently sent to the spectrometer or a calibrated silicon powermeter (Newport). Due to spectral limitations of the experimental setup, reflection measurements could only be performed from 1500 – 1650 nm. For polarization dependent measurements, a waveplate ( $\lambda/2$ ) was placed in the beam path before the microscope.

**Pump-Probe Experiments:** The pump-probe experiments were performed with the setup from section 3.4 and the MIIPS for pulse compression. To minimize dispersion effects, low group velocity dispersion mirrors and a dispersion-free reverse Cassegrain objective with NA = 0.5 were used to direct and focus the beams onto the sample. The experiments were conducted with a 5:1 (pump:probe) power ratio, using average powers of 10 and 2  $\mu$ W for pump and probe pulses, respectively. The collected signal was then sent to the spectrograph coupled to a low-noise photodiode (FEMTO). Lock-in detection was used by modulating the pump beam with a mechanical chopper operating at frequencies below 1 kHz. The instrument response function of the system is described by a Gaussian function with a full-width half-maximum of 10 fs, that approximates the convolution of pump and probe pulses.

**Numerical Simulations:** The numerical simulations were performed with Lumerical FDTD. Perfectly matched layer and periodic boundary conditions were used to mimic an infinitely extended sample surrounded by infinite space. A broadband plane wave source at normal incidence illuminated the sample. Field monitors above and below the film were used to collect the data for reflection and transmission calculations, respectively. The measured dielectric function of the MgO substrate and the NbP film were implemented as material data for the simulations.



# Chapter 6

## Ferroelectric semiconductor nanoflakes

This work is published in [113]:

Ibrahim Abdelwahab, Benjamin Tilmann, Yaze Wu, David Giovanni, Ivan Verzhbitskiy, Menglong Zhu, Rodrigo Berté, Fengyuan Xuan, Leonardo de S. Menezes, Goki Eda, Tze Chien Sum, Su Ying Quek, Stefan A. Maier, Kian Ping Loh

*"Giant second-harmonic generation in ferroelectric NbOI<sub>2</sub>"*

Nature Photonics 16(9), 644-650 (2022), DOI: 10.1038/s41566-022-01021-y

for publisher permission, see Appendix C

As previously discussed throughout this thesis, materials lacking inversion symmetry generally have a non-vanishing second-order nonlinear optical susceptibility. When this is combined with a permanent polarization, they can exhibit strong SHG [24] which is of paramount importance for applications such as coherent light generation, nonlinear auto- and cross-correlations, optical signal processing and imaging [180–185]. Furthermore, SHG is an optimal tool to probe material properties such as crystal symmetry, relative orientation, polar domains, magnetic ordering, surfaces and quantum interference [186–191]. However, the inherently weak photon-photon interactions in classical inversion-asymmetric materials demand high-intensity pumping, bulky interaction volumes, and complex phase-matching techniques to achieve appreciable SHG responses. This prevents the realization of miniature nonlinear optical devices that can function at moderate input powers. Two-dimensional ferroelectric materials (materials possessing a spontaneous electric polarization,  $P_s$ ) are a relatively new class of ultrathin materials, with potential applications in memory devices [192]. Ferroelectricity breaks the material's inversion symmetry, thus two-dimensional ferroelectrics are excellent candidates for realizing strong nonlinear responses over nanometre scale interaction lengths. Layered niobium oxide dihalides NbOX<sub>2</sub> (X = Cl, Br, I) [193–196] have a Peierls-distorted polar structure due to their anisotropic bonding along the in-plane b and c directions: only the b direction is polar, giving rise to strongly anisotropic ferroelectricity. Our density functional perturbation theory calculations predicted very large in-plane ferroelectric and piezoelectric responses for the NbOX<sub>2</sub> family

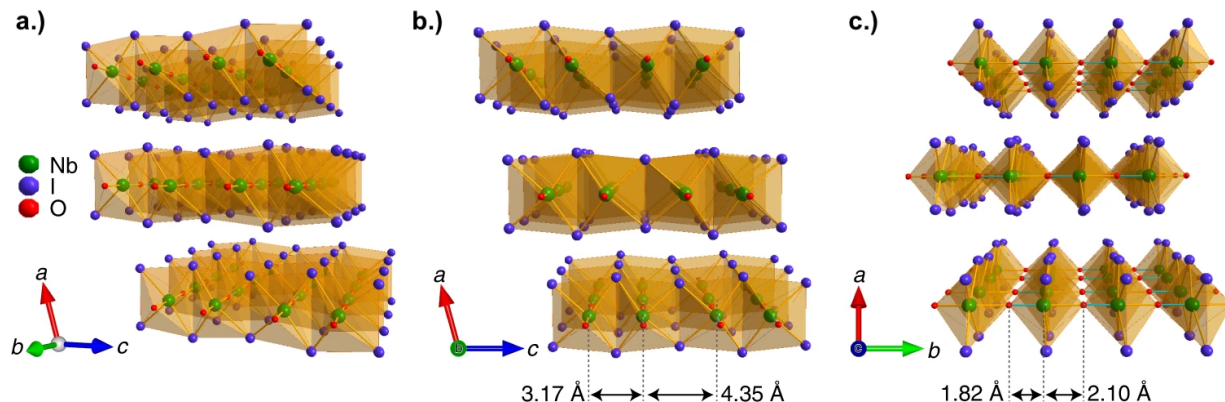


**Figure 6.1:** Atomic structure of ferroelectric layered NbOI<sub>2</sub>. **a.)** Three-dimensional schematic diagram of trilayer NbOI<sub>2</sub> monoclinic crystal structure (space group C<sub>2</sub>). Each NbOI<sub>2</sub> layer is composed of NbO<sub>2</sub>I<sub>4</sub> octahedra linked together by sharing the opposite iodine corners along the crystallographic *c*-axis and by sharing the opposite oxygen corners along the *b*-axis. **b.)** A side view of trilayer NbOI<sub>2</sub> along the non-polar *c*-axis showing an alternation of short and long Nb-Nb distances. **c.)** A side view of trilayer NbOI<sub>2</sub> along the polar *b*-axis showing an alternation of two unequal Nb-O bond lengths. The thickness of a NbOI<sub>2</sub> monolayer is 0.73 nm.

( $P_s = 1.43 \times 10^{-10} \text{ Cm}^{-1}$  and piezoelectric stress tensor element  $e_{22} = 31.6 \times 10^{-10} \text{ Cm}^{-1}$  for NbOI<sub>2</sub> monolayer) [197]. Given that the SHG intensity is proportional to spontaneous polarization [198], NbOX<sub>2</sub> is therefore highly promising for exploring large second-order optical nonlinearities.

This will be investigated in the following chapter, where 20 nm-thick NbOI<sub>2</sub> flakes are thoroughly characterized and investigated with respect to their second-order nonlinear response.

## 6.1 Fabrication and structural characterization

Starting with the fabrication, centimetre-sized NbOI<sub>2</sub> single crystals are grown by chemical vapour transport (CVT) (parameters can be found in the Experimental Details). The crystal structure of NbOI<sub>2</sub> is resolved using single-crystal XRD (SC-XRD) measurements. Bulk NbOI<sub>2</sub> crystallizes in a monoclinic crystal structure with space group *C*<sub>2</sub> (see Table 6.3 in the Experimental Details). Each NbOI<sub>2</sub> layer is composed of NbO<sub>2</sub>I<sub>4</sub> octahedra, which link together by sharing the opposite iodine corners along the crystallographic *c*-axis and by sharing the opposite oxygen corners along the *b*-axis, as shown in Fig. 6.1a. A first-order Peierls distortion occurs along the *c*-axis [199], which leads to the dimerization of niobium atoms. Consequently, an alternation of short and long Nb-Nb bond distances occurs along the NbI<sub>4</sub> chain direction (Fig. 6.1b). Furthermore, there occurs a second-order Peierls distortion along the *b*-axis, through which the niobium ions are displaced from the centre positions of the octahedra towards one of the bridging oxygen atoms. As

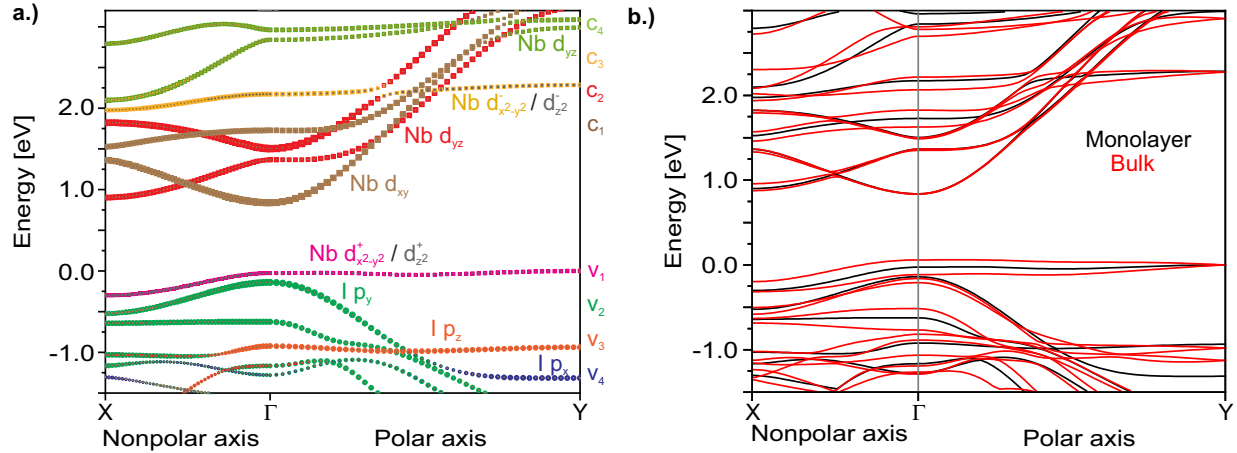


**Figure 6.2:** a.) Density functional theory-calculated band structure of NbOI<sub>2</sub> monolayer. The  $\Gamma \rightarrow Y$  and  $\Gamma \rightarrow X$  high-symmetry directions in the reciprocal space ( $k$ -space) correspond respectively to the polar and non-polar directions of NbOI<sub>2</sub> in real space, respectively. The valence band maximum is set to zero. Orbital component analysis is elucidated by different colours as indicated. The + and – superscripts for the niobium  $d$ -orbitals refer to the energy-split bands due to Peierls distortion. The  $x, y, z$  directions are the  $a, b, c$  crystal axes of the NbOI<sub>2</sub> unit cell, respectively. b.) Interlayer interactions in bulk NbOI<sub>2</sub> induce band splitting for the bands that arise from out-of-plane orbitals.

a result, an alternation of two unequal Nb-O bond lengths takes place (Fig. 6.1c), giving rise to spontaneous polarization. The Peierls distortions are energetically favorable as they lower the total electronic energy of the NbOI<sub>2</sub> system. The Nb-Nb...Nb alternation is 3.17 and 4.35 Å, whereas the Nb-O...Nb alternation is 1.82 and 2.10 Å along the  $c$ - and  $b$ -axes, respectively. The large niobium off-centre polar displacement ( $\sim 0.14$  Å) along the  $b$ -axis drives a robust in-plane ferroelectric polarization, which is among the highest  $P_s$  values in the two-dimensional ferroelectrics family [197, 200].

### Anisotropic band structure

The anisotropic band structure of NbOI<sub>2</sub> is responsible for its large anisotropic optical properties. Fig. 6.2a displays the density functional theory (DFT)-calculated energy-band structure of NbOI<sub>2</sub> monolayer with projection on atomic orbitals. The polar (Nb-O...Nb) and non-polar (Nb-Nb...Nb) directions correspond with the  $\gamma$  to Y and  $\gamma$  to X directions in the reciprocal space, respectively. The bottom four conduction bands are denoted as  $c_1, c_2, c_3$  and  $c_4$ , and arise primarily from niobium  $d$  orbitals. The top four valence bands are denoted as  $v_1, v_2, v_3$  and  $v_4$ . Although most of the valence bands are attributed to iodine  $p$  orbitals, the highest energy valence band  $v_1$  arises from niobium  $d_{x^2-y^2}$  and  $d_{z^2}$  orbitals due to the splitting of the niobium  $d_{x^2-y^2}/d_{z^2}$  bands resulting from Peierls distortion. Strikingly, there is strong mixing between the  $d_{x^2-y^2}$  and  $d_{z^2}$  orbitals in  $v_1$  and

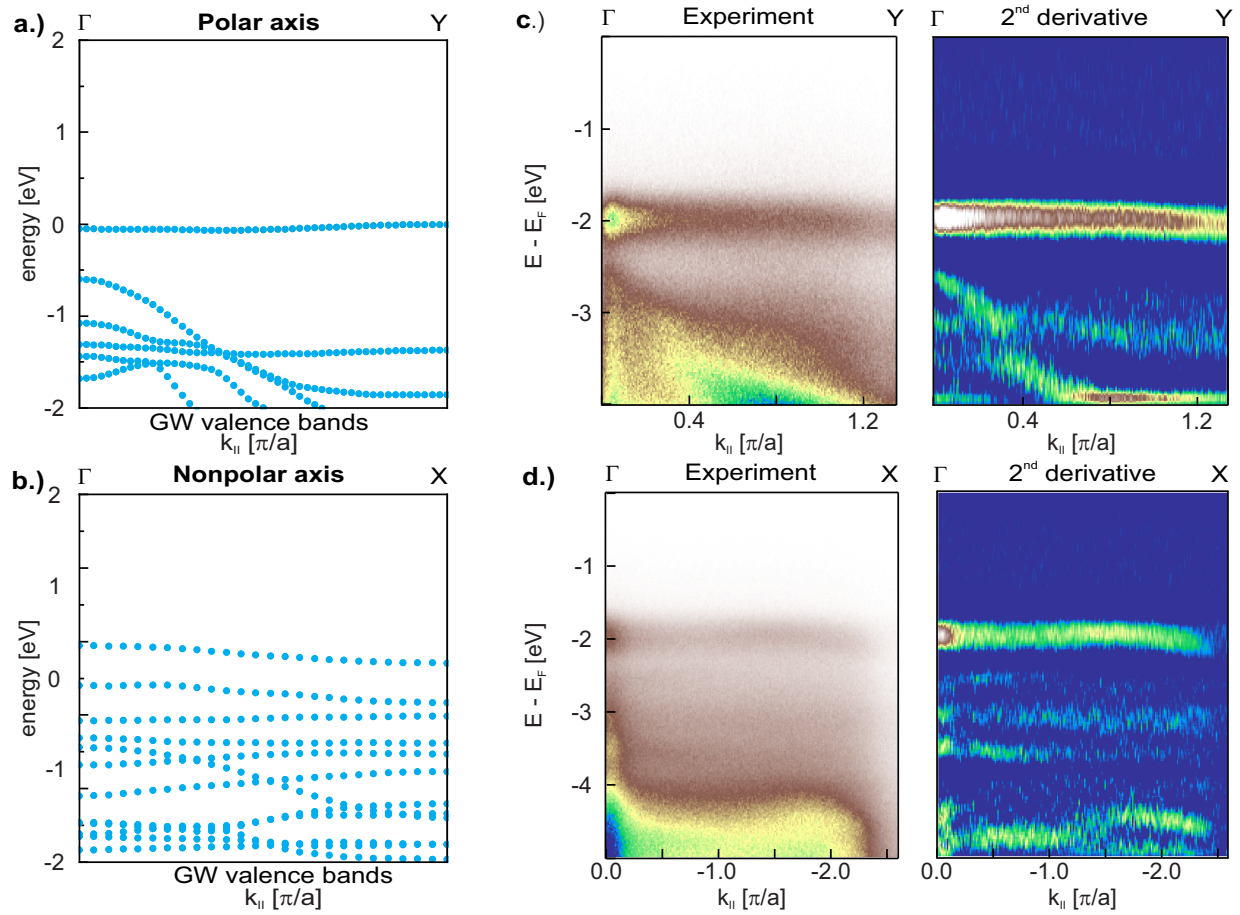


**Figure 6.3:** a.)-b.) ARPES intensity plots and their corresponding second-derivative plots of NbOI<sub>2</sub> along the polar (a.) and non-polar (b.) directions, where  $k_{\parallel}$  is the in-plane component of electron momentum. The Fermi level is at zero. c.)-d.), GW calculated band structure of NbOI<sub>2</sub> monolayer in the polar (c.) and nonpolar (d.) directions. The valence band maximum is set to zero energy. It can be observed that the highest energy valence band is broadened in the experiment, particularly at  $\Gamma$ . This can be attributed to interlayer interactions (see Fig. 6.2b).

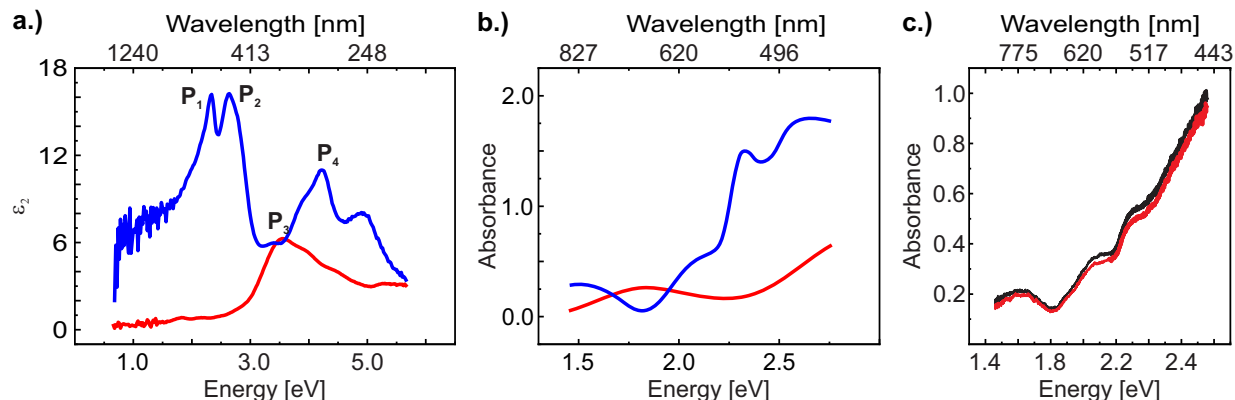


**Figure 6.4:** a.) The imaginary dielectric function  $\epsilon_2$  of  $\text{NbOI}_2$  along the polar (red) and non-polar (blue) directions, obtained by Mueller matrix ellipsometry measurements. Our GW-BSE calculations reveal that the  $P_1$  and  $P_2$  excitons arise from transitions from  $v_1$ ,  $v_2$  and  $v_3$  to  $c_1$ . b.) Linear absorbance spectra of a  $\text{NbOI}_2$  nanosheet collected with incident white light polarized along the polar and nonpolar directions. Blue (red) line: nonpolar (polar) axis. c.) Typical absorbance spectra of a  $\text{NbOI}_2$  nanosheet illuminated with right ( $\sigma^-$ , black curve)- and left ( $\sigma^+$ , red curve)-handed circularly polarized light.

$c_3$  throughout the entire Brillouin zone. The material has fully occupied valence bands and the nearly flat  $v_1$  band implies that the  $v_1$  electrons are highly localized.

The GW-calculated [201, 202] band structure of  $\text{NbOI}_2$  (Fig. 6.3a-b) indicates that the valence band maximum occurs at  $Y$ , while the conduction band minimum occurs at  $X$  (within the  $c_2$  band), giving an indirect bandgap ( $E_g = 2.24$  eV). The band structure is more dispersive along the polar direction than the non-polar direction. As  $k$  varies from  $\gamma$  to  $Y$ , the magnitude of the  $\pi$ -bond overlap between the niobium  $d_{yz}$  ( $d_{xy}$ ) and oxygen  $p_z$  ( $p_x$ ) orbitals increases quite substantially, bringing about highly dispersive  $c_1$  and  $c_2$  bands. The  $c_1$  and  $c_2$  bands are nevertheless weakly dispersive on going from  $\gamma$  to  $X$ . This is due to the opposing effects of the metal-metal ( $\text{Nb}(d_{yz}) - \text{Nb}(d_{yz})$ ) and metal-ligand ( $\text{Nb}(d_{yz}) - \text{I}(p_y)$ )  $\pi$ -bond interactions at  $X$  as well as the weak  $\text{Nb}(d_{xy}) - \text{Nb}(d_{xy})$   $\delta$ -bond interaction. Similarly, the  $v_2$  band varies rapidly in energy from  $\gamma$  to  $Y$  and smoothly from  $\gamma$  to  $X$ .

We have carried out ARPES measurements to confirm the band structure of  $\text{NbOI}_2$ . The valence-band ARPES spectra of  $\text{NbOI}_2$  clearly show the dispersive feature of the  $v_2$  band along  $\Gamma$ - $Y$ , and the dispersionless feature of the bands along  $\Gamma$ - $X$  (Fig. 6.3c-d), in good agreement with the band-structure calculations. A comparison of the ARPES results with the GW band structure shows good quantitative agreement (Fig. 6.3a-b); the similar valence band structure between monolayer (theory) and bulk (experiment)  $\text{NbOI}_2$  indicates that the band dispersion does not vary with thickness, which is different from transition metal dichalcogenides (TMDs) and graphene. Interlayer interactions in bulk  $\text{NbOI}_2$  induce band splitting for the bands that arise from out-of-plane orbitals (Fig. 6.2b). This can explain the broadening observed for some bands in the ARPES band structure.

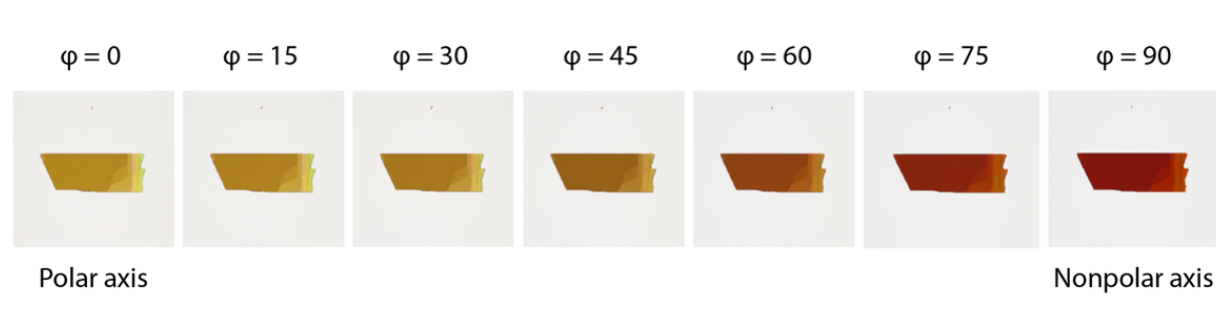


**Figure 6.5:** A series of optical images of a NbOI<sub>2</sub> nanosheet captured in transmitted light mode under different incident polarizations.  $\varphi$  is the polarization angle (relative to the polar axis) of the incident white light. The increase of the absorbance as the linear polarization varies from the polar to the nonpolar direction is due to the large oscillator strength of the nonpolar excitons in the visible region.

### Linear optical response

In line with its anisotropic band structure, the linear optical properties of NbOI<sub>2</sub> are markedly different along the polar and non-polar directions, which is confirmed by performing Mueller matrix ellipsometry measurements over a wide spectral range (6.2 – 0.65 eV, 200 – 1900 nm). The extracted imaginary part of the dielectric function ( $\epsilon_2$ ) is shown in Fig. 6.4a. We observe two predominant peaks confined along the non-polar direction in the visible range (at  $P_1 = 2.34$  eV, 530 nm; and  $P_2 = 2.64$  eV, 470 nm) and one broad peak confined along the polar direction in the near ultraviolet range (at  $P_4 = 3.54$  eV, 350 nm). According to our GW-BSE calculations, peaks  $P_1$  to  $P_4$  are excitonic in nature. The presence of strong optical anisotropy is also reflected from polarization-dependent absorption and transmission measurements (Figs. 6.4b and 6.5). In line with the ellipsometry data, two absorption peaks at  $\sim 530$  nm and 470 nm are detected when light is linearly polarized along the non-polar direction of NbOI<sub>2</sub> (Fig. 6.4b). By contrast, a much weaker absorption in the visible range is collected when light is polarized along the polar direction. Moreover, no circular dichroism signal was observed under circular optical excitation (Fig. 6.4c), excluding any optical activity (chirality) in NbOI<sub>2</sub>.

## 6.2 Second-harmonic generation of NbOI<sub>2</sub> nanoflakes

We isolate NbOI<sub>2</sub> flakes of sub-100-nm thicknesses from a single crystal for nonlinear optical studies. The NbOI<sub>2</sub> nanosheets are encapsulated with a thin layer of transparent hexagonal boron nitride (*h*-BN) to avoid any photo-oxidation effects. There are eight non-vanishing SHG tensor elements for space group  $C_2$ :  $d_{14}, d_{16}, d_{21}, d_{22}, d_{23}, d_{25}, d_{34}$  and  $d_{36}$ , where the SHG susceptibility  $\chi_{ijk}^{(2)}$  can be calculated by  $\chi_{ijk}^{(2)} = 2d_{ij}$ . Considering the Kleinman symmetry introduced in section 2.4,  $d_{16} = d_{21}; d_{14} = d_{25} = d_{36};$  and  $d_{23} = d_{34}$  which, using the approximation of a two-dimensional material, leads to the nonlinear

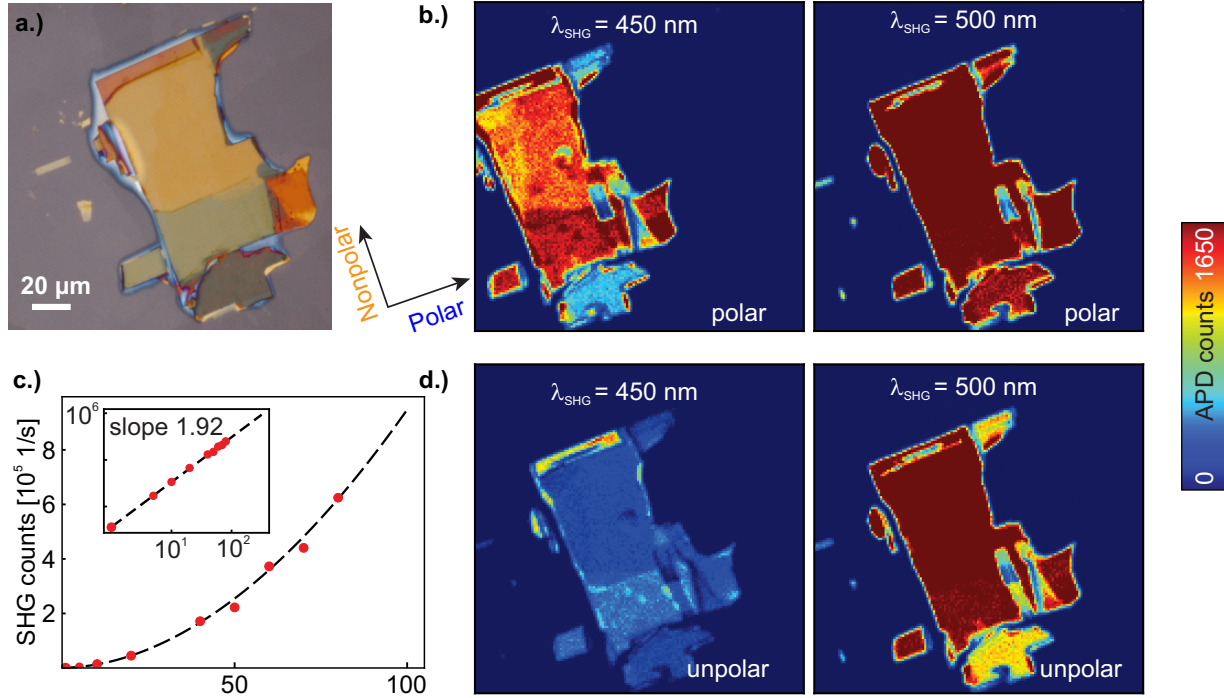


**Figure 6.6:** Characterization of SHG in NbOI<sub>2</sub>. **a.)** Optical image of NbOI<sub>2</sub> flake on quartz substrate after encapsulation with h-BN. **b.)** SHG intensity maps recorded with an avalanche photodiode (APD) of the sample shown in a at  $\lambda_{SHG} = 450$  nm and 500 nm, obtained by setting the excitation polarization parallel to the polar direction of NbOI<sub>2</sub>. **c.)** Excitation power dependence of the SHG signal (red dots) with quadratic fit (dash curve) at  $\lambda_{SHG} = 525$  nm for 20 nm-thick NbOI<sub>2</sub> flake. The inset shows the linear fit of the log-log plot with a slope equal to 1.92. **d.)** SHG intensity maps of the sample in a at  $\lambda_{SHG} = 450$  nm and 500 nm obtained by setting the excitation polarization parallel to the non-polar direction of NbOI<sub>2</sub>. All the maps in b and d are acquired using equally intense excitation pulses.

polarization of the form:

$$\begin{aligned} P_1 &= 2d_{16}E_1E_2 \\ P_2 &= d_{16}E^2 + d_{22}E_2^2 \end{aligned}$$

Here, the indices 1, 2 refer to the  $x, y$  axes, respectively, which are aligned with the polar ( $x$ ) and non-polar ( $y$ ) direction. Thus, the relation between the generated SHG intensity  $I$  and the polarization angle  $\varphi$  of the incident light can be expressed as:

$$I \propto (2d_{16} \cos \varphi \sin \varphi)^2 + (d_{16} \cos^2 \varphi + d_{22} \sin^2 \varphi)^2$$

To selectively probe the  $d_{22}$  coefficient, we pumped NbOI<sub>2</sub> nanosheets supported on a quartz substrate (Fig. 6.6a) with normally incident (along the  $a$ -axis) femtosecond laser

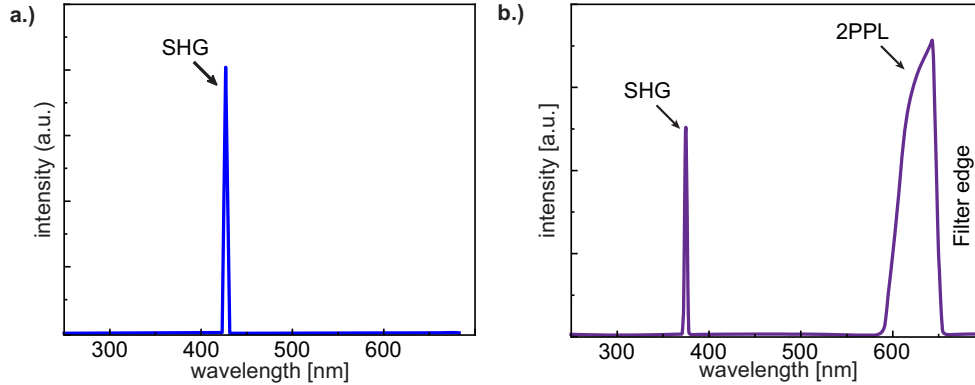


**Figure 6.7:** Nonlinear optical processes in NbOI<sub>2</sub>. Nonlinear spectra for the excitation wavelengths of  $\lambda_{pump} = 850$  nm **a.)** and 750 nm **b.)**. 2PPL: two-photon photoluminescence.

pulses whose linear polarization is parallel to the polar direction of NbOI<sub>2</sub>. Fig. 6.6b shows resultant SHG intensity maps of the sample at two representative SHG wavelengths ( $\lambda_{SHG} = 450$  nm and 500 nm). Notably, a highly efficient SHG signal covering  $\lambda_{SHG} = 425 - 525$  nm is detected for the NbOI<sub>2</sub> flakes (Fig. 6.6b), with negligible background contribution from the quartz substrate. The strong broadband  $d_{22}$ -SHG emission attained at low optical pumping losses (refer to the red curve in Fig. 6.4a) is a direct consequence of the large ferroelectricity of NbOI<sub>2</sub>. When the excitation wavelength is detuned below  $\lambda_{pump} = 800$  nm, we find that the SHG emission intensity is reduced significantly, and the two-photon absorption (2PA) process emerges (Fig. 6.7). This is anticipated, as the excitation photon energy is high enough ( $\hbar\omega > 1/2E_g$ ) to allow two-photon absorption to populate the conduction band of NbOI<sub>2</sub> and, as a result, the slow band-to-band two-photon absorption nonlinearity greatly outweighs the instantaneous SHG nonlinearity [24].

In accordance with the second-order nature of the process, the generated SHG power in NbOI<sub>2</sub> maintains a quadratic dependence on the average input laser power up to  $\sim 80 \mu\text{W}$  (2.2 kW peak power,  $\lambda_{pump} = 1050$  nm), as shown in Fig. 6.6c for 20 nm-thick NbOI<sub>2</sub>. Neither saturation nor hysteresis behaviour in the SHG profile was observed up to the maximum input power used, ruling out any laser-induced material damage. In addition to their thermal stability under laser illumination, the optical properties of NbOI<sub>2</sub> flakes show remarkable air stability over several months. Remarkably, an absolute SHG conversion efficiency ( $\eta_{SHG}$ ) - calculated as the ratio between SHG and excitation powers ( $\eta_{SHG} = P_{SHG}/P_{pump}$ ) - of  $\sim 0.006\%$  is attained for the NbOI<sub>2</sub> nanoflakes at  $\lambda_{pump} = 1050$  nm ( $\eta_{SHG}$  is on the order of 0.0001% for NbOI<sub>2</sub> monolayer), which is orders of magnitude higher than the values previously reported for other nonlinear two-dimensional materials (see Table 6.2 in the Supplementary Details). The measured SHG efficiency (0.006%) at 1000 – 1050 nm excitation is also orders of magnitude higher than that reported for NbOI<sub>2</sub> flake of similar thickness excited by a 1200 nm pump in ref. [203] ( $191 \times \eta_{\text{MoS}_2} \simeq 10^{-6}\%$ ). As shown in Fig. 6.8, the SHG response substantially drops for input wavelengths above 1050 nm.

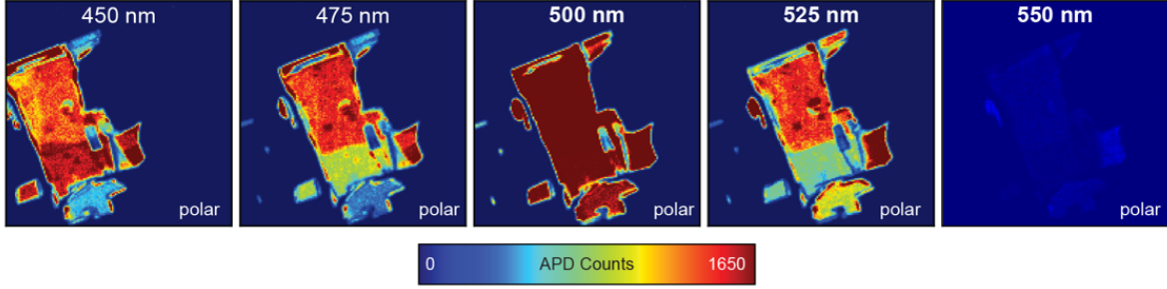


**Figure 6.8:** The intensity dependence of SHG on the fundamental wavelength. SHG maps of the sample in Fig. 6.6a at  $\lambda_{pump} = 900, 950, 1000, 1050,$  and  $1100$  nm. The sample is excited by equally intense excitation pulses linearly polarized along the polar axis. The enhancement of the SHG signal around  $\lambda_{pump} = 1000$  nm is attributed to the combined effect of ferroelectricity and two-photon resonance at the nonpolar exciton states (more in Experimental Details and Fig. 6.14a).

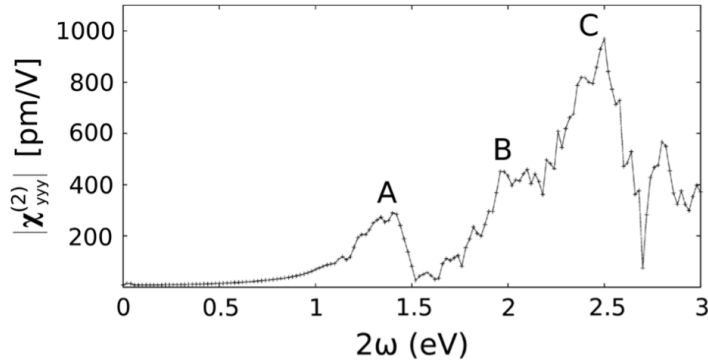


**Figure 6.9:** Calculated absolute value of  $|\chi_{yyy}^{(2)}|$  as a function of the energy of the out-going photon ( $2\omega$ ), where  $y$  is the polar direction. Table 6.1 provides information on the origin of the A, B and C peaks marked in the figure.

The effective bulk-like SHG susceptibility  $\chi_{eff}^{(2)}$  of NbOI<sub>2</sub> can be obtained by dividing the SHG sheet susceptibility  $\chi_s^{(2)}$  (as calculated in ref. [114]) by the NbOI<sub>2</sub> flake thickness. We estimate an  $\chi_{eff}^{(2)}$  of  $\sim 19 \times 10^{-11} \text{ mV}^{-1}$ , which is larger than those of commonly used non-linear crystals (for example, LiNbO<sub>3</sub> with  $5.2 \times 10^{-11} \text{ mV}^{-1}$ ).

This is corroborated by the large  $d_{22}$ -SHG coefficients that we calculate within the independent particle approximation using DFT. Here, the single particle SHG susceptibility can be defined according to equation 35 in Ref. [204]:

$$\chi_{ijk}^{(2)}(-2\omega, \omega, \omega) = \frac{e^3}{\tilde{\omega} \hbar^2 m^3 V} \sum_{knml} \frac{G_{nml}^{ijk}}{\omega_{mn}(k) - \tilde{\omega}} \left[ \frac{f_{nl}(k)}{\omega_{ln} - \tilde{\omega}} + \frac{f_{ml}(k)}{\omega_{ml}(k) - \tilde{\omega}} \right] \quad (6.1)$$

where  $G_{nml}^{ijk} = 1/2\Im \{ p_{nm}^i(k) [p_{ml}^j(k)p_{ln}^k(k) + p_{ml}^k(k)p_{ln}^j(k)] \}$ ,  $p_{nm}^i(k) = \langle u_{nk} | p^i | u_{mk} \rangle$  is the momentum matrix element,  $f_{nl}(k) = f_n(k) - f_l(k)$  is the occupation function difference,  $\hbar\omega_{mn}(k) = \epsilon_{mk} - \epsilon_{nk}$  is the single particle energies difference, which can be obtained by

| peak label | band transitions   | Brillouin zone |
|------------|--|----------------|
| A          | $v_1 \rightarrow c_1, v_1 \rightarrow c_2$   | $\Gamma$       |
| B          | $v_4 \rightarrow c_1, v_5 \rightarrow c_1, v_2 \rightarrow c_2, v_3 \rightarrow c_2$ | $X$            |
| C          | $v_4 \rightarrow c_2, v_6 \rightarrow c_2$   | $\Gamma$       |

**Table 6.1:** Analysis for the first three lowest energy peaks in the single particle SHG susceptibility  $|\chi_{yyy}^{(2)}|$ . These peaks arise from the poles, which correspond to the transitions shown in the table.  $v_4 \rightarrow c_2$  refers to the transition between the 4th highest-energy valence band and the 2nd lowest-energy conduction band.  $X$  and  $\Gamma$  are defined in Fig. 6.2a.

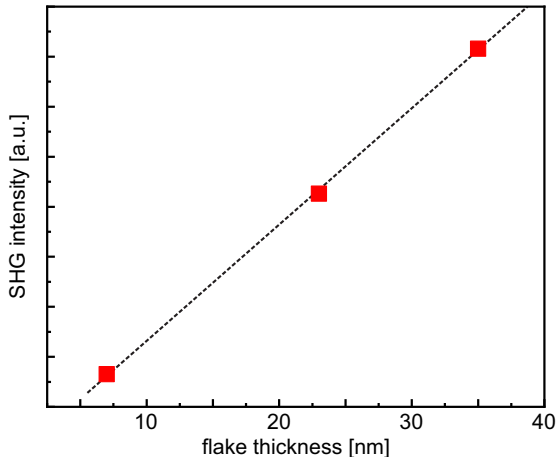


**Figure 6.10:** Nonlinear optical response of NbOI<sub>2</sub> as a function of thickness. The SHG intensity of NbOI<sub>2</sub> flakes of different thicknesses at  $\lambda_{pump} = 900$  nm. The samples are excited by equally intense excitation pulses linearly polarized along the polar axis.

solving the mean field single particle Hamiltonian  $H_k u_{nk} = \epsilon_{nk} u_{nk}$ . The single particle SHG susceptibility for unstrained monolayer NbOI<sub>2</sub> is calculated within DFT on a  $(48 \times 24 \times 1)$   $k$ -grid with 33 valence and 33 conduction bands. The monolayer cell volume ( $V$ ) in the above expression is defined using the thickness (0.73 nm) for monolayer NbOI<sub>2</sub>. The energy denominator in equation 6.1 contains a small imaginary part  $\tilde{\omega} = \omega + i\eta$ , which we choose to be the same as the energy step in  $\omega$  (0.01 eV). The numerical results are shown in Fig. 6.9 and Table 6.1. It should be noted that this approach ignores electron self-energy effects and excitonic effects. Evidently, the calculations predict large  $d_{22}$ -SHG coefficients corresponding to outgoing photon energies in the range  $\sim 2.0 - 2.6$  eV (peaks  $B$  and  $C$ ), as well as  $\sim 1.3 - 1.5$  eV (peak  $A$ ). The interband transitions giving rise to these peaks are shown in Table 6.1. We expect that electron self-energy effects will blue shift these peaks, while excitonic effects may increase the maximum SHG amplitudes.

The  $AB$  Bernal stacking of many two-dimensional materials (for example, the  $2H$  phases of group-VI TMDs) results in ultra thin flakes with thickness corresponding to even-layer number unit cells to be inversion symmetric and SHG-inactive, and only ultrathin flakes with thickness corresponding to odd-layer number unit cells can be SHG-active. This effectively constrains the nonlinear response to atomically thin interaction lengths for many TMD materials that possess bulk inversion symmetry. By contrast, NbOI<sub>2</sub> has a broken inversion symmetry regardless of thickness and its SHG response scales with thickness. Taking into consideration the coherence length of the generated SHG radiation and inter-

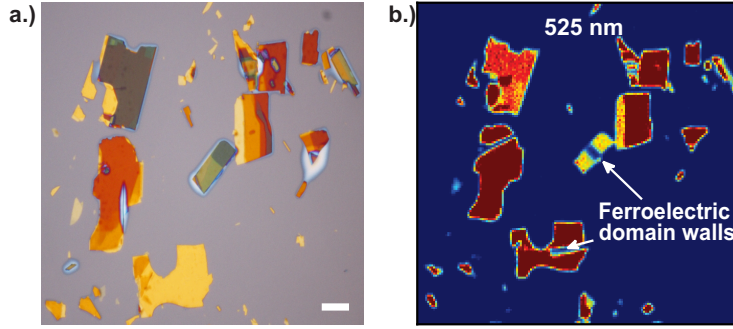


**Figure 6.11:** Ferroelectric domain walls in NbOI<sub>2</sub>. Optical image of NbOI<sub>2</sub> flakes on quartz substrate **a.)** and the corresponding SHG map at  $\lambda_{pump} = 1050 \text{ nm}$  **b.)** (same as in Fig. 6.9). The dark lines in the 2D SHG map point out 180° domain walls separating oppositely polarized FE domains.

ference effects [168, 205], the  $\chi_s^{(2)}$  of AA-stacked NbOI<sub>2</sub> scales with thickness (Fig. 6.10), rendering NbOI<sub>2</sub> practically useful for highly efficient parametric conversion processes. The deviation from the quadratic dependence of SHG intensity on the layer number, usually observed for ultrathin 2D films, can be attributed to the interference effects between the surface and bulk SHG contributions, which result in high-contrast oscillations in the overall nonlinear signal [206]. These SHG contributions are influenced by the absorption of the pump beam, the partial reabsorption of the emitted signal, the system's resonant energy, and the complex refractive index and associated phase mismatch effects, which vary with thickness [116, 207, 208].

Moreover, SHG can be used for the non-invasive visualization of nanoscale NbOI<sub>2</sub> ferroelectric domains that are otherwise challenging to probe. The white arrows in Fig. 6.11 point out 180° domain walls separating oppositely polarized ferroelectric domains. These are the only permissible domains due to the one-dimensional (1D) ferroelectric nature of NbOI<sub>2</sub>. Energetically, the side-by-side 180° domain walls between domains polarized in antiparallel directions are more favorable than the head-to-head (tail-to-tail) walls [200]. Although the antiparallel ferroelectric domains yield the same SHG intensity, their Ising-type 180° domain walls can still be seen as dark lines in the 2D SHG intensity maps. This happens because the SHG fields generated in the different domains are exactly 180° out-of-phase with each other, causing them to interfere destructively at the domain-domain interface.

To probe the spatial dependence of the nonlinear response, the total SHG intensity (that is, without an analysing polarizer in the detection channel) is measured as a function of the input laser polarization. Fig. 6.6d shows the SHG intensity maps of the NbOI<sub>2</sub> sample with excitation laser polarized along the non-polar direction. The results reveal that, outside the non-polar  $P_1 - P_2$  excitonic bands (consider the examples of  $\lambda_{SHG} = 450 \text{ nm}$  in Fig. 6.6b,d and  $\lambda_{SHG} = 750 \text{ nm}$  in Fig. 6.7),  $d_{22}$  is the dominant coefficient of  $\chi^{(2)}$  which leads to a dominant SHG signal for input light polarized in the polar direction as manifested in the anisotropic two-lobed SHG intensity pattern (Fig. 6.12). The ratio of SHG intensities along the two in-plane axes exceeds 7 for  $\lambda_{SHG} = 450 \text{ nm}$ ; however, when

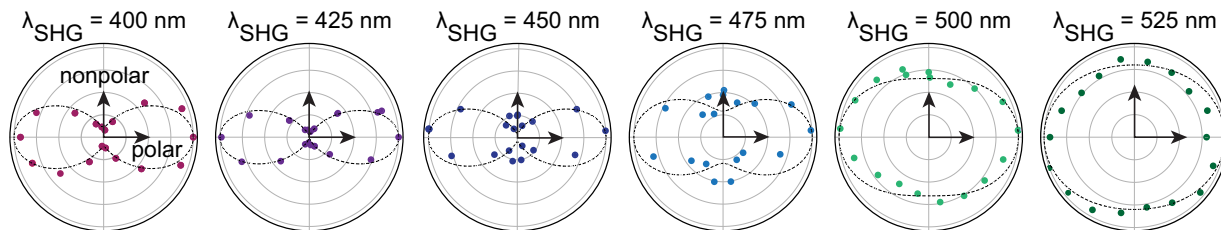


**Figure 6.12:** Polar plots of the total SHG intensity as a function of the polarization angle of the excitation beam at  $\lambda_{SHG} = 400 - 525$  nm. The coloured dots represent the experimental data while the dash lobes represent the theoretical (considering the Kleinman symmetry) predictions of the SHG intensity as a function of the input polarization.

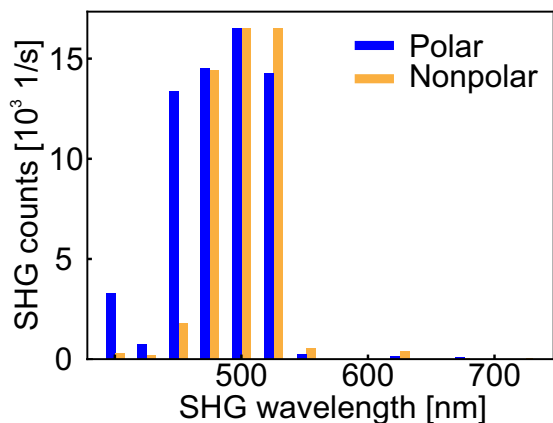


**Figure 6.13:** Bar chart showing the polar and non-polar SHG signals from the NbOI<sub>2</sub> flake in the range of  $\lambda_{SHG} = 400 - 750$  nm while maintaining constant excitation intensities. The polar SHG signal is 7.6-times the non-polar signal at 450 nm, but their signals reach similar intensities between 475 to 525 nm

the generated SHG signal is resonant with the energy of the  $P_1$  and  $P_2$  excitons (for example,  $\lambda_{SHG} = 525$  nm), the strong resonance and localization effects greatly magnify the  $d_{16}$  coefficient, enhancing the SHG signal for input light polarized in the non-polar direction to be comparable with the polar signal and resulting in an isotropic, near-circular SHG intensity pattern. The SHG polar plots in Fig. 6.12 and the polar and non-polar SHG signals in Fig. 6.13 clearly display this wavelength-dependent SHG anisotropy-isotropy cross-over. This contrasts with group-VI TMDs (for example,  $2H - \text{MoS}_2$ ), which show only isotropic SHG polar plots, and group-VII TMDs (for example,  $\text{ReS}_2$ ), which show only anisotropic SHG polar plots for the total SHG intensity [209,210]. The polarization of the emitted SHG signal is also analysed and found to be strongly polarized along the non-polar direction, regardless of the excitation polarization.

The polarization of the detected SHG signal is analyzed along the two in-plane crystallographic axes of the sample. In doing so, linear polarizers are used in the excitation and detection channels [211,212]. The excitation and detection polarizations are co-linearly ( $YY, ZZ$ ) or cross-linearly ( $YZ, XY$ ) polarized along either the  $b$  or  $c$  axis, giving a total of four different configurations (Fig. 6.14a). In accord with the theoretical model, the emitted SHG light is found to be strongly polarized along the nonpolar direction, regardless of the excitation polarization. Furthermore, polarization-resolved SHG spectra taken with circularly polarized light ( $\sigma = \pm 1$ ) are shown in Fig. 6.14b. As expected from a mon-

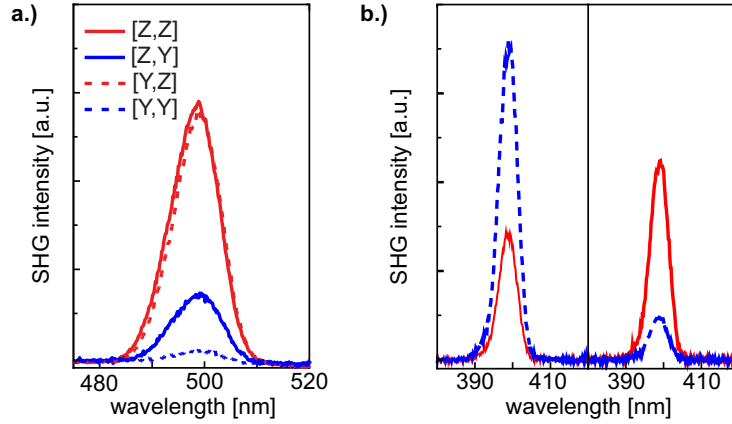


**Figure 6.14:** Polarization-resolved SHG in NbOI<sub>2</sub>. **a.)** Polarization-resolved SHG spectra obtained with co-linearly (YY, ZZ) and cross-linearly (YZ, XY) polarized excitation and detection. The fundamental wavelength is 1000 nm. Y indicates the polarization along the polar *b* axis of NbOI<sub>2</sub> while Z indicates the polarization along the nonpolar *c* axis. **b.)**, Polarization-resolved SHG spectra obtained with co-circularly and cross-circularly polarization configurations with a fundamental wavelength of 800 nm. Solid red (dashed blue) line:  $\sigma^+(\sigma^-)$  excitation. Left (right) panel:  $\sigma^+(\sigma^-)$  detection.

oclinic system under circular optical excitation perpendicular to the two-fold rotational axis [213], the cross-circularly polarized SHG component ( $\sigma^+/\sigma^-$  or  $\sigma^-/\sigma^+$ ) of NbOI<sub>2</sub> is always stronger than the co-circularly polarized SHG component ( $\sigma^+/\sigma^+$  or  $\sigma^-/\sigma^-$ ).

### 6.3 Manipulation of the nonlinear optical response

The structural polarity of NbOI<sub>2</sub> and, consequently, its nonlinear response, can be strongly modulated using external stimuli such as mechanical strain, temperature or an external electric field. Theoretically, the niobium polar displacement can be increased twofold by applying 3% tensile strain along the polar axis. The strong piezoelectric response predicted for NbOI<sub>2</sub> (ref. [197]) should lead to a strong built-in piezoelectric field and enhanced SHG signal in strained NbOI<sub>2</sub>. To validate this, we introduce a localized uniaxial strain along the polar direction via the buckling-induced delamination process [214]. Fig. 6.15a and Fig. 6.16 depicts buckling-induced NbOI<sub>2</sub> wrinkles separated by flat unstrained regions. The maximum tensile strain ( $\epsilon$ ) accumulated on top of the wrinkles can be estimated from the geometry of the wrinkles as [215]:

$$\epsilon \sim \frac{\pi ht}{(1 - \tilde{\nu})w^2}$$

where  $h$  and  $w$  are the height and width of the wrinkle,  $t$  is the thickness of the flake, and  $\tilde{\nu}$  is the NbOI<sub>2</sub> Poisson's ratio (0.087). The  $h$ ,  $w$ , and  $t$  are determined by atomic force

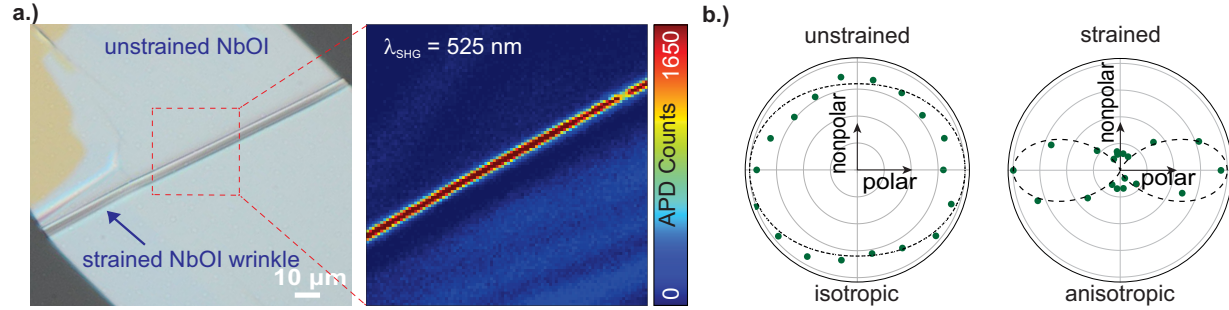


**Figure 6.15:** Effects of strain SHG in NbOI<sub>2</sub>. **a.)** Optical image of a wrinkled NbOI<sub>2</sub> flake (left), and corresponding SHG map at  $\lambda_{SHG} = 525$  nm (right). **b.)** Polar plots of the total SHG intensity as a function of the polarization angle of the excitation beam at  $\lambda_{SHG} = 525$  nm for the flat and strained NbOI<sub>2</sub> regions.

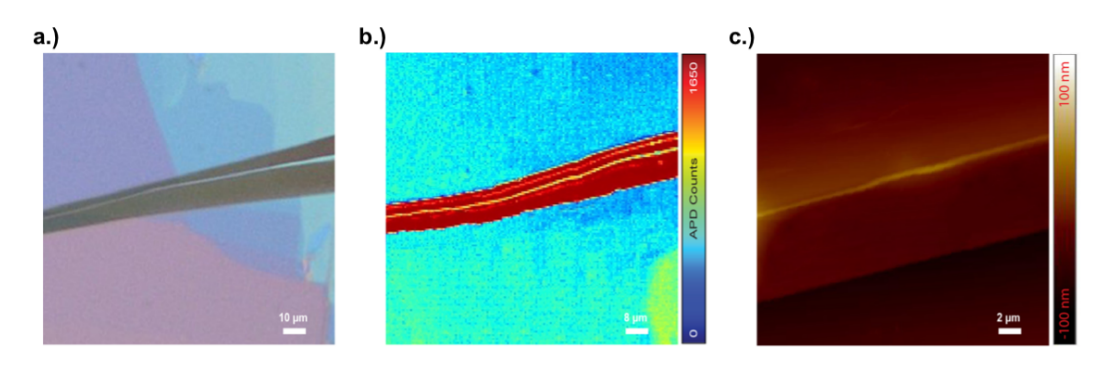


**Figure 6.16:** Characterization of wrinkled NbOI<sub>2</sub> flake. **a.)** Optical image, **b.)**, SHG map, and **c.)** topography image of a wrinkled NbOI<sub>2</sub> flake. The SHG map is collected at  $\lambda_{pump} = 1050$  nm.

microscopy, see Figure 6.16.

The presence of both curved and flat areas in the same NbOI<sub>2</sub> flake allows their nonlinear optical properties to be compared. We map the SHG intensity as a function of the spatial position of the sample with the pump polarized along the polar axis. As illustrated in Fig. 6.15a, in comparison to the flat areas, the NbOI<sub>2</sub> wrinkled regions (3.1% strain) show an up to 35-fold increase in the SHG intensity, reaching a record efficiency  $\eta_{SHG}$  of  $> 0.2\%$  ( $\chi_{eff}^{(2)} \sim 113 \times 10^{-11} \text{mV}^{-1}$ ). Furthermore, the SHG polar plot of the strained area reveals that the isotropic SHG response (within the non-polar exciton band) vanishes due to the lengthening of the  $d_{22}$  coefficient (Fig. 6.15b). The high nonlinear conversion efficiency of NbOI<sub>2</sub> motivates multiple applications in classical and quantum photonics. For example, it can be utilized as an ultrathin pump for parametric downconverters to produce high-flux squeezed and entangled quantum states of light, with applications in quantum computation and quantum cryptography [216–218].

Aside from the strain engineering of the nonlinear response, the SHG intensity increases

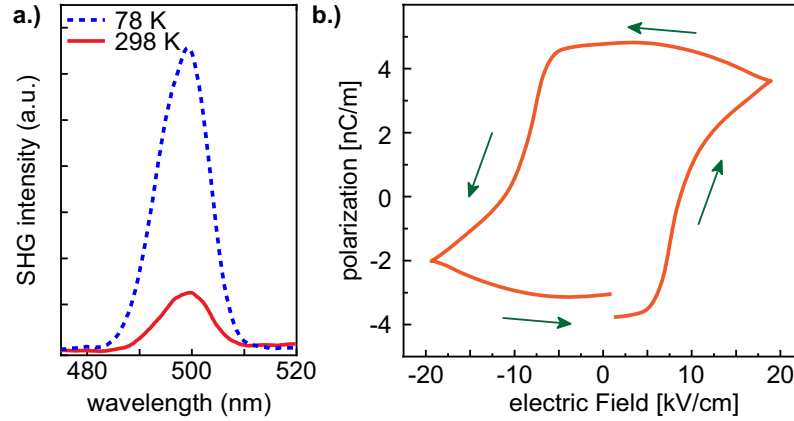


**Figure 6.17:** a.) Temperature-dependent SHG at 298 K (red solid line) and 78 K (blue dashed line). b.) Polarization versus electric field ( $P - E$ ) hysteresis loop of NbOI<sub>2</sub> nanosheet at room temperature.

fivefold (Fig. 6.17a) upon reducing the temperature to 78 K, implying enhanced ferroelectric polarization. This is further confirmed by low-temperature SC-XRD measurements (refer to CIFs, published online along the article [113]), showing that the niobium polar displacement extends from 0.14 Å at 298 K to 0.17 Å at 100 K.

The spontaneous polarization of a ferroelectric material, by definition, can be switched by an external electric field. Applying an external electric field  $E = (0, E_2, 0)$  along the polar direction can elongate or shorten the polar vector by an amount  $\Delta P = (0, \Delta P_2, 0)$ , where  $\Delta P_2 = \epsilon_0 \chi_{22}^{(1)} E_2 + \Delta P_s$  with  $\epsilon_0$  the vacuum permittivity and  $\chi_{22}^{(1)}$  is the linear electric susceptibility. Unlike the linear dielectric response ( $\epsilon_0 \chi_{22}^{(1)} E_2$ ), the history-dependent  $P_s$  scales nonlinearly with the electric field and is responsible for the hysteretic nature of the  $P - E$  characteristic. At low electric fields, the sample behaves like an ordinary dielectric. However, when the electric field is increased to a critical value (so-called coercive field  $E_c$ ), ferroelectric domains with oppositely oriented polarization begin to switch and align themselves along the electric field direction, resulting in the rapid increase of current and polarization. Under higher electric fields, the polarization is restored to linear and eventually reaches a saturation state due to the complete switch of the ferroelectric domains. When the field strength is swept backward, some domains would back-switch, however, a nonzero net polarization (remnant polarization  $P_r$ ) persists even after the electric field is removed. To obtain a zero polarization, an opposite-pointing coercive field is needed. With further increasing the opposite field strength, a similar polarization profile with the reverse sign is observed, indicative of polarization reversal. The ferroelectric property of NbOI<sub>2</sub> is verified from its polarization versus electric field ( $P - E$ ) characteristics (Fig. 6.17b) measured when an external electric field is applied along the polar direction. The curve exhibits a clear ferroelectric hysteresis loop. The coercive ( $E_c$ ) and saturation ( $E_{sat}$ ) fields are determined to be around 8.5 kV cm<sup>-1</sup> and  $\pm 17.5$  kV cm<sup>-1</sup>, respectively. The deviation of the  $P - E$  curve in Fig. 6.17b from ideal rectangular-like hysteresis is due to

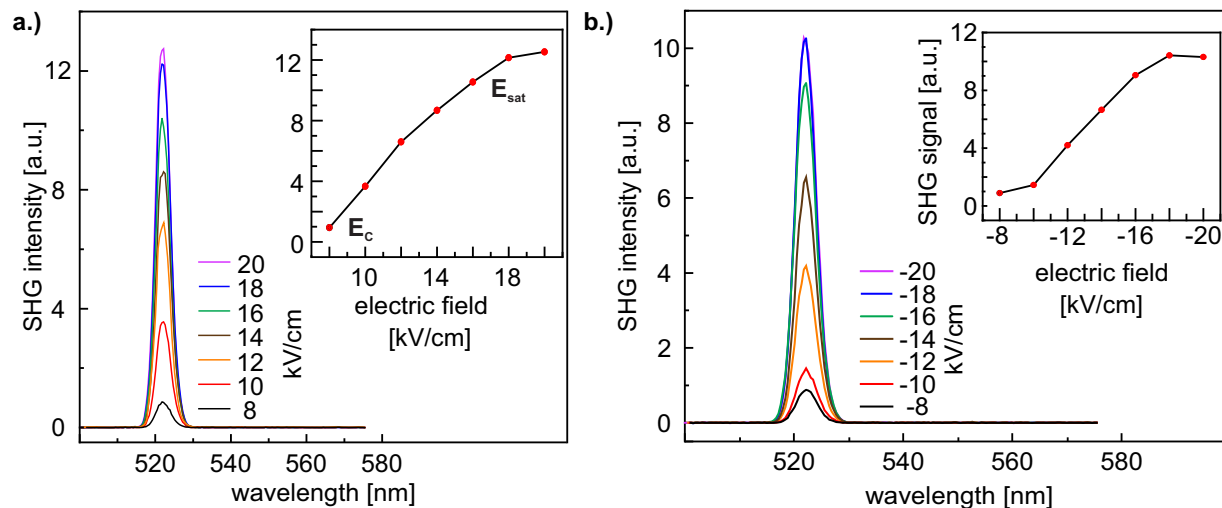


**Figure 6.18:** SHG spectra as a function of the external electric field strength. An in-plane electric field is applied along the polar direction of the NbOI<sub>2</sub> nanosheet. The fundamental wavelength is 1050 nm. The inset shows the peak SHG intensity as a function of external electric field strength. The SHG intensity is not zero at the coercive field due to the incomplete cross cancellation of the SHG intensity between antiparallel domains in the area of the sample being probed. Shown for a.) positive and b.) negative bias.

the relatively small bandgap of NbOI<sub>2</sub> and associated leakage issues [219]. The leakage current broadens the current peaks and yields a more rounded  $P - E$  hysteresis. It has also been shown that both the magnitude of polarization ( $P_s$ ) and the ferroelectric switching barrier ( $E_c$ ) can be controlled by strain [197]. We monitor the SHG intensity as a function of the applied in-plane electric field to study the dynamic properties of  $d_{22}$ -SHG, as shown in Fig. 6.18a for the positive electric field part. The SHG intensity increases rapidly once the coercive field threshold is overcome and eventually saturates, following the same trend as the polarization. The large modulation contrast ( $\leq 80\%$ ) of the SHG signal between two states (paraelectric at  $E_c$  and monodomain ferroelectric at  $E_{sat}$ ) by the electric field can potentially enable electrically tunable integrated light sources (for example, frequency combs) for sensing and on-chip communication [220, 221]. Similar dynamic control over the SHG signal is registered in the negative applied field region (Fig. 6.18b), affirming the polar switchability in NbOI<sub>2</sub> at room temperature. The polarization reversal (domain switching) in NbOI<sub>2</sub> implies that the sign of the nonlinear coefficient can be periodically reversed along the interaction length. This deterministic control of the sign and magnitude of the nonlinear coefficient at the nanoscale opens up a promising area for designing optical modulators and transistor devices with high SHG efficiencies for optical signal processing [222–224].

## 6.4 Conclusion

We demonstrate that polar two-dimensional NbOI<sub>2</sub> shows a very strong second-order parametric response. The strongly piezoelectric nature of NbOI<sub>2</sub> allows strain-tunable nonlinear response with a record SHG absolute conversion efficiency of > 0.2% without purposefully considering phase-matching conditions. The spatial profile of the polarized SHG response can be modulated by resonance or off-resonance excitations, as well as strain. Taking advantage of the switchable ferroelectric polarization of NbOI<sub>2</sub>, the SHG signal can be electrically modulated with modulation contrast exceeding 80%. The work in this chapter suggests that polar layered transition metal oxidehalides that combine strong piezo-electric and ferroelectric properties allow strain and polar order to be coupled with nonlinear responses, enabling a new generation of strain-tunable and electrical-tunable nonlinear optical devices.

## 6.5 Experimental details and supplementary material

**Crystal growth:** NbOI<sub>2</sub> single crystals were grown by chemical vapour transport. NbOI<sub>2</sub> crystals were synthesized from high-purity niobium (film), iodine (crystals) and Nb<sub>2</sub>O<sub>5</sub> (powder), which were mixed to form a stoichiometric ratio of Nb:O:I = 1:1:2, which was then sealed in the evacuated (10<sup>-5</sup> mbar) quartz ampule. Sealed ampules were placed in the horizontal dual-zone furnace and brought to 600 °C at a rate of 1 °C per min. The ampules were held at 600 °C for five days and then slowly cooled for ten days with the slightly different rates at the hot (1.2 °C per hour) and cold (1.5 °C per hour) zones. This small temperature gradient ensured the growth of centimetre-size high-quality crystals near the cold end of the ampule. After the slow-cooling process, the furnace was turned off allowing the ampules to cool down naturally. Crystals were extracted from the opened ampules under inert conditions of an N<sub>2</sub>-filled glove box and then stored for future use.

**X-ray crystallographic analysis:** The SC-XRD data were collected at room ( $T = 298$  K) and low ( $T = 100$  K) temperatures on a Bruker D8 Venture SC-XRD system equipped with molybdenum  $K\alpha$  radiation ( $\lambda = 0.71073$  Å), a KAPPA four-circle goniometer, a PHOTON 100 detector (CMOS APS) and an Oxford Cryostream. Data collection, integration and scaling were carried out using the Bruker APEX3 software package. The frames were integrated with the Bruker SAINT software package using a narrow-frame algorithm. Data were corrected for absorption effects using the multi-scan method (SADABS). The structures were solved and refined using the Bruker SHELXTL software package [232], using the space group  $C121$ , with  $Z = 4$  for the formula unit, I<sub>2</sub>NbO. The final anisotropic full-matrix least-squares refinement was performed on weighted  $F^2$  values. Relevant crystal, collection and refinement data for the crystal structures of NbOI<sub>2</sub> at 298 K and 100 K are summarized in Table 6.3. The crystallographic axes of the NbOI<sub>2</sub> crystals were identified from the SC-XRD analysis.

| material                                  | thickness | $\chi^{(2)}$ in $10^{-11} \text{ mV}^{-1}$ | $\eta_{SHG}$ in %    | $\lambda_0$ in $\mu\text{m}$ | ref.  |
|---|-----------|--|----------------------|------------------------------|-------|
| NbOI <sub>2</sub>                         | monolayer | 19   | $3 \times 10^{-4}$   | 1.05                         | [113] |
| NbOI <sub>2</sub> (3.1% strain)           | monolayer | 113  | $1 \times 10^{-2}$   | 1.05                         | [113] |
| MoS <sub>2</sub>                          | monolayer | 0.6-4.5                                    | $1 \times 10^{-8}$   | 1.35 – 1.6                   | [225] |
|   | monolayer | 32   | -                    | 0.81                         | [209] |
| MoSe <sub>2</sub>                         | monolayer | 5  | -                    | 1.62                         | [226] |
| WSe <sub>2</sub>                          | monolayer | 6  | $2.7 \times 10^{-8}$ | 1.5                          | [227] |
| <i>h</i> – BN                             | monolayer | 0.1  | -                    | 0.81                         | [209] |
| GaSe                                      | monolayer | 1.8  | $6 \times 10^{-8}$   | 1.56                         | [228] |
| GaTe                                      | monolayer | 0.115                                      | $1.3 \times 10^{-9}$ | 1.56                         | [229] |
| TaAs                                      | bulk      | 720  | -                    | 0.8                          | [152] |
| GaAs                                      | bulk      | 70   | -                    | 0.81                         | [213] |
| LiNbO <sub>3</sub>                        | bulk      | 5.2  | -                    | 0.852                        | [230] |
| $\beta$ – BaB <sub>2</sub> O <sub>4</sub> | bulk      | 10.2                                       | -                    | 0.88                         | [231] |
| Quartz                                    | bulk      | 0.08                                       | -                    | 0.884                        | [70]  |

**Table 6.2:** Second-harmonic generation susceptibility ( $\chi^{(2)}$ ) and absolute conversion efficiency ( $\eta_{SHG}$ ) of different nonlinear materials at room temperature

**ARPES measurements:** High-resolution ARPES measurements were performed in an ultrahigh-vacuum system under a pressure lower than  $8 \times 10^{-10}$  mbar. The ARPES chamber is equipped with a differentially pumped UVS300 helium discharge lamp (SPECS GmbH) as the light source, which provides monochromatized photon energies of 21.2 eV (He-I) and 40.8 eV (He-II) through a toroidal mirror monochromator (SPECS GmbH). Here we used He-I as the ARPES source. The temperature of the NbOI<sub>2</sub> bulk sample was kept at 77 K during the measurement.

**Spectroscopic ellipsometry:** The anisotropic in-plane complex refractive indices of NbOI<sub>2</sub> were characterized through Mueller matrix spectroscopic ellipsometry measurements, which is a technique that extends the ellipsometry that was introduced in section 3.3.1 for anisotropic samples. Spectra within the spectral range 6.2 – 0.65 eV (200 – 1900 nm), in steps of 20 meV, were obtained using a commercial rotating analyser instrument with a compensator (VASE, J.A. Woollam Co.). The samples were mounted on a precision rotation stage (RS40, Newport) to perform azimuth-dependent measurements, and the in-plane rotation angle  $\phi$  was varied from 0° to 360°. At each in-plane orientation, data were taken at three angles of incidence ( $50^\circ, 60^\circ, 70^\circ$ ). Such an angle-resolved measurement scheme is necessary for accessing the entire Mueller matrix and characterizing optically anisotropic samples [233, 234].

**Thin sample preparation:** For linear absorption and SHG characterizations, the bulk NbOI<sub>2</sub> crystals were mechanically exfoliated onto clean quartz substrates using the Scotch tape method. Atomic force microscopy was used to measure the thickness of the

| Temperature                     | 298 K   | 298 K   |
|---------------------------------|---|---|
| Chemical Formula                | I <sub>2</sub> NbO  | I <sub>2</sub> NbO  |
| Molecular weight                | 362.1 g/mol   | 362.1 g/mol   |
| Crystal system                  | monoclinic  | monoclinic  |
| Space group                     | C 1 2 1   | C 1 2 1   |
| Unit cell dimensions            | $a = 15.1882(15) \text{ \AA}$<br>$b = 3.9329(4) \text{ \AA}$<br>$c = 7.5232(8) \text{ \AA}$<br>$\alpha = 90^\circ$<br>$\beta = 105.404(4)^\circ$<br>$\gamma = 90^\circ$ | $a = 15.1243(15) \text{ \AA}$<br>$b = 3.9296(4) \text{ \AA}$<br>$c = 7.5061(7) \text{ \AA}$<br>$\alpha = 90^\circ$<br>$\beta = 105.420(4)^\circ$<br>$\gamma = 90^\circ$ |
| Volume                          | 433.24(8) $\text{\AA}^3$  | 430.05(7) $\text{\AA}^3$  |
| $Z$                             | 4   | 4   |
| Density (calculated)            | 5.561 g/cm <sup>3</sup>   | 5.602 g/cm <sup>3</sup>   |
| Absorption coefficient          | 16.824 mm <sup>-1</sup>   | 16.949 mm <sup>-1</sup>   |
| Theta range for data collection | 2.78 to 29.56   | 2.81 to 29.58   |
| Reflections collected           | 679   | 3424  |
| Independent reflections         | 679 [ $R_{\text{int}} = 0.0390$ ]   | 1201 [ $R_{\text{int}} = 0.0379$ ]  |
| Coverage of indep. reflections  | 99.3 %  | 99.6 %  |
| Goodness-of-fit on $F^2$        | 1.247   | 1.145   |
| Final R indices                 |   |   |
| $R_1, wR_2 [I > 2\sigma(I)]$    | 0.0390, 0.1147  | 0.0305, 0.0888  |
| $R_1, wR_2$ [all data]          | 0.0411, 0.1212  | 0.0307, 0.0892  |

**Table 6.3:** Crystal data and structure refinement for NbOI<sub>2</sub> at 298 K and 100 K

exfoliated flakes. The flakes were covered with a thin layer of hexagonal boron nitride (*h*-BN, < 10 nm) using the poly(dimethyl siloxane) stamp-transfer method to avoid any photo-oxidation effects during the SHG measurements. For the field-dependent SHG measurements, NbOI<sub>2</sub> devices were prepared by transferring thin NbOI<sub>2</sub> flakes onto laterally interdigitated electrodes via poly(dimethyl siloxane) stamping. The electrodes (Pt (70 nm)/Ti (30 nm)) were patterned on SiO<sub>2</sub>/Si wafers (SiO<sub>2</sub> = 300 nm) using electron beam lithography, electron beam evaporation and a lift-off process. A transfer station with an optical microscope and a rotating stage was used to transfer the NbOI<sub>2</sub> flakes in such a way that the device's lateral electrical field is aligned with the in-plane polar axis of the transferred flakes.

**Optical, electrical and optoelectronic characterizations:** The micro-absorption measurement was performed by placing the NbOI<sub>2</sub> sample between aligned microscope objectives (50x Mitutoyo, apochromat, infinity corrected), for light focusing and collection. Pulsed laser (Coherent Libra) with a fundamental wavelength of 800 nm, pulse width of ~ 50 fs, and repetition rate of 1 kHz, was focused on a sapphire crystal to generate a broad-

band white light. The light was passed through a 750 nm short-pass filter to eliminate the residual from the fundamental, before collimation using a parabolic mirror. The light was then sent to the objective and focused into  $\sim 2 \mu\text{m}$  spot for the absorption measurement. The absorption spectra were obtained by comparing the transmitted light spectra between the samples and a blank (quartz). Spectral detection was performed using a monochromator (Princeton Instrument) and a photomultiplier tube set-up. The SHG measurements were performed with the kHz laser system that was introduced in section 3.3. The excitation beam was focused onto the sample with a x100 (NA = 0.9) air objective from Nikon ( $\sim 1 \mu\text{m}^2$  spot size). The spectral range of the excitation beam was tuned from 700 to 1500 nm in steps of 50 nm. The excitation and detection polarizations were controlled with half- or quarter-wave plates, in combination with linear polarizers. A continuous-flow optical microscopy cryostat was used for the low-temperature measurements. For the electric-field switchable SHG measurements, the SHG signal was recorded while the drain-source bias (supplied by Keithley Model 6430 Sub-Femtoamp Remote SourceMeter) was swept forward and backward. The polarization-electric field ( $P - E$ ) curve was recorded using a ferroelectric tester (Precision Multiferroic II, Radiant Technologies).

**Computational methods:** The ab initio DFT calculations are performed using Quantum ESPRESSO [235, 236] working with Perdew-Becke-Ernzerhof-optimized norm-conserving Vanderbilt pseudopotentials [237, 238]. The full relaxations of the  $\text{NbOI}_2$  atomic structures are performed with semi-empirical Grimme’s D3 correction [239] using the conjugate gradient scheme until the maximum residual force smaller than  $1 \times 10^{-7} a.u.$  and the maximum energy difference between consecutive iterations is smaller than  $1 \times 10^{-9}$  Ry. A kinetic energy cut-off of 80 Ry for the pseudopotential and a Monkhorst-pack  $k$ -point mesh [240] of  $12 \times 6 \times 1$  is used. A vacuum height of 12 Å is added to prevent interactions between the periodic images. The GW calculation is performed with BerkeleyGW [201, 241, 242] on top of Quantum ESPRESSO with slab coulomb truncation [243], Hybertsen-Louie generalized plasmon pole model [201] and a dielectric matrix cut-off of 10 Ry. The non-uniform neck subsampling is used to sample the reciprocal space in GW [244]. The GW quasiparticle energies are calculated with 1536 bands, using a  $12 \times 6 \times 1$   $q$ -mesh with another 10  $q$ -points in the Voronoi cell around  $q = 0$ , forming an effective uniform grid of more than  $120 \times 60 \times 1$ .

# Chapter 7

## Summary and Outlook

The goal of this thesis was the search for new materials to enhance and enable control over nonlinear optical interactions at the nanoscale with particular focus on frequency conversion and all-optical switching. This chapter will conclude and summarize the works presented in this thesis, before ending with a perspective for the two main aspects of high-harmonic generation and ultrafast switching at the nanoscale.

- **Chapter 4: Gallium phosphide** The experimental part of this thesis started with the comprehensive study of GaP thin films for nonlinear optical applications. It was shown that MOCVD grown nanofilms perform similar to the bulk crystal of the material regarding SHG and THG conversion efficiencies and moreover the nonlinear susceptibilities were extracted. This not only places GaP as a material with among the highest nonlinear coefficients but, together with the low losses in the visible regime, makes it promising for applications at the nanoscale. For the sputtered, amorphous GaP films it was shown that the SHG signal is inherently small, but can be significantly enhanced by nanostructuring it. The investigation of more than one thousand individual a-GaP nanopatches could demonstrate a broad control of the SHG efficiency with particular influence of the light's polarization. With this, a-GaP was established as a cheap and flexible alternative to epitaxial grown thin films, particularly since the fabrication was demonstrated at CMOS compatible temperatures. Finally, the ultrafast optical response of GaP nanostructures were investigated by pump-probe spectroscopy with sub-10 fs pulses. Here it could be shown that the virtually lossless character of c-GaP leads to nonlinear responses within a few tens of femtoseconds that can be associated to the OKE and TPA. By specifically targeting the anapole excitation, modulation depth of close to 50 percent were reached, which makes the system to the currently most efficient all-optical switch at the nanoscale. Altogether, it was shown that GaP exhibits excellent linear and nonlinear optical properties which makes it to one of the most promising materials for nanophotonic applications. Hereby it should be noted that the possible areas of use exceed nonlinear applications. Other examples are photocatalysis [67], bio sensing [22] or flat metaoptics [23] where the unique combination of high refractive index and high transparency of GaP are beneficial. In order to make the fabrication of

c-GaP nanostructures more cost and time efficient, a new fabrication technique was developed that is shown in the Appendix A.2. Here, the wafer bonding process is replaced by a transfer method based on the encapsulation of the GaP structures inside a flexible polymer. This not only makes the fabrication of c-GaP structures less cost intensive but furthermore enables nanostructures in a flexible substrate. This could lead to new nanophotonic systems where parameters (for example the distance or period) can be tuned mechanically by applying pressure or strain.

- **Chapter 5: Niobium Phosphide** This chapter was focused on the optical properties of thin films of niobium phosphide, a Weyl semimetal with a unique electronic structure and topological surface states. It was shown that NbP exhibits a high THG efficiency and that it enhances the nonlinear signal by more than a factor of ten compared to the bulk crystal. By concise polarization dependent measurements, it could be shown that this enhancement can be related to the topological surface states of the material. Furthermore, the ultrafast optical response of NbP thin films was investigated, where a change of reflectivity with complete relaxation in below than 100 fs could be observed. Again, this response was more pronounced than for the bulk of the material what collectively paves the way towards efficient nanophotonics based on Weyl semimetal thin films. Evidently, their unique electronic and optical properties present a wide range of applications, well beyond nonlinear nanophotonics. Here, the ideas range from ultrafast optical detectors that make use of their huge electron mobility [153] or entire microelectronic systems that are based on the topological properties of WSMs [245]. Furthermore, the similar character of WSM to two-dimensional graphene could make it an interesting candidate for (nonlinear) terahertz photonics [246].
- **Chapter 6: Niobium oxide di-iodine** The final experimental chapter was focused on the two-dimensional semiconductor NbOI<sub>2</sub>. It was shown that the material exhibits a strong anisotropy within its electronic band structure and therefore its optical response, a consequence of its ferroelectric character. Additionally it was presented that the spontaneous polarization of the material leads to record-value SHG conversion efficiencies and a consequently high second-order nonlinear susceptibilities. Contrary to other two-dimensional materials, NbOI<sub>2</sub> has the great advantage that its nonlinear signal scales with the thickness of the nanoflakes. The strong piezoelectric character of the material allows furthermore to strongly modulate the nonlinear response by applying bias, cooling to cryogenic temperatures or the introduction of strain. Together with an additional work about the similar material NbOCl<sub>2</sub> which is not included in this thesis (ref. [50]), the presented results propose the entire family of niobium oxide di-halides as promising nonlinear materials. Their strong and tunable response together with their intrinsic ferroelectric character makes them viable for nanoscale elements with efficient frequency conversion.

## 7.1 Outlook: frequency conversion at the nanoscale

The findings that were reported within this thesis unveil a new set of possibilities to specifically engineer and enhance nonlinear optical interactions at the nanoscale. The three presented materials hold large potential for practical applications and progress in the field of nanophotonics such that the next logical step would be to further enhance the nonlinear optical response by implementing them into nanoscale system. This can for example be achieved through the adoption of the following two different approaches. The first revolves around the concept of photonic integrated circuits with waveguides, optical modulators and photodetectors and which presents the first step towards optical computing. The second entails the development of metasurfaces built from the period arrangement of nanostructures on a large ( $\mu\text{m}$  range) scale. Such metasurfaces can effectively manipulate light at the nanoscale were shown to significantly boost nonlinear optical interactions [17]. Hereby, the applications range from flat optical elements [247] over light harvesting [23] to nonlinear holography [248]. Lately, the attention started growing towards metasurfaces for spontaneous photon down conversion, which can be seen as the inverse process of SHG or sum-frequency generation. It is based on the annihilation of a high energy photon and the subsequent emission of two lower energy photons that form an entangled photon pair [9]. This proposes to be a viable source for quantum objects and therefore a promising resource for quantum optical applications and optical quantum computing.

Hereby, the great advantage of GaP is that the fabrication schemes for crystalline or amorphous nanostructures are already established. In combination with the intrinsically low losses of the material, this makes it particularly interesting for waveguiding applications. Here, the longer traveling time can significantly enhance the nonlinear signal and could exemplarily be used for optical switching (see next section). Furthermore, metasurfaces made of GaP could be especially promising for linear or nonlinear applications where strong optical confinement and low losses are a limiting factor.

In the case of NbP and NbOI<sub>2</sub>, the situation is different since currently there are no established nanofabrication techniques available. Therefore, the first step would be to develop reliable and high-quality nanofabrication procedures for both materials. This should be accompanied by suitable numerical simulations, where the results presented in this thesis provide important groundwork by benchmarking their linear and nonlinear optical performances. Although their nonzero losses make both materials less suitable for waveguiding applications, their high nonlinear coefficients proposes them as candidates for nonlinear metasurfaces or smaller optical components. Hereby the properties of NbOI<sub>2</sub> make it particularly promising for applications in the near-infrared to visible regime with a strong focus on ultrathin nonlinear devices. For NbP, a possible application could lie in photon energies larger than the visible regime. As shown, the material here manifests its metallic character and could therefore benefit from plasmonic resonances in a spectral regime that is not easily applicable for other materials given their strong optical absorption.

An alternative approach to built nanostructures for efficient nonlinear effects is the fabrication of hybrid materials, where the advantages of different systems can be combined. A

popular example would be the combination of resonant dielectric nanostructures and the high nonlinear optical coefficients of a two dimensional material [249] or systems composed of dielectric and metallic structures [250]. Another example is shown in the Appendix B.1, where GaP nanostructures are combined with a thin layer of ITO in their center. Hereby, the goal is to make use of the huge nonlinear coefficients of ITO in the vicinity of its epsilon near-zero wavelength and at the same time obtain the strong resonances and low losses of GaP. By tailoring the optical response of the hybrid nanostructures to specifically concentrate the electric field into the thin ITO layer, the results show that the nonlinear conversion efficiency can be enhanced. Particularly for SHG it is presented that the nonlinear signal can be boosted by more than a factor of two.

As a final notice, it should be said that in order of these materials to operate at the forefront of practical application a few challenges have to be met. The scalability of the fabrication techniques and their compatibility with existing systems are key aspects, together with a high reproducibility and stability of the optical properties over extended periods of time. Although the works presented in this thesis haven't met limitations in this regard, this has to be ensured by future investigations.

## 7.2 Outlook: all-optical switching

Given the results on all-optical switching that were presented in this thesis, the next step is to actually implement a nanoscale all-optical switch, ideally in combination with a photonic integrated circuit. Consequently, the points that were mentioned in the previous section hold here as well. In order to compete with current electronic devices, an optical switch should fulfill a few requirements. It has to have a small enough footprint to enable the integration into an integrated circuit, it should have a reasonable modulation depth (typically  $> 5$  dB [31]) and of course a fast switching speed. Under these aspects, the results that were presented for the c-GaP nanodiscs are more than promising and put a realization of all-optical switches based on GaP in perspective. Furthermore, the recently reported waveguides based on the material and its strong third-order nonlinear response [100] pave the way for GaP-based integrated photonic circuits. An alternative switching procedure can use the generation of new frequencies based on the second-order nonlinearity of a waveguide [4], which would benefit from the generally higher nonlinear coefficients of the material.

Regarding NbP, the ultrafast optical response of the material has a wide range of directions to investigate. Particularly the topological surface states and the unique electronic structure could provide 'slow' nonlinearities with relaxation times that are magnitude faster than for classical materials. Moreover, NbP is the first material of an entire family that was realized as high-quality thin film, which implies that there will be more candidates from the WSM family with interesting and promising ultrafast properties.

### Towards time-varying photonic crystals

Another field of photonics that works with the ultrafast change of the refractive index is the field of time-varying physics. It is based around systems where the dielectric function of a material is varied in time instead of in space which involves a multitude of exotic physics and phenomena [251]. Two examples are given by the works in ref. [252] and ref. [253], which are not included in this thesis but can be found in the Appendix B.2. Here, the analogue of a single and double-slit experiment are realized in the time domain, meaning instead of slits in space the refractive index of an ITO based metamaterial is modulated in time. In the classical experiments, the light interacts with the slits to form the well-known diffraction/ interference patterns that can be seen as modulation in the light's momentum. Contrarily, the frequency of the light is not affected in these experiments, which is a consequence of the temporal symmetry. In the time varying analogue experiment, the opposite situation is the case: here the time invariance of the system is broken such that the momentum is conserved while the frequency of the light is modulated. In the case of a temporal single slit (ref. [252]) this manifests as a broadening of the pulse spectrum and for the double slit in time (ref. [253]), the frequency spectrum broadens and shows an oscillatory shape, caused by interference in time.

Moreover, it is shown that this (temporal) interference pattern in the spectrum can be an effective probe of the ultrafast dynamics that happen in the material. In the case of the used ITO metamaterial, this was measured to be in the range of a few femtoseconds, which is much faster than previously expected and is at the time scale of a single optical cycle. This could open new possibilities for all-optical applications with switching speeds that are no longer limited by the pulse length of the laser itself. This is particularly remarkable since it was achieved with ITO, a material with significant contributions from non-parametric nonlinearities. Additionally, the presented results have the great advantage that the measurement and analysis of a pulse spectrum are easy to conduct, especially compared to other ultrafast experiments with complex pulse compression and data collection procedures.

The field of time-varying physics already present a promising approach for all-optical switching, but the possibilities go even further. The ultimate goal of time-varying physics is to extent the shown phenomena towards a time-varying photonic crystal, which would be the analogue of a traditional photonic crystal - a periodic lattice for light in space - but in the time domain. The realization of this technology could enable a plethora of interesting and new physics and could furthermore lead to applications such as parallelized all-optical switching or a new vision for quantum computing [251]. Hereby, materials with high and fast optical nonlinearities, as the systems presented in this thesis, are of particular interest and hold to be potential to be a platform for future time-varying systems.



# Appendix A

## Supplementary Information

### A.1 Fabrication - parameters

| material | gas flow (argon) | chamber pressure | deposition rate | temperature | rotation |
|----------|------------------|------------------|-----------------|-------------|----------|
| GaP      | 20 sccm          | 2 mTorr          | 0.5 Å/s         | RT - 350°C  | 10 rpm   |
| ITO      | 20 sccm          | 2 mTorr          | 0.3 Å/s         | RT - 350°C  | 10 rpm   |

**Table A.1:** Parameters for typical sputter depositions performed for this thesis. RT stands for room temperature.

| material         | gas 1 (flow)                | gas 2 (flow)                                | CVD power |
|------------------|-----------------------------|---|-----------|
| SiO <sub>2</sub> | N <sub>2</sub> O (512 sccm) | SiH <sub>4</sub> /N <sub>2</sub> (155 sccm) | 20 W      |

**Table A.2:** Parameters for typical PECVD depositions performed for this thesis.

| material         | gas 1 (flow) | gas 2 (flow)               | HF power | ICP power |
|------------------|--------------|----------------------------|----------|-----------|
| GaP              | Ar (30 sccm) | Cl <sub>2</sub> (10 sccm)  | 300 W    | 31 W      |
| SiO <sub>2</sub> | Ar (30 sccm) | CHF <sub>3</sub> (20 sccm) | 30 W     | –         |

**Table A.3:** Parameters for typical ICP-RIE etching performed for this thesis.

### A.2 Fabrication of c-GaP nanostructures

Within this thesis, a new technique for the fabrication of c-GaP nanostructures was developed in closed collaboration with Andreas Aigner. While the structures that were used for chapter 4.3 of this thesis were fabricated with a wafer bonding process, the alternative procedure is sketched in Fig. A.2. It starts with the purchase c-GaP films on top of a

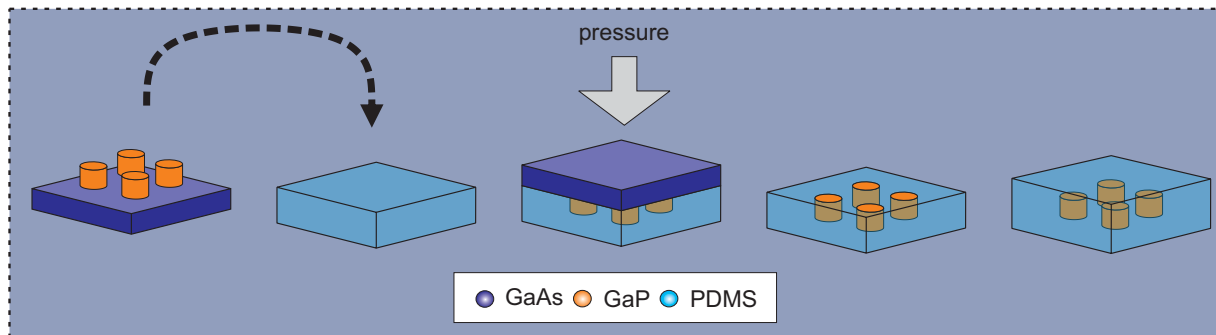


**Figure A.1:** Scheme of the fabrication for c-GaP nanostructures.

gallium arsenide (GaAs) wafer. Following the procedure described in the main part of this thesis (3.1.2), the desired nanostructure pattern is transferred into the c-GaP film. Then, the substrate transfer is performed using the polymer polydimethylsiloxane (PDMS) that can be prepared in a liquid phase. The nanostructure piece of GaAs is then pressed upside down into the liquid, such that the backside is not covered by the PDMS. Then, the PDMS is dried and hardened under vacuum, typically for about 24 hours. Next, the GaAs is dissolved by putting the material stack into a 5:1 mixture of citric acid ( $C_6H_8O_7$ , dissolved in water - ratio 1:1) and hydrogen peroxide ( $H_2O_2$ , 30% solution in water) for about seventeen hours (depending on the wafer piece size). Finally, a second layer of PDMS is put on top to completely encapsulate the c-GaP structures. The great advantage of this technique is that it doesn't need additional equipment (e.g. a wafer bonder) and that the substrate of the structures can be chosen freely. Furthermore, the complete encapsulation of the nanostructures is a great advantage for many optical resonances, e.g. quasi bound states in the continuum.

# Appendix B

## Supplementary works

### B.1 Hybrid nanostructures made of GaP and ITO

This section is based on a manuscript that is currently under preparation for submission. Romain Tirole, Benjamin Tilmann, Leonardo de S. Menezes, Stefano Vezzoli, Stefan A. Maier, Riccardo Sapienza

*"Dielectric epsilon near-zero hybrid nanogap antennas for nonlinear nanophotonics"*

The implementation of nonlinear optics at the nanoscale and at visible to near-infrared (IR) wavelengths is of great interest for technical applications such as quantum light sources, optical circuits and frequency control or biophotonics. Although, nanoantennas provide a gateway to efficiently couple incident light into structures at the nanoscale, other aspects such as lack of interaction volume or low damage threshold remain challenging. In particular the later limits the possible usage of plasmonic structures made of (noble) metals, together with their significant Ohmic losses. Hence, all-dielectric materials have proven to be a promising alternative platform for nanophotonics. Particularly, type IV and III-V semiconductors are transparent for energies below their electronic band-gap while exhibiting large linear refractive index as well as high nonlinear susceptibilities, making them ideal candidates for nonlinear applications [19, 254, 255]. Similar characteristics appear in two-dimensional materials and more specifically transition metal dichalcogenides, however, their naturally small interaction volume yields only low absolute signal and lowers the damage threshold due to high excitation intensities [256].

Semiconductor nanoantennas have shown efficient harmonic generation [21, 64, 69, 118, 257–260] and ultrafast nonlinear optical switching [37, 39, 134, 148] in various materials such as Silicon, (Aluminum) Gallium Arsenide, Gallium Phosphide (GaP) or Germanium. By acting as nanocavities they open the path to larger interaction volumes while maintaining strong resonant behavior with a high tolerance to incident field intensities. Particularly the magnetic dipole [21, 118, 257, 260] and anapole resonances [64, 69] of nanodisks have been exploited for harmonic generation given their characteristic strong field confinement within the medium. These single-particle modes can also be used as building blocks for collective resonances: dielectric metasurfaces with various geometries were shown to exhibit

high quality factors [125, 129, 133, 261], emerging from bound states in the continuum or constructive interference between single-antenna modes and lattice resonances.

Even though mode engineering in dielectric nanostructures is the main way to enhancing the light-matter interaction, the integration of multiple materials within a single antenna to enhance its properties is a current topic of interest within the nonlinear nanophotonics community [149, 167, 262–264]. In particular, creating a gap inside a dielectric nanoantenna in the lateral direction, filled either with air or a low-index material has been investigated to change local properties of the system [265]. Thanks to the optical contrast between the high-index dielectric and the gap, the field intensity and local density of states is increased proportionally to  $n_d^4/n_s^4$ , where  $n_d$  and  $n_s$  are the refractive indices of the antenna and the slot, respectively. Moreover, as long as the slot’s volume is significantly smaller than that of the dielectric structure, the antenna retains its resonant properties, determined by its effective refractive index. However, the integration of multiple materials within an antenna’s plane remains a fabrication challenge, and attention has been turned to the realisation of photonic gap antennas [266]. Recently, a photonic gap using a low index material slotted in Silicon was demonstrated and used for enhanced harmonic generation [267].

Here, we propose a comparison of a photonic gap antenna made of gallium phosphide (GaP) and antimony-tin-oxide (ITO) nanolayer against a GaP antenna. We demonstrate that the presence of the thin ITO layer allows for efficient generation of second- and third-harmonics over a broad range of frequencies, beyond the bandwidth of its Epsilon-Near-Zero (ENZ) condition. This is confirmed by comparison with a GaP-only antenna and we show that particularly the electric dipole (ED) resonance appears as a viable alternative to the magnetic dipole (MD) commonly used in harmonic generation in nanoantennas. This result opens new paths to the integration of ITO and ENZ materials in antennas, by enabling a new resonance for mode or directivity engineering, as well as time-modulated antennas for frequency control and holography [268, 269]. Furthermore, the concept of photonic gap antennas presents a new and flexible platform with possible applications such as Purcell-enhancement of quantum emitters or combination with two-dimensional materials.

### B.1.1 From classic to photonic gap antenna

#### Design and modelling

Our photonic gap antenna consist of a GaP nanoantenna with a thin layer of ITO in the center, sketched in Fig. B.1a. The hybrid nanodiscs were designed such that they have optical resonance in the near infrared (near-IR) spectrum, where ITO is in its ENZ region. Here, the real part of the dielectric function approaches (and crosses) zero, while the imaginary part is sufficiently small. Therefore, the optical contrast between the GaP disc and the gap material is the largest possible, as shown in Fig. B.1b. While the scattering properties of the hybrid structure are only weakly affected by the refractive index perturbation from the ITO layer (which makes only 7.5% of the volume of the antenna), the continuity of the displacement field vector  $\vec{D}$  requires a change in the electric near-field

distribution. This leads to strong field confinement in the low-index region (pink line in Fig. B.1b). A second advantage of ITO as gap material are its high nonlinear coefficients when working in the vicinity of the ENZ wavelength [40, 270, 271]. Looking into the simulated near field distribution within the  $(x, z)$  plane of the antenna, for a wavelength of 1160 nm and radius of 200 nm resonant at the MD, for a  $x$  polarised pump, one can see in Fig. B.1d that the field is mainly distributed at the edges of the ITO layer. This is quite different from the field distribution in a bulk GaP antenna, where it is distributed over a larger volume around the center of the antenna.

Contrarily, Fig. B.1c shows the near field of a GaP-only antennas, which is weakly concentrated of the nanoantenna's volume. The nanodiscs were designed to exhibit resonances in the range from 1.2 – 2  $\mu\text{m}$ , based on finite-difference time-domain (FDTD). The resulting simulated scattering cross section  $\sigma_{scat}$  is shown in Fig. B.1e as a function of radius and wavelength. The scattering spectrum is dominated by two resonances that can be associated with the electric (ED) and magnetic (MD) dipole, respectively. At the same time, linear scattering simulations confirm that the photonic gap antenna preserves the dielectric Mie resonances with a magnetic dipole (MD) and electric dipole (ED) resonance visible in the scattering cross section.

### Fabrication and harmonic measurement

We fabricated the hybrid structures by a multi-step sputtering process that results in a GaP-ITO-GaP film with the desired thicknesses. The nanodiscs were then defined by electron-beam lithography (EBL) and subsequent reactive ion etching (RIE), more details can be found in the Experimental Details. The distance between single antennas is kept at 3  $\mu\text{m}$  to prevent cross-antenna coupling. GaP-only nanodisks with the identical dimensions were fabricated following the same process. A scanning electron microscopy (SEM) image of the photonic gap discs with varying radii is shown in Fig. B.1f (bottom left). Looking at the tilted SEM image in the insets of Fig. B.1f, one can clearly observe the three distinct layers which confirms the successful fabrication of the photonic gap antennas. Furthermore, a measurement of the optical constants via spectral ellipsometry results in the expected permittivities shown in the Experimental Details. As expected, the dielectric function of ITO crosses zero at around 1350 nm and the ENZ regime indicated by the red shaded area in Fig. B.1g.

Next, the GaP and photonic gap nanodiscs were investigated with respect to their nonlinear optical response by using a microscopy setup, with a tunable wavelength laser with 100 kHz repetition rate and 225 fs (FWHM) pulses. The generated nonlinear signal is collected in reflection geometry and then either sent to a single photon detector or a spectrometer to respectively map out the resonances as a function of radius and illuminating wavelength, or measure the light's spectrum. To calculate the intensity at each wavelength, average excitation power and beam size were measured at the focal position. More details of the experimental setup can be found in the Experimental Details.

For an excitation wavelength of  $\lambda_0 = 1350$  nm and a nanogap disc radius of  $\sim 330$  nm, the corresponding SHG and THG spectrum are shown in Fig. B.1h. The collected

light is indeed harmonic centered at  $\lambda_{SHG} = 675 \text{ nm} = 1350 \text{ nm}/2$  and  $\lambda_{THG} = 450 \text{ nm} = 1350 \text{ nm}/3$ , with no photoluminescence evident. Measurement on GaP yield the same harmonic signals with different amplitudes. Due to the amorphous nature of the GaP, the SHG is expected to be largely generated by surface contributions, not the bulk of the material [24, 70]. Since THG doesn't have this limitation, we chose that as probe to investigate the nanodisks' resonances in the following.

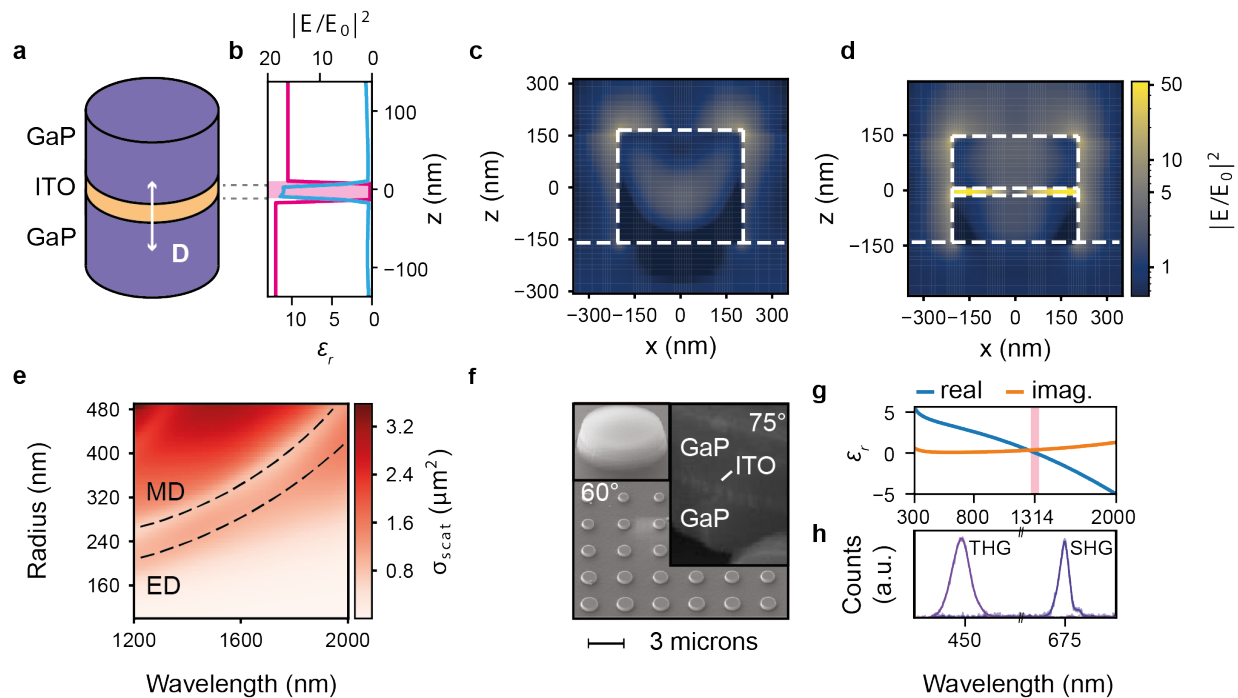


**Figure B.1:** GaP and photonic gap nanodisks for nonlinear light generation. **a** Sketch of the photonic gap antenna concept. The displacement field is represented by the white double-ended arrow. **b** Diagram of the expected field intensity distribution (pink) as a function of the centered antenna depth, resulting from the permittivity contrast (light blue). **c,d** Simulated field intensity profile in logarithmic scale, the XZ plane for a radius of 200 nm and 1160 nm wavelength for the GaP (**c**) and photonic gap (**d**) antennas. White dashed lines show the contour of the different materials. **e** FDTD simulation of the scattering cross section of a GaP antenna as a function of pump wavelength and antenna radius. The ED and MD modes are highlighted with the black dashed curves. **f** Scanning electron microscopy image of the sample, taken at angles of 60 and 75 degrees (tilted). **g** Refractive index spectrum of ITO: real (blue curve) and imaginary (orange curve) parts. The ENZ region is highlighted with the red-shaded area. **h** Second- and third-harmonic spectra from a photonic gap antenna of radius of 330 nm and illumination wavelength of 1350 nm.

## B.1.2 Comparison and discussion of the photonic gap antenna

### Harmonic resonances and broadband enhancement

For a qualitative and quantitative characterisation of nonlinear effects in the photonic gap antenna, it is necessary to study how the generation of harmonic light is affected by the introduction of the ITO layer in the GaP nanodisc. Fig. B.2a shows the measured THG counts per unit intensity for GaP discs with different radii and excitation wavelengths. Three distinct lines are clearly visible, and can be associated to the scattering simulation in Fig. B.1e. It follows that the lower and upper resonance correspond to the ED and electric quadrupole (EQ) resonance, which are accompanied by comparably low field confinement in the volume of the nanoantenna. Therefore, both resonance results in a weak emission of THG light in Fig. B.2a. For the MD on the other hand, more than one order of magnitude higher THG signal can be observed as here the nonlinear process is boosted by the concentration of the electric field inside the volume of the nanodisc. This is confirmed by nonlinear scattering simulations that qualitatively reproduce the measured THG signal with good agreement.

Following the same procedure, THG was measured for the hybrid GaP-ITO nanostructures, shown in Fig. B.2b. Again, the previous three resonances can clearly be seen, with the ED, MD and EQ appearing at similar radii and wavelengths as for the GaP-only structures. One can see the MD mode yields less signal further in the IR, around 1650 nm wavelength, but presents a higher generation efficiency in range near its ENZ wavelength (1300 – 1400 nm). Furthermore, the mode seems to be broader in wavelength, and the photonic gap antenna seems to exhibit a higher efficiency off resonance than the GaP. The photonic gap antenna shows a distinctive feature in mode evolution when compared to the GaP antenna in its ED resonance. Fig. B.2c represents the extracted resonant radii of the disks for each excitation wavelength. Each line corresponds to the evolution of a resonance's most harmonic efficient wavelength, for each radius. All three modes are clearly visible for GaP (light red), and as expected increase in wavelength with increasing radii as the GaP antenna is a cavity. This is verified by nonlinear scattering simulations (dark red, for more details refer to Experimental Details of section 4.1), which agrees very well with the experimental measurement. For the GaP-ITO antenna, a similar behavior can be observed for the MD and EQ resonances, agreeing well with the course of the GaP-only case and the simulations. For the ED however, a particular dip in the resonant wavelength can be observed for the ED mode, that happens around the ENZ region. Here, the course of the ED resonance drops by  $\sim 50$  nm when the illuminating pump wavelength is increased by the same amount.

As the purpose of the introduction of ITO in the GaP antenna is an enhancement of nonlinear properties around the ENZ wavelength, the second and third-harmonic signals from the antennas are shown at the wavelength of 1350 nm in Fig. B.2d. For THG (upper panel), the enhancement from the photonic gap (purple) against GaP (dark yellow) is very limited at the ED and MD mode, with only an enhancement by a factor of 1.3 (respective values of 10.45 and 8.01 kHz.cm<sup>2</sup>/GW). Yet, the resonances are significantly broadened

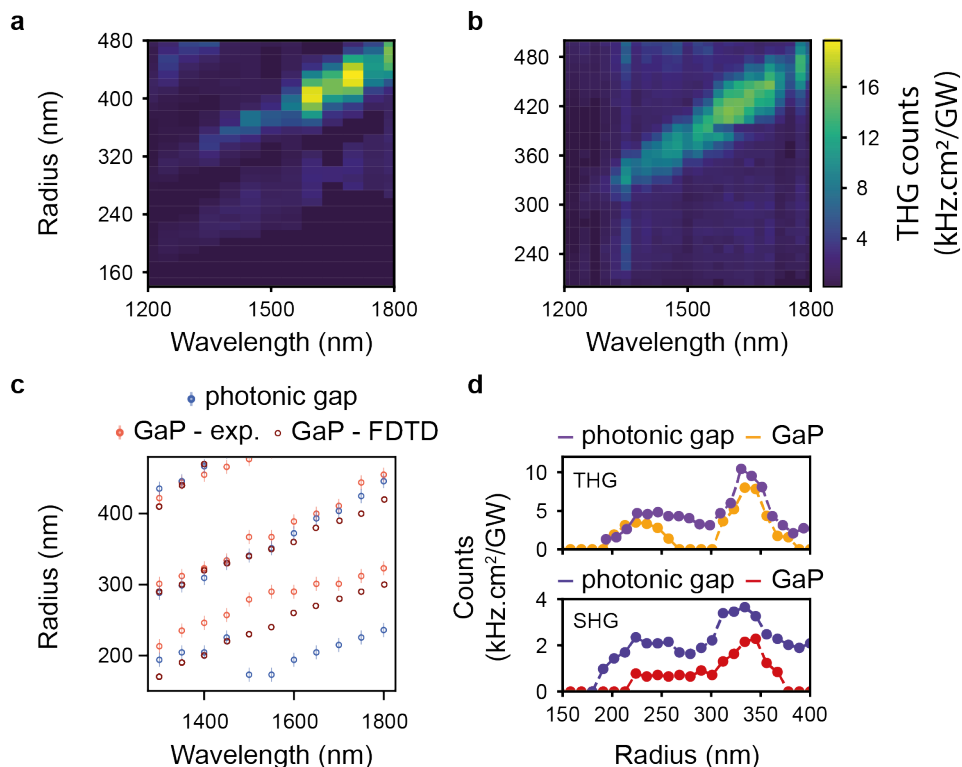


**Figure B.2:** Characterisation of the nanodisk's nonlinear signals. **a,b** Experimentally measured THG signal in counts per second per unit intensity as a function of disk radius and pump wavelength for GaP (a) and photonic gap (b) nanodisks. **c** Extracted resonant wavelength for the ED, MD and EQ modes as a function of radius for the photonic gap antenna (blue diamonds), GaP antenna (red diamonds) and as predicted by FDTD for GaP antennas (red circles). **d** Comparison of THG (top) and SHG (bottom) efficiency between the photonic gap (purple and blue curves) and the GaP (yellow and red curves) nanodisks, for a wavelength of 1350 nm.

over a range of radii, with counts staying at a constant level between 230 and 300 nm radius. On the other hand, SHG is increased over a broad range of radii (blue against red line, lower panel). This can be explained by the added amount of interfaces between layers, essential in the generation of the second-harmonic as it increases the surface area where SHG occurs [70], along with a potential higher second-order nonlinear susceptibility from the surface of ITO.

Though the photonic gap effect is visible thanks to a light enhancement of harmonic generation near the ENZ wavelength of ITO, this is not comparable to the values reported in [267]. This is a reminder to dive back into the fundamental ingredients of nonlinear optics: nonlinear susceptibility, volume and field enhancement. In nonlinear nanophotonics, focus is usually given to the later, but we will now show the barrier the first two still pose.

### Nonlinear susceptibility and field distribution

ITO is a well known material in the nonlinear nanophotonics community, and has been thoroughly characterised by Z-scan and pump-probe spectroscopy [41, 270]. Yet, these techniques are efficient at estimating third-order nonlinearities for the Kerr effect, corresponding to a nonlinear susceptibility tensor of taking the form of  $\chi^{(3)}(\omega, \omega, \omega, -\omega)$  where the first frequency refers to the outgoing wave and the following ones to the waves interacting via the nonlinearity. For THG, the nonlinear susceptibility is evaluated for different frequencies of  $\chi^{(3)}(3\omega, \omega, \omega, \omega)$  and can thus take a different value. Thus, observing strong Kerr nonlinearities in ITO does not guarantee observing efficient THG.

The  $\chi^{(3)}$  of GaP and ITO are compared to verify whether the later provides a viable option to enhance harmonic generation. To measure their nonlinear susceptibility, the samples are illuminated under low numerical aperture for various beam polarisations, and the generated third-harmonic is collected and then sent through a polariser to a detector. Then, the measured harmonic power is processed using nonlinear scattering theory (for more details refer to Experimental Details of section 4.1) and compared to the illuminating power to extract a value of the nonlinear susceptibility. A 400 nm thick GaP thin film as well as three thin films of ITO with various thicknesses (40, 100 and 310 nm) were investigated. A 20 nm ITO thin film was fabricated but yielded too weak harmonic signal in the following configuration to give an accurate value. The resulting third-harmonic nonlinear susceptibility spectra are presented in Fig. B.3a. As can be seen, GaP (in red) has a  $\chi^{(3)}$  an order of magnitude above that of ITO (in blue), with a value of  $6.95 \times 10^{-19} \text{ m}^2/\text{V}^2$  at 1350 nm wavelength. All three ITO samples, with various thicknesses and different ENZ wavelengths in the near-infrared region, have comparable third-harmonic susceptibility. For this reason, we assume the nonlinear susceptibility of the 21 nm layer of ITO within the photonic gap antennas to be equal to that of the 40 nm layer.

Hence, there is a conflict between the resonance of the antenna concentrating the field within the ITO layer and the higher optical nonlinearity within the GaP. We further investigate this by looking at FDTD simulations, more precisely at the average field enhancement (normalised to the illuminating field intensity), shown in Fig. B.3b (top panel) for a radius of 320 nm. Clearly, the field is highly concentrated into the ITO layer (blue line).

But evidently, this didn't lead to an increase of the total THG signal, which can be explained of the volume distribution, where the ITO layers occupies only 7.5% of the total. This explains the low shift in the overall antenna resonant radius, but as Fig. B.3b shows it also plays against the third-harmonic enhancement from the photonic gap effect. The scale of the generated signal can be estimated by integrating the generated harmonic ( $|E|^2/|E_0|^2$ )<sup>3</sup> over the height of each layer. The resulting estimation shows an even further reduced contribution of the harmonic signal from ITO, which is now similar to that of GaP, for a differing resonant wavelength, see Fig. B.3c.

Another parameter is a possible resonance of the nanodisc at the third-harmonic wavelength. To achieve a maximum harmonic generation, a strong resonance at the fundamental is not only needed: a resonance at the harmonic, with good coupling to free space and a compatible spatial and polarisation overlap is important in enhancing the up-conversion

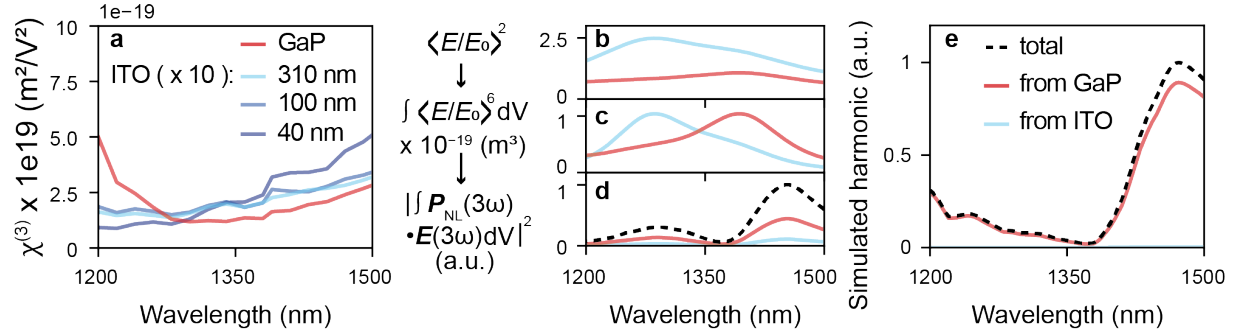


**Figure B.3:** Mechanisms reducing harmonic generation from the ITO layer. **a** Measured  $\chi^{(3)}$  of various ITO thin films, with 40 nm (dark blue curve), 100 nm (blue curve) and 310 nm (light blue curve) thicknesses, and of GaP (red curve). The nonlinear susceptibilities of ITO are multiplied by 10 for comparison. **b** Average intensity enhancement with regards to the incoming beam, in the ITO (light blue curve) and GaP (red curve) layers, simulated using FDTD. **c** Corresponding intensity enhancement integrated over the volume of the layers. **d** Harmonic signal as predicted from nonlinear scattering theory, taking into account mode overlap, interference and out-coupling of the harmonic. The total generated field intensity is shown with the dark dashed curve for comparison. **e** Predicted harmonic signal from nonlinear scattering theory taking into account the nonlinear susceptibility of the various layers.

process [272]. Using nonlinear scattering theory allows to observe the resulting change in harmonic generation efficiency from the ITO and GaP layers in Fig. B.3d: due to a better coupling and overlap in GaP at the harmonic wavelength, ITO is no longer the dominant THG layer of origin. The nonlinear scattering model not only takes into account the overlap of fundamental and harmonic modes, it also predicts for the interference from harmonic fields generated by nonlinear point currents located at different locations within the antenna. It is possible that beyond showing a lower overlap, the ITO layer also suffers from interference due to different regions within the layer having different phases. Yet, it can be seen in Fig. B.3d that the ITO layer interferes constructively with the harmonic light generated by the GaP layers by looking at the total generated field intensity (dark dashed line), supposing fields in ITO and GaP are in phase. Thus, it is a reasonable assumption that various harmonic fields in ITO are in phase, and the decrease in the layer's harmonic efficiency are due to poor spatial overlap in the nonlinear scattering model. Finally, by taking into account the amplitude of the nonlinear susceptibility, the contribution of harmonic from the ITO layer is further reduced by a factor of 10 in comparison to GaP, leaving GaP as the dominant medium for harmonic generation in the photonic gap antenna, as observed in Fig. B.3e, and showing a final enhancement from the presence of ITO of 1.17, close to the measured value of 1.3.

We have thus shown that the insertion of an ITO photonic gap in a high-index dielectric antenna brings little advantage in third-harmonic enhancement if the base material shows high nonlinearities. Similar results are expected to hold for Al-GaAs, Ge, or LiNbO<sub>3</sub>, with

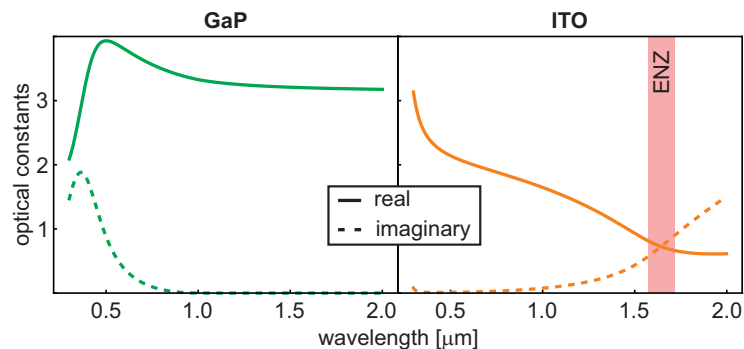


**Figure B.4:** Extracted optical constants for the sputtered GaP film (left) and ITO (right) film. The ENZ regime is indicated.

ITO or AZO as a photonic gap layer. Second-harmonic generation, on the other hand, is enhanced, which we attribute to the fact it is not generated in the bulk of centrosymmetric materials such as a-GaP or ITO [24, 70], and is proportional to area and not volume, thus mitigating the limited height of ITO. Furthermore, the field distribution is enhanced at the surface of the ITO, while for GaP the field is more evenly distributed throughout the volume.

Instead, we suggest an alternative application for nonlinear photonic gap antennas. To take advantage of the strong Kerr effect and field enhancement within the ITO layer, the photonic gap antennas could be used for ultrafast switching and frequency modulation via time-varying effects. By experiencing a strong and swift change in permittivity under pumping at the resonant wavelength, a probe beam at the same wavelength should undergo changes in carrier frequency [273] and spectral width [252]. Then, factors such as overlap and interference of the harmonic field are ruled out, while making use of the strong Kerr nonlinearity of ITO.

### B.1.3 Conclusion

In summary, we have characterised the crossing between the resonances of a GaP high-index dielectric antenna and the photonic gap effect from an ITO thin film, by measuring a broadband enhancement of SHG and THG signal from the nanodisks. The comparison to a GaP-only antenna shows the conservation of the mode resonances and a significantly increased second-harmonic signal across all photonic gap antenna radii, while the third-harmonic, though slightly enhanced, shows a limited increase in efficiency. We attribute this to a combination of lowered parametric nonlinearities in ITO in comparison to GaP, as well as the limitations of volume and field overlap affecting the overall signal generated by the photonic gap layer. This demonstrates the limited efficiency of ENZ photonic gap antennas for nonlinear light generation. The authors suggest that instead these nanodisks should be used to leverage the exceptional properties of ITO and other transparent conducting oxides for ultrafast switching or time-varying effects [40, 251].

## Experimental Details

**Sample fabrication:** The layered thin films were fabricated by subsequent sputter steps using the Angstrom deposition tool. First, a layer of GaP with the targeted thickness of 155 nm was deposited, followed by a 20 nm thin layer of ITO and finally a second layer of GaP with again 155 nm of thickness. During the process, the temperature is kept constant at 350 nm but the chamber is allowed to cool during the processes to avoid cross contamination of the materials. Finally, a 70 nm thick layer of SiO<sub>2</sub> was deposited on top via PECVD. The EBL process was carried out at 30 kV acceleration voltage, a 20 μm aperture and PMMA as photoresist. The development was done in MIBK:IPA for 50 s, subsequent rinsing in IPA and 10 s of oxygen plasma treatment (20 sccm and 40 % power). The 50 nm gold mask was deposited using electron beam evaporation before the lift-off was carried out by a bath in Remover 1165 at 80 °C for several hours. Next, the patterns are transferred into the SiO<sub>2</sub> layer via ICP-RIE and fluorine based chemistry, after which the gold mask is removed using a wet etchant. Finally, the structures etched into the GaP-ITO-GaP layer by another ICP-RIE step with chlorine gases.

**Linear optical characterization:** The samples were characterized using spectral ellipsometry. Thereby, additional substrates were added to the sputtering tool and removed after each step. This allowed to in the end have four different samples for characterization: the three single thin films and the three-layer film. First the three single films were measured independently to reduce the number of parameters compared to the stacked sample. For the latter, the fitting of the ellipsometry was then only used to identify small deviation. The resulting dielectric function of the three layers are shown in Fig. B.4.

**Nonlinear measurements:** The nonlinear measurement were performed at Imperial College London, using a similar setup to the one introduced in section 2.4. It consists of a 100 kHz laser system by Light Conversion Ltd that pumps an OPA for wavelength extension that delivers pulses with ~ 220 fs ultrashort pulses . The light is focused at the sample using a 60× objective (NA = 0.85) and the generated light is collected in reflection geometry. After suitable filters, the light is then sent to a Micro Photon devices PDM single photon detector, or alternatively to a Princeton Instruments spectrometer. The control over the illumination area is given by a Piezoconcept C3 3-axis piezo stage.

## B.2 Time-varying experiments with indium tin oxide metasurfaces

### B.2.1 Saturable time-varying mirror based on an ENZ material

This work is published in [252]:

Romain Tirole, Emanuele Galiffi, Jakub Dranczewski, Taran Attavar, Benjamin Tilmann, Yao-Ting Wang, Paloma A. Huidobro, Andrea Alu, John B. Pendry, Stefan A. Maier, Stefano Vezzoli, Riccardo Sapienza

*"Saturable time-varying mirror based on an ENZ material"*

Physical Review Applied 18(5), 054067 (2022), DOI: 10.1103/PhysRevApplied.18.054067  
for publisher permission, see Appendix C

Fundamental wave phenomena such as refraction and reflection rely on altering the wavevector of a wave by spatially modulating the permittivity, e.g. in a metamaterial. Conversely, a structured permittivity in the time domain manipulates the wave frequency.

Time-varying systems are a platform for a wealth of exotic physics [251], including nonreciprocity [274–276], amplification [277, 278] and topology [279–282], as well as quantum-relativistic effects [278, 283], promising novel applications including photonic refrigeration [284] and temporal aiming [285].

However, bridging the gap between theory and experiment in time-varying systems has proven especially challenging at optical frequencies and ultrafast time-scales. Until recently, optical experiments have been mostly confined to silicon waveguides [286], micro-ring resonators [287] or slow-light photonic crystals [288], but at the cost of a narrow bandwidth and a slow temporal response.

Instead, nonlinear optical interactions in epsilon-near-zero (ENZ) materials such as transparent conducting oxides (TCOs) exhibit very strong, broadband and ultrafast optical nonlinearities around their ENZ frequency [40, 270, 271, 289, 290], while featuring high damage thresholds. Because of these favorable properties, the photo-induced permittivity modulations in Indium-Tin-Oxide (ITO), based on the excitation and relaxation of intraband hot electrons, can be driven on sub-picosecond time scales [273] with order-of-unity refractive index changes [40]. Time-varying physics have been observed in TCOs, with effects such as time-refraction [291–294] and time-reversal [295] of pulses, as well as in hybrid metal-dielectric metasurfaces with strong-ultrafast switching [296, 297], frequency shifting [41, 273, 293, 298, 299], polarisation switching [297] and high-harmonic generation [300]. Frequency shifts as large as 11 THz were achieved in a bulk 610 nm thick film of ITO [291]. However, the translation to thinner films, below 100 nm, has proven challenging due to the lack of interaction volume and propagation length within the active medium, with shifts limited to 1-2 THz [273, 296, 301]. Time-varying effects have been boosted by exploiting optical resonances both in all-dielectric [35, 148, 261, 268] and hybrid plasmonic-ENZ metasurfaces [273, 292, 293], albeit limited by damage thresholds lower than in bulk ITO.

Here, we exploit the Berreman absorption resonance of a layered ITO-gold stack as a time-varying mirror. We demonstrate experimentally and model theoretically a giant, ul-

trafast modulation of its reflection coefficient, which leads to an absolute reflectivity change  $\Delta R \approx 0.6$  ( $\Delta R/R \approx 1000\%$ ). Moreover, for optical pumping beyond a saturation intensity  $I_{\text{pump}} \approx 100 \text{ GW/cm}^2$ , we observe the generation of new frequencies in the reflected probe spectrum which extend to a 31 THz range. We interpret this as a shortening of the response time of the time-varying mirror, which we confirm with a four-wave-mixing experiment.

In a subwavelength and ultrafast time-varying mirror, as depicted in Fig.B.5(a), an incident light pulse is reflected with a time-varying complex reflection coefficient  $r(t) = \rho(t) \exp[i\phi(t)]$ . The phase  $\phi(t)$  and amplitude  $\rho(t)$  of this modulation are imparted to the reflected light; however, as these are changing on a timescale comparable to the optical oscillations of the pulse, new frequency components will be generated. Qualitatively, as illustrated in Fig.B.5(b-c), a quick decrease of the Fresnel coefficient amplitude  $\rho(t)$  leads to a temporal narrowing and consequently to a spectral broadening of the reflected pulse, while a change of phase  $\phi(t)$  leads to a spectral shift. Therefore, a time-varying mirror can manipulate the frequency content of the reflected laser beam.

An ideal time-varying mirror should be able to provide a large change in its complex reflection coefficient, close to unity in amplitude, so that it can be completely switched on and off, and with a phase shift of order  $\pi$  radians, over time-scales of the order of the optical period ( $\sim$ fs), in order to give rise to significant spectral modulation. Moreover, for the mirror to be modelled as a time varying interface, it needs to consist in a material of subwavelength thickness.

We study a time-varying mirror consisting of a 40 nm thin film of Indium Tin Oxide (ITO) with ENZ frequency  $f_{\text{ENZ}} \approx 227 \text{ THz}$ , deposited on glass and covered by a 100 nm gold layer as depicted in Fig.B.6(a). The resulting structure is much thinner than the effective wavelength at  $f_{\text{ENZ}}$ , which is  $\approx 1322 \text{ nm}$  in free space ( $\sim 6.6 \mu\text{m}$  in the layer). As analytically computed in Fig.B.6(b) for our sample, thin films of ENZ materials exhibit plasmonic ENZ modes (black line) beyond the light cone (white dashed line), as well as a Berreman mode above the light line (red-marked reflectance dip) [302]. The deeply-subwavelength thickness of the system allows efficient coupling to the resonant guided Berreman mode from free space, without the need of complex coupling architectures, yet with a large density of states. The highly reflective gold layer increases the confinement of the Berreman mode into the ITO film, thus enabling higher pump field intensities over a large incident angular range, from  $60^\circ$  to  $70^\circ$ , allowing for the resonant coupling of both pump and probe beams.

As shown in Fig.B.6(c), experimental evidence of the efficient coupling to the Berreman mode is manifested in the strong reflection dip measured at an angle of  $65^\circ$  close to the Brewster angle, for frequencies just below  $f_{\text{ENZ}}$  (230 THz/1300 nm). This compares very well to the theoretical prediction shown in Fig.B.6(d) (dotted line), overimposed to the experiment (solid line).

The reflectivity of the time-varying mirror can be efficiently modulated by an ultrafast laser pulse, as a result of the consequent reduction in the plasma frequency of the ITO layer. The presence of the Berreman resonance, which redshifts together with the ENZ frequency of ITO upon pumping, enhances this change in reflectivity, as illustrated in Fig.B.6(e).

As can be seen in Fig.B.6(e), the reflectivity reaches a plateau when moving out of the

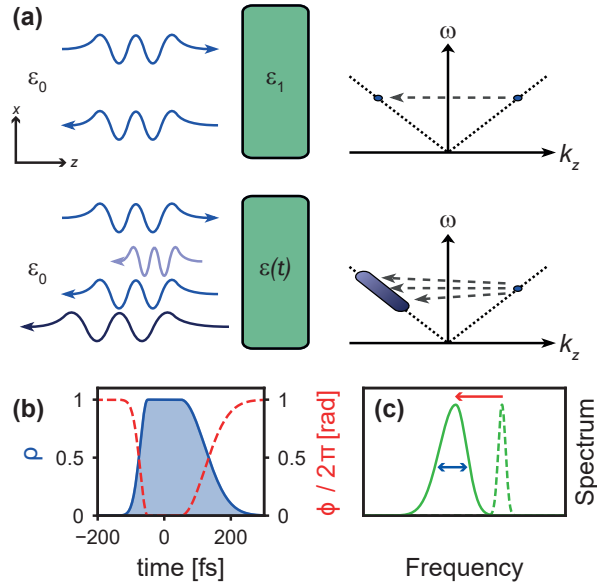


**Figure B.5:** (a) Concept of a purely time-varying mirror: reflection is a transition from  $k_z$  to  $-k_z$  for the static mirror (top right), while the frequency distribution broadens for the time-varying mirror (bottom right). (b) Diagram of the temporal evolution of the complex reflection coefficient in amplitude (blue) and phase (red). (c) Spectral evolution of a pulse reflected by the time-varying mirror: an incoming pulse (dashed green) is shifted (red arrow) and broadened (blue arrow) in frequency (continuous green) due the respective changes in phase and amplitude of the reflection coefficient.

Berremans resonance. This imposes a higher bound on the change of reflectivity that can be induced by the pump modulation. Hence, by increasing the pump intensity even further, the rise time of the modulation will shorten, as the reflectivity reaches the plateau faster, as depicted in Fig.B.6(f). A shorter rise time can enable temporal dynamics beyond the duration of the pump pulse as we will show later.

The measured reflectivity of the time-varying mirror when modulated with the 220 fs pump pulses is shown in Fig.B.7(a), for a probe with a carrier frequency of 230 THz (1300 nm) and 2.8 THz width (16 nm) incident at an angle of  $65^\circ$ , in a pump-probe spectroscopy experiment (pump and probe beams are degenerate and separated by  $10^\circ$ , see SM). The total reflection changes from  $R = 0.07$  (without pump) and converges to  $R = 0.66$  at intensities above saturation ( $I_{\text{sat}} \approx 100 \text{ GW/cm}^2$  see Fig.S1(d)), corresponding to an observed ultrafast modulation of  $\Delta R/R \sim 1000\%$ , as plotted in Fig.B.7(a). When the reflection of the glass substrate  $R_s = 0.04$ , which is not modulated, is subtracted, the relative reflectivity change of the mirror is as high as 2200%.

In the regime below saturation, for pump intensities below  $I_{\text{sat}} \approx 100 \text{ GW/cm}^2$  (blue line in Fig.B.7(a) for  $I_{\text{pump}} = 22 \text{ GW/cm}^2$ ), the temporal changes in the probe reflectivity can be reproduced by a linear time-varying model [296], which incorporates the Kerr effect as a shift in the plasma frequency  $f_p$  proportional to the pump intensity (dashed lines in

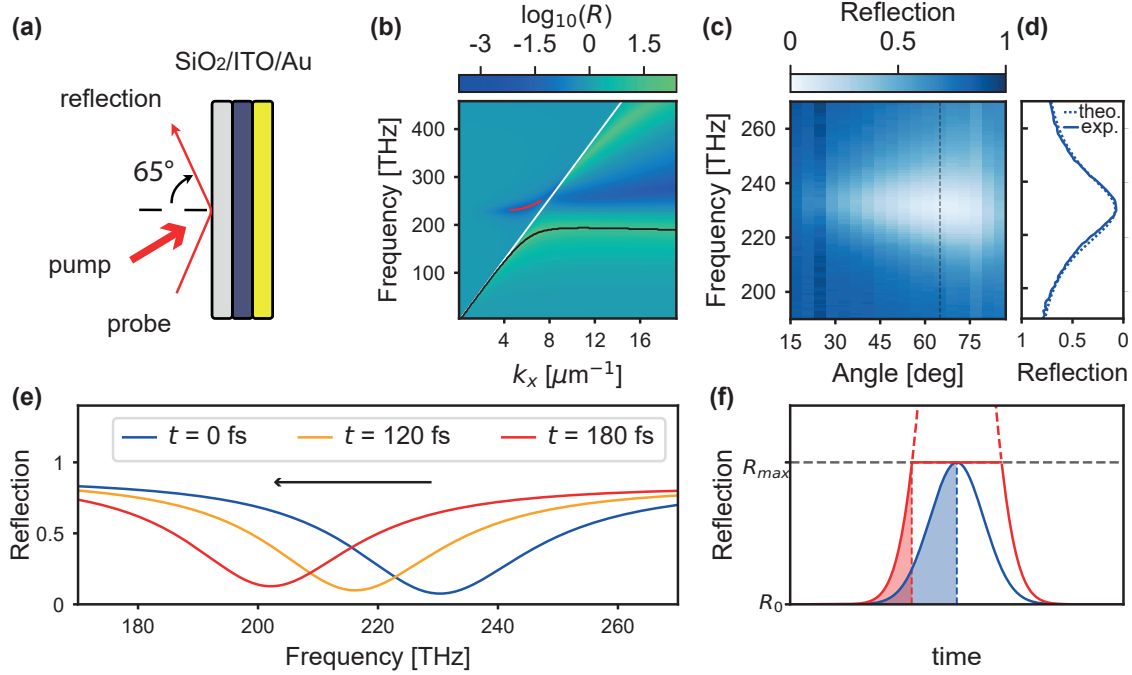


**Figure B.6:** (a) Sketch of a pump-probe experiment. (b) Dispersion diagram of the Berreman mode (red line), situated above the light line (white line), and of the plasmonic ENZ mode (black line). (c) Experimental reflection of the sample, versus angle and frequency. The black dashed line indicates the angle of 65° at which the reflection in panel (d) is shown. (d) Experimental (continuous blue) and numerically obtained (dotted blue) reflection of the sample at an incidence angle of 65°. (e) Simulated reflection spectrum for a pump intensity of 88 GW/cm<sup>2</sup> at 65° and at different times measured from the start of the rise. (f) Schematic of the saturation of the reflection coefficient at high intensities (red) as compared to below saturation (blue).

Fig.B.7(a)). This reduction in  $f_p$  is due to pump-induced intraband electronic transitions to states with higher effective mass, which cause a redshift of the plasma frequency  $f_p$  [303], increasing the ITO permittivity  $\epsilon$ . In general, the rise time of  $f_p(t)$  is limited by the temporal width of the pulse (here  $\approx 220$  fs FWHM) convoluted with a faster material response (below 50 fs [273]), whereas the decay time is typically slower ( $\approx 350$  fs [40]), as observed in Fig.B.7(a). However, the induced reflectivity change slows down at increasing pump intensities, and saturates for  $I_{\text{pump}} \approx I_{\text{sat}}$ . Beyond  $I_{\text{sat}}$ , the reflectivity reaches a plateau and features a longer decay time (yellow and red lines in Fig.B.7(a)). Our numerical simulations reproduce the temporal dynamics with good accuracy but overshoot in amplitude for high pump intensities. We attribute this to the simplified model of the material response with a purely linear change of plasma frequency with pump intensity.

In order to characterise the time-varying effects of the mirror, we focus on the spectral features of the probe signal undergoing modulation. Fig.B.7 shows the measured (b) and

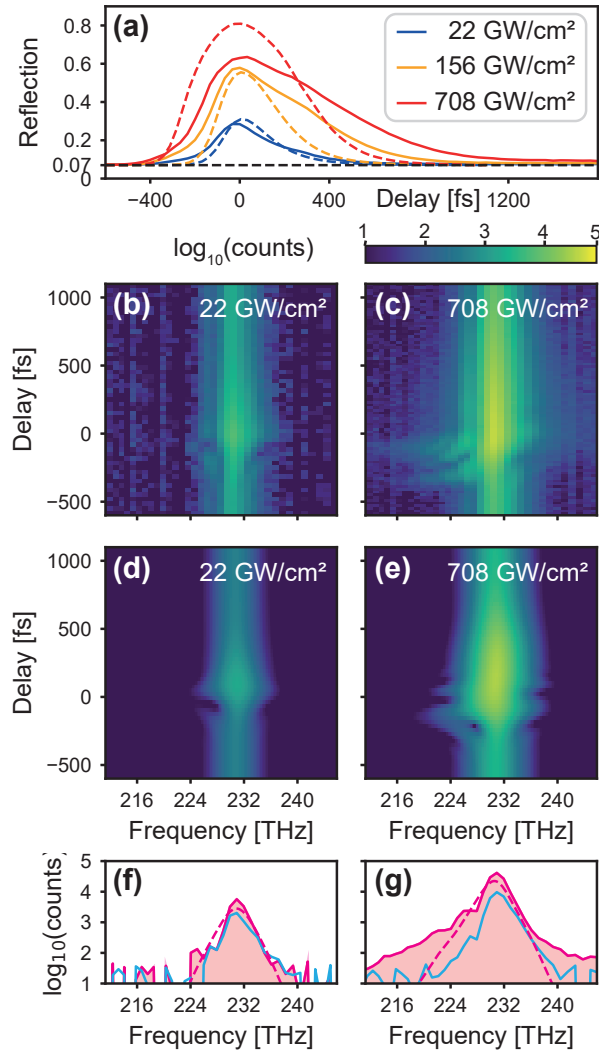


**Figure B.7:** (a) Experimental (continuous line) and numerically simulated (dashed line) evolution of the probe reflection as a function of the pump/probe delay for three pump intensities. (b-e) Comparison of the reflection as a function of delay and frequency, on a log scale, at low intensity (22 GW/cm<sup>2</sup>, (b) experiment, (d) theory) and at high intensity (708 GW/cm<sup>2</sup>, (c) experiment, (e) theory). (f,g) Cross-section of the experimental reflection signal shown in (b-c), at a delay of -90 fs (pink line) as well as -500 fs delay (light blue line) where no modulation happens. Numerically simulated modulated spectra from (d,e) are shown in dashed pink.

simulated (d) evolution of the probe spectrum at various delays, for a moderate pump power of  $I_{\text{pump}} = 22 \text{ GW/cm}^2$ , well below saturation. As expected, the change of reflectivity of the time-varying mirror occurs around zero delay, when pump and probe pulses overlap in time. A successive thinning and broadening in the spectrum around zero delay is observable in Fig.B.7(b), associated with the amplitude change of the reflection coefficient. Overall, for  $I_{\text{pump}} = 22 \text{ GW/cm}^2$ , the probe spectral content is largely unchanged, as shown in Fig.B.7(f) where the modulated (pink line) and unmodulated (light blue line) spectra are almost superposed.

These below-saturation dynamics, including the fine features around zero-delay, are well reproduced by the linear time-varying model shown in Fig.B.7(d) (see SM for details). As shown, since the modulation is significantly faster during the rise time, the time evolution of the spectrum is not symmetric and neither is the amount of blue and red shift at different delays.

In Fig.B.7(c) we present the spectral map for the maximum pump intensity achievable in our setup,  $I_{\text{pump}} = 708 \text{ GW/cm}^2$ , well beyond  $I_{\text{sat}}$ . New frequencies are generated beyond the bandwidth of the unmodulated spectrum. This is qualitatively similar to what is predicted by our model and plotted in Fig.B.7(e).

The frequency broadening is also evident in the section plotted in Fig.B.7(g) where new frequencies are observed in the modulated case (pink line), well beyond the frequency content of the unmodulated case (light blue line). The experimental broadening is well captured by the time-varying model (pink dashed line). Fringes extended from 214 to 245 THz appear in the map of Fig.B.7(c). This broadening is largest at slightly negative delay ( $-90 \text{ fs}$ ), on the rise time of the mirror reflectivity, when the temporal gradient of reflectivity is at its maximum. Moreover, the spectrum becomes visibly asymmetric, with a clear inclination towards the red. At high intensity ( $708 \text{ GW/cm}^2$ ), the FWHM is only marginally affected with an increase of 0.2 THz. The spectral broadening of the probe, of around 31 THz at an intensity of  $10^{-3}$  of the modulated pulse, 10x higher than the noise level, extends well beyond what could be expected from the bandwidth (2.8 THz) of the modulating pump pulse.

These spectral features can be understood by considering the time evolution of the Fresnel coefficient  $r(t)$ : beyond saturation, the material modulation becomes faster than the driving pump pulse, the supported bandwidth is increased, and additional frequencies can be generated upon reflection. We explain the low amplitude of the newly generated frequencies as once the reflectivity reaches its maximum and plateaus, the mirror modulation ends, the probe pulse is no longer affected, and therefore, the modulated signal is only a portion of the reflected probe signal.

The ultrafast response of the time-varying mirror, well beyond the driving pump pulse bandwidth, can be confirmed from four-wave-mixing (FWM), a different experiment capable of focusing only on rising time dynamics. FWM is only generated when pump and probe beams interact inside the ITO layer, during the time-switching of the time-varying mirror, before all light is reflected. For this reason, the FWM signal is much more sensitive to the time-modulation during the rise time of the mirror.

The measured FWM signal as a function of delay is shown in Fig.B.8(a), continuous

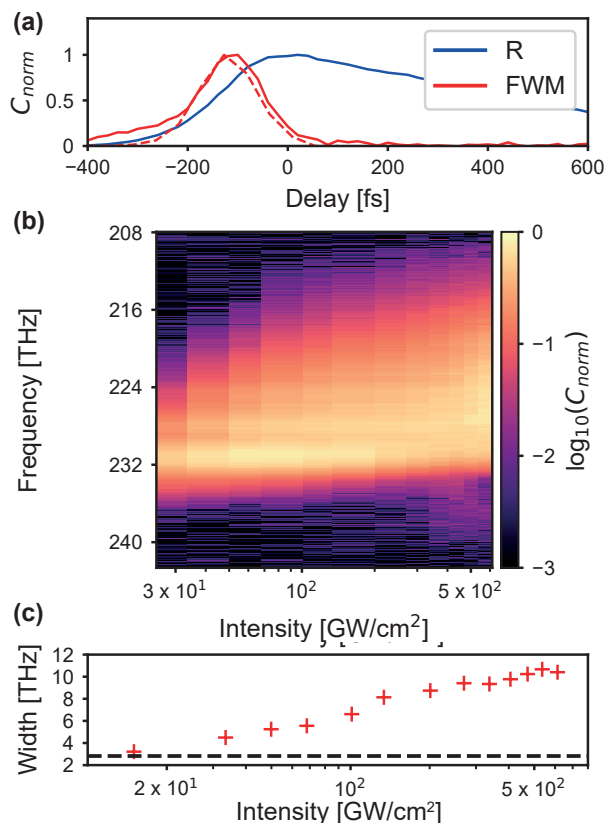


**Figure B.8:** (a) Measured evolution with pump/probe delay of the FWM signal (continuous red line) versus reflection (blue line). Simulated FWM signal is shown by the red dashed line. (b) Measured evolution of the FWM spectrum as a function of pump intensity: the spectrum gets broader with pump power, reaching a maximum bandwidth of 10.7 THz (61.5 nm) and a redshift of 3.8 THz (22 nm) for a pump intensity of 535 GW/cm<sup>2</sup>. (c) Measured broadening of the FWM signal as a function of pump intensity (red crosses), compared with the spectral width of the original input probe spectrum (dashed black line).

red line. As expected, FWM generation mainly occurs during the rise time of the reflection (blue line in Fig.B.8(a)), when the probe field can still penetrate the time-varying mirror, as confirmed by numerical simulation (dashed red line, see SM). In Fig.B.8(b) we plot the FWM signal as a function of the pump intensity at the delay at which FWM signal is maximum, showing an increasing spectral broadening and redshift. A high FWM efficiency of 4.5%, defined as the ratio of FWM power to the input probe power, is reached for a pump intensity of 127 GW/cm<sup>2</sup>. A further increase of the pump intensity contributes to the additional broadening of the spectrum with no further increase in amplitude of the peak frequency, additionally pushing the efficiency to 7.5% at 612 GW/cm<sup>2</sup>. The width of the FWM signal shown in Fig.B.8(b) is plotted in Fig.B.8(c) for a delay of about  $-150$  fs, which is the delay that maximises the power of the FWM signal. The spectral width is taken here at the FWHM, as the time modulation affects the whole FWM spectrum. The spectrum

starts from a nearly Gaussian shape centered at 231 THz and with a width of 3.2 THz at a pump intensity of 15 GW/cm<sup>2</sup>, which is very close to the original probe spectrum (230 THz frequency, 2.8 THz width). This spectrum evolves towards a broad distribution with a FWHM of 10.7 THz (61.5 nm) for pump powers of  $\sim 600$  GW/cm<sup>2</sup>, and which is also red-shifted by about 3.8 THz. Therefore, from this 3.8x increase in bandwidth, we can estimate that the rise time of the time-varying mirror shortens to  $\sim 30$  fs. The FWM spectral broadening stops increasing around  $\sim 400$  GW/cm<sup>2</sup>, as the medium reaches its intrinsic rise time. The value of 30 fs is likely an underestimation of the material response time, as other effects come into play in determining the FWM bandwidth, including higher order contributions to the Kerr effect, as well as material dispersion.

These large spectral features, achieved with relatively long and narrow-banded pump pulses (220 fs, 2.8 THz), are very useful for applications involving high-Q resonances, as short pulses cannot be coupled efficiently.

In conclusion, we have presented a time-varying mirror based on the Berreman resonance of an ITO-Au thin film, exhibiting a record modulation of over 1000% in reflection. Upon reflection from the time-mirror, new frequencies are generated, as far as 5 bandwidths away from the original carrier frequency. The concept of saturation we put forward here can also contribute to shine light on other recent non-perturbative experimental results [293, 300]. Ultrafast optical modulation of a subwavelength time-varying mirror without long space propagation reduces the effect of optical absorption, dispersion or self-broadening. The results described here represent a firm step towards full spatiotemporal control of light, and the development of next-generation active metamaterials for efficient spectral manipulation of light and ultrafast switching, with applications reaching from optical communications to analog computing.

### B.2.2 Double-slit time diffraction at optical frequencies

This work is published in [253]:

Romain Tirole, Stefano Vezzoli, Emanuele Galiffi, Iain Robertson, Dries Maurice,  
Benjamin Tilmann, Stefan A. Maier, John B. Pendry, Riccardo Sapienza  
*"Double-slit time diffraction at optical frequencies"*  
Nature Physics 19(7), 999-1002 (2023), DOI: 10.1038/s41567-023-01993-w  
for publisher permission, see Appendix C

Wave-matter interaction in time-varying media exhibits strikingly different dynamics than in conventional passive media, as energy can be exchanged between wave and medium, the wave frequency changes, and the propagation is no longer symmetric under an inversion of time. Temporal diffraction of matter waves was predicted by Moshinski in 1952 [304] and has been observed as a few oscillations in the particle arrival time [305–307]. Amidst the recent explosion of studies on optical time-varying media [251], time refraction [291,293,296] and time reversal [295] have been achieved in epsilon-near-zero (ENZ) semiconductors, as for example Indium-Tin-Oxide (ITO) [40,289] modulated by ultrafast laser pulses.

Here, we report the observation of the temporal analog of the double-slit experiment for light waves, showing a clear signature of spectral oscillations for the time-diffracted light, and an inversely proportional relation between slit separation and the period of the oscillations. Moreover, the observed oscillations serve as a sensitive probe of the ITO response time, which we measure to be of the order of an optical cycle, much faster than previously thought. In the conventional Young's double-slit experiment, the diffracted pattern has a characteristic oscillatory profile, with minima corresponding to momenta  $k$  for which destructive interference suppresses wave propagation, as illustrated in Fig. B.9a. These minima have a separation in momentum space that increases for decreasing spatial separation of the slits. In the Fraunhofer approximation of diffraction, i.e. for aperture size much smaller than the observation distance, the field distribution in the far field can be approximated as the Fourier transform  $A(k_x)$  of the aperture function  $A(x)$  (Fig. B.9b). The far field interference pattern can be plotted in a dispersion diagram, where it is described as horizontal transitions (Fig. B.9c), with new modes appearing, characterized by different momenta but the same frequency, as required by temporal translational invariance. In the temporal domain, the corresponding scenario, a temporal double-slit, consists of a deeply subwavelength slab characterized by a time-varying dielectric function which is an aperture function  $A(t)$  defining two time slits (Fig. B.9d). In this case the wave will be time-diffracted into a frequency spectrum of frequencies  $A(\omega)$ , the Fourier transform of the aperture function  $A(t)$ , around the incident carrier frequency (Fig. B.9e), whereas the in-plane momentum  $k_x$  will be conserved by translational symmetry (Fig. B.9f).

#### Experimental results

Experimentally, we create time slits by inducing an ultrafast change in the complex reflection coefficient of a time-varying mirror [252] made of a 40 nm thin film of ITO, with epsilon-near-zero (ENZ) frequency of 227 THz (1320 nm). The film is deposited on a glass

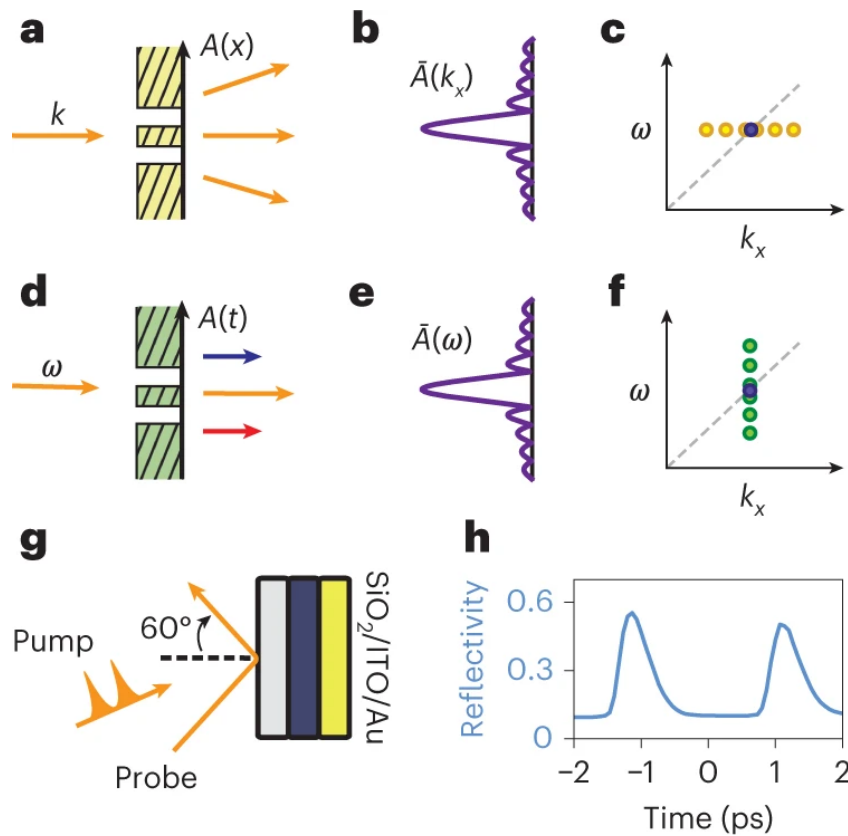


**Figure B.9:** Concept and realization of the double-slit diffraction experiment in time. **a** Conventional spatial double-slit experiment: as light diffracts from a spatial double slit with aperture  $A(x)$ , **b** the aperture changes the beam's in-plane momentum  $k_x$  into a distribution  $\bar{A}(k_x)$ , corresponding to **c** a horizontal transition in the frequency/momentum  $(\omega, k_x)$  dispersion diagram. **d** Temporal double-slit experiment: as light interacts with a double time modulation, **e** an aperture in time  $A(t)$  acts on the frequency  $\omega$  of the beam and redistributes the frequencies as  $\bar{A}(\omega)$ . **f** The transition is now vertical in the dispersion diagram. **g** Experimental realization: pump and probe beams are incident close to 60 deg onto a 40 nm ITO slab on glass, coated with a 100 nm gold film. **h** Temporal change of the sample reflectivity (blue line) with a 2.3 ps separation between the slits.

coverslip and covered by a 100 nm layer of gold to improve field confinement and reflectivity, as sketched in Fig. B.5g. The time modulation is driven by two 225 fs (FWHM) pulses at 230.2 THz (1300 nm), impinging near the Berreman angle ( $60^\circ$ ), ensuring efficient field coupling and an enhanced nonlinear response in ITO (see Methods for more details). We measure the temporal double-slit by a pump-probe experiment (Fig. B.9g blue line). The reflectivity of the sample changes from 0.08 to 0.6, giving a modulation contrast of 76% for pump intensities around 124 GW/cm<sup>2</sup>, large enough to saturate the mirror response (see Fig. B.11). The measured reflectivity has the shape of a double time slit, with a fast rise time and a slower decay, given by a convolution of the driving pump pulses, the probe and the material response. The time slits separation can be tuned by adjusting the relative delay of the two pump pulses via a delay line. The same pump-probe experiment on a glass or a gold layer yields no measurable modulation of the spectrum. This is to be expected for gold from the negligible penetration of the layer by the field (3.7%) and its Kerr coefficient is smaller than in ITO, while for SiO<sub>2</sub> the Kerr nonlinearities are 4 orders of magnitude smaller than in ITO, therefore making any time-modulation within the layer negligible.

Direct evidence of time diffraction from the temporal double slit is given by illuminating the sample with a probe pulse (230.2 THz carrier frequency, 1 THz bandwidth) of duration 794 fs (FWHM) and by monitoring the reflected probe spectrum. The probe pulse is spectrally broadened, exhibiting new frequency content up to  $\sim 10$  bandwidths away from the carrier frequency. A clear spectral modulation, with sinusoidal oscillations, is evident in Fig. B.10a,b (red lines), shown for two different time slit separations. Measurements with 800 fs slit temporal separation (Fig. B.10a) present much faster oscillations than with 500 fs (Fig. B.10b). The separation of the time slits determines the period of oscillations in the frequency spectrum, while the shape of each time slit constrains the oscillation decay and therefore the number of oscillations that are visible. Up to six oscillations in the spectrum are evident in Fig. B.10a,b, with an overall decay in intensity away from the central frequency of the probe. These spectral oscillations are very well captured by a simple diffraction model (purple line in Fig. B.10a,b). This model calculates the spectral evolution of the probe from the Fourier transform of the product of the time-varying reflection coefficient  $r(t)$ , i.e. the slit aperture function, and the probe pulse temporal profile. In such a model, the slit separation and the decay time of each slit are fixed by the pump/probe data (Fig. B.11), whereas the rise time is taken as a fitting parameter.

The oscillation decay with increasing change in frequency depends on the shape of the time slits, and in particular their rise time. Therefore, the measured spectral oscillations act as a very precise measurement of the ITO response time, with a resolution well beyond that of a conventional pump-probe experiment. Here, we find unexpected physics: many more oscillations are visible than expected from existing theory, implying a rise time for the leading edge estimated to be 1 – 10 fs, i.e. of the order of an optical cycle (4.4 fs); this is much faster than previously thought [291, 293, 296], although recent work has shown evidence of a speeding up of the response time for pump intensities beyond the linear regime [12]. Moreover, the oscillations are very close to the asymptotic limit of an ideal time slit with a Heaviside (infinitely fast) rise profile, for which the amplitude of the oscillations is

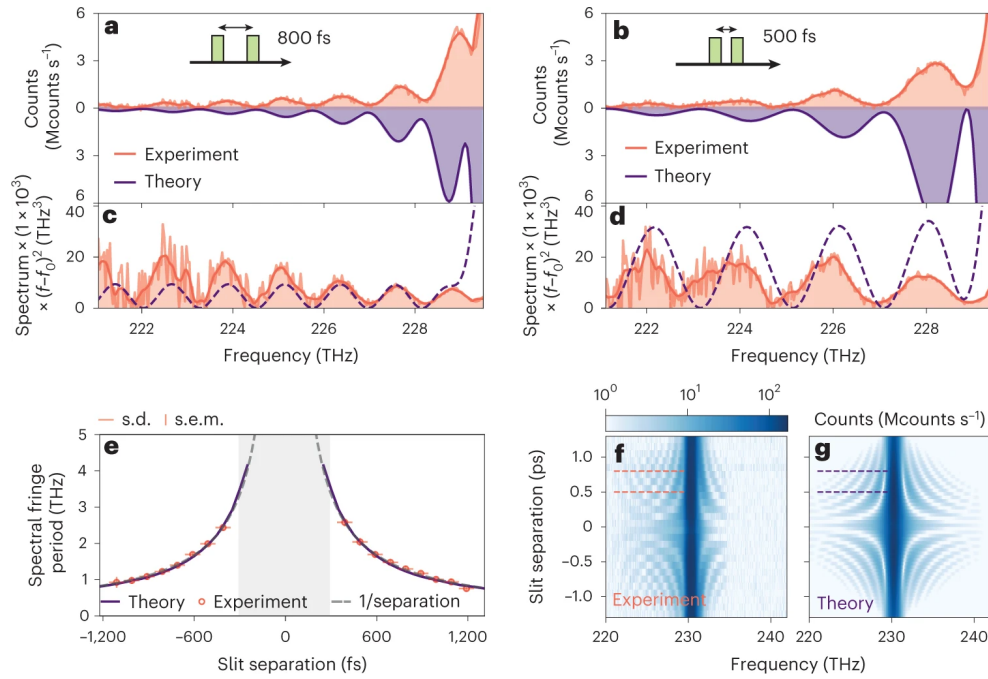


**Figure B.10:** Observation of a spectral diffraction pattern from temporal double-slits. **a,b** Oscillations in the reflection spectrum of a 794 fs probe pulse interacting with the double-slit temporal aperture: experiment (light red curve is raw data, dark red curve is the smoothed data) against theoretical model (purple line). The oscillations are visible up to 10 THz away from the incident frequency (230.2 THz, 1 THz bandwidth). **c,d** Experimental oscillations rescaled by  $(f - f_0)^2$ , and asymptotic theoretical curve (dashed purple line). The measured oscillation period of the spectral diffraction is plotted in **e** (red circles) as a function of slit separation, in very good agreement with the period extracted from our model (purple line) and the inverse slit separation dependence (gray dashed line). The grey area highlights separations smaller than 300 fs. **f,g** Full interferograms of the time diffracted light as a function of slit separation and frequency, (f) experiment and (g) theory. The dashed lines show the range where data in (a-d) are shown. Horizontal and vertical error bars respectively represent standard deviation and standard error of the mean.

expected to decay as  $1/(f - f_0)^2$ , where  $f$  is the frequency of oscillation and  $f_0$  the probe central frequency (230.2 THz). This is evident when the spectrum is rescaled by the inverse frequency squared, as its intensity is almost constant (Fig. B.10c,d). The dashed purple line in Fig. B.10c,d is the asymptotic theory with two Heaviside time slits (see Fig. B.12).

The signature of time diffraction is further revealed by the period of these oscillations which is inversely proportional to the slit separation, as plotted in Fig. B.10e. The agreement between the measured data (open circles) and the model is remarkable. The error bars show the accuracy of the slit separation (50 fs) and period ( $< 0.15$  THz). The shaded area identifies time slit separations smaller than 300 fs where the two time slits start to merge, and the oscillations are not visible anymore.

Further insight into the temporal diffraction process can be reached by analyzing the full interferogram of the time diffracted light as a function of the slit separation, as in Fig. B.10f. Oscillations appear more pronounced on the red side of the spectrum with frequencies as far out as 10 THz ( $\sim 60$  nm) while only exhibiting frequencies 4 THz away on the blue side (on top of the probe pulse initial spectral content of 1 THz width). The asymmetric interferogram is explained by the time evolution of the phase of the complex reflection coefficient, causing a Doppler shift of the spectrum, often dubbed time refraction [299]. The theoretical plot in Fig. B.10g does not capture this asymmetry, as it does not include a phase change during reflection. The observed spectral red-shift is reproduced when using a dispersive material-based model which includes a time modulation of the phase of the reflection coefficient, as shown in Fig. B.13c.

## Outlook

In conclusion, we report a direct observation of spectral oscillations, at optical frequencies, resulting from double-slit time diffraction, the temporal analogue of the Young's slits experiment. The measurements show a clear inverse proportionality between the oscillation period and the time slit separation. These oscillations reveal a 1-10 fs temporal dynamics of the ITO/Au bilayer, much faster than previously thought and beyond the adiabatic and linear intensity dependence assumed so far in most theoretical models [291, 299, 308] but compatible with recent modelling [309], calling for a new fundamental understanding of such ultrafast non-equilibrium responses. The observation of temporal Young's double-slit diffraction paves the way for optical realizations of time-varying metamaterials, promising enhanced wave functionalities such as nonreciprocity [274], new forms of gain [275, 277] time reversal [293, 310] and optical Floquet topology [280, 311]. The visibility of the oscillations can be used to measure the phase coherence of the wave interacting with it, similarly to matter-wave interferometers [312]. Double-slit time diffraction could be extended to other wave domains, e.g. matter waves [312], optomechanics [313] and acoustics [314, 315], electronics [316], and spintronics [317], with applications for pulse shaping, signal processing and neuromorphic computation.

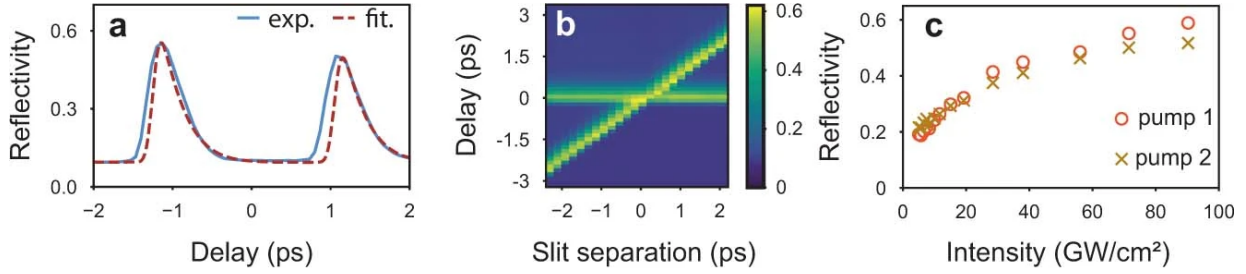


**Figure B.11:** Characterization of the temporal double slit with a short (225 fs) probe pulse. **a**, Experimental intensity reflectivity (blue line) for a 2.3 ps separation between the time slits, as a function of the probe delay. **b**, Reflectivity for a linear variation of the slit separation (horizontal axis) measured as a function of the probe delay with one of the pumps (vertical axis). **c**, Intensity dependence of the maximum achievable reflectivity for the two time slits driven by pump 1 (incident at  $54^\circ$ ) and pump 2 (incident at  $66^\circ$ ). The reflectivity saturates reaching a maximum value of 0.6.

### Experimental and supplementary material

**Temporal and spectral characterization of the probe and pump pulses:** All pulses are generated by a Light Conversion Pharos solid state laser, set to 230.2 THz with a Light Conversion Orpheus optical parametric amplifier, with a nominal full width at half maximum (FWHM) of the electric field envelope of 225 fs. The pulses are roughly Gaussian in shape. For the double slit experiment a probe pulse identical to the pump pulses is sent through a 4-f system, composed of a diffraction grating, a variable aperture and two lenses, which separates, filters and recombines different spectral components to broaden the pulse in time, in order to make it longer than the time slits separation. By selecting the spectral content of the probe beam with an aperture, the pulse is significantly extended in time. This is quantified by using cross-correlation measurements, where we collect the sum-frequency-generated (SFG) signal originating from the spatial overlap of the probe and the pump pulses in a 400  $\mu\text{m}$  thick Gallium Phosphide crystal with second-order non-linearity. As the analytical solution to the cross-correlation measurement is known for a Gaussian pulse, we fit the FWHM of the probe pulse amplitude assuming such a shape following the measurement of SFG between the pump and the probe pulses. The agreement between theory and experiment shows that this is a well-suited approximation for the main peak of the probe envelope. For reference, the pristine pump pulse autocorrelation measurement and fit are also measured. The probe pulse is measured to have a  $794 \pm 37$  fs FWHM, while the original pump pulse is recorded to have a  $225 \pm 5$  fs FWHM, close to device specifications. These values refer to the electric field amplitude of the pulse, the corresponding intensity FWHM are  $\sqrt{2}$  shorter.

**Modelling of the slits:** We model a single slit aperture function as:

$$f_{ss}(t) = \frac{1}{(1 + e^{-\alpha t})(1 + e^{\beta t})}$$

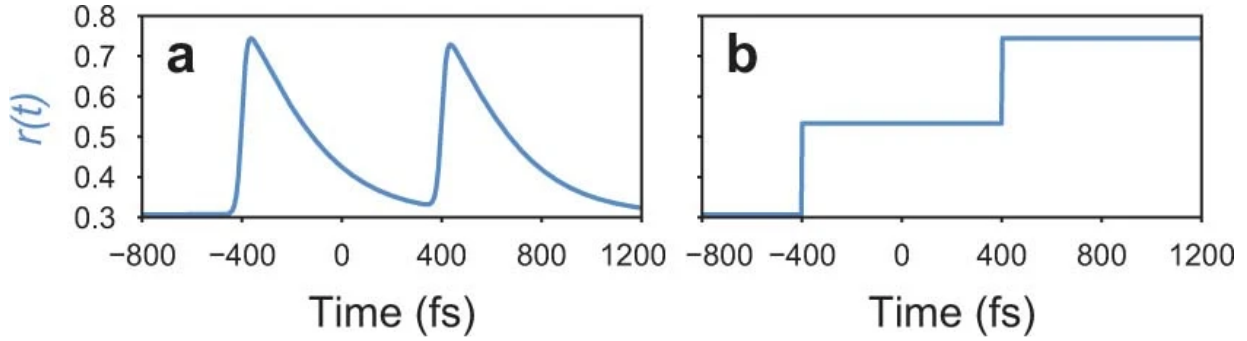


**Figure B.12:** Modelled reflection coefficient. **a**, Amplitude reflection coefficient  $r(t)$  corresponding to a realistic modulation of the time-varying mirror. **b**, Amplitude reflection coefficient in the asymptotic limit.

where  $\alpha$  and  $\beta$  are taken to be positive constants. The double slit modulation profile of the amplitude reflection coefficient can then be expressed as

$$r(t) = Af_{ss}(t - s/2) + Bf_{ss}(t + s/2) + C$$

where  $S$  is the slit separation,  $A$  and  $B$  are the respective slit amplitudes and  $C$  is a constant corresponding to the unmodulated reflection coefficient of the time-varying mirror. This function is normalized by fitting it to the measured intensity reflectivity change  $R(t) = |r(t)|^2$  (Fig. B.12a). In Fig. B.10c,d of the manuscript we compare the decay of the frequency oscillations to an asymptotic case, where the rise time becomes infinitely fast and the decay infinitely slow (that is when  $\alpha \rightarrow \infty$  and  $\beta \rightarrow 0$ ). We model this limiting case using two consecutive Heaviside functions (denoted  $H(t)$ ) as shown in Fig. B.12b, using the following expression:

$$r(t) = AH(t - s/2) + BH(t + s/2) + C$$

**Characterization of the temporal double slit:** In order to characterize the double slit time modulation, we use a short 225 fs FWHM probe in a degenerate pump-probe experiment. The probe is incident on the sample at a  $60^\circ$  angle to the normal, while the pump beams are incident at a  $6^\circ$  angle difference on either side of the probe. All beams are p-polarized to couple them to the Berreman resonance. The probe and one of the pumps go through a delay line to control the probe arrival time on the sample and the temporal separation between the two. The reflected probe signal is sent to a Princeton Instruments NIRvana camera for spectral characterization. For the double slit experiment, the same illumination and detection apparatus is used, with the exception that the probe is temporally broadened before the sample by passing through an additional 4-f system. We refer to our previous work [252] for a complete characterization of the ITO/Au sample's linear and nonlinear properties. The double slit aperture function, i.e. the reflectivity  $R(t) = |r(t)|^2$  with  $r(t)$  being the complex Fresnel coefficient, can be measured by pump probe spectroscopy, as shown in Fig. B.11a (blue line), where the probe reflectivity is

plotted as a function of the delay for a fixed slit separation. The theoretical fit (dashed red line) comes from the amplitude reflection coefficient  $r(t)$  defined in the previous section, convoluted with the envelope of the probe pulse in time  $E_{probe}(t - \tau)$  pulse arriving at a delay  $\tau$  (approximated to a Gaussian profile with 225 fs FWHM), which is why spectrally integrated measurements cannot determine the reflectivity rise time. In addition to fixing the values of normalization constants  $A$ ,  $B$  and  $C$ , the fitting of the pump/probe reflectivity measurements allows us to assign a value for the coefficient at  $1/400 \text{ fs}^{-1}$ , corresponding to a decay time of the intensity reflectivity (defined as the time to decrease from 90 % to 10 %) of 625 fs (or  $1/e$  of 330 fs, compatible with the literature [309]). From this measurement we can also set the relative amplitude of the second peak of the time slit to be 0.93 % of the first one. As the rise time is limited by the probe pulse, we cannot estimate a precise value for it from this measurement and instead spectral data as in Fig. B.10 are necessary. Our model reproduces well the rise and decay time of the modulation but does not account for the short plateau at the maximum of the modulation, which arises when pumping near or beyond the saturation of the mirror's temporal response [12]. As time-varying effects depend exclusively on the slope of the modulation, we focus on reproducing this behavior rather than the extent of the flat region at the maximum. A wide range of separations can be achieved by varying the delay between the two pumps (horizontal axis in Fig. B.11b) while the delay of the probe is varied to map the modulation (vertical axis in Fig. B.11b). An intensity dependence study of the modulation is illustrated in Fig. B.11c, showing that the double slit experiments are performed where the modulation contrast of the time-varying mirror is saturated with pump power. The two pumps have similar effect on the reflectivity change of the sample, although they illuminate it from different angles,  $54^\circ$  and  $66^\circ$  respectively, since the Berreman resonance is angularly wide [296].

**Time diffraction model:** The probe spectra in the double slit experiment are modelled as Fourier transforms of the product of the double slit reflection coefficient  $r(t)$  and the probe field amplitude  $E_{probe}(t)$  after the 4-f system (product of a Gaussian envelope with 794 fs FWHM and a carrier frequency 230.2 THz). The resulting spectrum  $I(f)$  is then squared to return the measured field intensity:

$$I(f) = |F(r(t)) \cdot E_{probe}(t - t_0)|^2$$

where  $t_0$  is a parameter to account for a possible offset of the probe pulse envelope peak and the temporal center of the two slits. This model neglects the dispersion of the complex reflection coefficient of the sample, as it assumes the same temporal response at all frequencies. It also neglects the time evolution of the phase of  $r(t)$  which is in principle a complex function but is assumed here real. Although this model reproduces well the period and amplitude of the oscillations of the double slit experiment, it fails to capture the asymmetry observed in the experimental spectrum, where more oscillations are visible on the red side (comparing Fig. B.13a and b). We attribute this to the time evolution of the phase of the complex reflection coefficient, which causes a Doppler shift of the spectrum, often dubbed time refraction [291]. A phenomenological model of the phase evolution cannot be built from our measurements, as the pump/probe data are only sensitive to the amplitude of

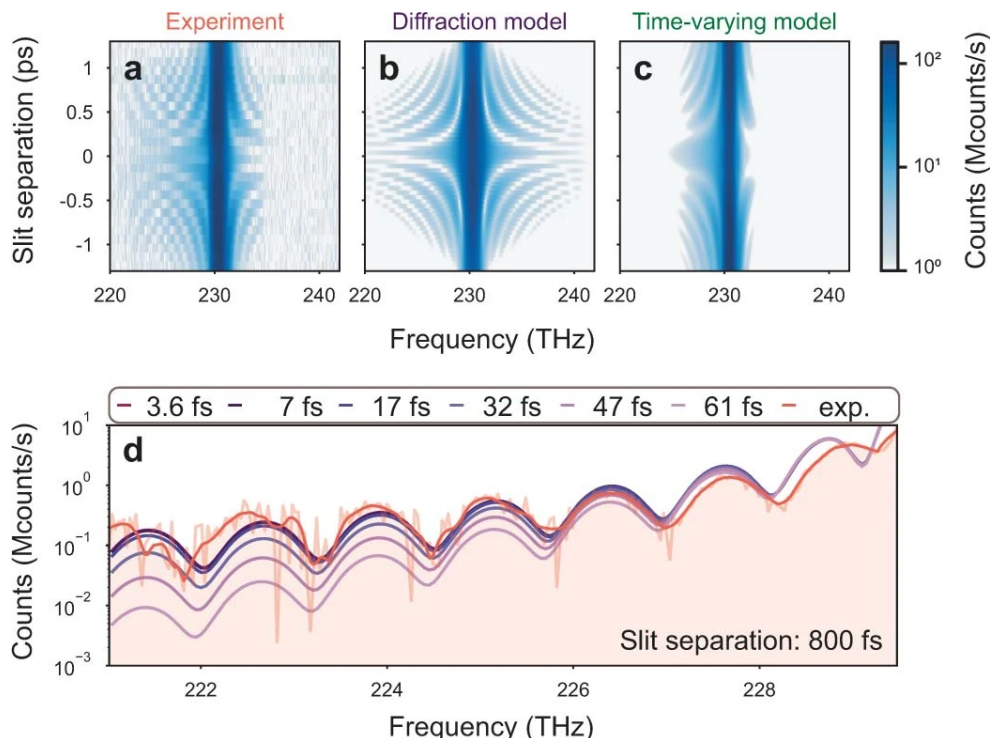


**Figure B.13:** Comparison of the models against experimental data. **a–c**, Signal against frequency and slit separation for experiment (a), the time diffraction model (b) and the adiabatic, dispersive time-varying model (c). The plots are color-saturated to ensure a fair quantitative comparison between the fringe visibility of the respective datasets. **d**, Experimental oscillation spectrum on a logarithmic scale at a slit separation of 800 fs compared to the theoretical one for various material response times.

the reflectivity. In order to understand better this asymmetry, we also model time diffraction using an adiabatic time-varying model which accounts for the phase evolution of the reflection coefficient as well as the material dispersion (see Fig. B.13c). The permittivity modulation is computed by calculating a negative shift in the plasma frequency from the convolution of the gaussian pump intensity with an exponential rise and decay response function [299, 309]. This model of the pump-induced modulation in ENZ materials can reproduce the spectral oscillations, period and the interferogram asymmetry observed in Fig. B.13a, however it fails to capture the full spectral extent of the oscillations because of the fast rise time of the experimental slit aperture function, which in our adiabatic simulations is fundamentally limited by the pump duration [291, 296]. This discrepancy highlights the need for new models to describe such non-adiabatic modulation. The diffraction model can be used to fit the experimental spectral data, giving a value for the parameter  $\alpha$  of  $1/2 \text{ fs}^{-1}$ , corresponding to an intensity reflectivity rise time (10 – 90 %) of 7 fs. As shown in Fig. B.13d, the data are close to the asymptotic limit of an infinitely fast rising slit, therefore the fitting is equally good for a reflectivity rise time (10 – 90 %) in the range 1 – 10 fs.



# Appendix C

## Publisher Permissions



Home



Help ▾



Live Chat



Sign in



Create Account



### Giant second-harmonic generation in ferroelectric NbO12

Author: Ibrahim Abdelwahab et al

Publication: Nature Photonics

Publisher: Springer Nature

Date: Jun 30, 2022

Copyright © 2022, The Author(s), under exclusive licence to Springer Nature Limited

#### Author Request

If you are the author of this content (or his/her designated agent) please read the following. If you are not the author of this content, please click the Back button and select no to the question "Are you the Author of this Springer Nature content?".

Ownership of copyright in original research articles remains with the Author, and provided that, when reproducing the contribution or extracts from it or from the Supplementary Information, the Author acknowledges first and reference publication in the Journal, the Author retains the following non-exclusive rights:

To reproduce the contribution in whole or in part in any printed volume (book or thesis) of which they are the author(s).

The author and any academic institution, where they work, at the time may reproduce the contribution for the purpose of course teaching.

To reuse figures or tables created by the Author and contained in the Contribution in oral presentations and other works created by them.

To post a copy of the contribution as accepted for publication after peer review (in locked Word processing file, of a PDF version thereof) on the Author's own web site, or the Author's institutional repository, or the Author's funding body's archive, six months after publication of the printed or online edition of the Journal, provided that they also link to the contribution on the publisher's website.

Authors wishing to use the published version of their article for promotional use or on a web site must request in the normal way.

If you require further assistance please read Springer Nature's online [author reuse guidelines](#).

For full paper portion: Authors of original research papers published by Springer Nature are encouraged to submit the author's version of the accepted, peer-reviewed manuscript to their relevant funding body's archive, for release six months after publication. In addition, authors are encouraged to archive their version of the manuscript in their institution's repositories (as well as their personal Web sites), also six months after original publication.

v1.0

BACK

CLOSE WINDOW



14-Jul-2023

This license agreement between the American Physical Society ("APS") and Benjamin Tilmann ("You") consists of your license details and the terms and conditions provided by the American Physical Society and SciPris.

#### **Licensed Content Information**

**License Number:** RNP/23/JUL/068428  
**License date:** 14-Jul-2023  
**DOI:** 10.1103/PhysRevApplied.18.054067  
**Title:** Saturable Time-Varying Mirror Based on an Epsilon-Near-Zero Material  
**Author:** Romain Tirole et al.  
**Publication:** Physical Review Applied  
**Publisher:** American Physical Society  
**Cost:** USD \$ 0.00

#### **Request Details**

**Does your reuse require significant modifications:** No  
**Specify intended distribution locations:** Worldwide  
**Reuse Category:** Reuse in a thesis/dissertation  
**Requestor Type:** Author of requested content  
**Items for Reuse:** Whole Article  
**Format for Reuse:** Electronic

#### **Information about New Publication:**

**University/Publisher:** Ludwig-Maximilians-Universität München  
**Title of dissertation/thesis:** New nanomaterials to boost nonlinear and ultrafast nanophotonics  
**Author(s):** Benjamin Tilmann  
**Expected completion date:** Jul. 2023

#### **License Requestor Information**

**Name:** Benjamin Tilmann  
**Affiliation:** Individual  
**Email Id:** b.tilmann@physik.uni-muenchen.de  
**Country:** Germany



- Home
- Help
- Live Chat
- Sign in
- Create Account

**Double-slit time diffraction at optical frequencies**

Author: Romain Tirole et al  
 Publication: Nature Physics  
 Publisher: Springer Nature  
 Date: Apr 3, 2023

**SPRINGER NATURE**

*Copyright © 2023, The Author(s), under exclusive licence to Springer Nature Limited*

**Author Request**

If you are the author of this content (or his/her designated agent) please read the following. If you are not the author of this content, please click the Back button and select no to the question "Are you the Author of this Springer Nature content?".

Ownership of copyright in original research articles remains with the Author, and provided that, when reproducing the contribution or extracts from it or from the Supplementary Information, the Author acknowledges first and reference publication in the Journal, the Author retains the following non-exclusive rights:

- To reproduce the contribution in whole or in part in any printed volume (book or thesis) of which they are the author(s).
- The author and any academic institution, where they work, at the time may reproduce the contribution for the purpose of course teaching.
- To reuse figures or tables created by the Author and contained in the Contribution in oral presentations and other works created by them.
- To post a copy of the contribution as accepted for publication after peer review (in locked Word processing file, of a PDF version thereof) on the Author's own web site, or the Author's institutional repository, or the Author's funding body's archive, six months after publication of the printed or online edition of the Journal, provided that they also link to the contribution on the publisher's website.
- Authors wishing to use the published version of their article for promotional use or on a web site must request in the normal way.

If you require further assistance please read Springer Nature's online [author reuse guidelines](#).

For full paper portion: Authors of original research papers published by Springer Nature are encouraged to submit the author's version of the accepted, peer-reviewed manuscript to their relevant funding body's archive, for release six months after publication. In addition, authors are encouraged to archive their version of the manuscript in their institution's repositories (as well as their personal Web sites), also six months after original publication.

v1.0

**BACK** **CLOSE WINDOW**

# Bibliography

- [1] Eugene Hecht. *Optik*. De Gruyter, dec 2018.
- [2] Valentina Parodi, Emanuela Jacchetti, Roberto Osellame, Giulio Cerullo, Dario Polli, and Manuela Teresa Raimondi. Nonlinear Optical Microscopy: From Fundamentals to Applications in Live Bioimaging. *Frontiers in Bioengineering and Biotechnology*, 8(October):1–18, oct 2020.
- [3] C. Manzoni and G. Cerullo. Design criteria for ultrafast optical parametric amplifiers. *Journal of Optics*, 18(10):103501, oct 2016.
- [4] Qiushi Guo, Ryoto Sekine, Luis Ledezma, Rajveer Nehra, Devin J Dean, Arkadev Roy, Robert M Gray, Saman Jahani, and Alireza Marandi. Femtojoule femtosecond all-optical switching in lithium niobate nanophotonics. *Nature Photonics*, jul 2022.
- [5] Mansoor Yousefi and Xianhe Yangzhang. Linear and Nonlinear Frequency-Division Multiplexing. *IEEE Transactions on Information Theory*, 66(1):478–495, jan 2020.
- [6] Paolo Minzioni, Cosimo Lacava, Takasumi Tanabe, Jianji Dong, Xiaoyong Hu, Gyorgy Csaba, Wolfgang Porod, Ghanshyam Singh, Alan E Willner, Ahmed Al-maiman, Victor Torres-Company, Jochen Schröder, Anna C Peacock, Michael J Strain, Francesca Parmigiani, Giampiero Contestabile, David Marpaung, Zhixin Liu, John E Bowers, Lin Chang, Simon Fabbri, María Ramos Vázquez, Vibhav Bharadwaj, Shane M Eaton, Peter Lodahl, Xiang Zhang, Benjamin J Eggleton, William John Munro, Kae Nemoto, Olivier Morin, Julien Laurat, and Joshua Nunn. Roadmap on all-optical processing. *Journal of Optics*, 21(6):063001, jun 2019.
- [7] A. A. Jørgensen, D. Kong, M. R. Henriksen, F. Klejs, Z. Ye, Ò. B. Helgason, H. E. Hansen, H. Hu, M. Yankov, S. Forchhammer, P. Andrekson, A. Larsson, M. Karlsson, J. Schröder, Y. Sasaki, K. Aikawa, J. W. Thomsen, T. Morioka, M. Galili, V. Torres-Company, and L. K. Oxenløwe. Petabit-per-second data transmission using a chip-scale microcomb ring resonator source. *Nature Photonics*, 16(11):798–802, nov 2022.
- [8] Álvaro Rodríguez Echarri, Joel D. Cox, and F. Javier García de Abajo. Direct generation of entangled photon pairs in nonlinear optical waveguides. *Nanophotonics*, 11(5):1021–1032, mar 2022.

- [9] Tomás Santiago-Cruz, Sylvain D Gennaro, Oleg Mitrofanov, Sadvikas Addamane, John Reno, Igal Brener, and Maria V Chekhova. Resonant metasurfaces for generating complex quantum states. *Science*, 377(6609):991–995, aug 2022.
- [10] Lukas Novotny and Niek Van Hulst. Antennas for light. *Nature Photonics*, 5(2):83–90, 2011.
- [11] Stefan A. Maier. *Plasmonics: Fundamentals and Applications*. Springer US, New York, NY, 2007.
- [12] Vincenzo Giannini, Antonio I. Fernández-Domínguez, Susannah C. Heck, and Stefan A. Maier. Plasmonic Nanoantennas: Fundamentals and Their Use in Controlling the Radiative Properties of Nanoemitters. *Chemical Reviews*, 111(6):3888–3912, jun 2011.
- [13] Naomi J. Halas, Surbhi Lal, Wei-Shun Chang, Stephan Link, and Peter Nordlander. Plasmons in Strongly Coupled Metallic Nanostructures. *Chemical Reviews*, 111(6):3913–3961, jun 2011.
- [14] Nina Jiang, Xiaolu Zhuo, and Jianfang Wang. Active Plasmonics: Principles, Structures, and Applications. *Chemical Reviews*, 118(6):3054–3099, 2018.
- [15] N C Panoiu, W E I Sha, D Y Lei, and G-C Li. Nonlinear optics in plasmonic nanostructures. *Journal of Optics*, 20(8):083001, aug 2018.
- [16] Martti Kauranen and Anatoly V Zayats. Nonlinear plasmonics. *Nature Photonics*, 6(11):737–748, nov 2012.
- [17] Guixin Li, Shuang Zhang, and Thomas Zentgraf. Nonlinear photonic metasurfaces. *Nature Reviews Materials*, 2(5):17010, may 2017.
- [18] Jacob B. Khurgin. How to deal with the loss in plasmonics and metamaterials. *Nature Nanotechnology*, 10(1):2–6, jan 2015.
- [19] Arseniy I. Kuznetsov, Andrey E. Miroshnichenko, Mark L. Brongersma, Yuri S. Kivshar, and Boris Luk’yanchuk. Optically resonant dielectric nanostructures. *Science*, 354(6314):aag2472, nov 2016.
- [20] Ludwig Hüttenhofer, Felix Eckmann, Alberto Lauri, Javier Cambiasso, Evangelina Pensa, Yi Li, Emiliano Cortés, Ian D. Sharp, and Stefan A. Maier. Anapole Excitations in Oxygen-Vacancy-Rich TiO<sub>2-x</sub> Nanoresonators: Tuning the Absorption for Photocatalysis in the Visible Spectrum. *ACS Nano*, 14(2):2456–2464, feb 2020.
- [21] Javier Cambiasso, Gustavo Grinblat, Yi Li, Aliaksandra Rakovich, Emiliano Cortés, and Stefan A. Maier. Bridging the gap between dielectric nanophotonics and the visible regime with effectively lossless gallium phosphide antennas. *Nano Letters*, 17(2):1219–1225, 2017.

- [22] Andreas Tittl, Aleksandrs Leitis, Mingkai Liu, Filiz Yesilkoy, Duk-Yong Choi, Dragomir N. Neshev, Yuri S. Kivshar, and Hatice Altug. Imaging-based molecular barcoding with pixelated dielectric metasurfaces. *Science*, 360(6393):1105–1109, jun 2018.
- [23] Emiliano Cortés, Fedja J. Wendisch, Luca Sortino, Andrea Mancini, Simone Ezen-dam, Seryio Saris, Leonardo de S. Menezes, Andreas Tittl, Haoran Ren, and Stefan A. Maier. Optical Metasurfaces for Energy Conversion. *Chemical Reviews*, 122(19):15082–15176, oct 2022.
- [24] Robert W. Boyd. The Nonlinear Optical Susceptibility. In *Nonlinear Optics*, pages 1–67. Elsevier, Amsterdam, 3. edition, 2008.
- [25] Jinghan He, Hong Chen, Jin Hu, Jingan Zhou, Yingmu Zhang, Andre Kovach, Constantine Sideris, Mark C. Harrison, Yuji Zhao, and Andrea M. Armani. Nonlinear nanophotonic devices in the ultraviolet to visible wavelength range. *Nanophotonics*, 9(12):3781–3804, sep 2020.
- [26] Lukas Novotny and Bert Hecht. *Principles of nano-optics*, volume 9781107005. Cambridge University Press, sep 2009.
- [27] Denis G. Baranov, Dmitry A. Zuev, Sergey I. Lepeshov, Oleg V. Kotov, Alexander E. Krasnok, Andrey B. Evlyukhin, and Boris N. Chichkov. All-dielectric nanophotonics: the quest for better materials and fabrication techniques. *Optica*, 4(7):814, 2017.
- [28] Binghai Yan and Claudia Felser. Topological Materials: Weyl Semimetals. *Annual Review of Condensed Matter Physics*, 8(1):337–354, mar 2017.
- [29] Constantin Simovski and Sergei Tretyakov. *An Introduction to Metamaterials and Nanophotonics*. Cambridge University Press, sep 2020.
- [30] Phaedon Avouris, Zhihong Chen, and Vasili Perebeinos. Carbon-based electronics. *Nature Nanotechnology*, 2(10):605–615, oct 2007.
- [31] G. T. Reed, G. Mashanovich, F. Y. Gardes, and D. J. Thomson. Silicon optical modulators. *Nature Photonics*, 4(8):518–526, aug 2010.
- [32] Zhen Chai, Xiaoyong Hu, Feifan Wang, Xinxiang Niu, Jingya Xie, and Qihuang Gong. Ultrafast All-Optical Switching. *Advanced Optical Materials*, 5(7):1600665, apr 2017.
- [33] Jacob B. Khurgin, Greg Sun, Wei Ting Chen, Wei-Yi Tsai, and Din Ping Tsai. Ultrafast Thermal Nonlinearity. *Scientific Reports*, 5(1):17899, dec 2015.
- [34] Mansoor Sheik-Bahae, D.C. Hutchings, D.J. Hagan, and E.W. Van Stryland. Dispersion of bound electron nonlinear refraction in solids. *IEEE Journal of Quantum Electronics*, 27(6):1296–1309, jun 1991.

- [35] Maxim R. Shcherbakov, Polina P. Vabishchevich, Alexander S. Shorokhov, Katie E. Chong, Duk-Yong Choi, Isabelle Staude, Andrey E. Miroshnichenko, Dragomir N. Neshev, Andrey A. Fedyanin, and Yuri S. Kivshar. Ultrafast All-Optical Switching with Magnetic Resonances in Nonlinear Dielectric Nanostructures. *Nano Letters*, 15(10):6985–6990, oct 2015.
- [36] Mark L. Brongersma, Naomi J. Halas, and Peter Nordlander. Plasmon-induced hot carrier science and technology. *Nature Nanotechnology*, 10(1):25–34, jan 2015.
- [37] Giuseppe Della Valle, Ben Hopkins, Lucia Ganzer, Tatjana Stoll, Mohsen Rahmani, Stefano Longhi, Yuri S Kivshar, Costantino De Angelis, Dragomir N Neshev, and Giulio Cerullo. Nonlinear anisotropic dielectric metasurfaces for ultrafast nanophotonics. *ACS Photonics*, 4(9):2129–2136, 2017.
- [38] Jacob B. Khurgin, Matteo Clerici, and Nathaniel Kinsey. Fast and Slow Nonlinearities in Epsilon-Near-Zero Materials. *Laser & Photonics Reviews*, 15(2):2000291, feb 2021.
- [39] Gustavo Grinblat, Michael P. Nielsen, Paul Dichtl, Yi Li, Rupert F. Oulton, and Stefan A. Maier. Ultrafast sub-30-fs all-optical switching based on gallium phosphide. *Science Advances*, 5(6):eaaw3262, jun 2019.
- [40] M. Zahirul Alam, Israel De Leon, and Robert W. Boyd. Large optical nonlinearity of indium tin oxide in its epsilon-near-zero region. *Science*, 352(6287):795–797, may 2016.
- [41] M. Zahirul Alam, Sebastian A. Schulz, Jeremy Upham, Israel De Leon, and Robert W. Boyd. Large optical nonlinearity of nanoantennas coupled to an epsilon-near-zero material. *Nature Photonics*, 12(2):79–83, 2018.
- [42] Mark Fox. *Optische Eigenschaften von Festkörpern*. De Gruyter, dec 2019.
- [43] John David Jackson. *Klassische Elektrodynamik*. De Gruyter, dec 1982.
- [44] K. S. Novoselov, A. K. Geim, S. V. Morozov, D. Jiang, Y. Zhang, S. V. Dubonos, I. V. Grigorieva, and A. A. Firsov. Electric Field Effect in Atomically Thin Carbon Films. *Science*, 306(5696):666–669, oct 2004.
- [45] Vigneshwaran Shanmugam, Rhoda Afriyie Mensah, Karthik Babu, Sidique Gawusu, Avishek Chanda, Yongming Tu, Rasoul Esmaeely Neisiany, Michael Försth, Gabriel Sas, and Oisik Das. A Review of the Synthesis, Properties, and Applications of 2D Materials. *Particle & Particle Systems Characterization*, 39(6):2200031, jun 2022.
- [46] Matthias Baudisch, Andrea Marini, Joel D. Cox, Tony Zhu, Francisco Silva, Stephan Teichmann, Mathieu Massicotte, Frank Koppens, Leonid S. Levitov, F. Javier García de Abajo, and Jens Biegert. Ultrafast nonlinear optical response of Dirac fermions in graphene. *Nature Communications*, 9(1):1018, dec 2018.

- [47] Sung-Young Hong, Jerry I. Dadap, Nicholas Petrone, Po-Chun Yeh, James Hone, and Richard M. Osgood. Optical Third-Harmonic Generation in Graphene. *Physical Review X*, 3(2):021014, jun 2013.
- [48] Maciej Koperski, Maciej R. Molas, Ashish Arora, Karol Nogajewski, Artur O. Slobodeniuk, Clement Faugeras, and Marek Potemski. Optical properties of atomically thin transition metal dichalcogenides: observations and puzzles. *Nanophotonics*, 6(6):1289–1308, mar 2017.
- [49] J Ribeiro-Soares, C Janisch, Z Liu, A L Elias, M S Dresselhaus, M Terrones, L G Cançado, and A Jorio. Second Harmonic Generation in WSe<sub>2</sub>. *2D Materials*, 2(4):045015, dec 2015.
- [50] Ibrahim Abdelwahab, Benjamin Tilmann, Xiaoxu Zhao, Ivan Verzhbitskiy, Rodrigo Berté, Goki Eda, William L Wilson, Gustavo Grinblat, Leonardo de S. Menezes, Kian Ping Loh, and Stefan A Maier. Highly Efficient Sum-Frequency Generation in Niobium Oxydichloride NbOCl<sub>2</sub> Nanosheets. *Advanced Optical Materials*, 11(7):2202833, apr 2023.
- [51] Lucca Kühner, Luca Sortino, Benjamin Tilmann, Thomas Weber, Kenji Watanabe, Takashi Taniguchi, Stefan A. Maier, and Andreas Tittl. High- Q Nanophotonics over the Full Visible Spectrum Enabled by Hexagonal Boron Nitride Metasurfaces. *Advanced Materials*, 35(13):2209688, mar 2023.
- [52] S.-Y. Xu, Ilya Belopolski, Nasser Alidoust, Madhab Neupane, Guang Bian, Chenglong Zhang, Raman Sankar, Guoqing Chang, Zhujun Yuan, C.-C. Lee, S.-M. Huang, Hao Zheng, Jie Ma, Daniel S. Sanchez, B. Wang, Arun Bansil, Fangcheng Chou, Pavel P. Shibayev, Hsin Lin, Shuang Jia, and M. Zahid Hasan. Discovery of a Weyl fermion semimetal and topological Fermi arcs. *Science*, 349(6248):613–617, aug 2015.
- [53] N. P. Armitage, E. J. Mele, and Ashvin Vishwanath. Weyl and Dirac semimetals in three-dimensional solids. *Reviews of Modern Physics*, 90(1):015001, jan 2018.
- [54] Hermann Weyl. GRAVITATION AND THE ELECTRON. *Proceedings of the National Academy of Sciences*, 15(4):323–334, apr 1929.
- [55] Ilya Belopolski, Su-Yang Xu, Daniel S. Sanchez, Guoqing Chang, Cheng Guo, Madhab Neupane, Hao Zheng, Chi-Cheng Lee, Shin-Ming Huang, Guang Bian, Nasser Alidoust, Tay-Rong Chang, Baokai Wang, Xiao Zhang, Arun Bansil, Horng-Tay Jeng, Hsin Lin, Shuang Jia, and M. Zahid Hasan. Criteria for Directly Detecting Topological Fermi Arcs in Weyl Semimetals. *Physical Review Letters*, 116(6):066802, feb 2016.
- [56] A. A. Burkov. Chiral anomaly and transport in Weyl metals. *Journal of Physics: Condensed Matter*, 27(11):113201, mar 2015.

- [57] Chandra Shekhar, Ajaya K. Nayak, Yan Sun, Marcus Schmidt, Michael Nicklas, Inge Leermakers, Uli Zeitler, Yuri Skourski, Jochen Wosnitza, Zhongkai Liu, Yulin Chen, Walter Schnelle, Horst Borrmann, Yuri Grin, Claudia Felser, and Binghai Yan. Extremely large magnetoresistance and ultrahigh mobility in the topological Weyl semimetal candidate NbP. *Nature Physics*, 11(8):645–649, aug 2015.
- [58] Gustav Mie. Beiträge zur Optik trüber Medien, speziell kolloidaler Metallösungen. *Annalen der Physik*, 330(3):377–445, 1908.
- [59] Craig F. Bohren and Donald R. Huffman. *Absorption and Scattering of Light by Small Particles*. Wiley, apr 1998.
- [60] P. Grahn, A. Shevchenko, and M. Kaivola. Electromagnetic multipole theory for optical nanomaterials. *New Journal of Physics*, 14(9):093033, sep 2012.
- [61] Tatsuki Hinamoto and Minoru Fujii. MENP: an open-source MATLAB implementation of multipole expansion for nanophotonics. *OSA Continuum*, 4(5):1640, 2021.
- [62] Mikhail F. Limonov, Mikhail V. Rybin, Alexander N. Poddubny, and Yuri S. Kivshar. Fano resonances in photonics. *Nature Photonics*, 11:543–554, 2017.
- [63] Jürgen D. Sautter, Lei Xu, Andrey E. Miroshnichenko, Mykhaylo Lysevych, Irina Volkovskaya, Daria A. Smirnova, Rocio Camacho-Morales, Khosro Zangeneh Kamali, Fouad Karouta, Kaushal Vora, Hoe H. Tan, Martti Kauranen, Isabelle Staude, Chennupati Jagadish, Dragomir N. Neshev, and Mohsen Rahmani. Tailoring second-harmonic emission from (111)-GaAs nanoantennas. *Nano Letters*, 19(6):3905–3911, 2019.
- [64] Andrey E. Miroshnichenko, Andrey B. Evlyukhin, Ye Feng Yu, Reuben M. Bakker, Arkadi Chipouline, Arseniy I. Kuznetsov, Boris Luk’yanchuk, Boris N. Chichkov, and Yuri S. Kivshar. Nonradiating anapole modes in dielectric nanoparticles. *Nature Communications*, 6(1):8069, nov 2015.
- [65] Kirill Koshelev, Gael Favraud, Andrey Bogdanov, Yuri Kivshar, and Andrea Frat-alocchi. Nonradiating photonics with resonant dielectric nanostructures. *Nanophotonics*, 8(5):725–745, mar 2019.
- [66] Ludwig Hüttenhofer, Andreas Tittl, Lucca Kühner, Emiliano Cortés, and Stefan A Maier. Anapole-Assisted Absorption Engineering in Arrays of Coupled Amorphous Gallium Phosphide Nanodisks. *ACS Photonics*, 8(5):1469–1476, may 2021.
- [67] Ludwig Hüttenhofer, Matthias Golibrzuch, Oliver Bienek, Fedja J. Wendisch, Rui Lin, Markus Becherer, Ian D. Sharp, Stefan A. Maier, and Emiliano Cortés. Meta-surface Photoelectrodes for Enhanced Solar Fuel Generation. *Advanced Energy Materials*, 11(46):2102877, dec 2021.

- [68] Gustavo Grinblat, Yi Li, Michael P. Nielsen, Rupert F. Oulton, and Stefan A. Maier. Efficient Third Harmonic Generation and Nonlinear Subwavelength Imaging at a Higher-Order Anapole Mode in a Single Germanium Nanodisk. *ACS Nano*, 11(1):953–960, 2017.
- [69] Gustavo Grinblat, Yi Li, Michael P. Nielsen, Rupert F. Oulton, and Stefan A. Maier. Enhanced third harmonic generation in single germanium nanodisks excited at the anapole mode. *Nano Letters*, 16(7):4635–4640, 2016.
- [70] Y. R. Shen. *The principles of nonlinear optics*. Wiley, 1985.
- [71] C. R. Ma, J. H. Yan, Y. M. Wei, and G. W. Yang. Second harmonic generation from an individual amorphous selenium nanosphere. *Nanotechnology*, 27(42):425206, 2016.
- [72] Alexander L. Gaeta. Catastrophic Collapse of Ultrashort Pulses. *Physical Review Letters*, 84(16):3582–3585, apr 2000.
- [73] Giulio Cerullo and Sandro De Silvestri. Ultrafast optical parametric amplifiers. *Review of Scientific Instruments*, 74(1):1–18, jan 2003.
- [74] Gadi Fibich and Alexander L. Gaeta. Critical power for self-focusing in bulk media and in hollow waveguides. *Optics Letters*, 25(5):335, mar 2000.
- [75] Ursula Keller. *Ultrafast Lasers*. Graduate Texts in Physics. Springer International Publishing, Cham, 2021.
- [76] Rana Jafari, Travis Jones, and Rick Trebino. 100% reliable algorithm for second-harmonic-generation frequency-resolved optical gating. *Optics Express*, 27(3):2112, feb 2019.
- [77] Rick Trebino, Kenneth W. DeLong, David N. Fittinghoff, John N. Sweetser, Marco A. Krumbügel, Bruce A. Richman, and Daniel J. Kane. Measuring ultrashort laser pulses in the time-frequency domain using frequency-resolved optical gating. *Review of Scientific Instruments*, 68(9):3277–3295, sep 1997.
- [78] Vadim V. Lozovoy, Igor Pastirk, and Marcos Dantus. Multiphoton intrapulse interference IV Ultrashort laser pulse spectral phase characterization and compensation. *Optics Letters*, 29(7):775, apr 2004.
- [79] Alberto Comin, Richard Ciesielski, Giovanni Piredda, Kevin Donkers, and Achim Hartschuh. Compression of ultrashort laser pulses via gated multiphoton intrapulse interference phase scans. *Journal of the Optical Society of America B*, 31(5):1118, may 2014.

- [80] Alberto Comin, Richard Ciesielski, Nicolás Coca-López, and Achim Hartschuh. Phase retrieval of ultrashort laser pulses using a MIIPS algorithm. *Optics Express*, 24(3):2505, feb 2016.
- [81] Umran S. Inan and Robert A. Marshall. *Numerical Electromagnetics*. Cambridge University Press, apr 2011.
- [82] Benjamin Gallinet, Jérémy Butet, and Olivier J. F. Martin. Numerical methods for nanophotonics: standard problems and future challenges. *Laser & Photonics Reviews*, 9(6):577–603, nov 2015.
- [83] Pushkar K. Gothe, Dhruv Gaur, and Venu Gopal Achanta. MPTMS self-assembled monolayer deposition for ultra-thin gold films for plasmonics. *Journal of Physics Communications*, 2(3):035005, mar 2018.
- [84] Andrea Damascelli, Zahid Hussain, and Zhi-Xun Shen. Angle-resolved photoemission studies of the cuprate superconductors. *Reviews of Modern Physics*, 75(2):473–541, apr 2003.
- [85] R.M.A. Azzam and N.M. Bashara. *Ellipsometry and Polarized Light*. North Holland Press, Amsterdam, 2 (1987) edition, 1977.
- [86] Anne-Laure Calendron, Hüseyin Çankaya, Giovanni Cirimi, and Franz X. Kärtner. White-light generation with sub-ps pulses. *Optics Express*, 23(11):13866, 2015.
- [87] Wendong Tian, Fei Liang, Shumeng Chi, Chang Li, Haohai Yu, Han Zhang, and Huaijin Zhang. Highly Efficient Super-Continuum Generation on an Epsilon-Near-Zero Surface. *ACS Omega*, 5(5):2458–2464, 2020.
- [88] F. A. Kish, F. M. Steranka, D. C. DeFevre, D. A. Vanderwater, K. G. Park, C. P. Kuo, T. D. Osentowski, M. J. Peanasky, J. G. Yu, R. M. Fletcher, D. A. Steigerwald, M. G. Craford, and V. M. Robbins. Very high-efficiency semiconductor wafer-bonded transparent-substrate (Al x Ga 1- x ) 0.5 In 0.5 P/GaP light-emitting diodes. *Applied Physics Letters*, 64(21):2839–2841, may 1994.
- [89] Richard Zallen and William Paul. Band structure of gallium phosphide from optical experiments at high pressure. *Physical Review*, 134(6A):1628–1641, 1964.
- [90] Benjamin Tilmann, Tahiyat Huq, Thomas Possmayer, Jakub Dranczewski, Bert Nickel, Haizhong Zhang, Leonid Krivitsky, Arseniy I. Kuznetsov, Leonardo de S. Menezes, Stefano Vezzoli, Riccardo Sapienza, and Stefan A. Maier. Comparison of Harmonic Generation from Crystalline and Amorphous Gallium Phosphide Nanofilms. *Advanced Optical Materials*, 2300269, jun 2023.
- [91] Robert W Boyd, Zhimin Shi, and Israel De Leon. The third-order nonlinear optical susceptibility of gold. *Optics Communications*, 326:74–79, sep 2014.

- [92] Yuri Kivshar. All-dielectric meta-optics and non-linear nanophotonics. *National Science Review*, 5(2):144–158, mar 2018.
- [93] Kirill Koshelev, Sergey Kruk, Elizaveta Melik-Gaykazyan, Jae-Hyuck Choi, Andrey Bogdanov, Hong-Gyu Park, and Yuri Kivshar. Subwavelength dielectric resonators for nonlinear nanophotonics. *Science*, 367(6475):288–292, jan 2020.
- [94] Reza Sanatinia, Marcin Swillo, and Srinivasan Anand. Surface second-harmonic generation from vertical GaP nanopillars. *Nano Letters*, 12(2):820–826, 2012.
- [95] Reza Sanatinia. *Ensemble and Individual III-V Semiconductor Nanopillars: Optical Properties and Applications*. PhD thesis, 2014.
- [96] Reza Sanatinia, Srinivasan Anand, and Marcin Swillo. Experimental quantification of surface optical nonlinearity in GaP nanopillar waveguides. *Optics Express*, 23(2):756–764, 2015.
- [97] L. Sortino, P. G. Zotev, S. Mignuzzi, J. Cambiasso, D. Schmidt, A. Genco, M. Aßmann, M. Bayer, S. A. Maier, R. Sapienza, and A. I. Tartakovskii. Enhanced light-matter interaction in an atomically thin semiconductor coupled with dielectric nano-antennas. *Nature Communications*, 10(1):5119, dec 2019.
- [98] Luca Sortino, Panaiot G. Zotev, Catherine L. Phillips, Alistair J. Brash, Javier Cambiasso, Elena Marensi, A. Mark Fox, Stefan A. Maier, Riccardo Sapienza, and Alexander I. Tartakovskii. Bright single photon emitters with enhanced quantum efficiency in a two-dimensional semiconductor coupled with dielectric nano-antennas. *Nature Communications*, (2021):1–9, 2021.
- [99] Kelley Rivoire, Andrei Faraon, and Jelena Vuckovic. Gallium phosphide photonic crystal nanocavities in the visible. *Applied Physics Letters*, 93(6):063103, aug 2008.
- [100] Dalziel J. Wilson, Katharina Schneider, Simon Hönl, Miles Anderson, Yannick Baumgartner, Lukas Czornomaz, Tobias J. Kippenberg, and Paul Seidler. Integrated gallium phosphide nonlinear photonics. *Nature Photonics*, 14(1):57–62, jan 2020.
- [101] Gianni Q. Moretti, Emiliano Cortés, Stefan A. Maier, Andrea V. Bragas, and Gustavo Grinblat. Engineering gallium phosphide nanostructures for efficient nonlinear photonics and enhanced spectroscopies. *Nanophotonics*, 10(17):4261–4271, 2021.
- [102] Aravind P. Anthur, Haizhong Zhang, Ramon Paniagua-Dominguez, Dmitry A. Kalashnikov, Son Tung Ha, Tobias W. W. Maß, Arseniy I. Kuznetsov, and Leonid Krivitsky. Continuous Wave Second Harmonic Generation Enabled by Quasi-Bound-States in the Continuum on Gallium Phosphide Metasurfaces. *Nano Letters*, 20(12):8745–8751, dec 2020.

- [103] Maxim R. Shcherbakov, Haizhong Zhang, Michael Tripepi, Giovanni Sartorello, Noah Talisa, Abdallah AlShafey, Zhiyuan Fan, Justin Twardowski, Leonid A. Krivitsky, Arseniy I. Kuznetsov, Enam Chowdhury, and Gennady Shvets. Generation of even and odd high harmonics in resonant metasurfaces using single and multiple ultra-intense laser pulses. *Nature Communications*, 12(1):10–15, 2021.
- [104] Aravind P. Anthur, Haizhong Zhang, Yuriy Akimov, Jun Rong Ong, Dmitry Kalashnikov, Arseniy I. Kuznetsov, and Leonid Krivitsky. Second harmonic generation in gallium phosphide nano-waveguides. *Optics Express*, 29(7):10307, mar 2021.
- [105] Kristin Persson. Materials Data on GaP (SG:216) by Materials Project.
- [106] Zeeshan H. Amber, Benjamin Kirbus, Lukas M. Eng, and Michael Rüsing. Quantifying the coherent interaction length of second-harmonic microscopy in lithium niobate confined nanostructures. *Journal of Applied Physics*, 130(13):133102, oct 2021.
- [107] Kevin O’Brien, Haim Suchowski, Junsuk Rho, Alessandro Salandrino, Boubacar Kante, Xiaobo Yin, and Xiang Zhang. Predicting nonlinear properties of metamaterials from the linear response. *Nature Materials*, 14(4):379–383, apr 2015.
- [108] Ruixuan Yi, Xutao Zhang, Chen Li, Bijun Zhao, Jing Wang, Zhiwen Li, Xuetao Gan, Li Li, Ziyuan Li, Fanlu Zhang, Liang Fang, Naiyin Wang, Pingping Chen, Wei Lu, Lan Fu, Jianlin Zhao, Hark Hoe Tan, and Chennupati Jagadish. Self-frequency-conversion nanowire lasers. *Light: Science and Applications*, 11(1), 2022.
- [109] Robert C. Miller. Optical second harmonic generation in piezoelectric crystals. *Appl. Phys. Lett*, 5(17):17–19, 1964.
- [110] Ichiro Shoji, Takeshi Kondo, and Ryoichi Ito. Second-order nonlinear susceptibilities of various dielectric and semiconductor materials. *Optical and Quantum Electronics*, 1961(34):797–833, 2002.
- [111] Jiantian Zhang, Weina Zhao, Peng Yu, Guowei Yang, and Zheng Liu. Second harmonic generation in 2D layered materials. *2D Materials*, 7(4):042002, oct 2020.
- [112] Yu Song, Siqi Hu, Miao-Ling Lin, Xuetao Gan, Ping-Heng Tan, and Jianlin Zhao. Extraordinary Second Harmonic Generation in ReS<sub>2</sub> Atomic Crystals. *ACS Photonics*, 5(9):3485–3491, sep 2018.
- [113] Ibrahim Abdelwahab, Benjamin Tilmann, Yaze Wu, David Giovanni, Ivan Verzhbitskiy, Menglong Zhu, Rodrigo Berté, Fengyuan Xuan, Leonardo De S Menezes, Goki Eda, Tze Chien Sum, Su Ying Quek, Stefan A. Maier, and Kian Ping Loh. Giant second-harmonic generation in ferroelectric NbOI<sub>2</sub>. *Nature Photonics*, 16(9):644–650, sep 2022.

- [114] R. I. Woodward, R. T. Murray, C. F. Phelan, R E P de Oliveira, T. H. Runcorn, E J R Kelleher, S. Li, E C de Oliveira, G J M Fehine, G. Eda, and C J S de Matos. Characterization of the second- and third-order nonlinear optical susceptibilities of monolayer MoS<sub>2</sub> using multiphoton microscopy. *2D Materials*, 4(1):011006, nov 2016.
- [115] Georgy A. Ermolaev, Yury V. Stebunov, Andrey A. Vyshnevyy, Dmitry E. Tatarkin, Dmitry I. Yakubovsky, Sergey M. Novikov, Denis G. Baranov, Timur Shegai, Alexey Y. Nikitin, Aleksey V. Arsenin, and Valentyn S. Volkov. Broadband optical properties of monolayer and bulk MoS<sub>2</sub>. *npj 2D Materials and Applications*, 4(1):21, jul 2020.
- [116] Mervin Zhao, Ziliang Ye, Ryuji Suzuki, Yu Ye, Han Yu Zhu, Jun Xiao, Yuan Wang, Yoshihiro Iwasa, and Xiang Zhang. Atomically phase-matched second-harmonic generation in a 2D crystal. *Light: Science and Applications*, 5(September 2015), 2016.
- [117] Valerie Yoshioka, Jian Lu, Zichen Tang, Jicheng Jin, Roy H Olsson, and Bo Zhen. Strongly enhanced second-order optical nonlinearity in CMOS-compatible AlScN thin films. *APL Materials*, 9(10):101104, oct 2021.
- [118] Benjamin Tilmann, Gustavo Grinblat, Rodrigo Berté, Mehmet Özcan, Viktoria F. Kunzelmann, Bert Nickel, Ian D Sharp, Emiliano Cortés, Stefan A. Maier, and Yi Li. Nanostructured amorphous gallium phosphide on silica for nonlinear and ultrafast nanophotonics. *Nanoscale Horizons*, 5(11):1500–1508, 2020.
- [119] Charles C. Wang, J. Bomback, W. T. Donlon, C. R. Huo, and J. V. James. Optical third-harmonic generation in reflection from crystalline and amorphous samples of silicon. *Physical Review Letters*, 57(13):1647–1650, 1986.
- [120] W. Ettoumi, Y. Petit, J. Kasparian, and J.-P. Wolf. Generalized Miller Formulæ. *Optics Express*, 18(7):6613, mar 2010.
- [121] Anna Popczyk, Aouatif Aamoum, Anna Migalska-Zalas, Przemyslaw Płóciennik, Anna Zawadzka, Jaroslaw Mysliwiec, and Bouchta Sahraoui. Selected Organometallic Compounds for Third Order Nonlinear Optical Application. *Nanomaterials*, 9(2):254, feb 2019.
- [122] Gustavo Grinblat, Haizhong Zhang, Michael P. Nielsen, Leonid Krivitsky, Rodrigo Berté, Yi Li, Benjamin Tilmann, Emiliano Cortés, Rupert F. Oulton, Arseniy I. Kuznetsov, and Stefan A. Maier. Efficient ultrafast all-optical modulation in a nonlinear crystalline gallium phosphide nanodisk at the anapole excitation. *Science Advances*, 6(34):eabb3123, aug 2020.
- [123] Gerald Brönstrup, Norbert Jahr, Christian Leiterer, Andrea Csäki, Wolfgang Fritzsche, and Silke Christiansen. Optical properties of individual silicon nanowires for photonic devices. *ACS Nano*, 4(12):7113–7122, 2010.

- [124] Luca Carletti, Kirill Koshelev, Costantino De Angelis, and Yuri Kivshar. Giant Nonlinear Response at the Nanoscale Driven by Bound States in the Continuum. *Physical Review Letters*, 121(3):033903, jul 2018.
- [125] Polina P. Vabishchevich, Sheng Liu, Michael B. Sinclair, Gordon A. Keeler, Gregory M. Peake, and Igal Brener. Enhanced second-harmonic generation using broken symmetry III-V semiconductor fano metasurfaces. *ACS Photonics*, 5(5):1685–1690, 2018.
- [126] L. Carletti, A. Locatelli, O. Stepanenko, G. Leo, and C. De Angelis. Enhanced second-harmonic generation from magnetic resonance in AlGaAs nanoantennas. *Optics Express*, 23(20):26544–26550, 2015.
- [127] Sergey V. Makarov, Mihail I. Petrov, Urs Zywiets, Valentin Milichko, Dmitry Zuev, Natalia Lopanitsyna, Alexey Kuksin, Ivan Mukhin, George Zograf, Evgeniy Ubyivovk, Daria A. Smirnova, Sergey Starikov, Boris N. Chichkov, and Yuri S. Kivshar. Efficient second-harmonic generation in nanocrystalline silicon nanoparticles. *Nano Letters*, 17(5):3047–3053, 2017.
- [128] Toshihiko Shibanuma, Gustavo Grinblat, Pablo Albella, and Stefan A. Maier. Efficient third harmonic generation from metal-dielectric hybrid nanoantennas. *Nano Letters*, 17(4):2647–2651, 2017.
- [129] Sheng Liu, Polina P. Vabishchevich, Aleksandr Vaskin, John L. Reno, Gordon A. Keeler, Michael B. Sinclair, Isabelle Staude, and Igal Brener. An all-dielectric metasurface as a broadband optical frequency mixer. *Nature Communications*, 9(1):2507, dec 2018.
- [130] Xiyuan Lu, Gregory Moille, Qing Li, Daron A. Westly, Anshuman Singh, Ashutosh Rao, Su Peng Yu, Travis C. Briles, Scott B. Papp, and Kartik Srinivasan. Efficient telecom-to-visible spectral translation through ultralow power nonlinear nanophotonics. *Nature Photonics*, 13(September):593–602, 2019.
- [131] Lavinia Ghirardini, Giuseppe Marino, Valerio Flavio Gili, Ivan Favero, Davide Rocco, Luca Carletti, Andrea Locatelli, Costantino de Angelis, Marco Finazzi, Michele Celebrano, Dragomir N. Neshev, and Leo Giuseppe. Shaping the nonlinear emission pattern of a dielectric nanoantenna by integrated holographic gratings. *Nano Letters*, 18(11):6750–6755, 2018.
- [132] Luca Carletti, Giuseppe Marino, Lavinia Ghirardini, Valerio F Gili, Davide Rocco, Ivan Favero, Andrea Locatelli, Anatoly V Zayats, Michele Celebrano, Marco Finazzi, Leo Giuseppe, Costantino de Angelis, and Dragomir N. Neshev. Nonlinear goniometry by second harmonic generation in AlGaAs nanoantennas. *ACS Photonics*, 5(11):4386–4392, 2018.

- [133] Salvatore Campione, Sheng Liu, Lorena I. Basilio, Larry K. Warne, William L. Langston, Ting S. Luk, Joel R. Wendt, John L. Reno, Gordon A. Keeler, Igal Brener, and Michael B. Sinclair. Broken symmetry dielectric Resonators for high quality factor fano metasurfaces. *ACS Photonics*, 3(12):2362–2367, 2016.
- [134] Maxim R. Shcherbakov, Polina P. Vabishchevich, Alexander S. Shorokhov, Katie E. Chong, Duk Yong Choi, Isabelle Staude, Andrey E. Miroshnichenko, Dragomir N. Neshev, Andrey A. Fedyanin, and Yuri S. Kivshar. Ultrafast All-Optical Switching with Magnetic Resonances in Nonlinear Dielectric Nanostructures. *Nano Letters*, 15(10):6985–6990, oct 2015.
- [135] D. L. Cui, J. Q. Pan, Z. C. Zhang, B. B. Huang, X. Y. Qin, M. H. Jiang, and S. M. Gao. Stability and surface reactivity of gallium phosphide nanocrystals. *Progress in Crystal Growth and Characterization of Materials*, 40(1):145–151, jan 2000.
- [136] Jeremy L. Bourque, Mark C. Biesinger, and Kim M. Baines. Chemical state determination of molecular gallium compounds using XPS. *Dalton Transactions*, 45(18):7678–7696, 2016.
- [137] Hal Emmer, Christopher T. Chen, Rebecca Saive, Dennis Friedrich, Yu Horie, Amir Arbabi, Andrei Faraon, and Harry A. Atwater. Fabrication of Single Crystal Gallium Phosphide Thin Films on Glass. *Scientific Reports*, 7(1):2–7, 2017.
- [138] B.D. Cullity and S.R. Stock. *Elements of X-Ray Diffraction*. 1978.
- [139] Edward D. Palik. Front Matter. In *Handbook of Optical Constants of Solids*, page iii. Elsevier, 1998.
- [140] Ramón Paniagua-Domínguez, Boris Luk’yanchuk, Andrey Miroshnichenko, and José A. Sánchez-Gil. Dielectric nanoresonators and metamaterials. *Journal of Applied Physics*, 126(15):150401, oct 2019.
- [141] Gustavo Grinblat, Ibrahim Abdelwahab, Michael P. Nielsen, Paul Dichtl, Kai Leng, Rupert F. Oulton, Kian Ping Loh, and Stefan A. Maier. Ultrafast All-Optical Modulation in 2D Hybrid Perovskites. *ACS Nano*, 13(8):9504–9510, 2019.
- [142] Gustavo Grinblat, Rodrigo Berte, Michael P P Nielsen, Yi Li, Rupert F Oulton, and Stefan A. Maier. Sub-20 fs All-Optical Switching in a Single Au-Clad Si Nanodisk. *Nano Letters*, 18(12):7896–7900, 2018.
- [143] Sunil Kumar, M. Khorasaninejad, M. M. Adachi, K. S. Karim, S. S. Saini, and A. K. Sood. Probing ultrafast carrier dynamics, nonlinear absorption and refraction in core-shell silicon nanowires. *Pramana - Journal of Physics*, 79(3):471–481, 2012.
- [144] B.E. Warren. *X-ray diffraction*. Dover Publications, 1990.

- [145] Lin Zhang, Anuradha M Agarwal, Lionel C Kimerling, and Jurgen Michel. Nonlinear Group IV photonics based on silicon and germanium: from near-infrared to mid-infrared. *Nanophotonics*, 3(4-5):247–268, aug 2014.
- [146] Jian Gao, Qiwen Zhan, and Andrew M. Sarangan. High-index low-loss gallium phosphide thin films fabricated by radio frequency magnetron sputtering. *Thin Solid Films*, 519(16):5424–5428, 2011.
- [147] Francesco Monticone, Dimitrios Sounas, Alex Krasnok, and Andrea Alù. Can a Nonradiating Mode Be Externally Excited? Nonscattering States versus Embedded Eigenstates. *ACS Photonics*, 6(12):3108–3114, dec 2019.
- [148] Maxim R. Shcherbakov, Sheng Liu, Varvara V. Zubyuk, Aleksandr Vaskin, Polina P. Vabishchevich, Gordon Keeler, Thomas Pertsch, Tatyana V. Dolgova, Isabelle Staude, Igal Brener, and Andrey A. Fedyanin. Ultrafast all-optical tuning of direct-gap semiconductor metasurfaces. *Nature Communications*, 8(1):17, may 2017.
- [149] Peijun Guo, Richard D. Schaller, John B. Ketterson, and Robert P.H. Chang. Ultrafast switching of tunable infrared plasmons in indium tin oxide nanorod arrays with large absolute amplitude. *Nature Photonics*, 10(4):267–273, 2016.
- [150] Nobuo Suzuki. FDTD Analysis of Two-Photon Absorption and Free-Carrier Absorption in Si High-Index-Contrast Waveguides. *Journal of Lightwave Technology*, 25(9):2495–2501, sep 2007.
- [151] Benjamin Tilmann, Avanindra Kumar Pandeya, Gustavo Grinblat, Leonardo de S. Menezes, Yi Li, Chandra Shekhar, Claudia Felser, Stuart S. P. Parkin, Amilcar Bedoya-Pinto, and Stefan A. Maier. Ultrafast Sub-100 fs All-Optical Modulation and Efficient Third-Harmonic Generation in Weyl Semimetal Niobium Phosphide Thin Films. *Advanced Materials*, 34(15):2106733, apr 2022.
- [152] Liang Wu, S. Patankar, T. Morimoto, N. L. Nair, E. Thewalt, A. Little, J. G. Analytis, J. E. Moore, and J. Orenstein. Giant anisotropic nonlinear optical response in transition metal monpnictide Weyl semimetals. *Nature Physics*, 13(4):350–355, apr 2017.
- [153] Junchao Ma, Qiangqiang Gu, Yinan Liu, Jiawei Lai, Peng Yu, Xiao Zhuo, Zheng Liu, Jian-Hao Chen, Ji Feng, and Dong Sun. Nonlinear photoresponse of type-II Weyl semimetals. *Nature Materials*, 18(5):476–481, may 2019.
- [154] Gavin B. Osterhoudt, Laura K. Diebel, Mason J. Gray, Xu Yang, John Stanco, Xiangwei Huang, Bing Shen, Ni Ni, Philip J. W. Moll, Ying Ran, and Kenneth S. Burch. Colossal mid-infrared bulk photovoltaic effect in a type-I Weyl semimetal. *Nature Materials*, 18(5):471–475, may 2019.

- [155] Catherine R. Rajamathi, Uttam Gupta, Nitesh Kumar, Hao Yang, Yan Sun, Vicky Süß, Chandra Shekhar, Marcus Schmidt, Horst Blumtritt, Peter Werner, Binghai Yan, Stuart Parkin, Claudia Felser, and C. N. R. Rao. Weyl Semimetals as Hydrogen Evolution Catalysts. *Advanced Materials*, 29(19):1606202, may 2017.
- [156] Chris P. Weber, Bryan S. Berggren, Madison G. Masten, Thomas C. Ogloza, Skylar Deckoff-Jones, Julien Madéo, Michael K. L. Man, Keshav M. Dani, Lingxiao Zhao, Genfu Chen, Jinyu Liu, Zhiqiang Mao, Leslie M. Schoop, Bettina V. Lotsch, Stuart S. P. Parkin, and Mazhar Ali. Similar ultrafast dynamics of several dissimilar Dirac and Weyl semimetals. *Journal of Applied Physics*, 122(22):223102, dec 2017.
- [157] Chris P. Weber, Leslie M. Schoop, Stuart S. P. Parkin, Robert C. Newby, Alex Nateprov, Bettina Lotsch, Bala Murali Krishna Mariserla, J. Matthew Kim, Keshav M. Dani, Hans A. Bechtel, Ernest Arushanov, and Mazhar Ali. Directly photoexcited Dirac and Weyl fermions in ZrSiS and NbAs. *Applied Physics Letters*, 113(22):221906, nov 2018.
- [158] M. R. van Delft, S. Pezzini, M. König, P. Tinnemans, N. E. Hussey, and S. Wiedmann. Surface and bulk superconductivity at ambient pressure in the Weyl semimetal TaP. pages 1–17, aug 2018.
- [159] Maja D. Bachmann, Nityan Nair, Felix Flicker, Roni Ilan, Tobias Meng, Nirmal J. Ghimire, Eric D. Bauer, Filip Ronning, James G. Analytis, and Philip J. W. Moll. Inducing superconductivity in Weyl semimetal microstructures by selective ion sputtering. *Science Advances*, 3(5):e1602983, may 2017.
- [160] Amilcar Bedoya-Pinto, Avanindra Kumar Pandeya, Defa Liu, Hakan Deniz, Kai Chang, Hengxin Tan, Hyeon Han, Jagannath Jena, Ilya Kostanovskiy, and Stuart S. P. Parkin. Realization of Epitaxial NbP and TaP Weyl Semimetal Thin Films. *ACS Nano*, 14(4):4405–4413, apr 2020.
- [161] Shu-Chun Wu, Yan Sun, Claudia Felser, and Binghai Yan. Hidden type-II Weyl points in the Weyl semimetal NbP. *Physical Review B*, 96(16):165113, oct 2017.
- [162] Amilcar Bedoya-Pinto, Defa Liu, Hengxin Tan, Avanindra Kumar Pandeya, Kai Chang, Jibo Zhang, and Stuart S. P. Parkin. Large Fermi-Energy Shift and Suppression of Trivial Surface States in NbP Weyl Semimetal Thin Films. *Advanced Materials*, 33(21):2008634, may 2021.
- [163] Shin-ichi Kimura, Hiroko Yokoyama, Hiroshi Watanabe, Jörg Sichelschmidt, Vicky Süß, Marcus Schmidt, and Claudia Felser. Optical signature of Weyl electronic structures in tantalum pnictides TaPn (Pn= P, As). *Physical Review B*, 96(7):075119, may 2017.
- [164] B. Xu, Y. M. Dai, L. X. Zhao, K. Wang, R. Yang, W. Zhang, J. Y. Liu, H. Xiao, G. F. Chen, A. J. Taylor, D. A. Yarotski, R. P. Prasankumar, and X. G. Qiu. Optical

- spectroscopy of the Weyl semimetal TaAs. *Physical Review B*, 93(12):121110, mar 2016.
- [165] Davide Grassano, Olivia Pulci, Adriano Mosca Conte, and Friedhelm Bechstedt. Validity of Weyl fermion picture for transition metals monopnictides TaAs, TaP, NbAs, and NbP from ab initio studies. *Scientific Reports*, 8(1):3534, dec 2018.
- [166] J. Buckeridge, D. Jevdokimovs, C. R. A. Catlow, and A. A. Sokol. Bulk electronic, elastic, structural, and dielectric properties of the Weyl semimetal TaAs. *Physical Review B*, 93(12):125205, mar 2016.
- [167] Tianning Zhang, K. J. A. Ooi, Wenchao Chen, L. K. Ang, and Yee Sin Ang. Optical Kerr effect and third harmonic generation in topological Dirac/Weyl semimetal. *Optics Express*, 27(26):38270, dec 2019.
- [168] N. Bloembergen and P. S. Pershan. Light Waves at the Boundary of Nonlinear Media. *Physical Review*, 128(2):606–622, oct 1962.
- [169] Hao Yang, Honghua Guan, Nicolas Biekert, Ghidewon Arefe, Damien C. Chang, Yawen Sun, Po Chun Yeh, Xiaoping Liu, Sung Young Hong, Ida Delač Marion, Marko Kralj, James C. Hone, Richard M. Osgood, and Jerry I. Dadap. Layer dependence of third-harmonic generation in thick multilayer graphene. *Physical Review Materials*, 2(7):1–5, 2018.
- [170] Shumeng Chi, Zhilin Li, Haohai Yu, Gang Wang, Shuxian Wang, Huaijin Zhang, and Jiyang Wang. Symmetrical broken and nonlinear response of Weyl semimetal TaAs influenced by the topological surface states and Weyl nodes. *Annalen der Physik*, 529(4):1600359, apr 2017.
- [171] Yan Sun, Shu-Chun Wu, and Binghai Yan. Topological surface states and Fermi arcs of the noncentrosymmetric Weyl semimetals TaAs, TaP, NbAs, and NbP. *Physical Review B*, 92(11):115428, sep 2015.
- [172] Shumeng Chi, Fei Liang, Hongxiang Chen, Wendong Tian, Han Zhang, Haohai Yu, Gang Wang, Zheshuai Lin, Jiangping Hu, and Huaijin Zhang. Surface Nonlinear Optics on Centrosymmetric Dirac Nodal-Line Semimetal ZrSiS. *Advanced Materials*, 32(2):1904498, jan 2020.
- [173] Shreyas Patankar, Liang Wu, Baozhu Lu, Manita Rai, Jason D. Tran, T. Morimoto, Daniel E. Parker, Adolfo G. Grushin, N. L. Nair, J. G. Analytis, J. E. Moore, J. Orenstein, and D. H. Torchinsky. Resonance-enhanced optical nonlinearity in the Weyl semimetal TaAs. *Physical Review B*, 98(16):165113, oct 2018.
- [174] Robert J. Kirby, Austin Ferrenti, Caroline Weinberg, Sebastian Klemenz, Mohamed Oudah, Shiming Lei, Chris P. Weber, Daniele Fausti, Gregory D. Scholes, and Leslie M. Schoop. Transient Drude Response Dominates Near-Infrared Pump–Probe

- Reflectivity in Nodal-Line Semimetals ZrSiS and ZrSiSe. *The Journal of Physical Chemistry Letters*, 11(15):6105–6111, aug 2020.
- [175] D. Brida, A. Tomadin, C. Manzoni, Y. J. Kim, A. Lombardo, S. Milana, R. R. Nair, K. S. Novoselov, A. C. Ferrari, G. Cerullo, and M. Polini. Ultrafast collinear scattering and carrier multiplication in graphene. *Nature Communications*, 4(1):1987, oct 2013.
- [176] Fatemeh Nematollahi, S. Azar Oliaei Motlagh, Vadym Apalkov, and Mark I. Stockman. Weyl semimetals in ultrafast laser fields. *Physical Review B*, 99(24):245409, jun 2019.
- [177] Chiara Trovatiello, Florian Katsch, Nicholas J. Borys, Malte Selig, Kaiyuan Yao, Rocio Borrego-Varillas, Francesco Scotognella, Ilka Kriegel, Aiming Yan, Alex Zettl, P. James Schuck, Andreas Knorr, Giulio Cerullo, and Stefano Dal Conte. The ultrafast onset of exciton formation in 2D semiconductors. *Nature Communications*, 11(1):5277, dec 2020.
- [178] Shakeel Ahmed, Xiantao Jiang, Feng Zhang, and Han Zhang. Pump-probe microspectroscopy and 2D materials. *Journal of Physics D: Applied Physics*, 53(47), 2020.
- [179] Kawon Oum, Thomas Lenzer, Mirko Scholz, Dae Yool Jung, Onejae Sul, Byung Jin Cho, Jens Lange, and Andreas Müller. Observation of ultrafast carrier dynamics and phonon relaxation of graphene from the deep-ultraviolet to the visible region. *Journal of Physical Chemistry C*, 118(12):6454–6461, 2014.
- [180] Tobias Helk, Emma Berger, Sasawat Jamnuch, Lars Hoffmann, Adeline Kabacinski, Julien Gautier, Fabien Tissandier, Jean-Philippe Goddet, Hung-Tzu Chang, Juwon Oh, C. Das Pemmaraju, Tod A. Pascal, Stephane Sebban, Christian Spielmann, and Michael Zuerch. Table-top extreme ultraviolet second harmonic generation. *Science Advances*, 7(21):6–11, may 2021.
- [181] S. Shwartz, M. Fuchs, J. B. Hastings, Y. Inubushi, T. Ishikawa, T. Katayama, D. A. Reis, T. Sato, K. Tono, M. Yabashi, S. Yudovich, and S. E. Harris. X-Ray Second Harmonic Generation. *Physical Review Letters*, 112(16):163901, apr 2014.
- [182] Rick Trebino, Kenneth W. DeLong, David N. Fittinghoff, John N. Sweetser, Marco A. Krumbügel, Bruce A. Richman, and Daniel J. Kane. Measuring ultrashort laser pulses in the time-frequency domain using frequency-resolved optical gating. *Review of Scientific Instruments*, 68(9):3277–3295, sep 1997.
- [183] Alan E Willner, Salman Khaleghi, Mohammad Reza Chitgarha, and Omer Faruk Yilmaz. All-Optical Signal Processing. *Journal of Lightwave Technology*, 32(4):660–680, feb 2014.

- [184] Periklis Pantazis, James Maloney, David Wu, and Scott E. Fraser. Second harmonic generating (SHG) nanoprobe for in vivo imaging. *Proceedings of the National Academy of Sciences*, 107(33):14535–14540, aug 2010.
- [185] Takaaki Manaka, Eunju Lim, Ryousuke Tamura, and Mitsumasa Iwamoto. Direct imaging of carrier motion in organic transistors by optical second-harmonic generation. *Nature Photonics*, 1(10):581–584, oct 2007.
- [186] Xiaobo Yin, Ziliang Ye, Daniel A. Chenet, Yu Ye, Kevin O’Brien, James C. Hone, and Xiang Zhang. Edge Nonlinear Optics on a MoS<sub>2</sub> Atomic Monolayer. *Science*, 344(6183):488–490, may 2014.
- [187] Y. R. Shen. Surface properties probed by second-harmonic and sum-frequency generation. *Nature*, 337(6207):519–525, feb 1989.
- [188] D. Hsieh, J. W. McIver, D. H. Torchinsky, D. R. Gardner, Y. S. Lee, and N. Gedik. Nonlinear Optical Probe of Tunable Surface Electrons on a Topological Insulator. *Physical Review Letters*, 106(5):057401, feb 2011.
- [189] D. R. Yakovlev, V. V. Pavlov, A. V. Rodina, R. V. Pisarev, J. Mund, W. Warkentin, and M. Bayer. Exciton Spectroscopy of Semiconductors by the Method of Optical Harmonics Generation (Review). *Physics of the Solid State*, 60(8):1471–1486, aug 2018.
- [190] J.-Y. Chauleau, E. Haltz, C. Carrétéro, S. Fusil, and M. Viret. Multi-stimuli manipulation of antiferromagnetic domains assessed by second-harmonic imaging. *Nature Materials*, 16(8):803–807, aug 2017.
- [191] Kai-Qiang Lin, Sebastian Bange, and John M. Lupton. Quantum interference in second-harmonic generation from monolayer WSe<sub>2</sub>. *Nature Physics*, 15(3):242–246, mar 2019.
- [192] Chaojie Cui, Fei Xue, Wei-Jin Hu, and Lain-Jong Li. Two-dimensional materials with piezoelectric and ferroelectric functionalities. *npj 2D Materials and Applications*, 2(1):18, jun 2018.
- [193] Harald Schaeber and Rudolf Gerken. Beitrage zur Chemie der Elemente Niob und Tantal. XXIX. NbOJ<sub>3</sub> und NbOJ<sub>2</sub>. Darstellung, Eigenschaften und thermisches Verhalten. *Zeitschrift fuer anorganische und allgemeine Chemie*, 317(1-2):105–112, aug 1962.
- [194] J Rijnsdorp and F Jellinek. The crystal structure of niobium oxide diiodide NbOI<sub>2</sub>. *Journal of the Less Common Metals*, 61(1):79–82, sep 1978.
- [195] H. Hillebrecht, P.J. Schmidt, H.W. Rotter, G. Thiele, P. Zönnchen, H. Bengel, H.-J. Cantow, S.N. Magonov, and M.-H. Whangbo. Structural and scanning microscopy

- studies of layered compounds  $MCl_3$  ( $M = Mo, Ru, Cr$ ) and  $MOCl_2$  ( $M = V, Nb, Mo, Ru, Os$ ). *Journal of Alloys and Compounds*, 246(1-2):70–79, jan 1997.
- [196] Johannes Beck and Christian Kusterer. Crystal Structure of  $NbOBr_2$ . *Zeitschrift für anorganische und allgemeine Chemie*, 632(14):2193–2194, oct 2006.
- [197] Yaze Wu, Ibrahim Abdelwahab, Ki Chang Kwon, Ivan Verzhbitskiy, Lin Wang, Weng Heng Liew, Kui Yao, Goki Eda, Kian Ping Loh, Lei Shen, and Su Ying Quek. Data-driven discovery of high performance layered van der Waals piezoelectric  $NbOI_2$ . *Nature Communications*, 13(1):1884, apr 2022.
- [198] A. M. Pugachev, V. I. Kovalevskii, N. V. Surovtsev, S. Kojima, S. A. Prosandeev, I. P. Raevski, and S. I. Raevskaya. Broken Local Symmetry in Paraelectric  $BaTiO_3$  Proved by Second Harmonic Generation. *Physical Review Letters*, 108(24):247601, jun 2012.
- [199] R.E. Peierls. *Quantum Theory of Solids*. Clarendon Press, 1996.
- [200] Yinglu Jia, Min Zhao, Gaoyang Gou, Xiao Cheng Zeng, and Ju Li. Niobium oxide dihalides  $NbOX_2$ : a new family of two-dimensional van der Waals layered materials with intrinsic ferroelectricity and antiferroelectricity. *Nanoscale Horizons*, 4(5):1113–1123, 2019.
- [201] Mark S. Hybertsen and Steven G. Louie. Electron correlation in semiconductors and insulators: Band gaps and quasiparticle energies. *Physical Review B*, 34(8):5390–5413, oct 1986.
- [202] Lars Hedin. New Method for Calculating the One-Particle Green’s Function with Application to the Electron-Gas Problem. *Physical Review*, 139(3A):A796–A823, aug 1965.
- [203] Yuqiang Fang, Fakun Wang, Ruiqi Wang, Tianyou Zhai, and Fuqiang Huang. 2D  $NbOI_2$ : A Chiral Semiconductor with Highly In-Plane Anisotropic Electrical and Optical Properties. *Advanced Materials*, 33(29):2101505, jul 2021.
- [204] R. Leitsmann, W. G. Schmidt, P. H. Hahn, and F. Bechstedt. Second-harmonic polarizability including electron-hole attraction from band-structure theory. *Physical Review B*, 71(19):195209, may 2005.
- [205] J. J. Hopfield and D. G. Thomas. Theoretical and Experimental Effects of Spatial Dispersion on the Optical Properties of Crystals. *Physical Review*, 132(2):563–572, oct 1963.
- [206] Skylar Deckoff-Jones, Jingjing Zhang, Christopher E. Petoukhoff, Michael K.L. Man, Sidong Lei, Robert Vajtai, Pulickel M. Ajayan, Diyar Talbayev, Julien Madéo, and Keshav M. Dani. Observing the interplay between surface and bulk optical nonlinearities in thin van der Waals crystals. *Scientific Reports*, 6(1):22620, mar 2016.

- [207] Fang Liu, Wenjing Wu, Yusong Bai, Sang Hoon Chae, Qiuyang Li, Jue Wang, James Hone, and X.-Y. Zhu. Disassembling 2D van der Waals crystals into macroscopic monolayers and reassembling into artificial lattices. *Science*, 367(6480):903–906, feb 2020.
- [208] Chiara Trovatiello, Andrea Marini, Xinyi Xu, Changhwan Lee, Fang Liu, Nicola Curveli, Cristian Manzoni, Stefano Dal Conte, Kaiyuan Yao, Alessandro Ciattoni, James Hone, Xiaoyang Zhu, P. James Schuck, and Giulio Cerullo. Optical parametric amplification by monolayer transition metal dichalcogenides. *Nature Photonics*, 15(1):6–10, 2021.
- [209] Yilei Li, Yi Rao, Kin Fai Mak, Yumeng You, Shuyuan Wang, Cory R. Dean, and Tony F. Heinz. Probing Symmetry Properties of Few-Layer MoS<sub>2</sub> and h-BN by Optical Second-Harmonic Generation. *Nano Letters*, 13(7):3329–3333, jul 2013.
- [210] Yu Song, Siqi Hu, Miao-Ling Lin, Xuetao Gan, Ping-Heng Tan, and Jianlin Zhao. Extraordinary Second Harmonic Generation in ReS<sub>2</sub> Atomic Crystals. *ACS Photonics*, 5(9):3485–3491, sep 2018.
- [211] Wontaek Kim, Je Yhoun Ahn, Juseung Oh, Ji Hoon Shim, and Sunmin Ryu. Second-Harmonic Young’s Interference in Atom-Thin Heterocrystals. *Nano Letters*, 20(12):8825–8831, dec 2020.
- [212] Ioannis Paradisanos, Andres Manuel Saiz Raven, Thierry Amand, Cedric Robert, Pierre Renucci, Kenji Watanabe, Takashi Taniguchi, Iann C. Gerber, Xavier Marie, and Bernhard Urbaszek. Second harmonic generation control in twisted bilayers of transition metal dichalcogenides. *Physical Review B*, 105(11):115420, mar 2022.
- [213] S. Bergfeld and W. Daum. Second-Harmonic Generation in GaAs: Experiment versus Theoretical Predictions of [Formula presented]. *Physical Review Letters*, 90(3):4, 2003.
- [214] Dominic Vella, José Bico, Arezki Boudaoud, Benoit Roman, and Pedro M. Reis. The macroscopic delamination of thin films from elastic substrates. *Proceedings of the National Academy of Sciences*, 106(27):10901–10906, jul 2009.
- [215] Andres Castellanos-Gomez, Rafael Roldán, Emmanuele Cappelluti, Michele Buscema, Francisco Guinea, Herre S. J. van der Zant, and Gary A. Steele. Local Strain Engineering in Atomically Thin MoS<sub>2</sub>. *Nano Letters*, 13(11):5361–5366, nov 2013.
- [216] Robert Fickler, Radek Lapkiewicz, William N. Plick, Mario Krenn, Christoph Schaeff, Sven Ramelow, and Anton Zeilinger. Quantum Entanglement of High Angular Momenta. *Science*, 338(6107):640–643, nov 2012.

- [217] Alessandro Fedrizzi, Thomas Herbst, Andreas Poppe, Thomas Jennewein, and Anton Zeilinger. A wavelength-tunable fiber-coupled source of narrowband entangled photons. *Optics Express*, 15(23):15377, 2007.
- [218] G. Zhang, J. Y. Haw, H. Cai, F. Xu, S. M. Assad, J. F. Fitzsimons, X. Zhou, Y. Zhang, S. Yu, J. Wu, W. Ser, L. C. Kwek, and A. Q. Liu. An integrated silicon photonic chip platform for continuous-variable quantum key distribution. *Nature Photonics*, 13(12):839–842, dec 2019.
- [219] Yevgeny Rakita, Omri Bar-Elli, Elena Meirzadeh, Hadar Kaslasi, Yagel Peleg, Gary Hodes, Igor Lubomirsky, Dan Oron, David Ehre, and David Cahen. Tetragonal CH<sub>3</sub>NH<sub>3</sub>PbI<sub>3</sub> is ferroelectric. *Proceedings of the National Academy of Sciences*, 114(28):E5504–E5512, jul 2017.
- [220] Daniel D. Hickstein, David R. Carlson, Haridas Mundoor, Jacob B. Khurgin, Kartik Srinivasan, Daron Westly, Abijith Kowligy, Ivan I. Smalyukh, Scott A. Diddams, and Scott B. Papp. Self-organized nonlinear gratings for ultrafast nanophotonics. *Nature Photonics*, 13(7):494–499, 2019.
- [221] Renee J. Tran, Krystal L. Sly, and John C. Conboy. Applications of Surface Second Harmonic Generation in Biological Sensing. *Annual Review of Analytical Chemistry*, 10(1):387–414, jun 2017.
- [222] David A. B. Miller. Are optical transistors the logical next step? *Nature Photonics*, 4(1):3–5, jan 2010.
- [223] Katia Gallo and Gaetano Assanto. All-optical diode based on second-harmonic generation in an asymmetric waveguide. *Journal of the Optical Society of America B*, 16(2):267, feb 1999.
- [224] M.M. Fejer, G.A. Magel, D.H. Jundt, and R.L. Byer. Quasi-phase-matched second harmonic generation: tuning and tolerances. *IEEE Journal of Quantum Electronics*, 28(11):2631–2654, 1992.
- [225] D. J. Clark, C. T. Le, V. Senthilkumar, F. Ullah, H.-Y. Cho, Y. Sim, M.-J. Seong, K.-H. Chung, Y. S. Kim, and J. I. Jang. Near bandgap second-order nonlinear optical characteristics of MoS<sub>2</sub> monolayer transferred on transparent substrates. *Applied Physics Letters*, 107(13):131113, sep 2015.
- [226] Chinh Tam Le, Daniel J. Clark, Farman Ullah, Velusamy Senthilkumar, Joon I. Jang, Yumin Sim, Maeng-Je Seong, Koo-Hyun Chung, Hyoyeol Park, and Yong Soo Kim. Nonlinear optical characteristics of monolayer MoSe<sub>2</sub>. *Annalen der Physik*, 528(7-8):551–559, aug 2016.
- [227] Kyle L. Seyler, John R. Schaibley, Pu Gong, Pasqual Rivera, Aaron M. Jones, Sanfeng Wu, Jiaqiang Yan, David G. Mandrus, Wang Yao, and Xiaodong Xu. Electrical

- control of second-harmonic generation in a WSe<sub>2</sub> monolayer transistor. *Nature Nanotechnology*, 10(5):407–411, 2015.
- [228] Lasse Karvonen, Antti Säynätjoki, Soroush Mehravar, Raul D. Rodriguez, Susanne Hartmann, Dietrich R. T. Zahn, Seppo Honkanen, Robert A. Norwood, N. Peyghambarian, Khanh Kieu, Harri Lipsanen, and Juha Riihonen. Investigation of Second- and Third-Harmonic Generation in Few-Layer Gallium Selenide by Multiphoton Microscopy. *Scientific Reports*, 5(1):10334, may 2015.
- [229] Jannatul Susoma, Lasse Karvonen, Antti Säynätjoki, Soroush Mehravar, Robert A. Norwood, Nasser Peyghambarian, Khanh Kieu, Harri Lipsanen, and Juha Riihonen. Second and third harmonic generation in few-layer gallium telluride characterized by multiphoton microscopy. *Applied Physics Letters*, 108(7):073103, feb 2016.
- [230] Ichiro Shoji, Takashi Kondo, Ayako Kitamoto, Masayuki Shirane, and Ryoichi Ito. Absolute scale of second-order nonlinear-optical coefficients. *Journal of the Optical Society of America B*, 14(9):2268, sep 1997.
- [231] A. Yariv and P. Yeh. *Photonics: Optical Electronics in Modern Communications*. Oxford University Press, 2007.
- [232] George M. Sheldrick. SHELXT – Integrated space-group and crystal-structure determination. *Acta Crystallographica Section A Foundations and Advances*, 71(1):3–8, jan 2015.
- [233] Daniel Schmidt, Benjamin Booso, Tino Hofmann, Eva Schubert, Andrew Sarangan, and Mathias Schubert. Monoclinic optical constants, birefringence, and dichroism of slanted titanium nanocolumns determined by generalized ellipsometry. *Applied Physics Letters*, 94(1):011914, jan 2009.
- [234] Mathias Schubert. Polarization-dependent optical parameters of arbitrarily anisotropic homogeneous layered systems. *Physical Review B*, 53(8):4265–4274, feb 1996.
- [235] P Giannozzi, Oliviero Andreussi, T Brumme, O Bunau, M Buongiorno Nardelli, M Calandra, R Car, C Cavazzoni, D Ceresoli, M Cococcioni, N Colonna, I Carnimeo, A Dal Corso, S de Gironcoli, P Delugas, R A DiStasio, A Ferretti, A Floris, G Fratesi, G Fugallo, R Gebauer, U Gerstmann, F Giustino, T Gorni, J Jia, M Kawamura, H-Y Ko, A Kokalj, E Küçükbenli, M Lazzeri, M Marsili, N Marzari, F Mauri, N L Nguyen, H-V Nguyen, A Otero-de-la Roza, L Paulatto, S Poncé, D Rocca, R Sabatini, B Santra, M Schlipf, A P Seitsonen, A Smogunov, I Timrov, T Thonhauser, P Umari, N Vast, X Wu, and S Baroni. Advanced capabilities for materials modelling with Quantum ESPRESSO. *Journal of Physics: Condensed Matter*, 29(46):465901, nov 2017.

- [236] Paolo Giannozzi, Stefano Baroni, Nicola Bonini, Matteo Calandra, Roberto Car, Carlo Cavazzoni, Davide Ceresoli, Guido L. Chiarotti, Matteo Cococcioni, Ismaila Dabo, Andrea Dal Corso, Stefano de Gironcoli, Stefano Fabris, Guido Fratesi, Ralph Gebauer, Uwe Gerstmann, Christos Gougoussis, Anton Kokalj, Michele Lazzeri, Layla Martin-Samos, Nicola Marzari, Francesco Mauri, Riccardo Mazzarello, Stefano Paolini, Alfredo Pasquarello, Lorenzo Paulatto, Carlo Sbraccia, Sandro Scandolo, Gabriele Sclauzero, Ari P. Seitsonen, Alexander Smogunov, Paolo Umari, and Renata M. Wentzcovitch. QUANTUM ESPRESSO: a modular and open-source software project for quantum simulations of materials. *Journal of Physics: Condensed Matter*, 21(39):395502, sep 2009.
- [237] D. R. Hamann. Optimized norm-conserving Vanderbilt pseudopotentials. *Physical Review B*, 88(8):085117, aug 2013.
- [238] John P. Perdew, Kieron Burke, and Matthias Ernzerhof. Generalized Gradient Approximation Made Simple. *Physical Review Letters*, 77(18):3865–3868, oct 1996.
- [239] Stefan Grimme. Semiempirical GGA-type density functional constructed with a long-range dispersion correction. *Journal of Computational Chemistry*, 27(15):1787–1799, nov 2006.
- [240] Hendrik J. Monkhorst and James D. Pack. Special points for Brillouin-zone integrations. *Physical Review B*, 13(12):5188–5192, jun 1976.
- [241] Michael Rohlfing and Steven G Louie. Electron-hole excitations and optical spectra from first principles. *Physical Review B*, 62(8):4927–4944, aug 2000.
- [242] Jack Deslippe, Georgy Samsonidze, David A. Strubbe, Manish Jain, Marvin L. Cohen, and Steven G. Louie. BerkeleyGW: A massively parallel computer package for the calculation of the quasiparticle and optical properties of materials and nanostructures. *Computer Physics Communications*, 183(6):1269–1289, jun 2012.
- [243] Sohrab Ismail-Beigi. Truncation of periodic image interactions for confined systems. *Physical Review B*, 73(23):233103, jun 2006.
- [244] Felipe H. da Jornada, Diana Y. Qiu, and Steven G. Louie. Nonuniform sampling schemes of the Brillouin zone for many-electron perturbation-theory calculations in reduced dimensionality. *Physical Review B*, 95(3):035109, jan 2017.
- [245] An-Qi Wang, Xing-Guo Ye, Da-Peng Yu, and Zhi-Min Liao. Topological Semimetal Nanostructures: From Properties to Topotronics. *ACS Nano*, 14(4):3755–3778, apr 2020.
- [246] Hassan A. Hafez, Sergey Kovalev, Jan Christoph Deinert, Zoltán Mics, Bertram Green, Nilesh Awari, Min Chen, Semyon Germanskiy, Ulf Lehnert, Jochen Teichert, Zhe Wang, Klaas Jan Tielrooij, Zhaoyang Liu, Zongping Chen, Akimitsu Narita,

- Klaus Müllen, Mischa Bonn, Michael Gensch, and Dmitry Turchinovich. Extremely efficient terahertz high-harmonic generation in graphene by hot Dirac fermions. *Nature*, 561(7724):507–511, 2018.
- [247] Ming Lun Tseng, Michael Semmlinger, Ming Zhang, Catherine Arndt, Tzu Ting Huang, Jian Yang, Hsin Yu Kuo, Vin Cent Su, Mu Ku Chen, Cheng Hung Chu, Benjamin Cerjan, Din Ping Tsai, Peter Nordlander, and Naomi J. Halas. Vacuum ultraviolet nonlinear metalens. *Science Advances*, 8(16):1–8, 2022.
- [248] Yisheng Gao, Yubin Fan, Yujie Wang, Wenhong Yang, Qinghai Song, and Shumin Xiao. Nonlinear Holographic All-Dielectric Metasurfaces. *Nano Letters*, 18(12):8054–8061, 2018.
- [249] Lucca Kühner, Luca Sortino, Rodrigo Berté, Juan Wang, Haoran Ren, Stefan A. Maier, Yuri Kivshar, and Andreas Tittl. Radial bound states in the continuum for polarization-invariant nanophotonics. *Nature Communications*, 13(1):4992, aug 2022.
- [250] Jun Guan, Jeong-Eun Park, Shikai Deng, Max J. H. Tan, Jingtian Hu, and Teri W. Odom. Light–Matter Interactions in Hybrid Material Metasurfaces. *Chemical Reviews*, 122(19):15177–15203, oct 2022.
- [251] Emanuele Galiffi, Romain Tirole, Shixiong Yin, Huanan Li, Stefano Vezzoli, Paloma A. Huidobro, Mário G. Silveirinha, Riccardo Sapienza, Andrea Alù, and J. B. Pendry. Photonics of time-varying media. *Advanced Photonics*, 4(01):1–32, feb 2022.
- [252] Romain Tirole, Emanuele Galiffi, Jakub Dranczewski, Taran Attavar, Benjamin Tilmann, Yao-Ting Wang, Paloma A. Huidobro, Andrea Alù, John B. Pendry, Stefan A. Maier, Stefano Vezzoli, and Riccardo Sapienza. Saturable Time-Varying Mirror Based on an Epsilon-Near-Zero Material. *Physical Review Applied*, 18(5):054067, nov 2022.
- [253] Romain Tirole, Stefano Vezzoli, Emanuele Galiffi, Iain Robertson, Dries Maurice, Benjamin Tilmann, Stefan A. Maier, John B. Pendry, and Riccardo Sapienza. Double-slit time diffraction at optical frequencies. *Nature Physics*, 19(7):999–1002, jul 2023.
- [254] Alexander Krasnok, Mykhailo Tymchenko, and Andrea Alù. Nonlinear metasurfaces: a paradigm shift in nonlinear optics. *Materials Today*, 21(1):8–21, 2018.
- [255] Kirill Koshelev, Sergey Kruk, Elizaveta Melik-Gaykazyan, Jae Hyuck Choi, Andrey Bogdanov, Hong Gyu Park, and Yuri Kivshar. Subwavelength dielectric resonators for nonlinear nanophotonics. *Science*, 367(6475):288–292, 2020.

- [256] J.W. You, S.R. Bongu, Q. Bao, and N.C. Panoiu. Nonlinear optical properties and applications of 2D materials: theoretical and experimental aspects. *Nanophotonics*, 8(1):63–97, dec 2018.
- [257] Luca Carletti, Andrea Locatelli, Dragomir Neshev, and Costantino De Angelis. Shaping the radiation pattern of second-harmonic generation from AlGaAs dielectric nanoantennas. *ACS Photonics*, 3(8):1500–1507, 2016.
- [258] Reza Sanatinia, Srinivasan Anand, and Marcin Swillo. Modal engineering of second-harmonic generation in single GaP nanopillars. *Nano Letters*, 14(9):5376–5381, 2014.
- [259] Rocio Camacho-Morales, Mohsen Rahmani, Sergey Kruk, Lei Wang, Lei Xu, Daria A. Smirnova, Alexander S. Solntsev, Andrey Miroschnichenko, Hark Hoe Tan, Fouad Karouta, Shagufta Naureen, Kaushal Vora, Luca Carletti, Costantino De Angelis, Chennupati Jagadish, Yuri S. Kivshar, and Dragomir N. Neshev. Nonlinear Generation of Vector Beams From AlGaAs Nanoantennas. *Nano Letters*, 16(11):7191–7197, nov 2016.
- [260] Giuseppe Marino, Alexander S. Solntsev, Lei Xu, Valerio F. Gili, Luca Carletti, Alexander N. Poddubny, Mohsen Rahmani, Daria A. Smirnova, Haitao Chen, Aristide Lemaître, Guoquan Zhang, Anatoly V. Zayats, Costantino De Angelis, Giuseppe Leo, Andrey A. Sukhorukov, and Dragomir N. Neshev. Spontaneous photon-pair generation from a dielectric nanoantenna. *Optica*, 6(11):1416, 2019.
- [261] Maxim R. Shcherbakov, Kevin Werner, Zhiyuan Fan, Noah Talisa, Enam Chowdhury, and Gennady Shvets. Photon acceleration and tunable broadband harmonics generation in nonlinear time-dependent metasurfaces. *Nature Communications*, 10(1):1345, dec 2019.
- [262] Heykel Aouani, Mohsen Rahmani, Miguel Navarro-Cía, and Stefan A Maier. Third-harmonic-upconversion enhancement from a single semiconductor nanoparticle coupled to a plasmonic antenna. *Nature Nanotechnology*, 9(4):290–294, apr 2014.
- [263] Sisira Suresh, Orad Reshef, M. Zahirul Alam, Jeremy Upham, Mohammad Karimi, and Robert W. Boyd. Enhanced Nonlinear Optical Responses of Layered Epsilon-near-Zero Metamaterials at Visible Frequencies. *ACS Photonics*, 8(1):125–129, jan 2021.
- [264] Nicolò Maccaferri, Attilio Zilli, Tommi Isoniemi, Lavinia Ghirardini, Marzia Iarossi, Marco Finazzi, Michele Celebrano, and Francesco De Angelis. Enhanced Nonlinear Emission from Single Multilayered Metal–Dielectric Nanocavities Resonating in the Near-Infrared. *ACS Photonics*, 8(2):512–520, feb 2021.
- [265] Yuanqing Yang, Vladimir A. Zenin, and Sergey I. Bozhevolnyi. Anapole-Assisted Strong Field Enhancement in Individual All-Dielectric Nanostructures. *ACS Photonics*, 5(5):1960–1966, 2018.

- [266] Ashutosh Patri, Kévin G. Cognée, David M. Myers, Louis Haeberlé, Vinod Menon, and Stéphane Kéna-Cohen. Hybrid epsilon-near-zero modes of photonic gap antennas. *Physical Review B*, 105(16):165126, apr 2022.
- [267] Félix Thouin, David M. Myers, Ashutosh Patri, Bill Baloukas, Ludvik Martinu, and Stéphane Kéna-Cohen. Broadband field-enhancement in epsilon-near-zero photonic gap antennas. nov 2022.
- [268] Nicholas Karl, Polina P. Vabishchevich, Maxim R. Shcherbakov, Sheng Liu, Michael B. Sinclair, Gennady Shvets, and Igal Brener. Frequency Conversion in a Time-Variant Dielectric Metasurface. *Nano Letters*, page acs.nanolett.0c02113, sep 2020.
- [269] Mohammad Karimi, M. Zahirul Alam, Jeremy Upham, Orad Reshef, and Robert W. Boyd. Time-varying gradient metasurface with applications in all-optical beam steering. *Nanophotonics*, 12(9):1733–1740, apr 2023.
- [270] Enrico Giuseppe Carnemolla, Lucia Caspani, Clayton DeVault, Matteo Clerici, Stefano Vezzoli, Vincenzo Bruno, Vladimir M. Shalaev, Daniele Faccio, Alexandra Boltasseva, and Marcello Ferrera. Degenerate optical nonlinear enhancement in epsilon-near-zero transparent conducting oxides. *Optical Materials Express*, 8(11):3392, nov 2018.
- [271] Ting S. Luk, Domenico de Ceglia, Sheng Liu, Gordon A. Keeler, Rohit P. Prasankumar, Maria A. Vincenti, Michael Scalora, Michael B. Sinclair, and Salvatore Campione. Enhanced third harmonic generation from the epsilon-near-zero modes of ultrathin films. *Applied Physics Letters*, 106(15):151103, apr 2015.
- [272] Kevin O’Brien, Haim Suchowski, Junsuk Rho, Alessandro Salandrino, Boubacar Kante, Xiaobo Yin, and Xiang Zhang. Predicting nonlinear properties of metamaterials from the linear response. *Nature Materials*, 14(4):379–383, 2015.
- [273] Kai Pang, M. Zahirul Alam, Yiyu Zhou, Cong Liu, Orad Reshef, Karapet Manukyan, Matt Voegtle, Anuj Pennathur, Cindy Tseng, Xinzhou Su, Haoqian Song, Zhe Zhao, Runzhou Zhang, Haoqian Song, Nanzhe Hu, Ahmed Almaiman, Jahan M. Dawlaty, Robert W. Boyd, Moshe Tur, and Alan E. Willner. Adiabatic Frequency Conversion Using a Time-Varying Epsilon-Near-Zero Metasurface. *Nano Letters*, 21(14):5907–5913, jul 2021.
- [274] Dimitrios L. Sounas and Andrea Alù. Non-reciprocal photonics based on time modulation. *Nature Photonics*, 11(12):774–783, dec 2017.
- [275] Theodoros T. Koutserimpas and Romain Fleury. Nonreciprocal Gain in Non-Hermitian Time-Floquet Systems. *Physical Review Letters*, 120(8):087401, feb 2018.

- [276] Paloma A. Huidobro, Emanuele Galiffi, Sébastien Guenneau, Richard V. Craster, and J. B. Pendry. Fresnel drag in space–time-modulated metamaterials. *Proceedings of the National Academy of Sciences*, 116(50):24943–24948, dec 2019.
- [277] E. Galiffi, P. A. Huidobro, and J. B. Pendry. Broadband Nonreciprocal Amplification in Luminal Metamaterials. *Physical Review Letters*, 123(20):206101, nov 2019.
- [278] Maria Chiara Braidotti, Andrea Vinante, Giulio Gasbarri, Daniele Faccio, and Hendrik Ulbricht. Zel’dovich Amplification in a Superconducting Circuit. *Physical Review Letters*, 125(14):140801, oct 2020.
- [279] Qian Lin, Meng Xiao, Luqi Yuan, and Shanhui Fan. Photonic Weyl point in a two-dimensional resonator lattice with a synthetic frequency dimension. *Nature Communications*, 7(1):13731, dec 2016.
- [280] Eran Lustig, Yonatan Sharabi, and Mordechai Segev. Topological aspects of photonic time crystals. *Optica*, 5(11):1390, nov 2018.
- [281] Li He, Zachariah Addison, Jicheng Jin, Eugene J. Mele, Steven G. Johnson, and Bo Zhen. Floquet Chern insulators of light. *Nature Communications*, 10(1):4194, sep 2019.
- [282] Amir Darabi, Xiang Ni, Michael Leamy, and Andrea Alù. Reconfigurable Floquet elastodynamic topological insulator based on synthetic angular momentum bias. *Science Advances*, 6(29):2–7, jul 2020.
- [283] P. D. Nation, J. R. Johansson, M. P. Blencowe, and Franco Nori. Colloquium : Stimulating uncertainty: Amplifying the quantum vacuum with superconducting circuits. *Reviews of Modern Physics*, 84(1):1–24, jan 2012.
- [284] Siddharth Buddhiraju, Wei Li, and Shanhui Fan. Photonic Refrigeration from Time-Modulated Thermal Emission. *Physical Review Letters*, 124(7):077402, feb 2020.
- [285] Victor Pacheco-Peña and Nader Engheta. Temporal aiming. *Light: Science & Applications*, 9(1):129, jul 2020.
- [286] Hugo Lira, Zongfu Yu, Shanhui Fan, and Michal Lipson. Electrically Driven Non-reciprocity Induced by Interband Photonic Transition on a Silicon Chip. *Physical Review Letters*, 109(3):033901, jul 2012.
- [287] Stefan F. Preble, Qianfan Xu, and Michal Lipson. Changing the colour of light in a silicon resonator. *Nature Photonics*, 1(5):293–296, may 2007.
- [288] T. Kampfrath, D. M. Beggs, T. P. White, A. Melloni, T. F. Krauss, and L. Kuipers. Ultrafast adiabatic manipulation of slow light in a photonic crystal. *Physical Review A*, 81(4):043837, apr 2010.

- [289] Nathaniel Kinsey, Clayton DeVault, Alexandra Boltasseva, and Vladimir M. Shalaev. Near-zero-index materials for photonics. *Nature Reviews Materials*, 4(12):742–760, sep 2019.
- [290] L. Caspani, R. P. M. Kaipurath, M. Clerici, M. Ferrera, T. Roger, J. Kim, N. Kinsey, M. Pietrzyk, A. Di Falco, V. M. Shalaev, A. Boltasseva, and D. Faccio. Enhanced Nonlinear Refractive Index in Epsilon-Near-Zero Materials. *Physical Review Letters*, 116(23):233901, jun 2016.
- [291] Yiyu Zhou, M. Zahirul Alam, Mohammad Karimi, Jeremy Upham, Orad Reshef, Cong Liu, Alan E. Willner, and Robert W. Boyd. Broadband frequency translation through time refraction in an epsilon-near-zero material. *Nature Communications*, 11(1):2180, may 2020.
- [292] Changxu Liu and Stefan A. Maier. High-Quality Optical Hotspots with Topology-Protected Robustness. *ACS Photonics*, 9(1):241–248, jan 2022.
- [293] Vincenzo Bruno, Stefano Vezzoli, Clayton DeVault, Enrico Carnemolla, Marcello Ferrera, Alexandra Boltasseva, Vladimir M. Shalaev, Daniele Faccio, and Matteo Clerici. Broad Frequency Shift of Parametric Processes in Epsilon-Near-Zero Time-Varying Media. *Applied Sciences*, 10(4):1318, feb 2020.
- [294] Marcello Ferrera and Enrico G. Carnemolla. Ultra-fast transient plasmonics using transparent conductive oxides. *Journal of Optics*, 20(2):024007, feb 2018.
- [295] Stefano Vezzoli, Vincenzo Bruno, Clayton DeVault, Thomas Roger, Vladimir M Shalaev, Alexandra Boltasseva, Marcello Ferrera, Matteo Clerici, Audrius Dubietis, and Daniele Faccio. Optical Time Reversal from Time-Dependent Epsilon-Near-Zero Media. *Physical Review Letters*, 120(4):043902, jan 2018.
- [296] Justus Bohn, Ting Shan Luk, Simon Horsley, and Euan Hendry. Spatiotemporal refraction of light in an epsilon-near-zero indium tin oxide layer: frequency shifting effects arising from interfaces. *Optica*, 8(12):1532, dec 2021.
- [297] Mohammad Taghinejad, Hossein Taghinejad, Zihao Xu, Yawei Liu, Sean P. Rodrigues, Kyu-Tae Lee, Tianquan Lian, Ali Adibi, and Wenshan Cai. Hot-Electron-Assisted Femtosecond All-Optical Modulation in Plasmonics. *Advanced Materials*, 30(9):1704915, mar 2018.
- [298] Changxu Liu, Stefan A. Maier, and Guixin Li. Genetic-algorithm-aided meta-atom multiplication for improved absorption and colouration in nanophotonics. *ACS Photonics*, 2020.
- [299] Justus Bohn, Ting Shan Luk, Craig Tollerton, Sam W. Hutchings, Igal Brener, Simon Horsley, William L. Barnes, and Euan Hendry. All-optical switching of an epsilon-near-zero plasmon resonance in indium tin oxide. *Nature Communications*, 12(1):1–6, 2021.

- [300] Yuanmu Yang, Jian Lu, Alejandro Manjavacas, Ting S. Luk, Hanzhe Liu, Kyle Kelley, Jon Paul Maria, Evan L. Runnerstrom, Michael B. Sinclair, Shambhu Ghimire, and Igal Brener. High-harmonic generation from an epsilon-near-zero material. *Nature Physics*, 15(10):1022–1026, 2019.
- [301] Cong Liu, M. Zahirul Alam, Kai Pang, Karapet Manukyan, Orad Reshef, Yiyu Zhou, Saumya Choudhary, Joel Patrow, Anuj Pennathurs, Hao Song, Zhe Zhao, Runzhou Zhang, Fatemeh Alishahi, Ahmad Fallahpour, Yinwen Cao, Ahmed Almainan, Jahan M. Dawlaty, Moshe Tur, Robert W. Boyd, and Alan E. Willner. Photon Acceleration Using a Time-Varying Epsilon-near-Zero Metasurface. *ACS Photonics*, 8(3):716–720, mar 2021.
- [302] Simon Vassant, Jean-Paul Hugonin, Francois Marquier, and Jean-Jacques Greffet. Berreman mode and epsilon near zero mode. *Optics Express*, 20(21):23971, 2012.
- [303] Heng Wang, Kang Du, Chuhao Jiang, Zhiqiang Yang, Lixia Ren, Wending Zhang, Soo Jin Chua, and Ting Mei. Extended Drude Model for Intraband-Transition-Induced Optical Nonlinearity. *Physical Review Applied*, 11(6):064062, jun 2019.
- [304] Marcos Moshinsky. Diffraction in Time. *Physical Review*, 88(3):625–631, nov 1952.
- [305] J. Felber, G. Müller, R. Gähler, and R. Golub. Time dependent neutron optics. *Physica B: Condensed Matter*, 162(3):191–196, jul 1990.
- [306] Pascal Szriftgiser, David Guéry-Odelin, Markus Arndt, and Jean Dalibard. Atomic Wave Diffraction and Interference Using Temporal Slits. *Physical Review Letters*, 77(1):4–7, jul 1996.
- [307] Časlav Brukner and Anton Zeilinger. Diffraction of matter waves in space and in time. *Physical Review A*, 56(5):3804–3824, nov 1997.
- [308] V. Bruno, C. DeVault, S. Vezzoli, Z. Kudyshev, T. Huq, S. Mignuzzi, A. Jacassi, S. Saha, Y. D. Shah, S. A. Maier, D. R. S. Cumming, A. Boltasseva, M. Ferrera, M. Clerici, D. Faccio, R. Sapienza, and V. M. Shalaev. Negative Refraction in Time-Varying Strongly Coupled Plasmonic-Antenna-Epsilon-Near-Zero Systems. *Physical Review Letters*, 124(4):043902, jan 2020.
- [309] Ieng-Wai Un, Subhajit Sarkar, and Yonatan Sivan. Electronic-Based Model of the Optical Nonlinearity of Low-Electron-Density Drude Materials. *Physical Review Applied*, 19(4):044043, apr 2023.
- [310] G. Lerosey, J. de Rosny, A. Tourin, A. Derode, G. Montaldo, and M. Fink. Time Reversal of Electromagnetic Waves. *Physical Review Letters*, 92(19):193904, may 2004.

- 
- [311] Avik Dutt, Qian Lin, Luqi Yuan, Momchil Minkov, Meng Xiao, and Shanhui Fan. A single photonic cavity with two independent physical synthetic dimensions. *Science*, 367(6473):59–64, jan 2020.
- [312] Alexander D. Cronin, Jörg Schmiedmayer, and David E. Pritchard. Optics and interferometry with atoms and molecules. *Reviews of Modern Physics*, 81(3):1051–1129, jul 2009.
- [313] Javier del Pino, Jesse J. Slim, and Ewold Verhagen. Non-Hermitian chiral phononics through optomechanically induced squeezing. *Nature*, 606(7912):82–87, jun 2022.
- [314] Romain Fleury, Dimitrios L Sounas, Caleb F Sieck, Michael R Haberman, and Andrea Alù. Sound Isolation and Giant Linear Nonreciprocity in a Compact Acoustic Circulator. *Science*, 343(6170):516–519, jan 2014.
- [315] Choonlae Cho, Xinhua Wen, Namkyoo Park, and Jensen Li. Digitally virtualized atoms for acoustic metamaterials. *Nature Communications*, 11(1):251, jan 2020.
- [316] Aravind Nagulu, Negar Reiskarimian, and Harish Krishnaswamy. Non-reciprocal electronics based on temporal modulation. *Nature Electronics*, 3(5):241–250, may 2020.
- [317] K. Schultheiss, N. Sato, P. Matthies, L. Körber, K. Wagner, T. Hula, O. Gladii, J. E. Pearson, A. Hoffmann, M. Helm, J. Fassbender, and H. Schultheiss. Time Refraction of Spin Waves. *Physical Review Letters*, 126(13):137201, mar 2021.

# Acknowledgments

First, I want to thank the supervisor of my thesis, **Prof. Dr. Stefan Maier** for hosting me for all these years, first as a Master and then as a PhD student. It was a great experience to work under his supervision and I'm very glad for the confidence and faith he put into my work, together with the numerous opportunities that he provided me.

Next, I have to thank the second supervisor of my thesis, **Prof. Dr. Jonathan Finley** and the other participants of my PhD committee, **Prof. Dr. Jan von Delft**, **Prof. Dr. Joachim Rädler** and **Prof. Dr. Monika Aidelsburger**.

Furthermore, I want to dedicate special thanks to **Prof. Dr. Leonardo de Souza Menezes** for always having an open door and ear for scientific or non-scientific discussions and the uncounted times we he supported me and my work.

I would like to thank **Prof. Dr. Emiliano Cortés** and **Prof. Dr. Gustavo Grinblat** for their huge scientific support and the unique opportunity to spend time in Buenos Aires. Similarly, I want to thank **Prof. Riccardo Sapienza**, **Dr. Stefano Veozzoli** and **Romain Tirole**, together with everyone else in London for the fruitful collaborations and the multiple opportunities to visit ICL.

Next, I want to thank **Dr. Luca Sortino** and **Dr. Ibrahim Abdelwahab** for the intense times that we had working on two-dimensional materials and in the ultrafast lab.

I want to thank all the numerous collaborators in Munich, Germany and all over the world, in particular **Dr. Yi Li**, **Dr. Haoran Ren** and **Dr. Amilcar Bedoya-Pinto**.

A huge thanks goes to all the colleagues of the chair who made the always enjoyable and easy to go to work. I want to particularly mention the people that I started with, **Ludwig**, **Lucca**, **Andrea**, **Matias**, **Lin** and **Simone**. Moreover, I want to especially thank **Christph** for the numerous lunches with Chinese food, **Andreas**, **Thomas** and **Jonas** for the collective struggling with the Eline and machines in the cleanroom in general and **Thomas P.** for the collaborative work in the ultrafast lab. In this context I want to dedicate special thanks to our supportive staff, **Martina Edenhofer**, **Denise Wedemeyer**, **Reinhold Rath** and **Namvar Jahanmehr**.

Finally, I want to particularly thank all of my friends and family which supported me over the long way towards the PhD. Here I want to especially mention Lucas and Lukas, which were always available for long discussions and long evenings. Moreover, I have to thank my parents and my brother who supported me uncountable amounts of time and who provided distraction. Without them, this work would not have been possible. Last but not least, huge thanks go towards my amazing girlfriend Naomi, which was always there when

I needed it the most, who was comprehensive and supportive particularly during the final phase of the thesis and who ensured that I don't forget to eat.